Moonlight Measurements of Stratospheric Trace Gases During the 2003 Antarctic Winter

A thesis
submitted in partial fulfilment
of the requirements for the Degree
of
Doctor of Philosophy in Physics
in the
University of Canterbury
by
Rebecca Batchelor

Department of Physics and Astronomy
University of Canterbury
2005

SICAL
ENCES
RARY
QC
381.2
.S8
B328
2005

Abstract

The first wintertime spectroscopic measurements of HCl in the Antarctic stratosphere have been made, using the moon as a light source. These measurements have been presented in conjunction with lunar measurements of HNO_3, solar measurements of both gases, and meteorological data, allowing a picture of the evolution of the trace gases during 2003 to be developed. The measurements have provided verification of our current understanding of winter processes, including the formation of polar stratospheric clouds, the conversion of HCl to active forms of chlorine, and the redistribution of nitrogen trace gases within the stratosphere. The springtime deactivation of chlorine has also been clearly demonstrated, with measurements of $ClONO_2$ used to investigate chlorine repartitioning at this time. Measurements of HNO_3 have been broken down into narrow altitude regions and used to demonstrate denoxification, denitrification, and nitrification processes, as well as the ability of FTIR measurements to produce height-resolved data. The HCl and HNO_3 measurements have also been compared to the chemical transport model SLIMCAT, showing generally good agreement, although this was limited by the equilibrium treatment of polar stratospheric cloud formation in the model. Finally, winter measurements of HNO_3 have been combined with lidar observations of polar stratospheric clouds, allowing an estimate of the rate of HNO_3 uptake to be determined and demonstrating a clear link between HNO_3 fluctuations and the phase of the clouds. A link between brief anomalous increases in the gas phase HNO_3 during otherwise denitrified conditions and large nitric acid-containing particles has also been proposed.

10 JUN 2005

Acknowledgements

This research could not have been conducted without the support of a huge number of people and organizations, all of whom I owe my eternal gratitude.

The research has been conducted as a joint project between the University of Canterbury and the National Institute for Water and Atmospheric Research, with financial and logistical support for the ten-month field campaign in Antarctica provided by Antarctica New Zealand. It has been fun being part of three organizations, and I'd really like to thank all of the people in all of these places for their part in helping me through this process.

I would especially like to acknowledge my supervisors, Darlene Heuff, Stephen Wood and Brian Connor. None of this would have been possible without you.

Additionally, I would like to acknowledge the huge amount of support and time given to me by the team at NIWA Lauder, technically, scientifically and emotionally. For a little place in the middle of nowhere, Lauder has definitely provided me with more opportunities than I could have dreamed of. Likewise, I'd like to acknowledge the Scott Base winter-over team of 2003 - a wonderful group of people who could make anything happen! Their support and encouragement over the long Antarctic winter made the field component of this research one of the best experiences of my life.

One of the most rewarding aspects of this work has been the chance to interact with a wide range of scientists from around the world. I'd particularly like to acknowledge the contributions made by Justus Notholt (University of Bremen), Martyn Chipperfield (University of Leeds), Terry Deshler (University of Wyoming), and especially Paola Massoli (Institute for Atmospheric Science and Climate, CNR). It has been wonderful to work with you.

Finally, I'd like to thank Phil and Miriam for helping me with editing and Ben and Marita for giving me a place to stay in my never-ending trips to Christchurch. Last, but by no means least, I'd like to thank my wonderful family - Mum, Dad, Jess, and Matt, for helping me through the good times and the bad, for late-night phone calls, organizing my wedding, sending care packages to the ice and for generally being the most amazing, wonderful, supportive family a girl could ask for. I could never have done it without you!

Contents

Figures

Tables

Chapter 1

Introduction

Few scientific questions in modern times have elicited the interest and attention that the Antarctic 'ozone hole' has. Since the first proposal that ozone destruction could be caused by chlorine catalysts introduced to the stratosphere as chlorofluorocarbons (CFCs) (*Molina and Rowland*, 1974) and the subsequent discovery of the 'ozone hole' over Antarctica (*Farman et al.*, 1985), the chemistry of the stratosphere over the polar regions has been the subject of many investigations (*WMO*, 1994, 1998, 2002). Absent from most of these investigations, however, is a consistent set of measurements made during the Antarctic polar night. The combination of continuous darkness and limited accessibility to the continent has meant that trace gas measurements during the winter months have largely been excluded. This research addresses this deficiency by taking the first-ever Antarctic infrared spectroscopic measurements of the chlorine reservoir species hydrogen chloride (HCl) using the light of the moon. In addition, measurements of nitric acid (HNO_3), a nitrogen reservoir species and key component of polar stratospheric clouds, have been made. In combination, these measurements provide a clearer picture of the stratospheric processes occurring during the polar night.

1.1 Polar measurements of ozone-related trace gases

While ozone was first identified as the trace gas responsible for the absorption of solar UV within our atmosphere as early as 1881, and was studied in depth from the early 1900's (*Fabry and Buisson*, 1913; *Dobson and Harrison*, 1926; *Brewer and Milford*, 1960; *Dobson*, 1968), it wasn't until the proposal of *Bates and Nicolet* (1950) that it was realized that other trace gases could play an important role in regulating the amount of ozone in our atmosphere.

Bates and Nicolet (1950) proposed that hydrogen compounds, produced in the stratosphere by photolysis of water vapour, could catalytically destroy ozone. This was followed by the realization that nitrogen (*Crützen*, 1970; *Johnston*, 1971), chlorine (*Molina and Rowland*, 1974; *Stolarski and Cicerone*, 1974), and bromine (*Wofsy et al.*, 1975) species could also contribute to ozone regulation through catalytic reactions in the atmosphere.

Perhaps the most important of these realizations was the proposal that anthropogenic chlorine, released to the stratosphere as chlorofluorocarbons (CFCs), could result in

widespread ozone loss (*Molina and Rowland*, 1974). While this immediately became an issue of intense study, it was thought that the effect on the ozone layer in the immediate future would be minimal, and ozone loss of the order of 5 - 19% would be observed over the next 50 - 100 years (*Wuebbles*, 1983; *Cicerone et al.*, 1983; *Prather et al.*, 1984; *Solomon*, 1988). There was no reason to predict that the Antarctic atmosphere would be any more likely than anywhere else to experience this depletion (*Solomon*, 1999), and as such, when the significant depletion of ozone in the Antarctic spring stratosphere was discovered (*Farman et al.*, 1985), there were few corresponding trace gas measurements in the region to identify why.

The first major Antarctic field study of the trace gases in the Antarctic stratosphere was carried out in the spring of 1986. The primary goal of NOZE (the National Ozone Expedition) was to measure as many ozone-related chemical constituents as possible in the Antarctic atmosphere (*Hofmann*, 1988). It was based primarily at McMurdo Station (78°S, 167°E) and included measurements made from balloons (*Rosen et al.*, 1988a; *Hofmann*, 1988; *Hofmann et al.*, 1988) as well as ground-based visible, infrared, and millimetre-wave measurements (*Farmer et al.*, 1987; *Mount et al.*, 1987; *Solomon et al.*, 1987a,b; *Murcray et al.*, 1989). Some of the UV and visible measurements were made by the light of the full moon, allowing measurements to be made during the long nights of early spring (*Mount et al.*, 1987; *Solomon et al.*, 1987b; *Sanders et al.*, 1987, 1989).

Measurements of chlorine species showed chlorine to be highly perturbed (*deZafra et al.*, 1987; *Solomon et al.*, 1987a,b; *Farmer et al.*, 1987), in line with the halocarbon (or CFC) ozone depletion theory of *Farman et al.* (1985) and *Solomon et al.* (1986). This theory suggested a strong link between chlorine in the atmosphere and loss of ozone, intensified by the Antarctic winter conditions. The formation of polar stratospheric clouds (PSCs) in the polar vortex (*McCormick et al.*, 1982; *McCormick and Trepte*, 1986) was the key to the theory, as on their surface heterogeneous reactions were able to occur that converted chlorine from its reservoir species to active forms, which were then able to catalytically destroy ozone with the return of the sun in spring (*McElroy et al.*, 1986a,b).

Subsequent ground-based measurements were carried out in the spring of 1987 (*Hofmann et al.*, 1989a; *Kuester et al.*, 1989; *Carroll et al.*, 1989; *Jaramillo et al.*, 1989) and were supplemented with data collected from AAOE, the Airborne Antarctic Ozone Experiment (*Special Edition*, 1989a,b; *Tuck et al.*, 1989; *Kelly et al.*, 1989). These campaigns were very successful in making simultaneous measurements of a wide variety of ozone-related tracers, chlorine and bromine molecules, atmospheric parameters, and ozone (*Special Edition*, 1989a,b). The measurements confirmed the earlier observations that active chlorine species such as ClO and OClO exhibited very high concentrations in early spring (*deZafra et al.*, 1989; *Brune et al.*, 1989; *Sanders et al.*, 1989; *Solomon et al.*, 1989; *Wahner et al.*, 1989b) while reservoir species such as HCl showed very low values, climbing

to much higher values with the sunlight in late September (*Toon et al.*, 1989; *Coffey et al.*, 1989). Additionally, the Antarctic atmosphere was shown to be dehydrated (*Kelly et al.*, 1989) and denitrified (*Wahner et al.*, 1989a; *Fahey et al.*, 1989a). This was thought to relate to the solid nitric acid trihydrate and ice composition of polar stratospheric clouds (*Toon et al.*, 1986; *Hamill et al.*, 1986; *Ramaswamy*, 1988; *Fahey et al.*, 1989a; *Kinne et al.*, 1989).

Some of the first Arctic measurements made were full moon, near-UV measurements of OClO by *Solomon* (1988) in the winter of 1987/1988. Scattered sunlight and direct moon observations of ozone and NO_2 were also made in that winter (*Mount et al.*, 1988). These measurements suggested that the Arctic stratosphere was also perturbed and that ozone loss in this hemisphere was imminent. The proximity of the Arctic polar vortex to highly populated areas made the understanding of ozone depletion in this region even more important than for the Antarctic (*Solomon*, 1999), so much of the attention was focused there.

The first major Arctic campaign was AASE, the Airborne Arctic Stratospheric Expedition. This was launched to determine the mechanisms, if any, of ozone depletion and redistribution in the northern polar stratosphere, including the influences of Arctic meteorology and PSCs formed at low temperatures (*Turco et al.*, 1990). While it was known that the polar vortex in the Arctic was less robust than its counterpart in the south, and subsequently experienced warmer temperatures, PSCs had been observed in the Arctic (*McCormick et al.*, 1982) and hence ozone loss was possible.

Similar instruments to those used in AAOE the year before were flown on the aircraft (*Turco et al.*, 1990), allowing a variety of trace gas measurements to be made (*Mankin et al.*, 1990; *Toohey et al.*, 1990; *Hubler et al.*, 1990; *Fahey et al.*, 1990; *Carroll et al.*, 1990; *Kelly et al.*, 1990). Additional measurements were made from balloons and the ground (*Hofmann et al.*, 1989b; *Kondo et al.*, 1990). Chlorine chemistry was shown to be perturbed in a way comparable to chemistry in the Antarctic (*Brune et al.*, 1990; *Schiller et al.*, 1990; *Mankin et al.*, 1990).

Importantly, studies of polar stratospheric clouds were made as part of AASE (*Kruger*, 1990; *Hofmann*, 1990), showing both Type I (containing nitric acid) and Type II (water ice) clouds to be present (*McCormick et al.*, 1990; *Browell et al.*, 1990). Type I clouds were shown to exist in two forms, consistent with solid clouds (probably nitric acid trihydrate) and liquid clouds (possibly supercooled ternary solutions of nitric acid, sulfuric acid and water) (*Browell et al.*, 1990; *Toon et al.*, 1990b). These could be identified by their optical properties (*Browell et al.*, 1990). Denitrification processes were linked with PSC formation (*Wofsy et al.*, 1990; *Gandrud et al.*, 1990; *Toon et al.*, 1990a), though a consistent theory was not established at this time (*Turco et al.*, 1990).

A second Airborne Arctic Stratospheric Expedition (AASE-II) through the north-

ern hemisphere winter of 1991/1992 (*Anderson and Toon*, 1993) was launched to further address questions of ozone chemistry in the Arctic and upper mid-latitudes. Results from these studies were published in special editions of Geophysical Research Letters and Science (*Special Edition*, 1993a,b). Of particular importance were studies involving simultaneous measurements of ClO and HCl. Combined with air parcel trajectory analysis, large losses of HCl were shown to be a result of conversion to ClO and Cl_2O_2 at temperatures less than 196 $\pm$ 4 K (*Webster et al.*, 1993b,a; *Toohey et al.*, 1993; *Schoeberl et al.*, 1993). Decreases of ClO in the spring were consistent with the rapid formation of $ClONO_2$ by recombination of ClO with nitrogen dioxide (NO_2) released photochemically from the nitric acid contained in Type I PSCs (*Webster et al.*, 1993b; *Schoeberl et al.*, 1993). This was in contrast to the Antarctic, where the loss of active chlorine was to HCl in the slower reaction Cl + CH_4, a result of nitrogen being lost by denitrification (*Webster et al.*, 1993b; *Toohey et al.*, 1993; *Douglass et al.*, 1995).

Simultaneously with the AASE-II campaign, the European scientific community came together to perform ground-based, balloon and aircraft measurements under the European Arctic Stratospheric Ozone Experiment (EASOE) (*Pyle et al.*, 1994; *Special Edition*, 1994). Balloon-borne instruments gave detailed vertical profile information of chlorine, bromine, and nitrogen species (*Schmidt et al.*, 1994; *Pommereau and Piquard*, 1994b,a; *Arnold and Spreng*, 1994; *Fabian et al.*, 1994; *Murcray et al.*, 1994; *Kondo et al.*, 1994b). Column measurements of ClO, HCl, O_3 and HNO_3 were made from aircraft (*Crewell et al.*, 1994; *Blom et al.*, 1994; *Brandtjen et al.*, 1994). Ground-based measurements included millimetre-wave emission measurements (*deZafra et al.*, 1994; *Emmons et al.*, 1994), lidar observations (*Neuber et al.*, 1994; *Beyerle and Neuber*, 1994; *Beyerle et al.*, 1994), and UV-visible spectroscopic measurements (*Goutail et al.*, 1994; *Fish et al.*, 1994). In addition, the first wintertime FTIR trace gas measurements were made by the light of the moon (*Notholt et al.*, 1993; *Notholt*, 1994; *Notholt and Schrems*, 1994, 1995; *Notholt et al.*, 1995, 1997b,a; *Notholt and Lehmann*, 2003). A specialized lunar InSb detector allowed zenith column density measurements of O_3, N_2O, CH_4, NO_2, C_2H_6, HCl and HF to be made. An unadapted MCT detector on the same instrument increased the range to include $ClONO_2$ and HNO_3. This work showed a considerable reduction in the amount of stratospheric HCl and $ClONO_2$ by mid-December, when several weak PSC events had occurred (*Notholt et al.*, 1995). More importantly, it represented a major step forward in allowing ground-based infrared measurements to be made when the solar light source was unavailable.

Another important data source came in the form of UARS (the Upper Atmosphere Research Satellite), which was launched on September 12th, 1991 (*Reber et al.*, 1993). On board UARS were four instruments of particular importance for extending our understanding of ozone-related trace gases. These were MLS (the Microwave Limb Sounder)

which was able to take measurements of O_3, ClO, H_2O, HNO_3, temperature and pressure using thermal emission techniques (*Barath et al.*, 1993); CLAES (the Cryogenic Limb Array Etalon Spectrometer) which measured temperature, pressure, O_3, H_2O, CH_4, N_2O, NO, NO_2, N_2O_5, HNO_3, $ClONO_2$, CCl_3F, CCl_2F_2 and aerosol absorption coefficients using infrared emission interferometry (*Roche et al.*, 1993a); ISAMS (the Improved Stratospheric And Mesospheric Sounder), which measured CO, CO_2, CH_4, NO, N_2O, NO_2, N_2O_5, HNO_3 and H_2O using pressure modulator radiometry (*Taylor et al.*, 1993); and HALOE (the HALogen Occultation Experiment) which was able to take vertical profiles of O_3, HCl, HF, CH_4, H_2O, NO, NO_2 and measure aerosol extinction, temperature, and pressure, using solar occultation techniques (*Russell et al.*, 1993). These instruments were able to make measurements at latitudes up to 80° north and south, providing a large quantity of trace gas measurements from the Arctic and Antarctic stratospheres. These observations have been used for many studies of stratospheric processes (*Special Edition*, 1993c; *Dessler et al.*, 1998, and references therein), including some important studies of nitric acid during the Antarctic winter (*Santee et al.*, 1996, 1998). Of note, however, is the fact that because HALOE is a solar occultation instrument, it can only make measurements during UARS orbit sunrise and sunsets. As such, while measurements can be made to 80° latitude, there are no measurements from this instrument through the polar winter.

Measurements of various trace gas species were also made as part of the Atmospheric Trace Molecule Spectroscopy (ATMOS) experiment (*Gunson et al.*, 1996). The ATMOS Fourier transform spectrometer was flown on board the space shuttle in November 1994 and included sunrise and sunset occultation measurements inside and outside the Antarctic vortex. Again this instrument did not make measurements during the polar night.

Back on Earth, a range of campaigns have continued in the Arctic. These include the second and third European stratospheric ozone experiments, SESAME (Second European Arctic and Mid-latitude Experiment) and THESEO (Third European Stratospheric Experiment on Ozone) (*Newman et al.*, 2002). THESEO was additionally combined with the NASA SOLVE (SAGE III Ozone Loss and Validation Experiment) campaign (*Newman et al.*, 2002). QUOBI (Quantitative Understanding of Ozone losses by Bipolar Investigations) has been one of the most recent campaigns, involving ozonesondes launched throughout the northern and southern polar winters, coupled with extensive modelling campaigns (*Braathen*, 2002). While these campaigns have provided much-needed information on a range of processes occurring during the northern hemisphere winter, few of these measurement programs have been carried out in the southern hemisphere.

To the best of my knowledge, the only Antarctic campaign to include wintertime measurements of the chlorine reservoir species HCl was the ASHOE/MAESA (Airborne Southern Hemisphere Ozone Experiment/Measurements for Assessing the Effects of Strato-

spheric Aircraft) campaign (*Tuck et al.*, 1997). This was an airborne campaign designed to address the depletion of ozone in southern mid-latitudes and additionally address the effects of stratospheric aircraft. A total of 19 flights reached the Antarctic vortex edge region, during four time periods of 1994. Results from this campaign were published in two special editions of the Journal of Geophysical Research (*Special Edition*, 1997a,b). In-situ measurements of HCl were made at an altitude of approximately 15 - 20 km during these flights and showed chlorine activation to be occurring in the polar vortex when temperatures fell below 195 K (*Jaegle et al.*, 1997; *Kawa et al.*, 1997).

While major measurement campaigns provide 'snapshots' of the trace gases and processes that contribute to ozone loss, long-term observational programs are needed in order to study trends and develop a better picture of the annual cycle. In addition to satellite measurement programs such as UARS, many of the Antarctic stations have ground-based measurement programs that include ozone-related trace gases (*Cronn et al.*, 1986; *Kondo et al.*, 1994a; *Hofmann et al.*, 1997; *Ricaud et al.*, 1998). Many of these measurements do not appear regularly in the literature. Arrival Heights (77.83° S, 166.65°), where this work has been carried out, is a Network for the Detection of Stratospheric Change (NDSC) primary station. As such, long-term measurements of stratospheric trace gases are made in the microwave (*Solomon et al.*, 2000, 2002), UV/visible (*Nichol and Valenti*, 1993; *Nichol et al.*, 1996; *Kreher et al.*, 1996, 1997), and infrared (*Murcray et al.*, 1989; *Keys et al.*, 1993, 1998; *Wood et al.*, 2002, 2004) regions. Measurements of the two trace gases this work focuses on, HCl and HNO_3, from the Fourier transform infrared spectrometer (FTIR) at Arrival Heights, are presented in Figure 1.1.

These FTIR time series provide important information for quantifying long-term trends in the trace gases and additionally provide observational data for understanding the spring period when ozone depletion is occurring. The obvious deficiency in them, however, is the four-month gap through the austral winter when the stratosphere is being primed for ozone depletion. The advancement of our understanding of the preconditioning of the polar stratosphere during the winter which would be gained by addressing this seasonal gap has provided the motivation for this research.

1.2 Thesis layout

In this research, first-ever infrared spectroscopic measurements of the chlorine reservoir species HCl have been made in Antarctica using the moon as a light source, following the work of *Notholt* (1994); *Notholt and Lehmann* (2003). In addition, measurements of the nitrogen reservoir species HNO_3 have been made. Measurements of both trace species are presented with their corresponding solar measurements to provide a picture of the evolution of these gases throughout the entire 2003 Antarctic year. The layout of the

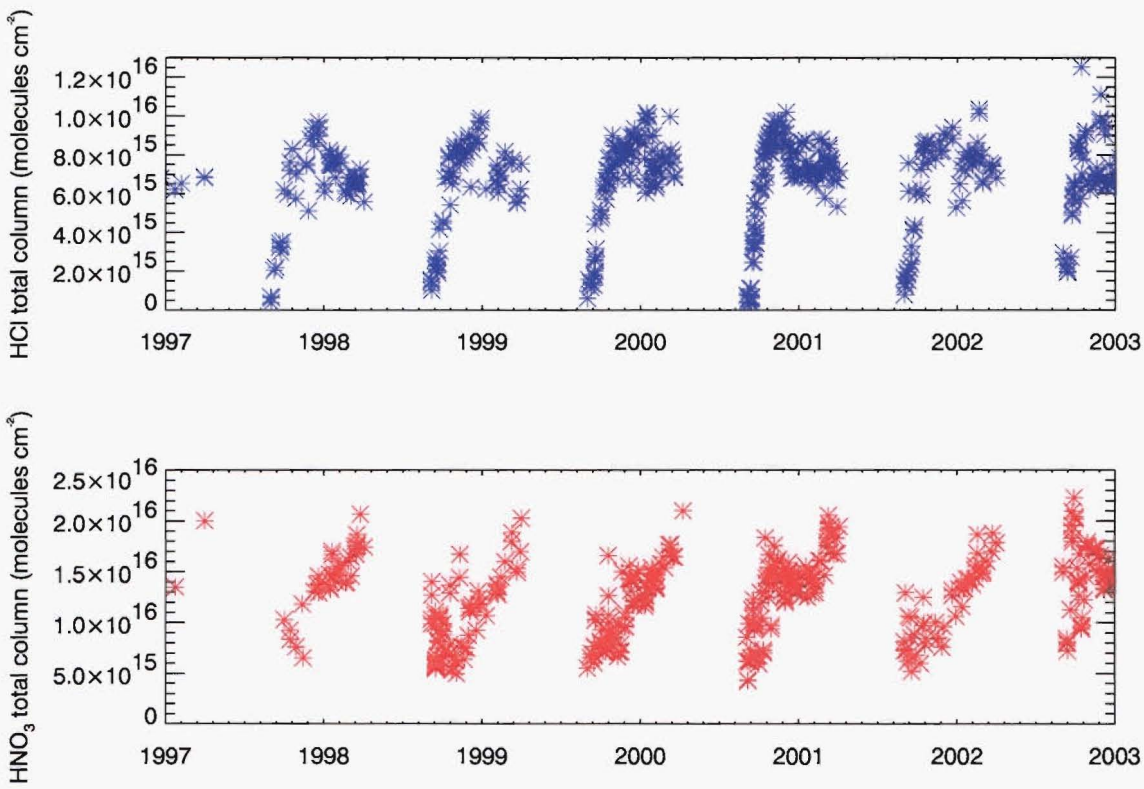

Figure 1.1: Time series of HCl and HNO_3 total column amounts made from Arrival Heights, Antarctica, with a Fourier transform infrared spectrometer using the sun as a light source [Stephen Wood, National Institute of Water and Atmosphere, personal communication].

thesis is as follows:

Chapter 2 provides a short introduction to the stratospheric physics and chemistry that result in springtime polar ozone depletion. Included in this chapter is a section on polar stratospheric clouds, whose existence serves to link the trends observed in the HCl and HNO_3 partial column amounts.

In Chapter 3, the tools used for the research are presented. The chapter will look first at the Fourier transform infrared spectrometer which has been used for obtaining the absorption spectra of HCl and HNO_3, and then at the retrieval tools that have been used for obtaining trace gas profiles from those spectra. This will be followed in Chapter 4 by the measurement details of both the HCl and HNO_3 data sets. Information on the complementary meteorological data sets used for interpreting the observations will also be presented in this chapter.

Chapter 5 outlines the analysis and error quantification of the trace gas measurements. While the analysis of both solar and lunar measurements of HCl and HNO_3 will be presented, the description focuses particularly on the moonlight measurements. Moonlight FTIR measurements have previously been made in the Arctic (*Notholt*, 1994; *Notholt and*

Lehmann, 2003), and the analysis of the HNO_3 measurements is based on this work. Little has been published regarding the analysis of lunar HCl spectra, however, and the analysis of these observations has therefore been described in depth. A detailed error analysis, based on the work of *Rodgers* (2000), will also be presented.

The evolution of HCl and HNO_3 partial column amounts through the 2003 year will be discussed in Chapter 6. The measurements have been presented in conjunction with meteorological analyses and will be compared and contrasted with studies in the literature. The year has been broken down to look at the pre-winter, early winter, late winter, and spring periods. In addition, the HNO_3 measurements have been broken down into the smallest partial columns that the measurements can realistically provide information on, allowing the heights of the denoxification and denitrification processes that occur in the Antarctic stratosphere to be demonstrated.

In Chapter 7, the HCl and HNO_3 measurements have been compared to a recent run of the three-dimensional chemical transport model, SLIMCAT. As much of our understanding of the processes involved in ozone depletion is based on models of the processes occurring during the Antarctic winter, this is an opportunity to test how well our current understanding matches the observed atmosphere.

Chapter 8 expands on the link between observations of nitric acid and polar stratospheric cloud processes by presenting a first-ever coupling of nitric acid measurements and lidar observations of PSCs from co-located ground-based instruments. This work uses HNO_3 measurements made since 1998 to look for links between PSC processes and gas phase nitric acid. The work is a collaborative project between myself and PhD student Paola Massoli (Institute for Atmospheric Science and Climate, CNR, Rome), and as such, her doctoral thesis 'Study of Polar Stratospheric Clouds in Antarctica through LIDAR measurements' (*Massoli*, 2005) serves as a companion paper to this chapter.

Finally, Chapter 9 provides a summary of the entire thesis. Also presented in this chapter are my contributions to the overall understanding of Antarctic stratospheric processes and some suggestions for further work.

Chapter 2

Background

In this chapter, a brief introduction to the stratospheric chemistry and dynamics needed to explain springtime polar ozone depletion will be presented. Additionally, a short section on polar stratospheric clouds, whose existence serves to link the observed trends in the HCl and HNO_3 partial column amounts, will be given.

2.1 Dynamics, distribution and the polar vortex

2.1.1 Large scale circulation

The general circulation of the stratosphere[1] was first identified by Dobson and Brewer as a result of early studies of ozone (*Dobson et al.*, 1927, 1930) and water vapour (*Brewer*, 1949). Ozone was observed to have a latitudinal gradient, with minimum amounts near the equator, where most ozone was created, and maximum amounts nearer the poles. Additionally, a seasonal dependence showing maximum amounts in the autumn and minimum amounts in the spring was identified (*Dobson et al.*, 1930). These studies led to an understanding of the dynamical motion of the stratosphere, known as the Dobson-Brewer circulation, whereby heated air rises near the equator, moves poleward, cools, and descends in the mid-high latitudes.

The Dobson-Brewer motion is responsible for the transport of trace gases from the troposphere into the stratosphere near the tropics and the subsequent distribution of long-lived species through the entire stratosphere. The latitudinal gradient observed in many trace gases (see, for example, the UARS reference atmosphere project trace gas profiles at http://www.sparc.sunysb.edu) can be broadly attributed to this process. A schematic of the motion of the atmosphere, including the large scale ascent and descent of the Dobson-Brewer diabatic motion and the stirring effects of planetary waves, as given in *WMO* (1998), is shown in Figure 2.1.

[1]The stratosphere is the region of the atmosphere between approximately 15 and 50 km above the Earth's surface, where temperatures increase with altitude as a result of absorption of UV by ozone molecules. The bottom of the stratosphere is known as the tropopause, below which is the troposphere. The altitude of the tropopause varies with season and is at its lowest (approximately 7 km) in the winter polar regions.

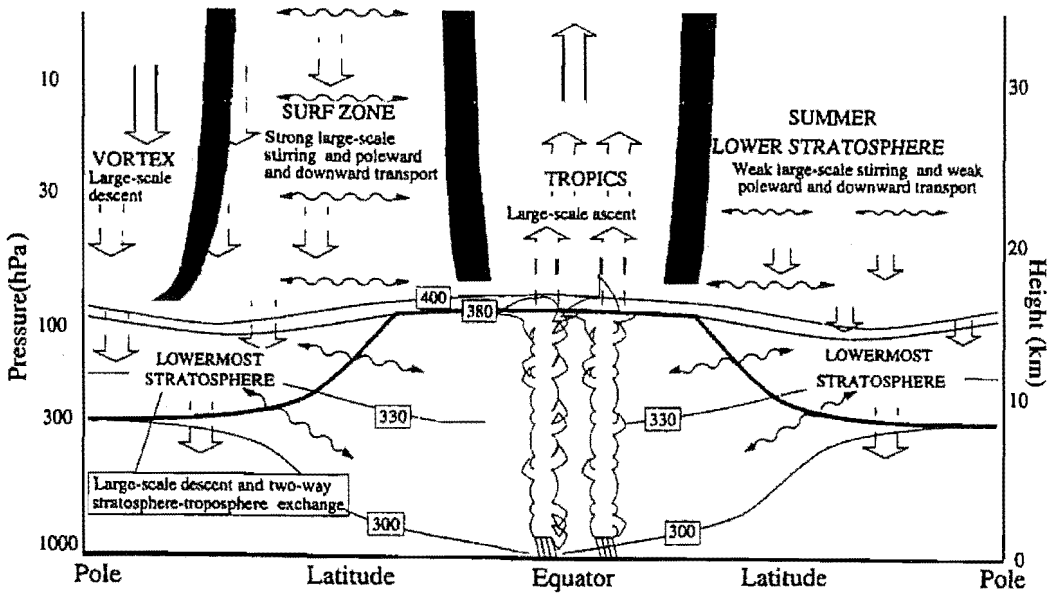

Figure 2.1: Principal regions of the lower stratosphere showing the major transport characteristics. The winter hemisphere is shown on the left and the summer on the right. Broad arrows show diabatic (Brewer-Dobson) circulation and wavy arrows show stirring along isentropic surfaces. The solid line starting at around 7 km at the pole and reaching about 15 km at the equator denotes the tropopause. Lighter lines with boxed labels indicate potential temperature surfaces. Schematic from *WMO* (1998, page 7.20)

2.1.2 The polar vortex

During the winter, the steep latitudinal gradient in temperature resulting from 24-hour darkness in the polar region causes a strong jet of westerly winds, known as the polar vortex, to form in the stratosphere. These winds, which reach velocities of more than 100 m s^{-1} (*Wayne*, 2000), act as a barrier for long-range transport and prevent mixing of polar air with warmer mid-latitude air. The polar vortex may be thought of as an approximately cylindrical mass of air in which descent caused by radiative cooling results in a flow from the stratopause to the tropopause, with very little leakage to the sides (*Wauben et al.*, 1997). The vortex is not completely isolated, but experiences a small, typically outward, flow from the vortex edges and in the lowermost regions of the stratosphere (*Schoeberl et al.*, 1992; *Bowman*, 1993; *Manney et al.*, 1994; *Wauben et al.*, 1997). It is, however, generally considered to be a strong barrier to latitudinal mixing above approximately 400 K ($\sim$ 15 km, see Figure 2.1) (*Schoeberl et al.*, 1992; *Bowman*, 1993; *Manney et al.*, 1994).

Inside the vortex, the isolated air radiatively cools and descends (*Rosenfield et al.*, 1994), reaching temperatures below the condensation point of nitric acid ($\sim$ 195 K) and often even below the condensation point of water ($\sim$ 188 K). This results in the formation of polar stratospheric clouds (Section 2.2), which provide surfaces for heterogeneous

chemistry (Section 2.3.2). Because the air inside the vortex is isolated, chemically perturbed air is contained over the polar regions. In the southern hemisphere, this results in the well defined 'ozone hole', which remains over the Antarctic continent until the vortex breaks down.

Outside the vortex region, circulation and descent result in a build-up of many trace gases at the vortex edge. This is seen particularly clearly in the 'collar region' of HNO_3 and $ClONO_2$ identified in CLAES data (*Roche et al.*, 1993b, 1994).

While the vortex serves as a containment vessel for most of the air within, planetary waves can influence the shape and location of the vortex. The Antarctic polar vortex is typically fairly symmetrical around the pole due to the large expanses of ocean around the continent limiting planetary wave activity (*Waugh and Randel*, 1999; *Waugh et al.*, 1999). As such, most of the vortex experiences 24-hour darkness, temperatures become very low, and PSC cover of the vortex region is extensive (*McCormick and Trepte*, 1986; *McCormick et al.*, 1989). In contrast, topographical features in the northern mid to high latitudes mean that planetary wave activity in the Arctic is more intense, hence the vortex is less symmetrical and more variable than in the south (*Waugh and Randel*, 1999; *Waugh et al.*, 1999). This allows more movement of the vortex into sunlit areas, warmer temperatures and thus fewer PSCs (*McCormick et al.*, 1982; *McCormick and Trepte*, 1986). Total ozone mapping spectrometer (TOMS) images of ozone from spring are shown in Figure 2.2. The well defined, symmetrical vortex is clearly visible in the southern hemisphere,

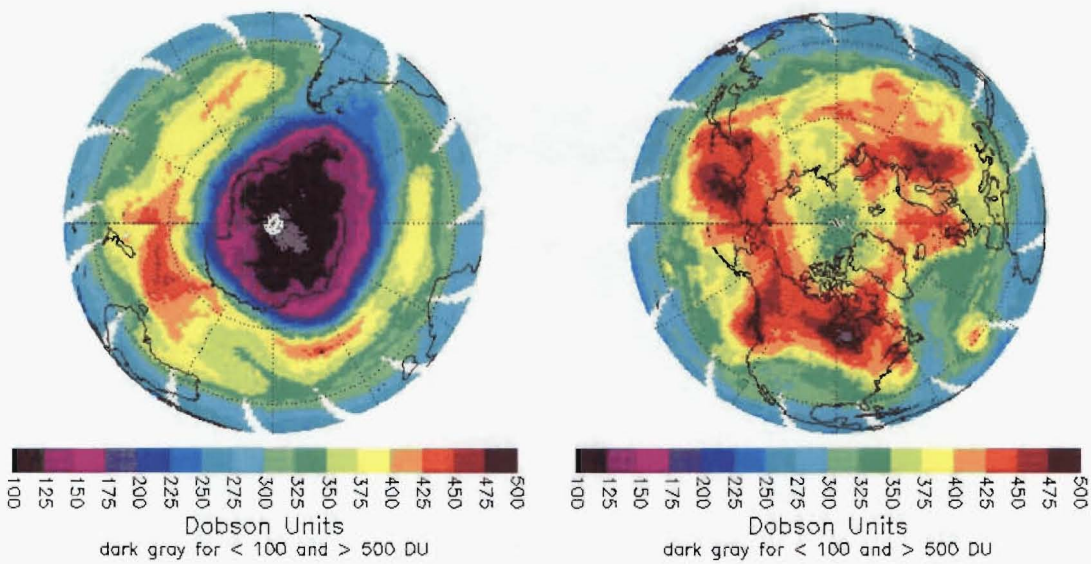

Figure 2.2: Total column ozone amount, as determined by the Total Ozone Mapping Spectrometer, for the southern (left) and northern (right) springtime. Measurements correspond to October 1st and April 1st, 2003, respectively. The vortex edge is clearly defined by the ozone amounts in both plots, though the Arctic vortex is much less symmetrical than the Antarctic vortex as a result of wave activity. Plots are from the TOMS website, http://jwocky.gsfc.nasa.gov.

with severe ozone depletion contained within. The northern hemisphere experiences less ozone depletion than the south, but the vortex edge is visible by the dynamically induced build-up of ozone on the equatorward side of it.

The final break up of the polar vortex typically occurs in late spring (northern hemisphere) or early summer (southern hemisphere). It is characterized by the mixing of air below 400 K (*Bowman*, 1993) and regions of material being stripped off the vortex and drawn out as filaments into the mid-latitudes (*Bowman*, 1993; *Manney et al.*, 1994). The mixing of ozone-poor air from the Antarctic polar vortex has been shown to result in an average 5-6% reduction in the total column ozone amount over the southern mid-latitudes (*Ajtic et al.*, 2004), with larger localized depletions resulting from individual events (*Atkinson and Plumb*, 1997; *Ajtic et al.*, 2003). The resulting increase in UV at the surface has the potential for significant health effects in populated areas (*UNEP*, 1994, 1998, 2002).

2.2 Polar stratospheric clouds

Polar stratospheric clouds (PSCs), with their stunning, luminous colours that lighten the sky before the sun rises in the spring (Figure 2.3), have been admired since the earliest days of Antarctic exploration (see, for example, the diary of Robert Falcon Scott, August 1st, 1911).

Figure 2.3: Polar stratospheric clouds, as observed over Ross Island, Antarctica, in early spring, 2003. Photo by Matt Okraszewski.

The name 'polar stratospheric cloud' was first coined by *McCormick et al.* (1982) when satellite observations showed clouds to be present in the Antarctic stratosphere. Since

their role in ozone depletion was discovered, the study of PSCs has been intense, yet they remain one of the least understood aspects of the ozone depletion process (*WMO*, 2002).

Polar stratospheric clouds were originally classified as being one of two types: Type I PSCs, which were thought to contain nitric acid, probably in the form of solid nitric acid trihydrate (NAT) and which formed at temperatures several degrees above the ice frost point (*Toon et al.*, 1986; *Crützen and Arnold*, 1986; *Hanson and Mauersberger*, 1988; *Pueschel et al.*, 1990); and Type II PSCs, which formed at the ice frost point and were composed mainly of water ice (*Steele et al.*, 1983).

Based on lidar observations (*Browell et al.*, 1990; *Toon et al.*, 1990b), Type I PSCs were subsequently subdivided into two main types: Type Ia and Type Ib.

Type Ia PSCs were identified as non-spherical solid particles, with low backscatter, high depolarization and typical radii between 1.5 and 2.5 μm (*Browell et al.*, 1990; *Toon et al.*, 1990b; *Deshler et al.*, 1991; *Adriani et al.*, 1995). Early laboratory studies suggested that NAT was the most likely component of Type Ia PSCs (*Hanson and Mauersberger*, 1988; *Hanson et al.*, 1994), and a NAT composition has recently been confirmed by in-situ measurements (*Voigt et al.*, 2000). Nitric acid dihydrate (NAD) may additionally be a component of solid clouds (*Middlebrook et al.*, 1992; *Worsnop et al.*, 1993; *Santee et al.*, 1998; *Tabazadeh et al.*, 2001). The formation process of Type Ia clouds remains uncertain (*WMO*, 2002), but they have been associated with periods of slow cooling (*Beyerle and Neuber*, 1994; *Adriani et al.*, 1995; *Larsen et al.*, 1997; *Tabazadeh et al.*, 2001) and temperatures below the nitric acid condensation temperature, T_{NAT} (*Pueschel et al.*, 1990; *Larsen et al.*, 1996; *David et al.*, 1998).

Type Ib PSCs were identified as spherical liquid particles, with high backscatter and low depolarization (*Browell et al.*, 1990; *Toon et al.*, 1990b; *Adriani et al.*, 1995; *Larsen et al.*, 1997), consisting of supercooled ternary solutions (STS) of H_20, HNO_3 and H_2SO_4 (*Toon et al.*, 1990b; *Molina et al.*, 1993; *Tabazadeh et al.*, 1994b; *Carslaw et al.*, 1994). Type Ib PSCs have been associated with periods of fast, smooth, synoptic cooling (*Deshler et al.*, 1991; *Adriani et al.*, 1995; *Larsen et al.*, 1997) and are formed by the rapid uptake of gas phase nitric acid and water on aqueous H_2SO_4 aerosols at a temperature approximately 3 - 4 K below T_{NAT}. The composition and volume of the aerosols depends on the temperature and the amounts of each of the constituents (*Tabazadeh et al.*, 1994a; *Carslaw et al.*, 1995; *Luo et al.*, 1995), but their size is typically limited to radii of less than 0.5 μm (*Toon et al.*, 1990b).

A further PSC type, Type Ic, was proposed by *Tabazadeh and Toon* (1996). They inferred solid phase meta-stable water-rich HNO_3/H_2O clouds that were a possible precursor of the stable NAT or NAD in Type Ia PSCs. Measurements from the MLS instrument have provided evidence of these clouds (*Santee et al.*, 1998).

Type I and Type II polar stratospheric clouds play a dual role in ozone depletion. In

addition to providing a surface for heterogeneous reactions (to be discussed in Section 2.3.2), they also play a role in the redistribution of nitric acid in the atmosphere. This will be discussed further in Chapter 6.

2.3 Chemistry of ozone and ozone-related trace gases

2.3.1 Gas phase ozone chemistry

Ozone (O_3) is found in a distinct layer in the stratosphere, known as the ozone layer. The ozone layer is found between altitudes of approximately 10 and 25 km, as shown by the ozonesonde profile in Figure 2.4.

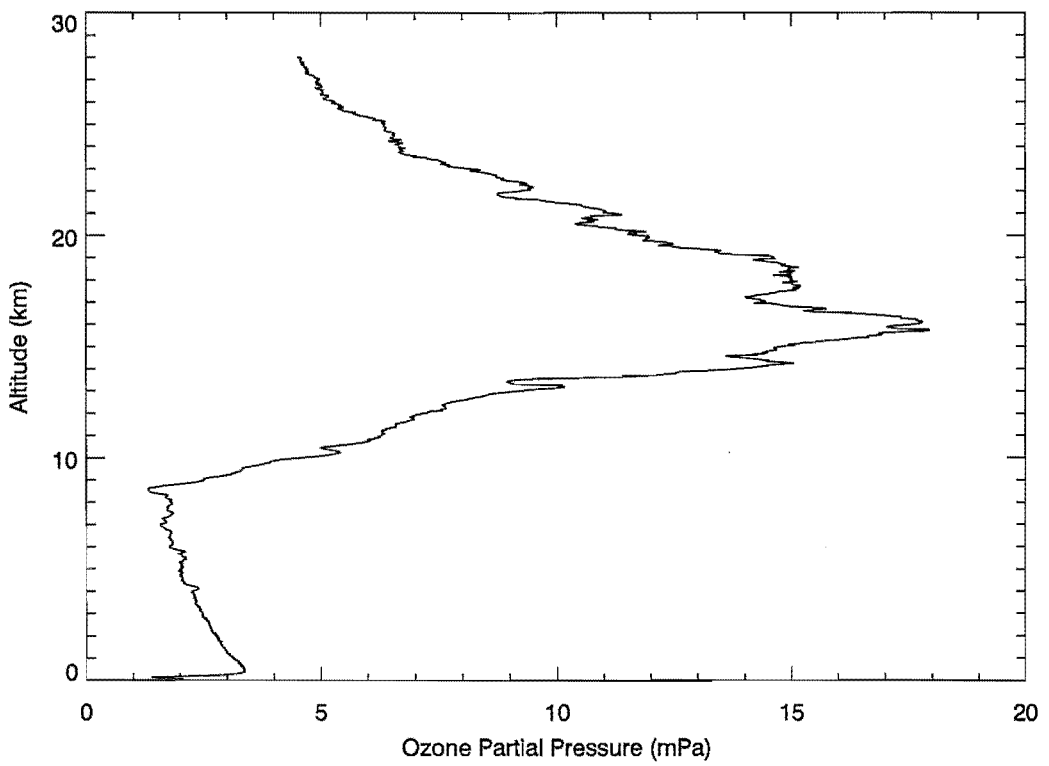

Figure 2.4: A typical non-depleted ozone profile, as measured with an ozonesonde from McMurdo Station, Antarctica, on July 12th, 2003. [Profile courtesy of Terry Deshler, University of Wyoming, personal communication.]

Ozone is created in and above the ozone layer by the disassociation of oxygen molecules by high-energy sunlight through the reactions

$$O_2 + h\nu \rightarrow O + O \tag{2.1}$$

$$O + O_2 + M \rightarrow O_3 + M \tag{2.2}$$

where $h\nu$ indicates sunlight and M is a third body such as O_2 or N_2. It is subsequently destroyed by photolysis through the reactions

$$\begin{aligned} O_3 + h\nu &\rightarrow O + O_2 \quad (2.3) \\ O + O_3 &\rightarrow 2O_2 \quad (2.4) \end{aligned}$$

Reactions 2.1 to 2.4 are known as the Chapman equations (*Chapman*, 1930) and for many years were thought to completely explain ozone chemistry. As measurements of ozone were made and ozone production and destruction rate parameters became better understood (*Götz et al.*, 1934; *Brewer and Milford*, 1960; *Dobson*, 1968), it was found that the Chapman oxygen cycles predicted nearly double the amount of ozone than was actually observed (*Wayne*, 2000). In order to explain this discrepancy, it was proposed that catalytic cycles involving hydrogen, photolysed from stratospheric water vapour, could cause ozone destruction through the reactions

$$\begin{aligned} H + O_3 &\rightarrow OH + O_2 \quad (2.5) \\ OH + O &\rightarrow H + O_2 \\ Net: O + O_3 &\rightarrow O_2 + O_2 \end{aligned}$$

and

$$\begin{aligned} OH + O_3 &\rightarrow HO_2 + O_2 \quad (2.6) \\ HO_2 + O_3 &\rightarrow OH + 2O_2 \\ Net: 2O_3 &\rightarrow 3O_2 \end{aligned}$$

(*Bates and Nicolet*, 1950; *Hampson*, 1964). It was subsequently found that nitrogen (*Crützen*, 1970; *Murcray et al.*, 1968; *Johnston*, 1971), chlorine (*Stolarski and Cicerone*, 1974; *Molina and Rowland*, 1974), and bromine (*Wofsy et al.*, 1975; *Yung et al.*, 1980) compounds could also catalytically destroy ozone, through the general reaction cycle

$$\begin{aligned} X + O_3 &\rightarrow XO + O_2 \quad (2.7) \\ XO + O &\rightarrow X + O_2 \\ Net: O + O_3 &\rightarrow O_2 + O_2 \end{aligned}$$

where X may be replaced with NO, Cl, or Br.

H and OH; N and NO; Br and BrO; and Cl, ClO, OClO, Cl_2 and Cl_2O_2 are known as HO_x, NO_x, BrO_x and ClO_x respectively, and are often referred to as 'active species'.

These reactions are naturally balanced by a series of 'null' or 'holding' cycles, which convert the active species to other species within the family without destroying ozone (*Wayne*, 2000; *Findlayson-Pitts and Pitts*, 1986). These null cycles may serve the additional benefit of locking the catalytic molecules in a form which cannot easily be reverted to an active species. Species which are fairly unreactive and hence effective for preventing these catalytic reactions are known as reservoir species. Important reservoir species include hydrogen chloride (HCl), chlorine nitrate ($ClONO_2$) and nitric acid (HNO_3).

Hydrogen chloride is the main chlorine reservoir. It is predominantly formed in the stratosphere by the reaction of Cl with methane (CH_4). Approximately 70% of non-CFC stratospheric chlorine (also known as Cl_y) is thought to be present as HCl (*Wayne*, 2000).

Chlorine nitrate is formed predominately through the reaction of ClO with NO_2. As such, it is both a chlorine reservoir species and a reservoir for NO_x. This highlights the relationship between the families and the importance of studying several species simultaneously.

Nitric acid, formed as the end product of several different reactions within the nitrogen family, is the most important NO_x reservoir, with about half of the stratospheric NO_x load stored in this form (*Wayne*, 2000). While nitric acid is photolysed to regenerate OH and NO_2, this process is relatively slow and, importantly for polar regions, non-existent during periods of darkness. HNO_3 also serves as a link between chemical families, storing both NO_x and HO_x species.

This is by no means an exhaustive picture of stratospheric chemistry (see, for example, *Wayne*, 2000; *Findlayson-Pitts and Pitts*, 1986), but it does serve to demonstrate the importance that the various trace gas families play in regulating the quantity of ozone that is present in the stratosphere. A summary of key reactions, as documented in *Solomon* (1999), is reproduced in Table 2.1.

Anthropogenic emissions of chlorine, nitrogen and bromine potentially serve to upset the natural balance and result in additional ozone depletion. Early studies of the effect of anthropogenic emissions, which were based solely on this gas phase chemistry, showed the effect to be minimal, as outlined in Chapter 1. Additional mechanisms are therefore needed to explain the large scale ozone depletion observed in the Antarctic spring stratosphere.

2.3.2 Heterogeneous chemistry and ozone depletion

The first suggestion that ozone depletion could be attributed to heterogeneous reactions on the surface of polar stratospheric clouds came from *Solomon et al.* (1986). While the

Chapman Chemistry	
$O_2 + h\nu \rightarrow 2O$	$O+O_2 + M \rightarrow O_3 + M$
$O_3 + h\nu \rightarrow O_2 + O(^1D)$	$O(^1D) + M \rightarrow O + M$
$O_3 + h\nu \rightarrow O_2 + O$	$O + O + M \rightarrow O_2 + M$
$O + O_3 \rightarrow 2O_2$	

Illustrative Odd Hydrogen Catalytic Cycles	
$O + OH \rightarrow O_2 + H$	$OH + O_3 \rightarrow HO_2 + O_2$
$H + O_2 + M \rightarrow HO_2 + M$	$HO_2 + O_3 \rightarrow OH + 2O_2$
$O + HO_2 \rightarrow O_2 + OH$	*Net Cycle:* $2O_3 \rightarrow 3O_2$
Net Cycle: $O + O + M \rightarrow O_2 + M$	

Illustrative Odd Nitrogen Catalytic Cycle	
$NO + O_3 \rightarrow NO_2 + O_2$	
$O + NO_2 \rightarrow NO + O_2$	
Net Cycle: $O + O_3 \rightarrow 2O_2$	

Illustrative Odd Chlorine Catalytic Cycles	
$Cl + O_3 \rightarrow ClO + O_2$	$Cl + O_3 \rightarrow ClO + O_2$
$Cl + O_3 \rightarrow ClO + O_2$	$ClO + O \rightarrow Cl + O_2$
$ClO + ClO + M \rightarrow Cl_2O_2 + M$	*Net Cycle:* $O + O_3 \rightarrow 2O_2$
$Cl_2O_2 + h\nu \rightarrow Cl + ClO_2$	
$ClO_2 + M \rightarrow Cl + O_2 + M$	
Net Cycle: $2O_3 \rightarrow 3O_2$	

Illustrative Cl-Br Catalytic Cycle	
$Cl + O_3 \rightarrow ClO + O_2$	
$Br + O_3 \rightarrow BrO + O_2$	
$BrO + ClO \rightarrow Br + ClO_2$	
$ClO_2 + M \rightarrow Cl + O_2 + M$	
Net Cycle: $2O_3 \rightarrow 3O_2$	

Some Important Coupling and Reservoir Reactions	
$ClO + NO \rightarrow Cl + NO_2$	$ClO + NO_2 + M \rightarrow ClONO_2 + M$
$Cl + CH_4 \rightarrow HCl + CH_3$	$OH + NO_2 + M \rightarrow HNO_3 + M$
$HO_2 + ClO \rightarrow HOCl + O_2$	

Key Heterogeneous Reactions	
$HCl + ClONO_2 \rightarrow HNO_3 + Cl_2$	$N_2O_5 + H_2O \rightarrow 2HNO_3$
$ClONO_2 + H_2O \rightarrow HNO_3 + HOCl$	$HCl + HOCl \rightarrow H_2O + Cl_2$
$BrONO_2 + H_2O \rightarrow HNO_3 + HOBr$	$HCl + BrONO_2 \rightarrow HNO_3 + BrCl$
$HCl + HOBr \rightarrow H_2O + BrCl$	

Table 2.1: Chemical processes and catalytic cycles involved in ozone regulation. Table reproduced from *Solomon* (1999).

majority of chlorine in the stratosphere normally resides in the chlorine reservoir species HCl and $ClONO_2$, reactions that perturb the chlorine partitioning by moving chlorine from the inactive reservoirs to active forms are able to occur on the surface of the clouds.

Most importantly, the reservoir species HCl and $ClONO_2$ are able to react together, releasing chlorine through the reaction

$$HCl + ClONO_2 \rightarrow Cl_2 + HNO_3 \tag{2.8}$$

Reaction 2.8 acts in two ways. Most importantly, chlorine is released from the stable reservoir forms. Additionally, nitrogen is trapped in the form of HNO_3, which remains within the PSC particle. This stops the chlorine from reacting with NO_2 to reform $ClONO_2$. Whether this is a permanent loss of the nitrogen (denitrification) or a temporary loss (denoxification) depends on whether the PSC particle subsequently sediments out of the region.

Reaction 2.8 has been shown to occur rapidly on ice, NAT or NAD particles, supercooled liquid sulfate aerosols, and on frozen sulfate aerosols (*WMO*, 1994, 1998, 2002, and references therein), leading to rapid chlorine activation regardless of the phase of the cloud particle. Additional heterogeneous reactions which serve to either release active species, or to prevent reformation of reservoirs, are listed in Table 2.1.

With the return of the sunlight in spring, the released Cl_2 is rapidly photolysed to form ClO and its dimer, Cl_2O_2. These species are then able to react with ozone through the reactions given in Section 2.3.1 and in Table 2.1. The reaction involving Cl_2O_2, originally proposed by *Molina and Molina* (1987), is now recognized as being responsible for about 75% of the ozone removal in the Antarctic stratosphere (*Solomon*, 1999).

As temperatures in the vortex increase above temperatures where PSCs can exist, the heterogeneous reactions which activate chlorine can no longer occur. The chlorine rapidly returns to the reservoir species (a process known as deactivation) and further ozone loss is limited. As outlined in Chapter 1, in the Antarctic vortex this typically occurs through the reaction of Cl with CH_4 to form HCl, as denitrification limits the reformation of $ClONO_2$. Measurements of HCl, HNO_3 and springtime $ClONO_2$ will allow this point to be further demonstrated in Chapter 6.

Chapter 3

The Tools of the Trade

In this chapter, the two major tools used for this research will be described. The first section will introduce the Fourier transform infrared spectrometer (FTIR) used for obtaining the absorption spectra. It will begin with some general theory of Michelson interferometers, then look at the specifics of the Bruker 120M spectrometer and its detectors. Some information regarding the Arrival Heights site will also be presented here. The second section will introduce the algorithm used for obtaining trace gas measurements from the absorption spectra. Again, this section will begin with some general theory, introducing the concept of a forward model and an inverse model. It will then focus on the specifics of SFIT2, the radiative transfer and profile retrieval algorithm used for this study.

3.1 The measurement tools

3.1.1 Michelson interferometers

An interferometer is an instrument that uses interference patterns to determine the spectral distribution of irradiance. The most well-known of all interferometers is the Michelson interferometer, which was used in the famous Michelson-Morley experiment in the late 1800s to prove that the Earth does not move through an aether (*Michelson and Morley*, 1887). The Michelson interferometer remains the back-bone of many interferometers in use today.

The basic Michelson interferometer is schematically represented in Figure 3.1. Incident radiation entering the interferometer is reflected or transmitted by a beamsplitter into two arms. In one arm the light is reflected off a stationary mirror, and in the other arm light is reflected off a moving mirror, which introduces a path difference between the two beams. After reflection off their respective mirrors, the two light beams are recombined and the combined light beam is recorded on a detector.

For a monochromatic light source, the interference pattern observed on the detector as the moving mirror travels along the arm is a sine wave, as a result of the optical path difference causing the beams to move in and out of phase with each other. For a multi-wavelength source, the observed interference pattern is a summation of the sine waves of each wavelength of light. At the point where the path-length is identical for both

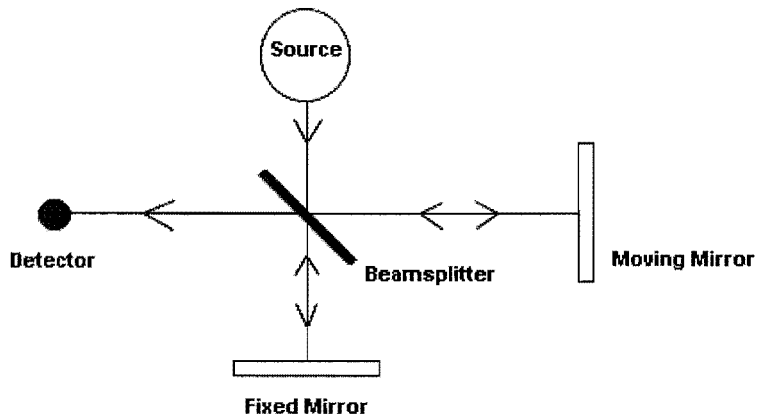

Figure 3.1: Schematic of a basic Michelson interferometer.

arms (known as the ZPD or zero path difference), all wavelengths of light constructively interfere. As the moving mirror moves away from this point, the different wavelengths constructively or destructively interfere with each other, and the signal on the detector gets weaker. The pattern of intensity versus path difference recorded on the detector through one 'scan' of the mirror moving down the arm of the instrument is called an interferogram. By performing a Fourier transform on the interferogram, the frequency information of the incident light is returned. This plot of intensity versus wavenumber, where wavenumber is the traditional unit for frequency in FTIR spectroscopy (in cm^{-1}), is called a spectrum.

Interferometers have several advantages over a prism or diffraction grating spectrometer. The most notable is that because the wavelengths of light are being separated using a Fourier transform, rather than physically separated with a prism, all of the wavelengths can be measured simultaneously. This means that acquiring the same sized spectrum takes less time with an interferometer than with a dispersive instrument, hence more scans can be carried out in a given time period. As the noise in the spectrum is proportional to the observing time, this results in a higher signal to noise ratio (S/N) than would be obtained with a prism or diffraction grating instrument. Additionally, all of the incident radiation reaches the detector. This increases the signal strength at the detector and also results in a higher S/N. These two advantages are known as the multiplex and throughput advantages, and have resulted in interferometry being the spectroscopy of choice for astronomical, atmospheric and laboratory applications (*Bell*, 1972; *Smith*, 1996; *Davis et al.*, 2001).

3.1.2 The Bruker 120M spectrometer

The Bruker 120M is a commercial Fourier transform infrared spectrometer (FTIR) made by Bruker Optik, Germany. It is a permanently aligned Michelson interferometer that has been specifically designed for high resolution atmospheric measurements and is routinely used at locations from the Arctic to the Antarctic by the NDSC infrared community (*Blumenstock et al.*, 1997; *Nakajima et al.*, 1997; *Notholt et al.*, 2000; *Wood et al.*, 2004). The Bruker 120M used for this research belongs to the University of Denver and is operated by NIWA. It has been optimized for the measurement of mid-infrared radiation, where absorptions by atmospheric trace gases are observed as a result of the vibrational and rotational transitions within the molecules.

The layout of the instrument is shown schematically in Figure 3.2 and in the photo of the instrument in Figure 3.3. The optics have been designed to minimize the space used by the instrument, while still providing high resolution measurements.

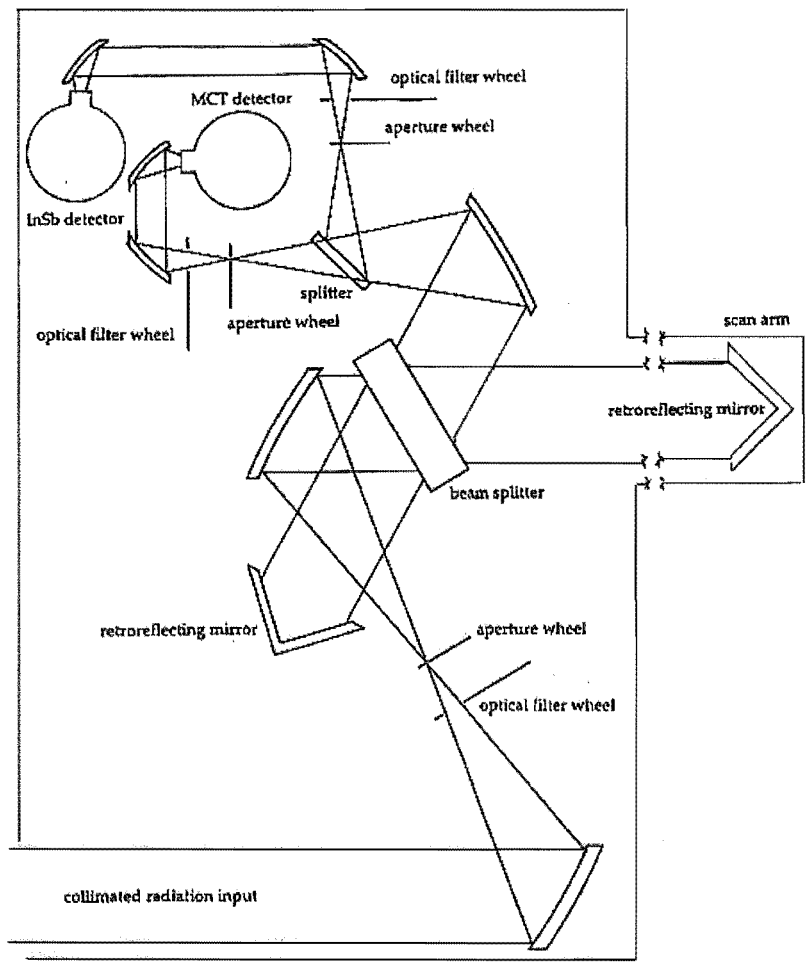

Figure 3.2: Schematic of the layout of the Bruker 120M FTIR spectrometer.

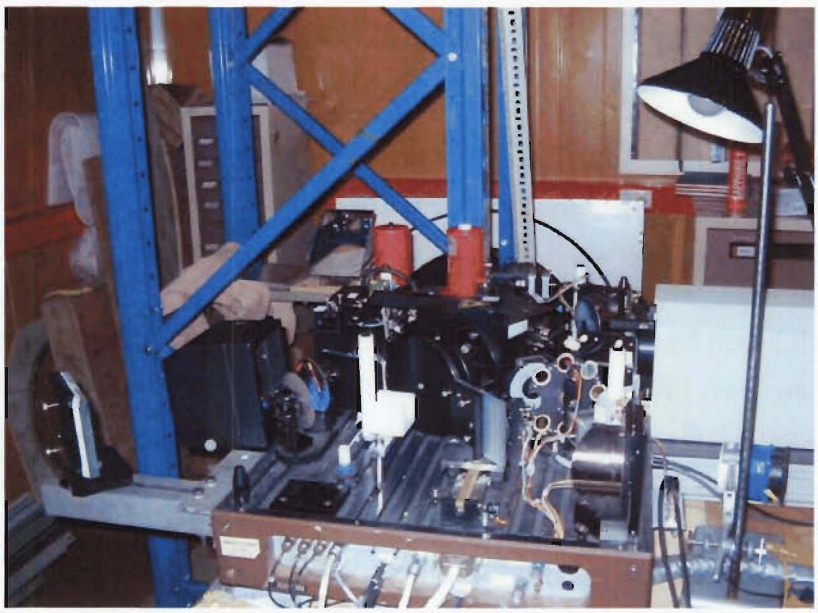

Figure 3.3: Inside the Bruker 120M. The filter wheel is clearly visible as the wheel with the coloured circles. The aperture wheel is behind it, with the beamsplitter behind that. The detectors are identifiable by their red dewars.

Light entering the instrument is focused through computer controlled filter and aperture wheels, then re-collimated into the beamsplitter. The filter and aperture are user-selected to optimize the instrumental response for the conditions. Apertures ranging from 0.3 to 10 mm are available to counter the effects of angular divergence. Bigger apertures allow more light into the instrument but serve as a limit to the resolution of the spectra. Filters are used to limit the wavelengths of light incident on the detector, increasing the signal to noise ratio of the measurement. The beamsplitter in the instrument is permanently aligned at a 30° angle of incidence, with a rigid mounting system that allows the beamsplitter to be removed and replaced reliably. The beamsplitter used for this work is made from potassium bromide (KBr) with a thin coating of germanium sandwiched between the layers to split the beam (*Smith*, 1996). Because KBr is hydroscopic, the beamsplitter is stored outside the instrument in a dry container except when in use.

The moving retro-reflecting mirror uses high-quality mechanical bearings to reduce friction, with the location precisely controlled using a reference He-Ne Laser. A voice-coil mechanism is used for fine positioning. The maximum path length of the moving mirror is 250 cm, giving the instrument a maximum resolution of 0.0035 cm^{-1}.

After recombination of the beam, a computer controlled mirror directs light through an additional aperture into one of two detectors. The instrument is usually set up with an indium antimonide (InSb) detector for the 1 - 5.5 μm wavelength region and a mercury cadmium telluride (MCT) detector for the 4 - 14 μm wavelength region. In this work a specialized InSb detector for the lunar HCl observations has also been used. This was

inserted into the instrument in place of the standard InSb detector for the winter months.

The InSb detectors

Indium antimonide detectors are photovoltaic detectors which produce current when exposed to infrared radiation. In this work two InSb detectors have been used – a standard commercial Judson InSb detector for solar measurements and a specially adapted commercial Judson InSb detector for lunar measurements.

Both detectors are similar in that they contain a 1 mm diameter InSb detector housed inside a liquid nitrogen-filled dewar. The detectors operate at a temperature of 77 K, to reduce the noise associated with infrared radiation from the room, instrument and detector itself. Light enters the dewar through a calcium fluoride entrance window with a 20′ wedge and a 30° field of view.

The standard solar detector has no internal filters, relying instead on external filters in the filter wheel. This makes the detector suitable for measurements of radiation between 1 and 5.5 μm. The adapted lunar detector has a cooled filter, housed within the dewar, which restricts radiation to wavelengths less than 3 μm. The response curve from the lunar detector, as tested in the factory, is shown in Figure 3.4.

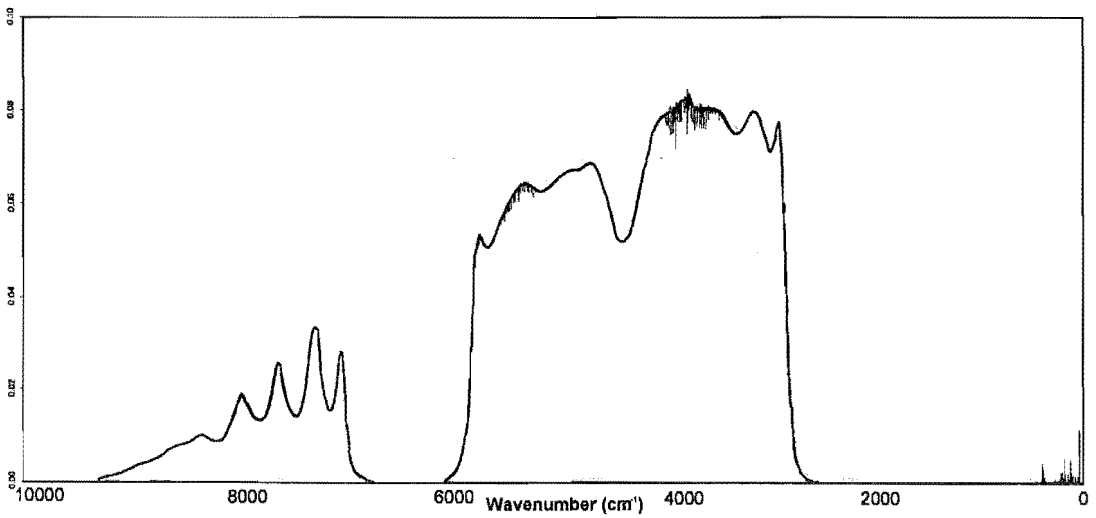

Figure 3.4: Response curve of the lunar InSb detector with wavenumber. The units on the y axis are arbitrary units of transmission.

Coupled with each detector is a preamplifier which is designed to convert the current output of the photovoltaic detector into a voltage output. The photocurrent produced by the detector induces a voltage across the preamplifier, which is then amplified (*Judson-Technologie*, 2005). Four user-defined gain settings in the preamplifier allow the signal to be increased to a maximum level without saturation.

Unfortunately, the preamplifier supplied with the lunar detector had insufficient gain

for the lunar signal, and only one of the four levels was able to be adjusted to a suitable gain without creating instability. Optimization of the signal reaching the lunar detector therefore required changes to be made to the aperture size, rather than the preamplifier gain. As the noise in the signal is proportional to the preamplification, this lack of adjustability meant that the signal was frequently noisier than it would have been if the preamplifier had performed as expected.

The MCT detector

The mercury cadmium telluride detector is a photoconductive detector, meaning that current is produced as a result of the absorption of photons causing electrons to jump from the valence band to the conductive band. The energy between the two bands is called the bandgap and is responsible for the wavelength cut-off of these detectors (*Smith*, 1996). The MCT detector used for this work was a commercial Judson narrow-band MCT detector, sensitive between 4 and 14 μm wavelengths. This 1 $\times$ 1 mm detector also operated at 77 K, so was housed in a liquid-nitrogen filled dewar. The field of view of the MCT detector was 30°, with a 20′ wedged thallium bromo-iodide entrance window. An external, uncooled, 7 - 14 μm filter was used to restrict the wavelength range for this work.

The MCT detector's preamplifier also has four gain settings, allowing the amplification to be optimized for the conditions. A photoconductive detector works by having a constant bias voltage applied across the detector element. As such, a capacitor is used in the MCT preamplifier to block the constant DC bias, and the voltage changes resulting from photons hitting the detector are amplified (*Judson-Technologie*, 2005).

3.1.3 The Arrival Heights laboratory

The Bruker 120M is located inside a heated laboratory at Arrival Heights, Antarctica (77.83°S, 166.65°E, Figures 3.5 and 3.6). The site is elevated (200 m above sea level) and is approximately 4 km from the United States' McMurdo Station and 8 km from New Zealand's Scott Base, so is typically uncontaminated by local emissions. It is an NDSC primary station and is located within the electromagnetically quiet Antarctic Specially Protected Area No. 122 (*Antarctic Treaty Secretariat*, 2004). The viewing horizon is mostly non-restricted, although Mt Erebus, almost due north, restricts measurements in that direction to those above 6° elevation. The atmosphere is very cold and very dry, with surface temperatures typically around -35°C in the winter and seldom above freezing even in the middle of summer. The instrument is housed in a specialized room within the building, with the room maintaining a typical temperature of approximately 20°C. Light is directed from the tracker, which is at ambient temperature on the roof of the building,

Figure 3.5: Arrival Heights Laboratory, Ross Island, Antarctica.

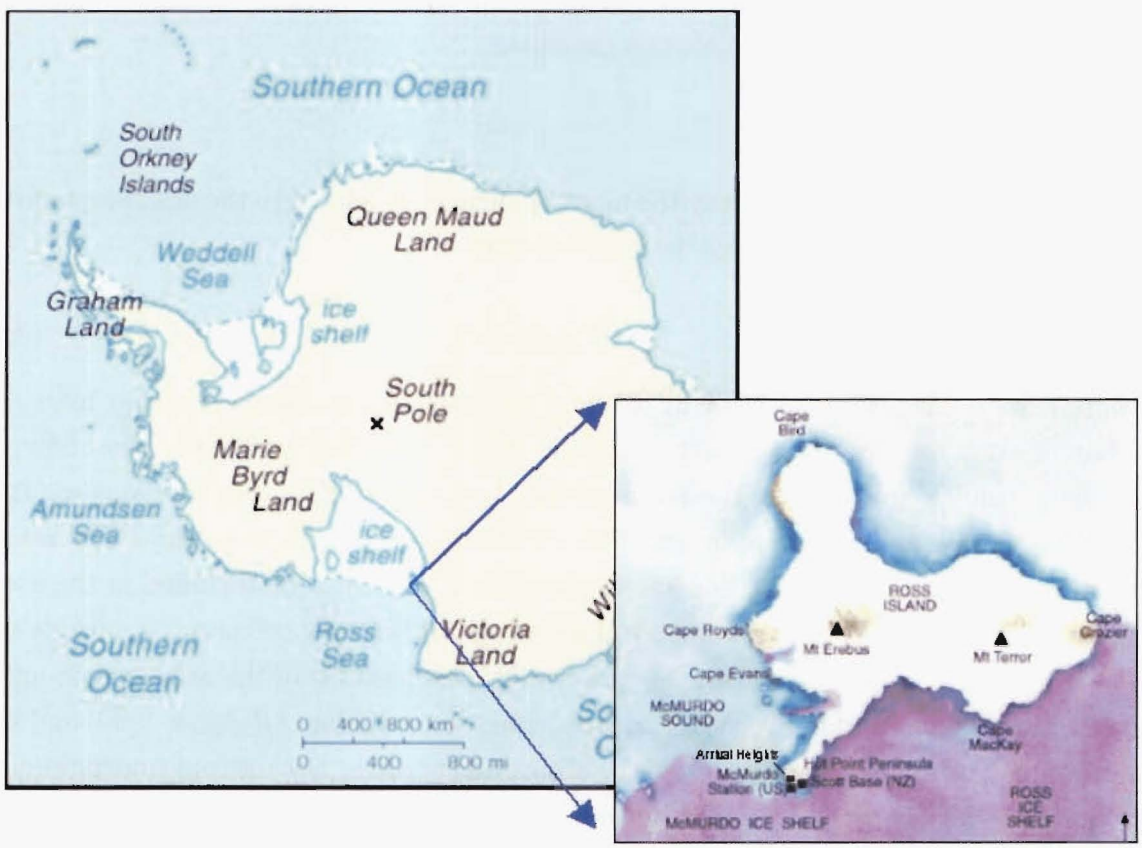

Figure 3.6: Location of Arrival Heights laboratory, on Ross Island, Antarctica. Map adapted from (*Waterhouse*, 2001).

into the instrument via two mirrors in the room, which are at room temperature. The tracker is a home-made, two-mirror system which uses a computer algorithm to track the sun or the moon. Small adjustments to the tracker alignment can be made by the operator in order to maximize the signal. Sun or moon elevations are limited to a maximum of 35° above the horizon, as a result of the protective cover over the tracker.

3.2 The retrieval tools

Fourier transform absorption spectra obtained using ground-based instruments contain information on the altitude profile of the absorbing molecules in the atmosphere. The altitude information is contained in the details of the observed line shape, primarily as a result of pressure broadening of the spectral lines. Because the altitude profile is not an explicit function of the absorption spectra, a retrieval, or inverse, process must be used to determine the profile from the spectra. In this work the retrieval of profiles from the absorption spectra has been carried out using an algorithm called SFIT2.

In this section a brief introduction to retrieval theory and the quantification of the errors included in the solution will be given. The theory presented is based on the work of *Rodgers* (1976, 1990, 2000). The SFIT2 algorithm used to retrieve atmospheric profiles from the absorption spectra will also be presented.

3.2.1 Theory

The model used to describe the way the measurement, y, is related to the desired quantity, x, is known as the forward model. It can be written

$$y = F(x, b) + \epsilon \tag{3.1}$$

where ϵ is the measurement error in y, and b includes all the parameters that influence y but are not the desired quantity (*Rodgers*, 2000). For this work, y is the observed spectrum, and x (also called the state vector) is a vector describing the vertical HCl or HNO_3 profile at 29 discrete layers. Several other parameters, including scale factors for interfering gases and some line shape parameters, may also be included in the state vector. The parameters which influence the retrieval but are not retrieved, b, include the temperature and pressure profiles, the absorption cross sections of the atmospheric gases and the instrument profile. The error, ϵ, is assumed to be random (*Rodgers*, 1990) and has a variance determined from the S/N of the absorption spectra. Because our understanding of all the processes occurring in the atmosphere is not complete, the forward model is made up of our best estimate of the atmospheric and instrumental physics that contribute to the observed absorption line.

The inverse or retrieval method, R, is the process by which the retrieved profile, $\hat{x}$, is determined from y.

$$\begin{aligned} \hat{x} &= R(y, \hat{b}, \hat{c}) \\ &= R(F(x, b) + \epsilon, \hat{b}, \hat{c}) \end{aligned} \tag{3.2}$$

where $\hat{b}$ is our best estimate of b, and $\hat{c}$ is any additional parameters used in the retrieval which do not appear in the forward model (e.g., *a priori* information).

Following the work of *Rodgers* (2000), it is useful to linearize Equation 3.2. Because we don't know the true state of the atmosphere, we linearize about our best estimate of the true atmosphere, with $x = x_a$, where x_a is our best *a priori* estimate of the state vector, and $b = \hat{b}$.

$$\hat{x} = R[F(x_a, \hat{b}), \hat{b}, \hat{c}] + \frac{\partial R}{\partial y}\frac{\partial F}{\partial x}(x - x_a) + \frac{\partial R}{\partial y}\frac{\partial F}{\partial b}(b - \hat{b}) + \frac{\partial R}{\partial y}\epsilon \tag{3.3}$$

In order to simplify Equation 3.3, we make several definitions. We define the gain matrix or contribution function, G_y, as

$$G_y = \frac{\partial R}{\partial y} \tag{3.4}$$

where G_y characterizes the retrieval with respect to the measurement. Each column of G_y shows the contribution to the solution of a unit change in an element of y (*Rodgers*, 1990).

The weighting function matrix, K_x, is defined as

$$K_x = \frac{\partial F}{\partial x} \tag{3.5}$$

The weighting function matrix describes the sensitivity of the forward model to the state vector. Physically, the columns of K_x describe the change in the measured spectrum that results from a change in the state profile at each of the altitudes in the vector. The rows of K_x give an idea of the information content of the measurements, as they show the part of the profile that is represented by each measurement (*Rodgers*, 1990). Similarly, we define K_b to be the sensitivity of the forward model to the forward model parameters

$$K_b = \frac{\partial F}{\partial b} \tag{3.6}$$

Finally, the averaging kernel matrix, A, which characterizes the combined forward

model and retrieval system with respect to the true atmosphere, is defined as

$$A = \frac{\partial[R(F(x,b),b,c)]}{\partial x} = G_y K_x \tag{3.7}$$

Columns of the averaging kernel matrix can be thought of as the response of the observing system to a δ-function disturbance in the state profile. The rows of A are the averaging kernels, or smoothing functions. They describe what proportion of each of the altitude layers in the true profile is used in the determination of that retrieved altitude layer. Ideally A would be a unit matrix, with 100% of the information in the retrieved layer coming from that layer and none from outside of it. In reality, however, the averaging kernels exist as peaked functions (hopefully peaking at the altitude that the averaging kernel represents), with the width of the peak giving a quantitative measure of the resolution of the observing system. Summing the elements in the rows of A gives the area of the averaging kernel, which is a rough measure of the fraction of the retrieval that comes from the data rather than the *a priori*. The area should be approximately unity where the retrieval is accurate (*Rodgers*, 2000).

Substituting these definitions back into Equation 3.3, the retrieved profile is given as

$$\hat{x} = R[F(x_a,\hat{b},\hat{c}),\hat{b},\hat{c}] + A(x - x_a) + G_y K_b(b - \hat{b}) + G_y\epsilon \tag{3.8}$$

For an accurate retrieval system, $R[F(x_a,\hat{b},\hat{c}),\hat{b},\hat{c}] = x_a$, i.e., in the absence of real measurements and experimental error, the retrieval system will retrieve the *a priori* profile (*Rodgers*, 2000).

As such, the retrieved profile can be seen as a linear combination of the *a priori* and the true profile, smoothed by the averaging kernel, with additional contributions from the uncertainties in the model parameters and measurement noise.

$$\hat{x} = x_a + A(x - x_a) + G_y K_b(b - \hat{b}) + G_y\epsilon \tag{3.9}$$

Error analysis

From Equation 3.9, a breakdown of the errors in the retrieval process is straightforward. The difference between $\hat{x}$ and x is given by

$$\begin{aligned} \hat{x} - x = (A - I)(x - x_a) \quad & \text{smoothing error} \\ +G_y K_b(b - \hat{b}) \quad & \text{model parameter error} \\ +G_y\epsilon \quad & \text{measurement error} \end{aligned} \tag{3.10}$$

where I is the identity matrix (*Rodgers*, 2000). Each of these error terms can be individually quantified, allowing an estimate of the total uncertainty in the retrieved profile to be made.

It should be noted that an additional error term, due to the error associated with the forward model as a representation of the measurement process, should also be included in Equation 3.10. Because the forward model used in SFIT2 includes our best estimate of the known physics of the atmosphere and instrument, this term is thought to be minimal, and hence has been omitted for simplicity.

Smoothing error The smoothing error can be thought of as the error associated with smoothing the true atmospheric profile by the averaging kernel and *a priori* profile. In many situations the smoothing error can be essentially eliminated by using the averaging kernel and *a priori* to smooth measurements or model results in the same way that the true atmospheric profile has been smoothed (*Connor et al.*, 1994, 1995; *Rodgers and Connor*, 2003). This will be further explained in Chapter 7. For stand-alone measurements, however, an estimate of the uncertainty in the column or partial column amount due to this smoothing is required. The smoothing error covariance, S_S, has been determined using the definition of *Rodgers* (1990),

$$S_S = (A - I)S_x(A - I)^T \tag{3.11}$$

where S_x is a covariance matrix made up of our best estimate of the covariance of the atmosphere about the *a priori* profile.

Model parameter error The error in the retrieval due to errors in the parameters associated with the forward model can be calculated for each parameter b, as detailed in *Connor et al.* (1995); *Rodgers* (2000). A description of the covariance, S_F, for each parameter is given by

$$S_F = G_y K_b S_b K_b^T G_y^T \tag{3.12}$$

where S_b is the covariance matrix (or variance scalar, depending on the parameter), determined using a realistic estimate of the uncertainty in the parameter.

Measurement error Also known as retrieval noise, the measurement error is the noise associated with errors in the spectral measurement. As outlined in *Rodgers* (1990), the measurement error covariance, S_M, is given by

$$S_M = G_y S_\epsilon G_y^T \tag{3.13}$$

Because the measurement noise is uncorrelated and random, S_ϵ is taken to be a diagonal matrix, with the diagonal components determined from the S/N of the measurement.

Information content in FTIR measurements

While a measurement contains m pieces of information, these are not necessarily all linearly independent and relevant to the quantity that you are trying to determine. The number of relevant independent pieces of information contained in the measurement is called the rank, and in principle this would be the number of useful pieces of information that could be determined from the measurement set. In the presence of measurement error, however, these pieces of information will also have an associated uncertainty that may be so large as to make the measurement worthless (*Rodgers*, 2000).

In order to avoid over-interpretation of the retrieved quantities, some measure of the amount of information in the quantity which has been contributed by the measurement is desirable. *Rodgers* (2000) introduces the concept of 'degrees of freedom for signal', d_s, as a measure of the number of independent pieces of information which are useful and 'degrees of freedom for noise', d_n, as the number which are not. The simplest way to calculate d_s is to determine the trace of the averaging kernel, $tr(A)$ (*Rodgers*, 2000).

For a column or partial column measurement, we are looking for one piece of information – the partial column value. Values of d_s near unity show that there is a relevant piece of information provided by the measurement to the partial column. Values of d_s less than 0.5 mean that little information is coming from the measurement and that the usefulness of the retrieved partial column amount should be questioned. Values of d_s over one show there to be more information attainable from the measurement than is necessary for determining the partial column amount. While the majority of the measurements presented in this thesis have $d_s \gg 1$, in Section 5.2.7 the partial columns will be subdivided to the maximum extent of the information available in the measurement, and as such, the degrees of freedom will become an important tool for determining the information content of the measurement.

3.2.2 SFIT2

SFIT2 is a radiative transfer and profile retrieval algorithm developed by C.P. Rinsland (NASA Langley) and B.J. Connor (NIWA Lauder). It is routinely used for the retrieval of gas profiles from infrared absorption spectra made by NDSC stations throughout the world (*Pougatchev et al.*, 1995; *Connor et al.*, 1998; *Rinsland et al.*, 2003; *Wood et al.*, 2004). It, and its predecessor, SFIT, have been thoroughly compared with other retrieval codes and shown to give consistent and reliable results (*Goldman et al.*, 1999; *Hase et al.*, 2004). The method is based on the fitting of a calculated spectrum to the recorded one by

means of adjustment of the gas profile and supplementary instrument-related parameters. Atmospheric ray-tracing and calculation of mass paths are supplied externally. Brief details of each of the steps in the algorithm are given in the following sections.

Raytrace

Raytrace, also known as FASTCODE or FSCATM, is the program used to perform the atmospheric ray tracing and calculation of mass path information (*Wood et al.*, 2004; *Meier et al.*, 2004). Input for Raytrace includes site-specific information such as pressure and temperature data, an *a priori* mixing ratio profile and details of the measurement conditions, such as zenith angle. Temperature and pressure data for the Arrival Heights site are from the NCEP meteorological analyses, which will be discussed further in Section 4.2.1. Output from Raytrace is three measurement-specific files containing pressure and temperature information, vertical and zenith angle mass path information, and a mixing ratio profile, on the 29-layer altitude grid used by the SFIT2 algorithm.

Forward model

The forward model of SFIT2 is a multi-layer, multi-species line-by-line radiative transfer model developed at the NASA Langley Research Centre for the analysis of FTIR spectra (*Pougatchev et al.*, 1995; *Connor et al.*, 1998). The key assumptions and characteristics of this model are (1) homogeneous layers in local thermodynamic equilibrium, (2) a Voigt line shape function, (3) refractive ray-tracing calculations (as outlined above) and (4) instrumental line shape function calculations made in interferogram space with a Fourier transform technique to include the effects of apodization, maximum optical path difference, and a finite field of view (*Pougatchev et al.*, 1995). Multiple spectral windows can be handled simultaneously. Additional instrumental parameters are included to model the variation of the instrument response function with wavenumber and wavenumber shifts between the measured and calculated spectra (*Pougatchev et al.*, 1995).

For this work, a total of 29 atmospheric layers have been used in the forward model, with 2 km vertical thicknesses to 50 km, 10 km thicknesses from 50 to 80 km, and a final 20 km layer from 80 to 100 km. While the limited resolution of ground-based spectra means that the retrieved layers on this grid are not independent, this fine grid is necessary for the radiative transfer calculations (*Pougatchev et al.*, 1998). Line-by-line calculations of the atmospheric spectrum use the line parameters in the HITRAN2000 database (*Rothman et al.*, 2003).

Retrieval

The retrieval, or inverse model, in SFIT2 uses optimal estimation based on the formalism of Rodgers (*Rodgers*, 1976, 1990, 2000), with Newtonian iteration to account for non-linearities in the spectral calculation.

The ensemble of possible solutions is ranked by weighting the measurement and any *a priori* information by the measurement error and an estimate of the uncertainty in the *a priori*, assuming Gaussian error statistics (*Rodgers*, 1976). The optimal solution from this class of solutions is the maximum *a posteriori* solution (*Rodgers*, 2000), where the resulting state is that which maximizes the probability density function. In simpler language, this amounts to using the error estimates of the *a priori* and measurement to find the most likely solution. Because the problem is non-linear, the solution must be found numerically and iteratively (*Rodgers*, 2000). Newtonian iteration as given in *Rodgers* (1976) is used in SFIT2 to determine the optimal solution. The solution is deemed to have converged when the difference between successive iterations changes the calculated spectrum by less than the estimated error times a tolerance factor. For this work, a tolerance factor of 0.1 has been used, with the estimated error given by the inverse of the signal to noise ratio of the measurement.

Column calculations

As suggested in *Pougatchev et al.* (1998), the resolution of the absorption spectra is insufficient for individually resolved layers. As such, in many cases, the desired output from the retrieval is a column or partial column amount. Partial column calculations in SFIT2 are calculated by an external program, SFIT2rdz, and are determined from the retrieved mixing ratio profile and the number of air molecules in each layer as determined by Raytrace. Mixing ratios are assumed to be constant through each layer. Averaging kernels corresponding to the retrieved partial columns are also weighted by the number of air molecules in each layer in order to be consistent with the partial column calculations.

While traditionally total column amounts of trace gases have been presented, in this research we have chosen to present 12 - 28 km partial column amounts instead. The reason for this is two-fold. First, the retrievals from lunar measurements have been shown to have very little sensitivity outside of this height range. This will be demonstrated in Chapter 5. As such, total column amounts include a large *a priori* contribution from above and below this region, particularly from the troposphere where there are more air molecules. As the tropospheric profiles of HCl and HNO_3 are not well quantified in the Antarctic region, their inclusion in the quoted column amounts provides little value. Second, the processes that are occurring in the Antarctic stratosphere which lead to ozone loss in the spring are known to occur between 12 and 28 km, as this is where polar stratospheric

clouds are observed (*Adriani et al.*, 2004). Additionally, this is where the majority of ozone in the atmosphere is found, as shown in Chapter 2 (Figure 2.4). By presenting observations incorporating just the 12 - 28 km region, the information coming from the measurement is maximized, and the observed trends are clearly linked with the processes occurring in the polar stratosphere.

Chapter 4

The Measurements

This chapter will provide details of the measurement conditions and observational methods used to obtain the absorption spectra from which HCl and HNO_3 partial column amounts will be determined. In addition, information regarding two ancillary data sets, the National Centers for Environmental Prediction meteorological analyses, and Ertel's potential vorticity as a definition of the vortex boundary, will also be presented.

4.1 Spectroscopic measurements

Spectroscopic measurements of HCl and HNO_3 have been made with the sun as a light source using the Bruker 120M at Arrival Heights since 1998 (*Connor et al.*, 1998; *Wood et al.*, 2002, 2004). For the first time at this site, however, these measurements have been expanded into the polar winter using the moon as a light source.

As detailed in Chapter 1, FTIR measurements were first made using the moon as a light source in the Arctic winter of 1992/1993 (*Notholt et al.*, 1993; *Notholt*, 1994). While the radiation of sunlight reflected from the moon's surface is approximately 400,000 times less than that of direct sunlight (*Notholt and Lehmann*, 2003), the moon radiates in the infrared as a result of the absorption and re-emission of incident sunlight. This significantly contributes to the infrared intensity observed on Earth (*Notholt et al.*, 1993; *Notholt*, 1994; *Notholt and Lehmann*, 2003). Figure 4.1 shows the intensity of blackbody radiation from objects at the temperature of the sun, full moon, and Earth's atmosphere. Additionally, the intensity of radiation from sunlight reflected from the moon is shown.

It can be seen that in the 870 cm^{-1} wavenumber region where HNO_3 measurements are made, while the reflected sunlight from the moon's surface is very low in intensity, there is a significant infrared source from the emission of the moon itself (Figure 4.1). The combined intensities from these two sources mean that the radiation from the moon in this region is high enough that measurements can be made with a standard solar MCT detector. It should, however, be noted that there is also a significant contribution to the radiation in this region from the Earth's atmosphere. Corrections due to this source will be considered in Chapter 5. In the 2900 cm^{-1} wavenumber region where HCl measurements are made, the total infrared intensity from the combination of reflected sunlight and the moon's emission is still significantly lower than the solar infrared intensity, and as

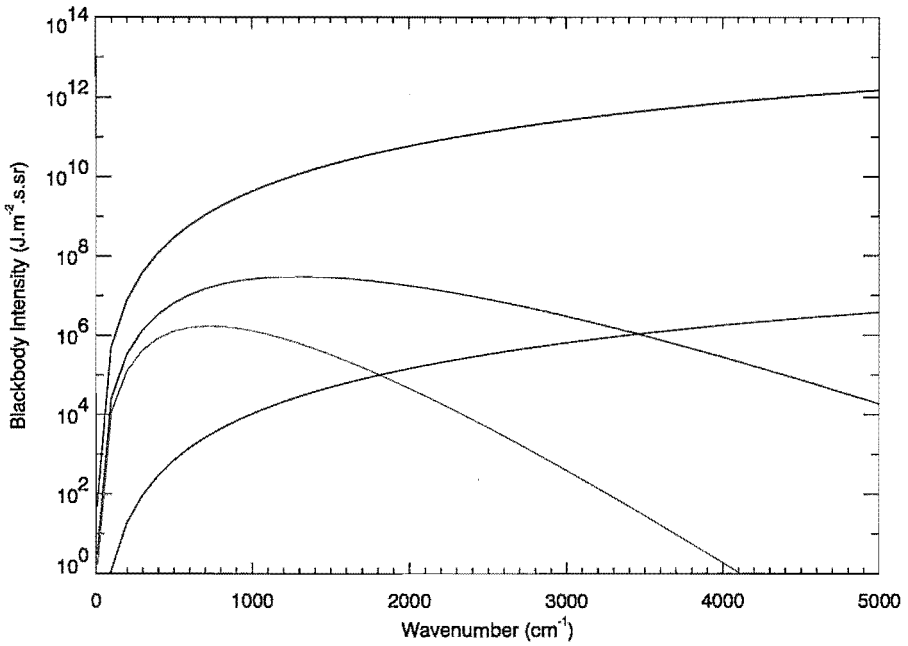

Figure 4.1: Blackbody intensities calculated for the sun (5870 K, red), full moon (375 K, blue), Earth's atmosphere (212 K, green) and reflected sunlight (sun/400000, pink). Note the logarithmic scale. Solar and full moon temperatures are from *Zeilik et al.* (1992) and the atmospheric temperature is from the mean annual temperature at 20 km over Arrival Heights, as determined from the NCEP data. HNO_3 and HCl measurements were made at approximately 870 cm^{-1} and 2900 cm^{-1} respectively.

such, the specialized lunar detector outlined in Chapter 3 is necessary. Fortunately the contribution in this region from the Earth's atmosphere is negligible.

As a result of the difference in intensity between the radiation from the sun and the moon, different measurement techniques must be used for obtaining absorption spectra from each of these sources. In this section, these techniques will be presented for both HCl and HNO_3 measurements.

4.1.1 Measurement conditions

For both gases, lunar measurements were possible for approximately four days on either side of the full moon, when conditions were clear. Outside of this time the infrared intensity was insufficient for a detectable signal. Solar measurements could be made on any day when the weather was suitable. Neither solar nor lunar measurements were made when cloud was thick or variable, when there was blowing snow, or when winds were greater than 35 knots. Thin cloud or haze caused fluctuations in the intensity of the signal and was avoided as much as possible, though some sub-visible cloud, especially polar stratospheric clouds during the winter, may have been present. Zenith angles of the sun or moon during the measurements were between 55° and 87°.

4.1.2 Hydrogen chloride

Lunar measurements

Lunar HCl measurements were made with the lunar-adapted InSb detector introduced in Chapter 3. Each lunar measurement consisted of 20 single-sided fast-return scans, representing nearly 10 minutes of integration time. A single-sided fast-return scan is one in which measurements are made in one direction of scanner travel only, though a small path on the other side of the centre burst is included in order to calculate phase. The measurements were at a resolution of 0.02 cm^{-1}, where resolution is defined as 0.9/scan length. This resolution, while insufficient for profile retrievals, was chosen as it was sufficient to retrieve the desired partial column amounts. A higher resolution measurement with the low light intensity from the moon would take many hours, over which time the tracker would not be stable enough to remain centred on the moon. The aperture size for the measurements was chosen to maximize the photon intensity on the detector without saturation or limiting the resolution. It was typically 0.85 mm, 1.1 mm or 1.4 mm (corresponding to a field of view of 3.86, 5.00 and 6.36 milliradians respectively), depending on the phase of the moon, its height in the sky, and any thin cloud or haze that was present. Intensity levels were checked between each measurement and aperture changes, as well as small adjustments to the tracker alignment, were made as necessary. Up to four hours worth of measurements were made in any measurement session.

The wavelength region being recorded by the instrument was restricted by the use of filters, both optical and digital. The optical filter was primarily responsible for the cut-off of the absorption spectra below 2800 cm^{-1}, as shown in Figure 3.4. Digitally, intensities outside of the 2800 - 4000 cm^{-1} wavenumber range were reduced to zero, in order to avoid these frequencies being aliased into the wavenumber region of interest during the Fourier transform.

Solar measurements

HCl measurements have been made regularly at this site using the sun as a light source from September until April (when the sun is above the horizon) as part of the NDSC measurement program (e.g., *Connor et al.*, 1998; *Keys et al.*, 1998). These measurements use the standard InSb detector described in Chapter 3. The solar measurements have been made at a higher resolution than the lunar measurements, with a resolution of 0.0035 cm^{-1} and typically a 0.5 mm aperture, giving a 2.27 milliradian field of view. The much greater intensity of the light source means that solar measurements result in spectra with higher signal to noise ratios than lunar ones. As such, each solar measurement consists of just one scan, taking less than two minutes.

An optical filter has been used to restrict the wavenumber range to approximately

2350 - 3200 cm^{-1}. Digital filtering has reduced values outside the 1975 - 3950 cm^{-1} range to zero to avoid aliasing.

4.1.3 Nitric acid

Lunar measurements

Wintertime measurements of nitric acid have been made at Arrival Heights since 1998 (*Wood et al.*, 2004). In order to ensure consistency between years, a standard task file has been used. Each task file consists of three lunar measurements, with the tracker alignment adjusted to maximize the intensity of the signal between each measurement, followed by a background sky scan. Each lunar measurement was made up of 20 single-sided fast-return scans and was at a resolution of 0.02 cm^{-1}. An aperture size of 1.4 mm, giving a field of view of 6.364 milliradians, was used. The background sky scan was made pointing at the sky at the same elevation but 10 degrees forward in azimuth to the moon and was used for the empirical correction of the broadband emission from the tracker and instrument. This measurement consisted of 10 scans at the lower resolution of 0.1 cm^{-1}, with a 1.4 mm aperture.

For both solar and lunar measurements, an optical filter was used to limit the wavenumber region of the spectra to between 700 and 1400 cm^{-1}. Digital filters were used to remove anything above 1974 cm^{-1} for the Fourier transform.

Solar measurements

Sunlit HNO_3 measurements at Arrival Heights have also been made regularly as part of the NDSC measurement program (*Wood et al.*, 2002, 2004). These measurements were made at the higher spectral resolution of 0.0035 cm^{-1} and have typically been made with a 0.85 mm or 0.65 mm aperture (3.86 or 2.96 millirad field of view), depending on the intensity of the sunlight. The measurements usually consist of two scans, with each scan taking less than two minutes.

4.2 Ancillary data

The interpretation of measurements of stratospheric trace gases made during the Antarctic winter would not be complete without some discussion of the associated meteorological conditions. In this section brief overviews of the NCEP meteorological analyses and the potential vorticity calculations used in this study are presented.

4.2.1 NCEP (NMC) meteorological analyses

Temperature and pressure information used for this work came from the meteorological analyses of the National Centers for Environmental Prediction, NCEP (formerly known as the National Meteorological Center, NMC). Temperature and geopotential height profiles on 18 pressure levels between the surface and 0.4 hPa were determined for the NDSC community by the Climate Prediction Center of NCEP for all of the NDSC sites, including Arrival Heights (*Miller*, 2004). These are freely available at http://www.ndsc.ncep.noaa.gov.

NCEP/NMC geopotential height and temperature profiles were determined from two analysis systems (*Newman*, 1996; *Kempler*, 2002; *Miller*, 2004). Tropospheric (1000 - 100 hPa) data fields were 1200 GMT fields from the NCEP Global Daily Assimilation System (GDAS). GDAS meteorological fields were made from assimilated height, temperature and wind data from ground stations, satellites, radiosondes, aircraft, buoys, ships and other measuring systems (*McPherson et al.*, 1979; *Trenberth and Olson*, 1988; *Kanamitsu*, 1989; *Derber et al.*, 1991). Stratospheric analyses (70 - 0.4 hPa) were 1200 GMT NCEP Climate Predictions Center operational analyses. These analyses were produced using a modified Cressman analysis (*Gelman et al.*, 1986) where fields were iteratively adjusted by weighted data from radiosondes and satellites, depending on the distance from the grid point (*Kempler*, 2002; *Miller*, 2004).

The NCEP/NMC analyses were determined on a 65 $\times$ 65 NMC polar stereographic grid with a resolution of about 2.5° latitude by 2.0° longitude (*Kempler*, 2002). Profiles for the NDSC stations were then determined by interpolation of the analysis fields to the station location (*Miller*, 2004).

4.2.2 Potential vorticity

Potential vorticity is a measure of the vorticity that an air parcel would have if it was moved to a standard altitude and latitude. It is a conserved quantity on an isentropic (constant potential temperature) surface, which makes it a useful tool for tracking movement of air parcels in the atmosphere. Ertel's potential vorticity for adiabatic frictionless flow, EPV, is defined as

$$EPV = -g(\zeta_\theta + f)\frac{\partial \theta}{\partial p} \tag{4.1}$$

where g is the acceleration due to gravity, p is pressure, θ is potential temperature and f is the Coriolis parameter. ζ_θ is the relative vorticity on an isentropic surface and is determined from the horizontal wind fields (*Salby*, 1996).

Ertel's potential vorticity is commonly used to define the polar vortex boundary region – a region of approximately 5° latitude in width which is characterized by steep gradients in

potential vorticity and strong winds which serve as a barrier to transport. The definitions of the polar vortex edge and polar vortex boundary regions used in this work follow the work of *Nash et al.* (1996). The polar vortex edge is defined as the location of the highest EPV gradient, constrained by the proximity of a reasonably strong jet. The equatorward and poleward boundaries are defined as the local maximum convex and concave curvatures in the EPV surrounding this vortex edge (*Nash et al.*, 1996). The EPV has been calculated daily at 0000 UT for Arrival Heights using the NCEP meteorological analyses on the 450 and 550 K potential temperature surfaces (approximately 19 and 22 km respectively) by Greg Bodeker [National Institute of Water and Atmospheric Research, personal communication]. The potential vorticity corresponding to the vortex edge and vortex boundary region edges have been calculated at the same time. Potential vorticities in the southern hemisphere are negative. Those with absolute values larger than that of the polar vortex correspond to regions within the vortex, while smaller values correspond to regions on the equatorward side of the vortex.

Chapter 5

Data Analysis

As outlined in Chapter 3, a retrieval scheme is necessary to determine trace gas amounts from the absorption spectra. In this chapter, the analysis and retrieval details of the HCl and HNO_3 partial column amounts will be presented. The description focuses particularly on the new lunar measurements, with a brief description of the complementary solar analyses presented at the end of each section. A particular emphasis has been placed on the previously unpublished lunar HCl observations. Detailed error analyses for each of the data sets, based on the work of *Rodgers* (2000), will also be presented.

5.1 Hydrogen chloride

5.1.1 The data

As noted in Chapter 4, lunar HCl measurements were made during the 2003 winter on every clear opportunity during the week surrounding the full moon. A total of 363 individual spectra were recorded over 28 days spanning the April to September full moon periods. May was particularly affected by weather, with only two days of measurements made, approximately four days after the full moon. July and August were the most successful months, with measurements being made on seven days during each period, up to four days out from the actual full moon date. The S/N of the individual spectra, calculated from an average S/N in two windows, 2925.75 - 2925.85 cm^{-1} and 2925.95 - 2926.05 cm^{-1} (on either side of the HCl absorption line) ranged from 4.4 to 47.9, with an average value of 17.2. An example is shown in Figure 5.1. A typical solar spectrum, which would generally have an S/N around 200 in the same region, is shown for comparison.

While most of the difference in S/N between the solar and lunar spectra can be attributed to the huge intensity difference between the two light sources, further noise in the lunar spectrum can be attributed to noise caused by the radiation of the room and instrument, enhanced by the high levels of amplification that the lunar detector required in order to measure a signal from the moon.

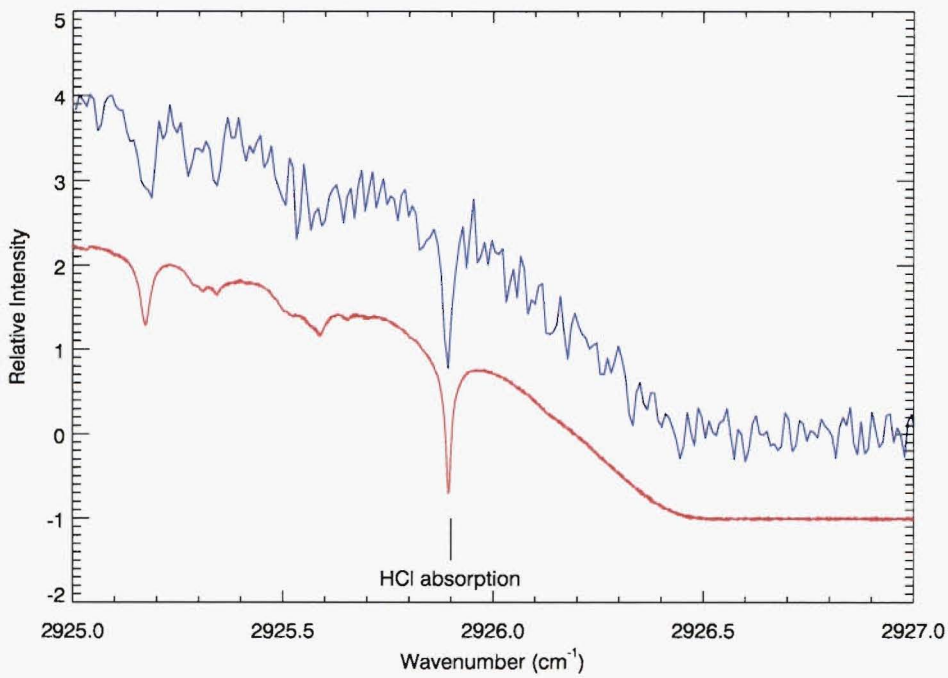

Figure 5.1: HCl absorption spectra measured on April 14th 2003 using the moon (blue) and sun (red) as the light source. The solar spectrum has been shifted down by 1 for ease of comparison. The S/N of the lunar spectrum, made at a resolution of 0.02 cm^{-1} as detailed in Chapter 4, is 15.6. The S/N of the solar spectrum, made at a resolution of 0.0035 cm^{-1}, is 190.

5.1.2 Processing the data

Because the individual spectra have such low signal to noise ratios, the information content in the measurement is limited and it becomes likely that the retrieval will either over-fit the measurements, taking information out of noise, or that the retrieved profile will be dominated by information from the *a priori* profile. As such, it is desirable to improve the raw data to increase the signal to noise ratio, and hence increase the amount of information that the retrieval is able to take out of the measurements. This has been achieved by averaging a number of spectra together.

Averaging the spectra works on the assumption that random noise has a mean value of zero, and hence by averaging a number of spectra together, spectral components caused by noise should tend to cancel out. The advantage of this method of improving the S/N over alternatives such as apodization or truncating the spectrum is that there is no corresponding loss of resolution or information.

Simply adding spectra together, however, does not take into consideration the effects of changing path-length on the observed spectra. Spectral lines observed through large airmasses (large zenith angles) will be seen as deeper than those observed from directly above, as there are fewer molecules of the gas in the path to absorb the light in the latter

case. This effect occurs in a non-linear way, as given by the Lambert-Beer law

$$I(\lambda) = I_0(\lambda)e^{-\tau m} \tag{5.1}$$

where $I(\lambda)$ is the intensity of light arriving at the Earth at a particular wavelength, $I_0(\lambda)$ is the intensity of light incident on the top of the atmosphere, τ is the optical depth of the atmosphere (including contributions from scattering and absorption by gases and particles) and m is the airmass, or ratio of the amount of gas in the light path to the amount of gas directly above.

As such, in order to add spectra made at different airmasses, the spectra must be corrected to an appropriate average airmass and added consistently with Equation 5.1. Additionally, because the intensities of the individual spectra may be different due to small atmospheric fluctuations or airmass variations, the spectra should be normalized. Assuming that τ remains constant over the course of the measurements, an average normalized spectrum, I_{avg}, for an average airmass, m_{avg}, is therefore given by

$$I_{avg} = e^{(\sum \frac{ln(I_n)}{m_n} . m_{avg})} \tag{5.2}$$

where m_n and I_n are the airmasses and normalized intensities of the individual spectra.

For this study, the normalization factor for each individual spectrum has been determined by calculating the average value of points between 2925.75 and 2925.85 cm^{-1}. This region has been chosen as it is within the micro-window used for the retrieval (see Section 5.1.3) yet is mostly unaffected by large absorptions of the gases in the micro-window and is therefore representative of a background intensity. By using an average value, individual noise spikes within the region are not dominating the normalization factor.

The airmass, m_n, for each spectrum has been calculated for an altitude of 20 km (i.e., the middle of the 12 - 28 km partial column region that we are interested in) using output from Raytrace (Chapter 3). The airmass for each altitude layer is slightly different, as it depends on the amount of gas in the layers as well as on the curvature of the Earth, with the airmass at the ground most closely matching the typical approximation of the secant of the zenith angle.

Between 3 and 15 measurements made with identical settings during the same measurement session have been used for each averaged spectrum. Individual measurements with a S/N of less than 10 or those that resulted in fits with a root-mean-squared difference between the fit and the measured spectra of more than 10% have been excluded (a total of 53 spectra). These can generally be identified as being weather affected. A further 14 from the original data set were not included as there were fewer than 3 spectra remaining in a given time-frame with the same parameters. A total of 45 averaged spectra were created, showing a significant increase in S/N. These ranged from 20.9 to 99.0 with

an average value of 44.9.

5.1.3 Defining the retrieval

While the retrieval algorithm has been outlined in Chapter 3, there are many considerations that must be made regarding the way that the retrieval will be implemented for a particular gas, at a particular time of the year. This section will outline and justify the decisions made in defining the retrieval scheme for the lunar HCl measurements.

Choice of micro-window

Absorption lines seen in the infrared part of the electromagnetic spectrum are a result of the quantized absorption of radiation that causes vibrational and rotational transitions of molecules in the atmosphere. The fundamental absorption band, corresponding to a jump in vibrational energy from the ground to first excited state of the diatomic molecule HCl, is centred at a wavenumber of 2886 cm^{-1} and has a band envelope of about 150 cm^{-1} (*Alpert et al.*, 1970). At a given vibrational level there can be many rotational levels, and changes in the rotational energy are seen in this absorption band as discrete lines.

The choice of a particular absorption line to retrieve information about the gas profile depends on several factors, the most important being the influence of other absorption lines in the region of interest. For this study the HCl $R(2)$ line at 2925.9 cm^{-1} has been used. While this line is on the wings of a broad methane line, there is little interference from other species, and as such, fewer gases need to be well known in order to accurately retrieve an HCl column amount from the measured spectrum. Other lines in the HCl absorption band have been investigated for this research, but have been eliminated either because the optical filter removes their wavelength region or because the region is dominated by water vapour absorption. While the amount of water in the Antarctic atmosphere is significantly less than other regions on Earth, it is still not well quantified, and hence adds considerable uncertainty to the retrieved column amounts.

The micro-window chosen for the retrieval, including this absorption line, is 2925.75 - 2926.05 cm^{-1}. This micro-window is routinely used for solar HCl measurements made using this instrument, so continuing to define the lunar retrieval over the same region makes these two sets of measurements comparable. Other studies of HCl have also used this absorption line and similar micro-windows (*Rinsland et al.*, 1991; *Connor et al.*, 1998; *Goldman et al.*, 1999). In this window the only gases with any notable absorption features are methane (CH_4) and nitrogen dioxide (NO_2), as shown in Figure 5.2. While the effect of NO_2 is very small, the profile of CH_4 should ideally be well known in order to correctly determine the curvature of the background for the HCl retrieval. A profile-scaling technique, where the profile was scaled by a single multiplicative factor in order

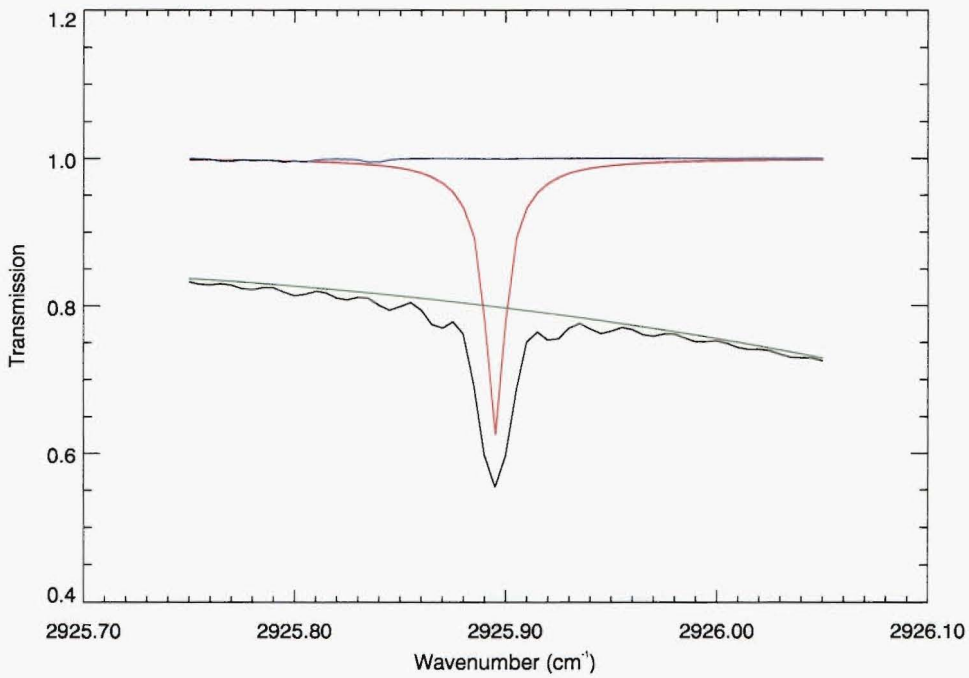

Figure 5.2: Absorption by gases in the HCl retrieval micro-window. The absorptions due to HCl, CH_4 and NO_2 are shown in red, green and blue respectively. The spectrum shown in black is the total absorption of the gases in the micro-window, as would be observed by a 45cm path length (0.02 cm^{-1} resolution) spectrometer using the moon as a light source. Oscillations in this total spectrum are a result of the limited instrumental path length, which causes an abrupt truncation of the interferogram. The spectra have been calculated using the simulation program of Justus Notholt [University of Bremen, personal communication].

to best fit the data, was used to determine both of these gases during the retrieval.

Signal to noise ratio

The S/N of the measurement is used for the determination of the measurement covariance matrix, S_ϵ, and the calculation of the averaging kernels. It plays an important role, as it serves as the means by which the retrieval evaluates how much information it can take from the measurement.

Two options exist for how to best define the S/N for a retrieval. For comparison of the data with model results, the averaging kernels and *a priori* should be used to smooth the model profiles in the same way that the retrieval smoothed the atmospheric profile, so that the error due to smoothing can be removed. In the case of a large data set it may be preferable to use one S/N for all of the retrievals, even though it means a loss of data in some of the measurements. This has the advantage of having only one averaging kernel which can then be used for smoothing all of the model results for comparison with all of the data. Ideally this value should lean towards values consistent with the lower-quality

measurements, so that the retrieval applied to these measurements does not attempt to take information out of the noise. For a small number of measurements, individual averaging kernels can be calculated for each measurement, allowing the retrieval to be optimized.

For the lunar HCl measurements, an individual S/N, calculated as described in Section 5.1.1, has been used for each retrieval.

Choice of an *a priori* profile

The choice of an *a priori* profile is inherently going to affect the retrieval, so it is desirable to make it as accurate an estimate as possible. HCl has not been widely measured in the Antarctic, especially during the winter, and as such, there is limited data available to use for the makeup of this profile. The HALOE instrument made measurements of the HCl profile over a wide range of latitudes, as outlined in Chapter 1 (*Russell et al.*, 1993; *Reber et al.*, 1993). The combined measurements from 1994-2000 have been used to create the UARS reference atmosphere profiles, available from the SPARC data centre (http://www.sparc.sunysb.edu). Average monthly profiles from October - April for 72° S equivalent latitude have been used to make a summertime *a priori* profile between 15 and 46 km. Between 8 and 15 km, averaged data from MkIV balloon HCl measurements made on 4 days from Esrange, Sweden, have been used [Geoffrey Toon, Jet Propulsion Laboratory, personal communication]. Below 8 km, where there is no data available, the profile has been extrapolated back to a mixing ratio of 1×10^{-11} at 6 km and maintained at this value to the ground. Above the summertime profile there is also no data, so the HCl mixing ratio has been kept constant at 2.9×10^{-9}, which was the average value calculated for the HALOE-based profile at 46 km. The complete assumed profile, hereafter referred to as the HALOE profile, is shown in Figure 5.3.

During the Antarctic winter, the HCl vertical profile is known to change significantly as a result of chemical reactions on the surface of PSCs. Because the HALOE *a priori* profile contains only summertime measurements, it cannot reasonably be expected to give sensible results during the winter. This was clearly the case for the June - September measurements retrieved with this profile, as the results were seen to go negative in one or more regions. As such, *a priori* profiles with depleted values of HCl were developed for use in the winter months. The work of *Moore et al.* (1990) suggests that HCl will react with $ClONO_2$ on the surface of polar stratospheric clouds in less than one day. As such, real PSC observational data could be used to identify regions where and when the *a priori* profile should be depleted.

The first polar stratospheric cloud of 2003 was observed by an aerosol lidar at McMurdo Station on May 22nd. It wasn't until June 11th, however, that PSCs became

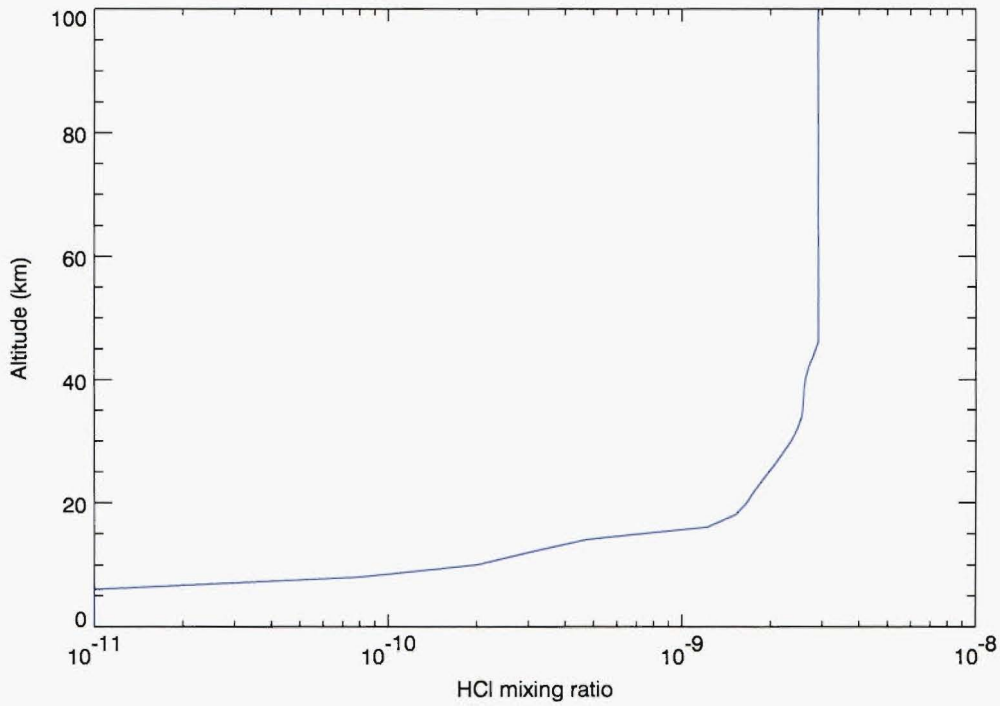

Figure 5.3: HCl *a priori* profile derived from HALOE summertime measurements and other sources, as described in the text.

an almost permanent feature of the Antarctic stratosphere [Paola Massoli, Institute for Atmospheric Science and Climate, CNR, Rome, personal communication]. PSCs were typically observed between 12 and 25 km. HCl profiles with various amounts of depletion in this region were investigated, with the final profiles used for the retrievals of measurements made in June and in July - September shown in Figure 5.4. Reassuringly, consistent column amounts were obtained with a range of *a priori* profiles, showing the final choices to be largely arbitrary.

Secondary gases in the micro-window also required an *a priori* profile. The CH_4 profile used was an average of year-round monthly average profiles from the UARS reference atmosphere between 15 and 46 km, from 72°S equivalent latitude. Top and bottom were smoothly joined to a profile developed by Geoffrey Toon from MkIV balloon measurements measured in the northern mid-latitudes (*Toon*, 1991; *Toon et al.*, 1999) and subsided for high-latitude use [Geoffrey Toon, Jet Propulsion Laboratory, personal communication]. Experiments using a winter-months-only averaged profile, and an averaged profile subsided by 4 km in the winter showed no significant effect on the HCl retrieved partial column amounts, and hence were excluded. The NO_2 profile used was also that of Toon [Geoffrey Toon, Jet Propulsion Laboratory, personal communication].

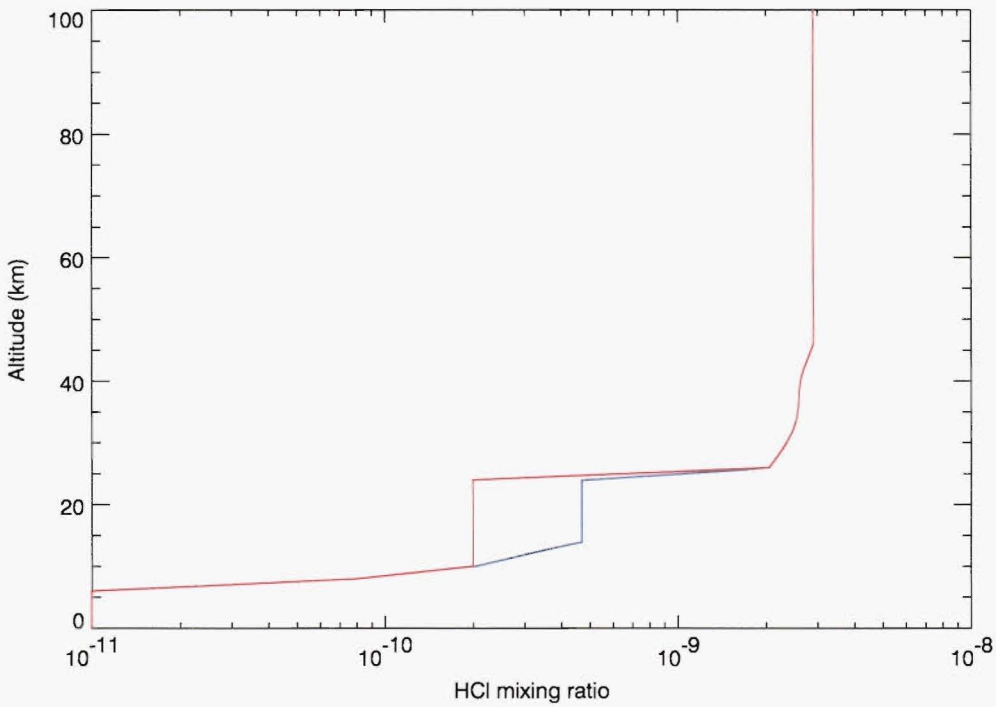

Figure 5.4: Depleted HCl *a priori* profiles used during the winter months. The blue profile was used for the June retrievals and the red one for July - September.

A priori uncertainty

Just as important in defining the way the retrieval behaves, the *a priori* uncertainty matrix is what constrains the retrieval to the *a priori*. For those retrievals which used the HALOE profile (April and May measurements), the actual 2-sigma standard deviations from the averaged HALOE data were used for the *a priori* uncertainty, though any values less than 10% were set at 10%. In the region below the HALOE measurements, uncertainties were set at 70%, as this area is a real unknown. Above the HALOE measurements, uncertainties were set at 10%, though this value was largely arbitrary due to the small amount of gas and lack of sensitivity of the retrieval in this region.

For the June profile, the *a priori* uncertainty profile had the same percentage uncertainties as the HALOE profile. This gave a large enough absolute uncertainty that results consistent with those obtained with the HALOE *a priori* profile could be retrieved. For the July - September profile, the uncertainty profile was created to match the absolute uncertainty applied to the June profile. If the same percentage uncertainties as had been used for the other two profiles were used with this one, the absolute variation possible for the retrieved profile was so small over the depleted region that the retrieval was effectively forced to retrieve the *a priori* over that region and put any changes into the region above, creating instabilities and unrealistic partial column amounts. Using the same absolute

values in the *a priori* uncertainty profile also meant that the retrieval algorithm would technically be able to retrieve a similar profile using either of the depleted *a priori* profiles. Attempts were made to give all three profiles the same absolute uncertainties, but the resulting percentage uncertainties were so high for the depleted profile cases that the retrievals became very unstable. These absolute uncertainties were, however, used for the error analysis in Section 5.1.5.

A priori uncertainties for the profile-scaled secondary gases were set to 100% uncertainty in the scale factor. The fitting of these gases, and CH_4 in particular, is important to account for the slope observed in the spectrum. As such, it is desirable that there is a large enough uncertainty in the secondary gas profiles that the retrieval is able to move these gases around to recreate the slope without having an influence on the HCl retrieval. Tests showed that an uncertainty of less than 100% in the CH_4 scaling factor meant that the retrieval was occasionally forced to account for the slope shown by altering the HCl profile, causing large changes in the column amount. Higher values, however, had no effect on the retrieved column amount, suggesting that the slope was being adequately modelled using the 100% uncertainty figure.

5.1.4 Spectral fits and the sensitivity of the retrieval

The profile retrieved by SFIT2 is determined by the optimal fit of a synthetic spectrum to the measured spectrum. The quality of this fit depends on the noise in the spectrum, how closely the *a priori* profile matches the true state of the atmosphere, and how the retrieval has been defined. Examples of the spectral line fits achieved by SFIT2 to the measured lunar spectra are shown in Figure 5.5 for example spectra from April, June and August. Each of these spectra has an S/N of approximately 40.

While SFIT2 is a profile retrieval algorithm, the retrieved profiles must be treated with caution, as individual layers are not independent. An understanding of the limitations of the retrieval can be gained from the averaging kernels, as introduced in Chapter 3. Figure 5.6 shows two representations of the averaging kernels corresponding to the April 18th fit in Figure 5.5.

The two representations give different information. The left plot in Figure 5.6 shows the averaging kernels of individual layers in the fit. The area under each of these curves shows how much information comes from the measurement for that altitude, and the width and position of the kernels gives an idea of the resolution and which parts of the atmosphere are contributing to the retrieved profile at that altitude. Note that there is no information from the measurement below 7 km, or above 40 km, so the retrieval has no sensitivity in these areas (it will return the *a priori*). Note also that where there is information in the measurement, the kernels are much broader than an individual layer,

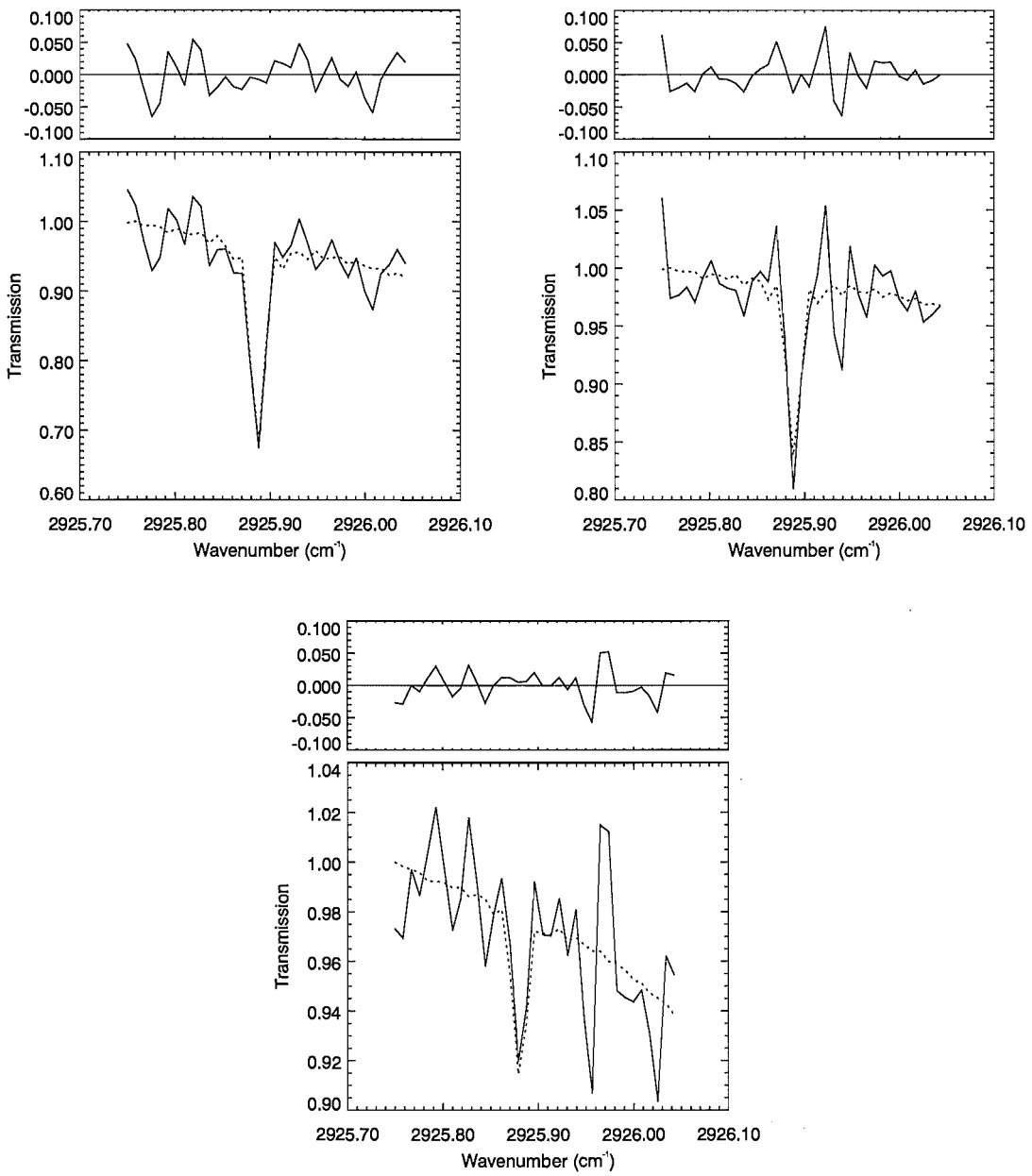

Figure 5.5: Fits obtained by SFIT2 for April 18th (top left), June 14th (top right) and August 8th (bottom) lunar HCl measurements. The measured and calculated absorption lines are shown by the solid and dashed lines respectively. The residual differences between these two curves are shown in the top panels.

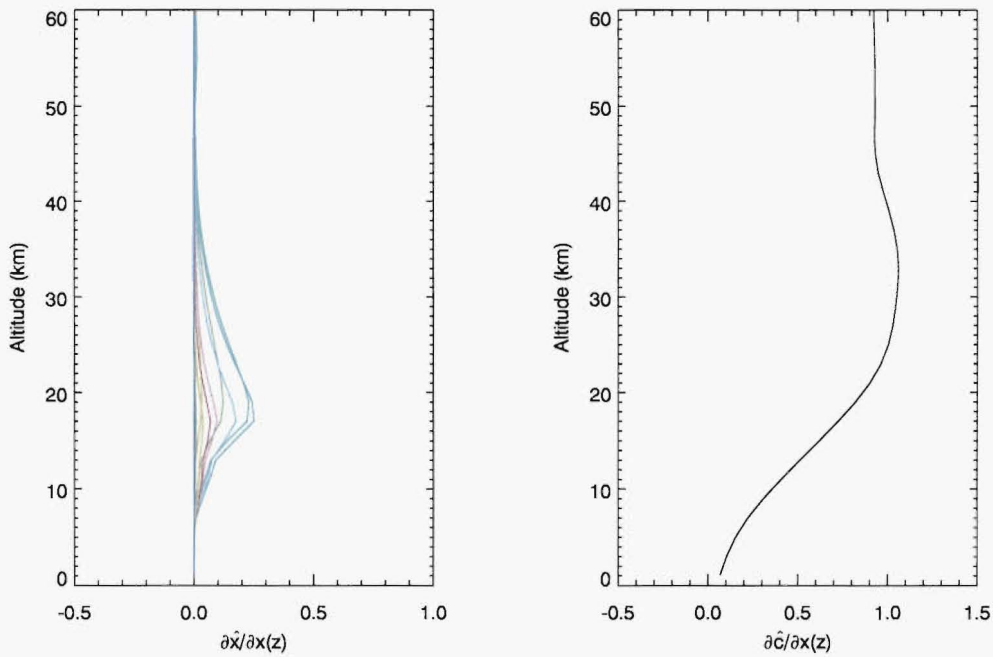

Figure 5.6: Averaging kernels corresponding to the April 18th fit in Figure 5.5. The left plot shows individual averaging kernels for each profile layer from the ground to 50 km, with layers spaced regularly at 2 km intervals. The averaging kernel for the entire 12 - 28 km partial column is shown on the right. For further discussion, see text.

overlapping, and may not even peak at their expected altitude. This is due to the limited information content of the measurements and clearly shows that the retrieved layers are not independent of each other. The right plot in Figure 5.6 is the partial column averaging kernel. It is determined from the averaging kernel information for each layer, weighted by the HCl density profile, and then summed over the 12 - 28 km partial column. This representation gives an indication of which parts of the atmosphere are affecting the quoted partial column amount. Ideally values above and below 28 and 12 km respectively would be zero, but the fact that the values remain high above 28 km shows that the retrieval is unable to differentiate changes at that height from changes in the 12 - 28 km partial column region. As there are very few molecules above 28 km, and we expect very few changes to occur in this region, this should have little effect on the partial column amount. The gradual reduction in the averaging kernel values below 12 km shows that there may still be some contribution to the retrieved column amount as a result of changes low down. Over most of the retrieved column height range, values are close to one. This shows that information is being obtained from the measurements, rather than the *a priori*, and is a good indication that there is sufficient information in the measured spectrum to retrieve the amount of HCl in this partial column. Partial column averaging kernels are also shown for the June and August fits in Figure 5.7.

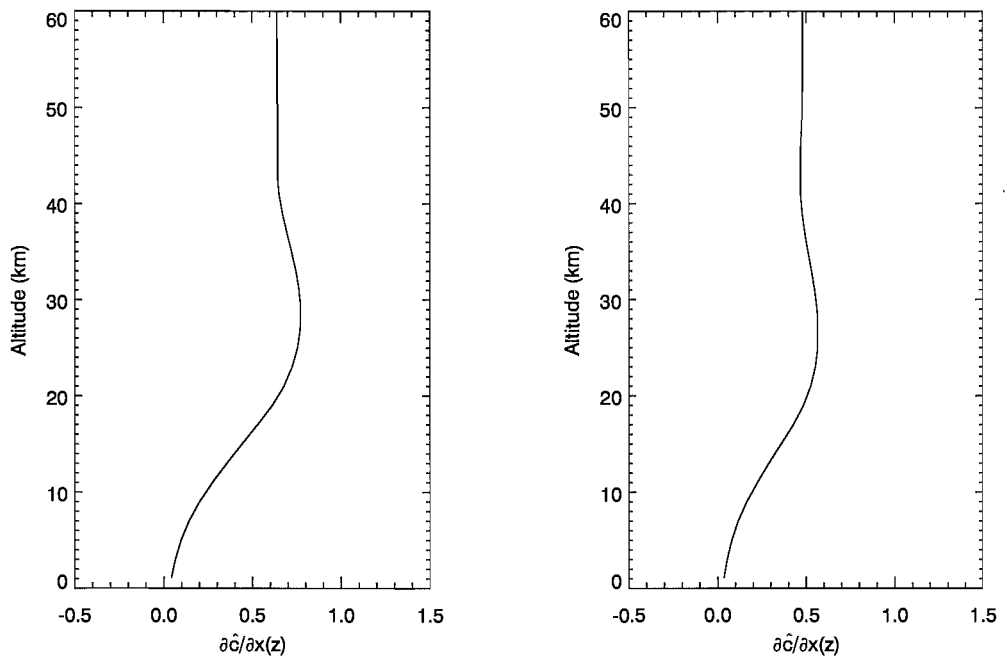

Figure 5.7: 12 - 28 km partial column averaging kernels for the June 14th (left) and August 8th (right) fits shown in Figure 5.5.

Figure 5.7 shows that less information is being taken from the measurement and more from the *a priori* in these months than was seen in April. Because the S/N are similar for all the spectra, we can assume that the amount of information in the absorption line would be similar for similar amounts of HCl, and hence can conclude that the lack of information coming out of the measurements is due to the lack of information in the measurements, i.e., that there is so little HCl that the absorption line can provide little information. A look at the reduction in the depth of the fitted absorption lines (Figure 5.5) supports this conclusion.

5.1.5 Error analysis

The error analyses for the 12 - 28 km HCl partial column measurements have been carried out following the work of *Rodgers* (1990, 2000) and *Connor et al.* (1995), as presented in Chapter 3. Each term of Equation 3.10 arises from some aspect of the retrieval process and can be quantified individually. This section outlines the calculation of each error term and determines the effect of that term on the retrieved partial column amount. The estimated uncertainty due to each term will be presented in Table 5.2, at the conclusion of the section, including a final estimate of the combined uncertainty associated with each partial column measurement.

Smoothing error

While for many situations the smoothing error can essentially be eliminated, as outlined in Chapter 3, in order to present partial column amounts an estimate of the effect of the smoothing error has to be made.

The uncertainty in the partial column amounts due to the smoothing error has been determined following the work of Rodgers (*Rodgers*, 1990), with the smoothing error covariance given by Equation 3.11. Because the true variability of the atmosphere about the mean is unknown, the S_x covariance matrix used in these calculations has been assumed to be diagonal and was constructed using the real variance in the HALOE measurements that were used to create the April - May *a priori* profile, as described in Section 5.1.3. While this variance is likely to be slightly too small, due to the lack of winter measurements in the profiles, this is the best source of information on the true state of the atmosphere that is available to us. The absolute value of this variance has been used for creating covariance matrices for the June - September periods, giving these times very large relative S_x matrices and hence large smoothing errors. Figures quoted in Table 5.2 at the end of the section are those relevant for average spectra for each of the April - May, June and July - August periods. As the large variation in S/N between individual measurements results in correspondingly large variations in their smoothing errors, individual smoothing errors have been calculated for each retrieved partial column amount. These values are given in Appendix A.1.

Model parameter error

The error in the retrieved partial column amounts due to errors in the parameters associated with the forward model can be calculated for each parameter, b, as outlined in Chapter 3. The variance, S_F, was determined following the formalism given in Equation 3.12 for each parameter, as outlined below. Tests were carried out using three spectra, one in April, one in June and one in August, each with a S/N of approximately 40, giving error estimates for each of the April - May, June, and July - September periods. The results are presented in Table 5.1.

Temperature Uncertainty in the temperature profile affects the retrieved partial column amounts as a result of the temperature dependence of the absorption and through the dependence of pressure, and hence pressure-broadening, on temperature. Temperature data for this study was from the NCEP data set (Chapter 4).

The K_b matrix was determined by perturbing the temperature profile by $\delta T = 2K$ in each of the profile altitude layers sequentially, each time calculating a column of the K_b matrix from the difference between the perturbed and unperturbed spectrum, divided by

δT.

The covariance matrix, S_b, was created using realistic errors from those quoted with the NCEP data for this site (*Miller*, 2004), i.e., 2.5 K at pressures equal to or greater than 40 mb; 3.5 K between 7 and 40 mb; 5 K between 3 and 7 mb; 6 K between 1 and 3 mb; 7 K between 0.5 and 1; and 9 K for pressures less than 0.5 mb. Values in the matrix were given by

$$\rho\sigma_i\sigma_j \tag{5.3}$$

where σ is the uncertainty at a particular height as explained above, and ρ is a correlation factor given by $\rho = e^{-\frac{|z_i - z_j|}{z_c}}$, where z_c is the correlation length in kilometres. An 8 km correlation length has been assumed for these calculations.

Zenith angle Each lunar measurement took approximately 10 minutes, during which time the zenith angle of the moon could change by up to 0.5°. Uncertainty in the zenith angle can cause errors in the airmass calculations, and hence in the partial column amount. The zenith angle used for the calculation of the airmass for each individual measurement was calculated using information on the number of scans, length of the scans, and the time of ZPD crossings. The zenith angle used for the retrieval was that which corresponded to the average airmass used in the calculation of the averaged spectra. A very conservative estimate of the uncertainty in this zenith angle is the variation of the zenith angle of the individual measurements through the course of a measurement, approximately $\pm$ 0.2°. This value was used for S_b. A perturbation of this size was also used for the calculation of K_b. Because the zenith angle is a single parameter, S_b is a scalar and K_b is a vector.

Instrument line shape The retrieval of the HCl profile from an observed spectrum can be made because pressure broadening of the spectrum is height dependent. An accurate knowledge of the effect of the instrument, the 'instrument line shape', on the spectrum is hence essential for an accurate profile retrieval. For these column retrievals, a perfect instrument line shape was assumed, which leads to an uncertainty in the retrieved column amount. Regular realignment and monthly HBr cell tests (*Hase et al.*, 1999) are carried out for this instrument to ensure that the instrument alignment is maximized and stable. Cell tests carried out during the 2003 winter showed the instrument alignment to be stable over the period, meaning that this assumption is likely to cause an approximately systematic bias. The tests did, however, show that over the full 250 cm path-length of the instrument, with an 0.65 mm aperture, there was a decrease in the modulation efficiency (or movement away from the ideal line shape) of approximately 10%. This corresponds to a decrease of approximately 3-4% at 45 cm, the maximum path-length of these measurements. For a larger aperture this is likely to be slightly bigger, and as the measurements have been made at apertures of 0.65 mm - 1.4 mm, the uncertainty for S_b

has been estimated at 10%. The K_b vector has been determined by setting the retrieval to assume a linear reduction in the modulation efficiency over the path-length, with the modulation coefficient at the maximum path-length equal to a 10% reduction.

Line parameters Line parameters are from the HITRAN2000 line list, including the updates that were released in 2001. Uncertainties in the line parameters will cause systematic biases in the retrieved column amounts. For this error analysis, perturbations of the line intensity and air-broadened half-width of the HCl line at 2925.897 cm^{-1} and the large saturated CH_4 line at 2927.076 cm^{-1} were carried out. Uncertainties quoted in the line list for the line intensity and air-broadened half-width (*Rothman et al.*, 2003) have been used for the S_b scalar for each test. The K_b vector for each parameter has also been determined by perturbing the parameter by this amount.

Interfering gases Because they are included in the state vector, technically the uncertainties due to interfering gases present in the retrieved micro-window are a type of smoothing error called an 'interference error' (*Rodgers and Connor*, 2003). It is, however, conceptually simpler to treat them as model parameters. As this results in a conservative error estimate compared to the interference error treatment, this is a valid substitution. Both CH_4 and NO_2 are fitted in the retrieval by scaling the profile by a multiplicative factor, with an *a priori* estimate of this scale factor equal to 1. The uncertainty in the quoted partial column amounts due to these gases has been estimated by perturbing this scale factor.

CH_4 For determining the K_b vector, the scale factor was perturbed by 20%. For S_b, an estimated uncertainty of 34% has been used, determined from the average standard deviation of the mean monthly profiles used for creating the *a priori* profile.

NO_2 The K_b vector for NO_2 has also been determined by a perturbation of 20%. Because NO_2 undergoes depletion in the Antarctic winter, the profile can be expected to change significantly, so the uncertainty in the scale factor has been estimated at 50%.

Net forward model parameter errors The calculated uncertainties in the 12 - 28 km HCl partial column amounts for each of the forward model parameters are presented for the April - May, June and July - September periods in Table 5.1. The higher level of uncertainty in the April - May period can be attributed to having less dependence on the *a priori*, and hence greater flexibility in the retrieval, due to the larger amount of HCl gas in the atmosphere during this time. Uncertainties have been added in quadrature (or linearly

in variance), with no distinction made between systematic and random uncertainties, as recommended in *ISO* (1993).

Uncertainty Source	April - May	June	July - September
Temperature profile	2.87%	2.33%	2.18%
Zenith angle	0.82%	0.64%	0.54%
Instrument line shape	2.68%	2.04%	1.84%
HCl line intensity	1.92%	1.64%	1.66%
HCl air-broadened half width	0.59%	0.54%	0.50%
CH_4 line intensity	0.07%	0.04%	0.04%
CH_4 air-broadened half width	0.07%	0.05%	0.03%
CH_4 profile scale factor	1.57%	1.28%	1.27%
NO_2 profile scale factor	0.18%	0.19%	0.28%
Total uncertainty	**4.76%**	**3.83%**	**3.62%**

Table 5.1: Forward model parameter errors for lunar HCl measurements. The total uncertainty has been determined by adding uncertainties quadratically.

Measurement error

Also known as retrieval noise, the measurement error is the noise associated with errors in the spectral measurement. It has been determined using Equation 3.13. Because the measurement noise is uncorrelated and random, S_ϵ was taken to be a diagonal matrix with the S/N as the values of σ^{-1}. Values quoted in Table 5.2 are those for average measurements in each time period. Because the S/N varies so much between measurements, an individual calculation of the measurement error for each data point was determined using the S/N of the measurement. These are listed in Appendix A.1. The difference in the uncertainties due to retrieval noise for the April - May, June and July - September periods can be attributed to similar absolute uncertainties in the column amounts, which result in higher percentage uncertainties in times of depletion.

Net uncertainty

The total estimated uncertainty in the 12 - 28 km HCl partial column amounts, as determined using the uncertainties calculated for each error source in the April - May, June, and July - September measurement periods, is presented in Table 5.2.

5.1.6 Solar measurements

In order to make the solar and lunar measurements comparable, the retrieval of the HCl partial column amounts from solar measurements made in 2003 has been conducted as

Measurement Period	Smoothing Error	Model Parameter Error	Measurement Error	Total Uncertainty
April - May	7.46%	4.76%	9.37%	12.89%
June	24.28%	3.83%	11.18%	27.00%
July - September	42.99%	3.62%	20.93%	47.95%

Table 5.2: Estimated uncertainties in the 12 - 28 km HCl partial column amounts determined from lunar measurements for each of the April - May, June, and July - September periods, as described in the text.

described for the April - May measurements, using the HALOE *a priori* profile. A constant S/N of 200 has been assumed for all of the retrievals. Error calculations have been performed for these measurements in the same way as described for lunar measurements in Section 5.1.5, except that the uncertainty in the zenith angle has been reduced to 0.1, to reflect the smaller measurement time. While the effect of the instrument line shape is greater for higher resolution measurements, this is compensated for by the smaller aperture used for solar measurements. As such, an estimate of 10% uncertainty in the modulation efficiency over the path-length has been used, consistent with the instrument line shape deduced from the cell measurements. Total uncertainties for the solar measurements are given in Table 5.3. Quoted measurement and smoothing errors are average values. Uncertainties due to individual parameters are listed in Appendix A.2.

Measurement Period	Smoothing Error	Forward model Error	Measurement Error	Total Uncertainty
September - April	4.02%	3.80%	1.77%	5.81%

Table 5.3: Estimated uncertainties in the 12 - 28 km partial column amounts for solar measurements, as described in the text.

5.2 Nitric acid

Lunar HNO_3 measurements have been made on clear nights surrounding the full moon in each winter since the winter of 1998. While the analysis of these measurements is based largely on the work of Notholt (*Notholt*, 1994; *Notholt et al.*, 1997b; *Notholt and Lehmann*, 2003) and has been reported in our paper, *Wood et al.* (2004), the analysis details for the 2003 winter will be presented here for completeness. In addition, *Wood et al.* (2004) is based entirely on total column measurements, so results for partial column measurements consistent with those presented for HCl will be detailed. Partial column

amounts determined over smaller height ranges than the standard 12 - 28 km will also be introduced, in order to look for evidence of sedimentation and denitrification.

5.2.1 The data

Lunar measurements were made in 2003 on the same days that HCl measurements were made, with a measurement set typically being carried out prior to each HCl series. A total of 98 HNO_3 spectra were recorded during the winter. Signal to noise ratios for each spectrum were determined from the 868.65 - 868.95 cm^{-1} and 869.1 - 869.35 cm^{-1} wavenumber regions and ranged from 107 to 305, with an average value of 200. An example of a typical spectrum and its corresponding background sky scan are shown in Figure 5.8.

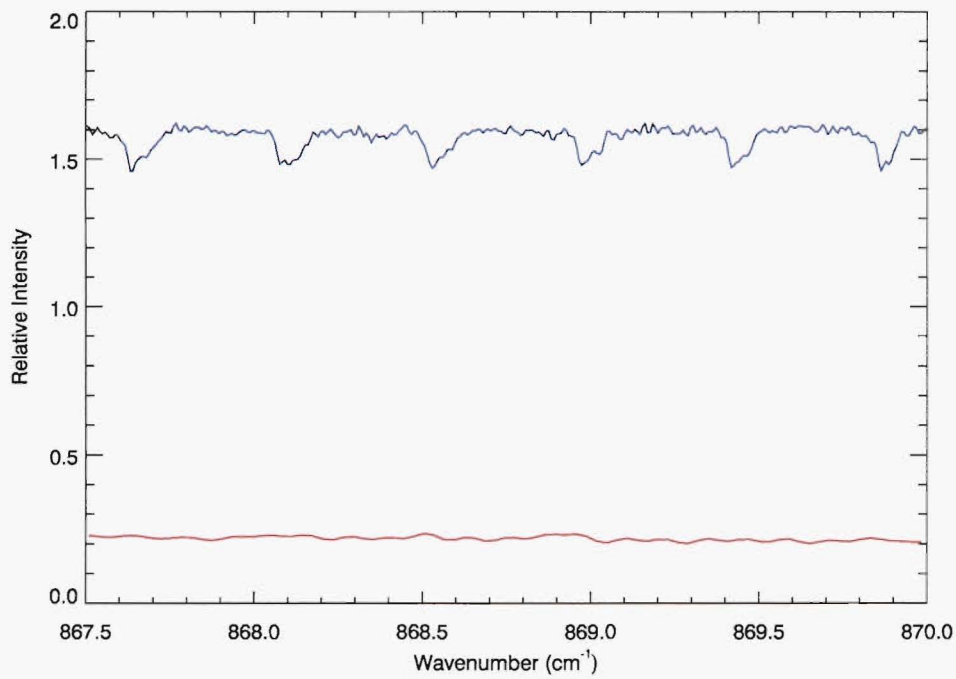

Figure 5.8: HNO_3 absorption spectrum (blue) measured on June 14th, 2003 using the moon as the light source. The S/N of the spectrum is 200.8. The corresponding background sky scan, made at the same elevation but 10 degrees forward in azimuth is also shown (red).

5.2.2 Processing the data

While the HNO_3 measurements had S/N that were sufficiently high that averaging was not required, moonlight measurements made in this wavelength region are affected by the emission of the atmosphere, room and instrument. These emission effects have been

corrected for in two ways, as suggested by *Notholt* (1994); *Notholt et al.* (1997b) and *Meier* (1997).

Zero-level correction

Broadband emission from the room and instrument is seen in the lunar spectrum as a shift of the baseline of the spectrum away from zero (*Notholt*, 1994). This is shown clearly in Figure 5.9. A solar spectrum made on the same day is not affected by this emission.

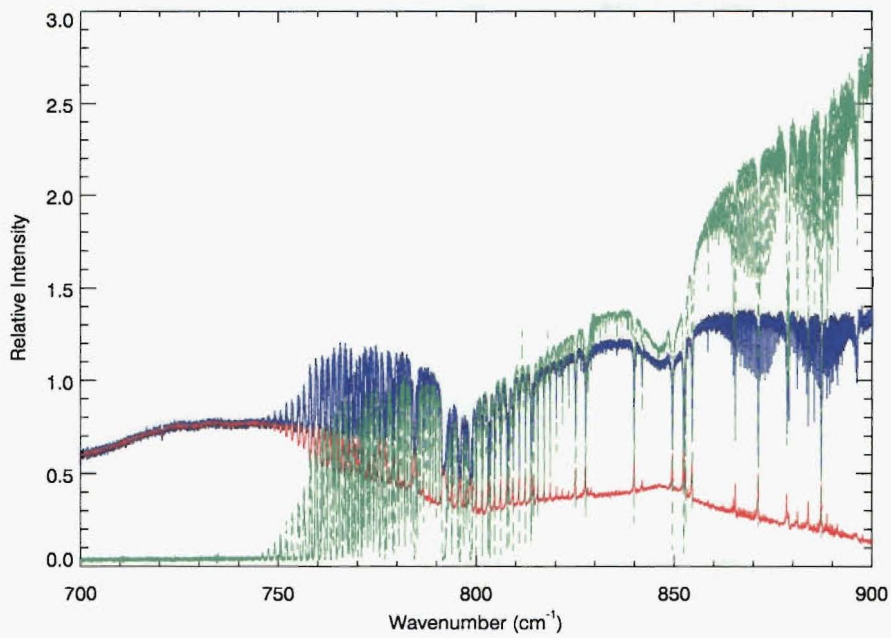

Figure 5.9: HNO_3 solar (green), lunar (blue) and sky (red) spectra made on April 14th, 2003. The broadband emission is clearly seen in the lunar spectra as a zero-level shift corresponding to the background sky spectra, but is not seen in the direct sun measurement.

Correction for the broadband emission has been made empirically using the background sky scans. In the 867.5 - 870 cm^{-1} wavenumber region that the nitric acid was retrieved in, average intensities of the background sky spectrum and lunar spectrum (in regions not absorbing) were determined. The correction was then calculated from the difference between these intensities. The effect of this correction was to increase the depth of the absorption line by shifting the baseline back to zero. The calculated zero-level shift, which was input directly to SFIT2 as a retrieval parameter for each spectrum, ranged from 0.10 to 0.43.

While a zero-level correction was not explicitly included in the solar retrievals, it is likely that a small zero-level offset is present in those measurements too, causing a slight bias in the retrieved column amounts. This will be further quantified in the error analysis.

Atmospheric emission

As well as broadband emission, the nitric acid in the atmosphere is emitting some radiation specifically in the regions where we see absorption lines in the lunar spectrum. This is visible (for strong lines) in the sky spectra shown in Figure 5.9. This emission is a function of the temperature and the amount of nitric acid in the path, and ideally would be treated within the forward model. As SFIT2 only models absorption, however, the effect of this emission must be treated separately.

While an ideal correction for the atmospheric emission would be the subtraction of a background sky spectrum taken at the same zenith angle but different azimuthal angle from the moon, we would need a spectrum of similar characteristics and resolution to the lunar spectrum in order to avoid introducing phase effects. The time required for this makes it impractical (*Meier*, 1997). Instead, we have calculated the emission contribution theoretically, as suggested by *Notholt et al.* (1997b).

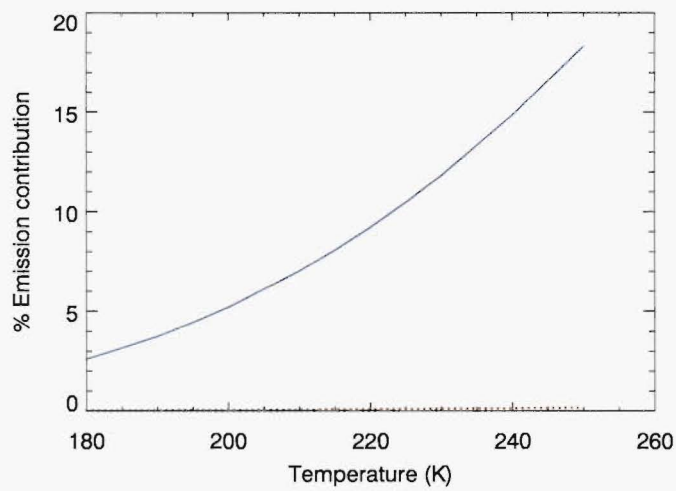

Figure 5.10: The contribution to the lunar (blue solid) and solar (red dotted) absorption lines from emission of the atmosphere, as detailed in the text. Typical average winter temperatures are 215 K for April, 205 K for May and 193 K for June - August.

The emission contribution to the absorption peaks is calculated from the ratio of the intensities of an atmospheric blackbody and a lunar blackbody. An average blackbody temperature for the atmosphere is calculated by weighting the temperature of each layer of the atmosphere by the amount of nitric acid in that region, as determined from the profile (*Notholt et al.*, 1997b). The intensity of this blackbody, at 868.75 cm^{-1} (the centre of the retrieval micro-window), is then ratioed with the intensity of a blackbody at the assumed full moon lunar surface temperature, 375 K, at the same wavenumber. This shows the contribution of the emission to the absorption lines at this wavelength to be between 8% early in the winter season and 4% in the colder months, as shown in Figure

5.10. A simple correction factor from this can be applied directly to the retrieved column amounts. A calculation of the effect of this emission in a solar measurement shows that the effect is negligible (also shown in Figure 5.10).

5.2.3 Defining the retrieval

Choice of micro-window

As for the HCl measurements, the micro-window used for the HNO_3 retrievals has been chosen to be consistent with the solar retrievals made from the same instrument. In this case, the window was 867.5 - 870 cm^{-1}. This micro-window contains six separate manifolds of HNO_3 absorption lines, allowing the retrieval to make maximum use of the information contained in the measurement. Minor interfering gases in the window are H_2O, OCS, and NH_3, as shown in Figure 5.11.

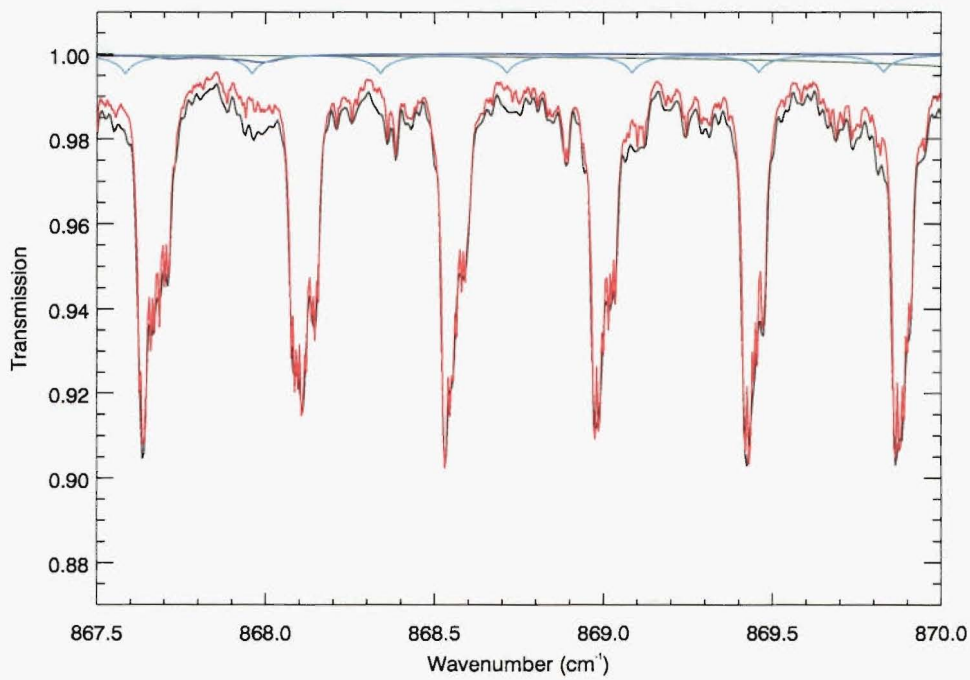

Figure 5.11: Absorption by gases in the HNO_3 retrieval micro-window. The absorptions due to HNO_3, H_2O, NH_3 and OCS are shown in red, green, blue and cyan respectively, with the total absorption including instrumental effects, as detailed in Figure 5.2, shown in black. The spectra shown are transmittance spectra calculated using the simulation program of Justus Notholt [University of Bremen, personal communication] as detailed in Figure 5.2.

Signal to noise ratio

Individual S/N calculated for each spectrum, as outlined in Section 5.2.1, have been used to accurately constrain the retrieval measurement uncertainty.

Choice of an *a priori* profile

Unlike HCl, HNO_3 has been measured during the winter months before, with both the CLAES (*Roche et al.*, 1993b, 1994) and the MLS (*Santee et al.*, 1995, 1998, 1999) instruments on board the Upper Atmosphere Research Satellite. As such, there is good quality *a priori* information available to use for the determination of the *a priori* vertical profile. It was decided to use just one *a priori* profile for all of the retrievals, incorporating the year-round variability captured in the satellite measurements.

The chosen *a priori* vertical mixing ratio profile was an annual average of HNO_3 profiles from 72°S equivalent latitude made by the CLAES instrument on board the UARS satellite between October 1991 and May 1993. This data was from monthly average profiles in the SPARC reference atmosphere project, available at http://www.sparc.sunysb.edu. Above 40 km, an average of two standard mixing ratio profiles, the Toon profile described previously and the standard refmod95 profile (based on the US standard atmosphere), was used. Below 14 km, the CLAES profile was smoothly interpolated to an *a priori* mixing ratio below 8 km of 5 pptv, consistent with that recorded at surface level at the Neumeyer Antarctic station (*Jones et al.*, 1999). The complete profile is shown in Figure 5.12.

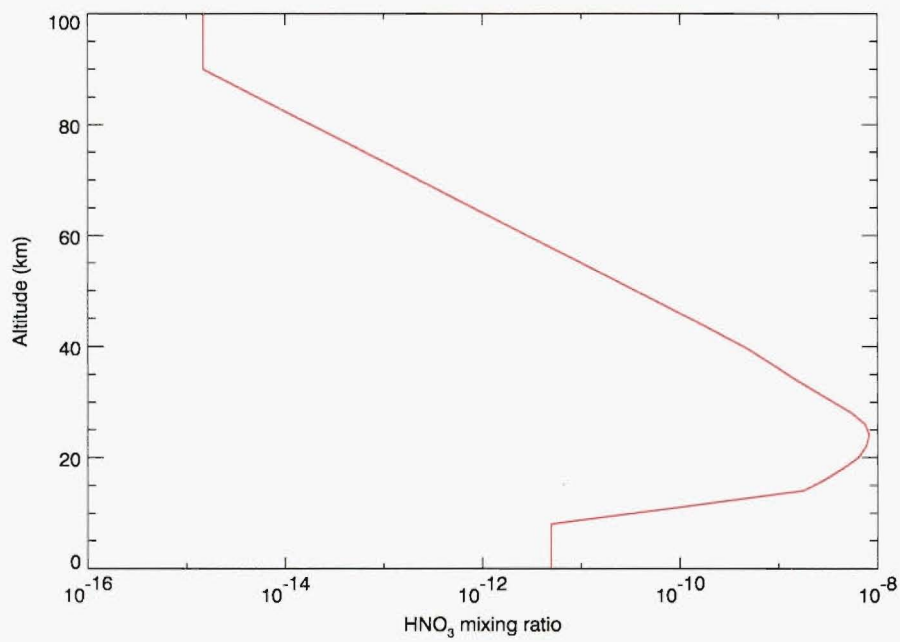

Figure 5.12: HNO_3 *a priori* profile derived from monthly averaged CLAES measurements and other sources, as described in the text.

The interfering gases H_2O, OCS and NH_3 were again profile scaled, with their *a priori* profiles from the refmod95 profiles, though the H_2O has been divided by 10 from the US

standard atmosphere in order to give a more realistic Antarctic profile.

A priori uncertainty

As with the HCl summer profile, uncertainties in the HNO_3 *a priori* profile were based on the variability of the profiles that went into the annual mean. Two-sigma standard deviations from the averaged monthly mean CLAES profiles were used. At other altitudes, the uncertainty was set to 20%.

A priori uncertainties for the profile-scaled secondary gases were set at 100% uncertainty in the scale factor, as for the HCl retrievals.

5.2.4 Spectral fits and the sensitivity of the retrieval

The HNO_3 lunar measurements were also retrieved using SFIT2 (*Wood et al.*, 2004), with 12 - 28 km partial column amounts determined for this study. Examples of the lunar fits are presented in Figure 5.13 for typical spectra from each of the April - May, June and July - August periods. Each of the fitted spectra has an S/N of approximately 200.

Averaging kernels are shown in Figure 5.14 for the April fit with both the multi-layer and partial column representations, as discussed in Section 5.1.4. A comparison of the multi-layer averaging kernels (left plot) with those characterizing the HCl retrievals for the same day (Figure 5.6, left plot) shows the HNO_3 measurements to contain significantly more information than the HCl measurements, as seen by the larger number of curves with an area beneath the curve greater than zero. Additionally, those layers where information is coming from the measurement have narrower curves, indicating better resolution, and are more centred on the correct height layer, indicating that there is some profile information contained in these measurements that was not seen in the HCl averaging kernels. This increase in the information contained in the measurement is largely due to the increase in the signal to noise ratio of the measurements (200 vs. 40 for the HCl measurements).

The partial column averaging kernel (Figure 5.14, right plot) shows that the correct region is contributing to the partial column amounts. As with the HCl measurements, changes above the 12 - 28 km region are not likely to be distinguished from those within the region, and there is likely to be some effect on the column amounts if there are changes below 12 km. The averaging kernel also shows the information in the 12 - 28 km region to be coming from the measurement, rather than the *a priori*, as seen by values close to one over the height range. Averaging kernels for the June and July - August periods are shown in Figure 5.15 and also show the information to be coming from the measurements over most of the altitude region, though the region of sensitivity decreases in the winter due to the reduction in the amount of gas phase HNO_3 present.

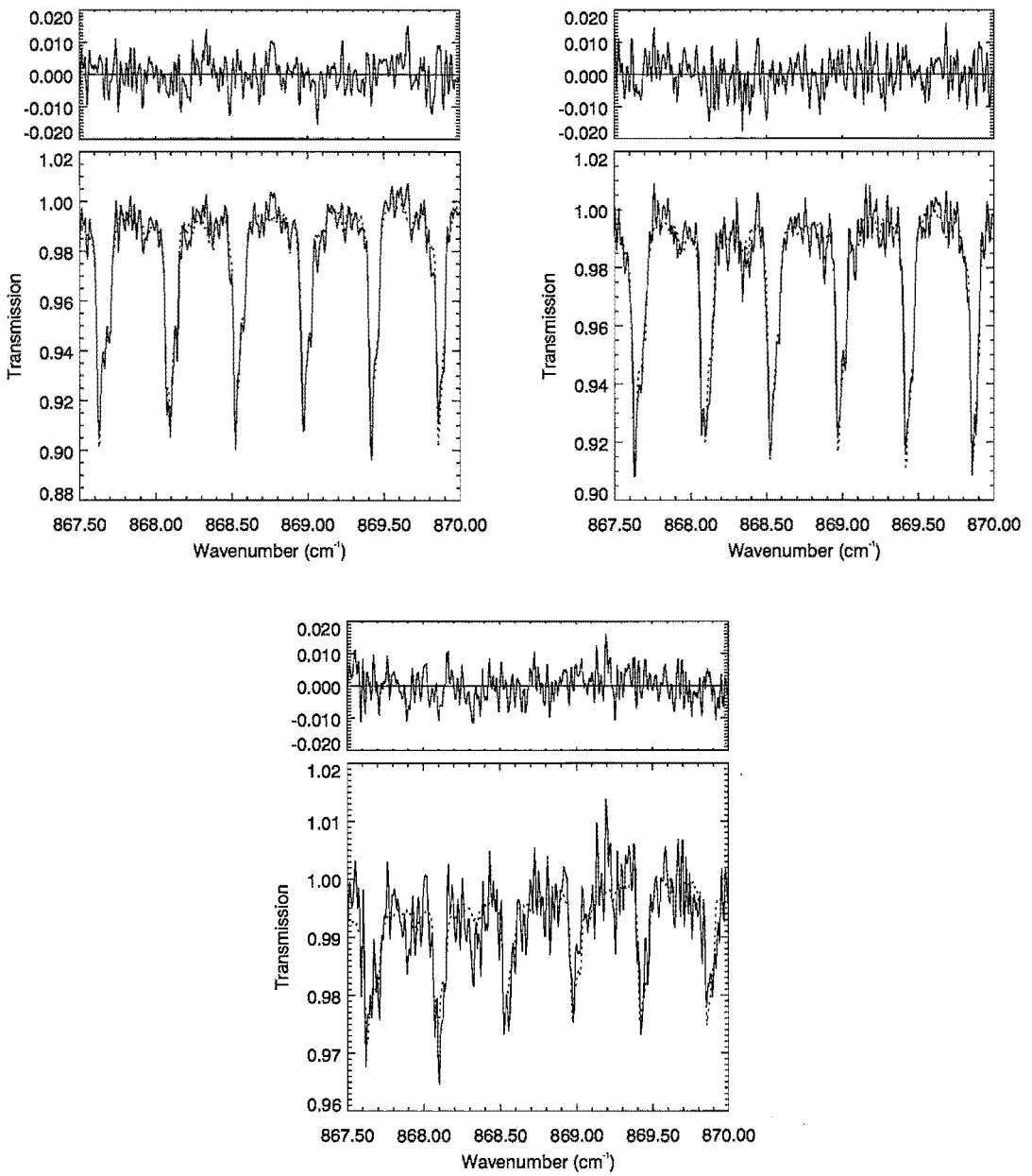

Figure 5.13: Fits obtained by SFIT2 for April 18th (top left), June 14th (top right) and July 15th (bottom) lunar HNO_3 measurements. Note the different transmittance scales on these graphs. The measured and calculated absorption lines are shown by the solid and dashed lines respectively, and the residual differences between the two curves are shown in the top panels.

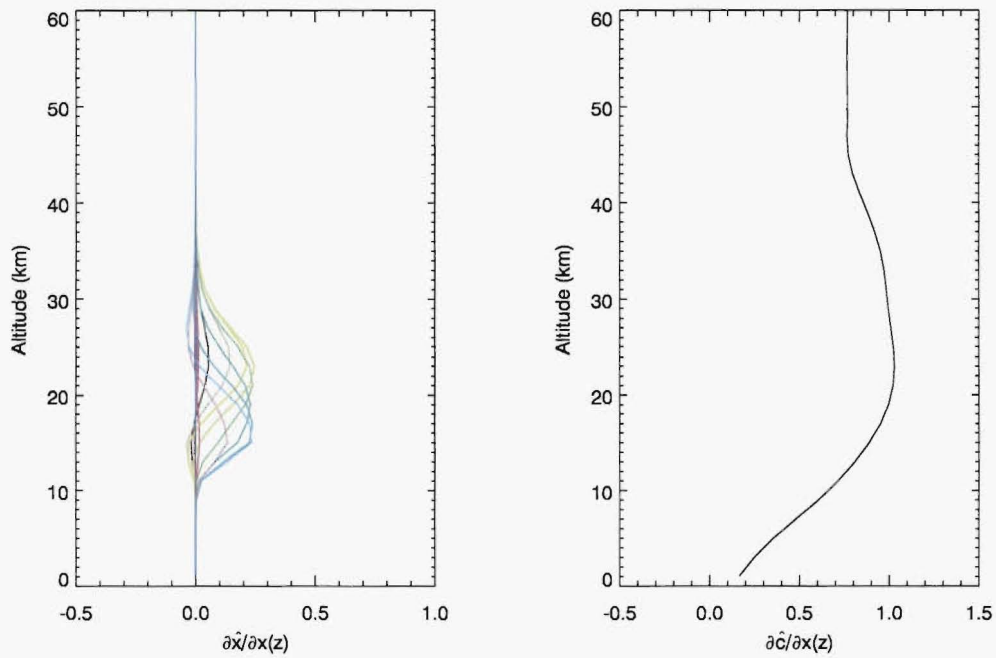

Figure 5.14: Averaging kernels corresponding to the April 18th fit in Figure 5.13. The left plot shows individual averaging kernels for each profile layer from the ground to 50 km, with layers spaced regularly at 2 km intervals. The averaging kernel for the entire 12 - 28 km partial column is shown on the right. For further discussion, see text.

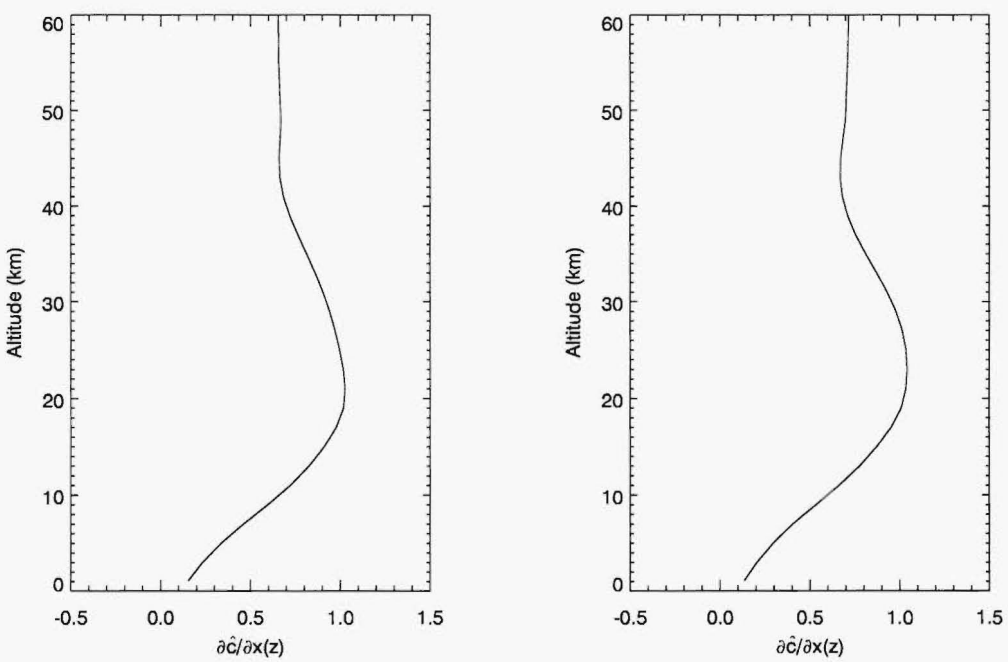

Figure 5.15: 12 - 28 km partial column averaging kernels corresponding to the June 14th (left) and July 15th (right) fits shown in Figure 5.13.

5.2.5 Error analysis

The error analysis has been carried out for the 2003 measurements in the same way as explained in the HCl section, and hence will only be presented briefly here.

Smoothing Error

The smoothing error has been determined using the formalism of *Rodgers* (1990), as shown in Equation 3.11. The S_x matrix used for the determination of the smoothing error was equal to the *a priori* covariance matrix described in Section 5.2.3, except with greater uncertainties in the troposphere to reflect our real uncertainty in this region. Individual smoothing errors have been determined for each spectrum, reflecting the range in quality of the measurements. These are presented in Appendix A.1. An average smoothing error for the entire winter period is quoted in Table 5.5.

Model parameter error

Model parameter error estimates have been made using a sample spectrum from each of the April - May, June and July - August periods. Each spectrum had an S/N of approximately 200. In addition to the parameter errors included in the HCl section, additional considerations have been made for the emission corrections. All results are presented in Table 5.4.

Temperature Uncertainty in the partial column amounts due to uncertainty in the temperature profile is slightly more complex in the HNO_3 case than for HCl, as the temperature effects the retrieval and the emission correction factor. The uncertainty has been quantified in a similar way to that given in Section 5.1.5, with a perturbation of 2 K at each level, but the perturbed temperature profile has also been used to determine the correction factor. Because the correction factor is applied after the profile has been retrieved, the combined G_yK_b vector (Equation 3.12) has been determined from the derivative of the emission-corrected partial column amount with respect to temperature, rather than determining K_b and then multiplying it with the gain matrix. This is mathematically equivalent and gives consistent results with the alternative method if the correction factor is not included. The S_b matrix determined from the uncertainty quoted with the NCEP temperature data set (*Miller*, 2004), as given in Section 5.1.5, has then been used to determine the quoted uncertainty.

Zenith angle HNO_3 lunar observations, like the corresponding HCl observations, each take approximately 10 minutes. As such, the uncertainty due to the determination of the

zenith angle has been calculated as explained in Section 5.1.5, with a value of 0.2° used for the S_b scalar and the calculation of the K_b vector.

Instrument line shape The instrument line shape has been assumed to be perfect for the HNO_3 retrievals. The uncertainty in this assumption has been estimated using a 10% reduction in the modulation efficiency over the path-length, as explained in Section 5.1.5.

Line parameters The line parameters used for this retrieval are also from the HITRAN2000 line list, as explained previously. Uncertainties in the partial column amounts due to the line parameters have been estimated by perturbing both the air-broadened half widths and the line intensities of the HNO_3 lines in the micro-window by 5%. An uncertainty of 20% has been used for S_b for the air-broadened half widths, consistent with the uncertainty given in the line list (*Rothman et al.*, 2003). An uncertainty of 14% has been used for S_b for the line intensity, as determined by laboratory studies of the HNO_3 line intensity in this region (*Toth et al.*, 2003; *Rothman et al.*, 2003).

Interfering gases As for the HCl retrievals, interfering gases in the HNO_3 retrieval microwindow have been fitted using profile scaling with a single multiplicative factor. The *a priori* estimate for this scale factor has been set to 1. The uncertainty due to the gases has been estimated by perturbing the scale factor by 20% for the calculation of K_b, and a realistic estimate has been made of the variability of each gas for the determination of S_b.

H_2O While the Antarctic atmosphere is naturally very dry due to the cold conditions, almost complete dehydration has been observed to occur in the Antarctic winter stratosphere (*Kelly et al.*, 1989; *Ramaswamy*, 1988). As such, the variability in the profile is likely to be large, and an estimated uncertainty of 100% has been used for the S_b scalar.

OCS Carbonyl sulfide is primarily a tropospheric gas, produced by phytoplankton in the open oceans. As such, its production is very light dependent, giving large differences in the ocean-surface OCS concentrations at high latitudes between the summer and the winter (*Preiswerk and Najjar*, 2000). OCS retrievals from ground-based solar FTIR spectra have been carried out at Arrival Heights, and these also show considerable variation in the profiles, both near the surface and higher up in the stratosphere [Stephen Wood, NIWA, personal communication]. As such, an uncertainty of 100% has been used for the determination of the OCS S_b scalar.

NH_3 Ammonia is also primarily a tropospheric gas, with the majority of NH_3 in the atmosphere due to anthropogenic emissions. As Antarctica is largely free of anthropogenic emissions, the profile can be expected to be relatively stable, and an estimated uncertainty of 50% has been used for the determination of S_b.

Zero-level correction For lunar measurements, the background radiation can be measured with an estimated uncertainty of $\pm$ 5%. As the calculated zero-level correction is input directly as a parameter to SFIT2, a perturbation of 0.01 in the zero-level shift, equal to 5% of the average value, has been used to determine the K_b vector and as the estimation of the uncertainty for the S_b scalar. This is also a reasonable assumption for the uncertainty in the zero-level for the solar measurements, which is assumed to be zero for the retrieval process.

Net forward model parameter errors The calculated uncertainties in the 12 - 28 km HNO_3 partial column amounts for each of the forward model parameters are presented for the April - May, June and July - September periods in Table 5.4. As with the HCl error analysis, uncertainties have been added in quadrature with no distinction made between systematic and random uncertainties, as recommended in *ISO* (1993). It can be seen that there is very little difference in the uncertainties determined for the various months. This is as expected, as a constant *a priori* profile has been used for all of the lunar retrievals. As such, an average value for the entire winter period has been calculated and is presented in Table 5.5.

Uncertainty Source	April - May	June	July - September
Temperature profile	4.77%	4.72%	4.56%
H_2O profile scale factor	0.05%	0.03%	0.04%
OCS profile scale factor	0.08%	0.11%	0.08%
NH_3 profile scale factor	0.00%	0.00%	0.01%
Zenith angle	1.09%	1.25%	0.79%
Instrument line shape	0.25%	0.10%	0.37%
HNO_3 line intensity	13.80%	13.72%	13.81%
HNO_3 air-broadened half width	4.19%	4.27%	3.96%
Zero-level correction	0.89%	0.91%	0.90%
Total uncertainty	**15.26%**	**15.20%**	**15.13%**

Table 5.4: Forward model parameter errors contributing to the retrieved partial column amounts. Note that the temperature profile uncertainty also includes the uncertainty in the emission correction factor. The total uncertainty has been determined by adding uncertainties quadratically.

The high uncertainty associated with the temperature profile can be attributed to the profile information contained within the measurements. Because the temperature affects

the pressure broadening of the line, altitude information requires an accurate knowledge of the temperature at each height, and uncertainty in the profile carries through to the retrieved partial column amount. The variation seen in the uncertainty as a result of zenith angle is more a result of the zenith angle for the representative spectra used for the tests than a function of time of year, with the uncertainty in the zenith angle being higher for measurements made through large airmasses. By far the biggest uncertainties are those relating to the line parameters. As the uncertainty in the intensity is (nearly) equal to the uncertainty in the partial column amount as a result of the uncertainty in the intensity, it is clear that the lack of information about the line parameters is the biggest limiting factor in the measurements. The effect of the line parameters is, however, systematic, so while the partial column amounts contain this uncertainty, trends in the amounts can be determined with a lot more confidence.

Measurement error

The measurement error has been determined from *Rodgers* (1990), as shown in Equation 3.13. As with the HCl lunar measurements, the S/N for the lunar HNO_3 measurements vary considerably and as such the measurement error has been determined for each observation. These are presented in Appendix A.1. An average measurement error for the winter period is presented in Table 5.5.

Net uncertainty

The total uncertainty in the 12 - 28 km HNO_3 partial column amounts is presented in Table 5.5. Because a constant *a priori* profile has been used though the entire winter, there is no clear monthly variation in the uncertainties. As such, an average uncertainty for all of the lunar observations has been determined.

Measurement Period	Smoothing Error	Model Parameter Error	Measurement Error	Total Uncertainty
April - September	2.61%	15.20%	2.06%	15.56%

Table 5.5: Estimated uncertainty in the 12 - 28 km HNO_3 partial column amounts determined from lunar measurements, as described in the text.

5.2.6 Solar measurements

Solar measurements made using the Arrival Heights instrument have also been processed to make them comparable with the lunar observations, as outlined in *Wood et al.* (2004),

with the 12 - 28 km partial column amounts determined for use in this comparison. The *a priori* used for the retrievals was the same as that given in Section 5.2.3, and the S/N has been set at a constant 300. Corrections have not been made for emission of the broadband or atmospheric emission, as these are negligible compared to the direct intensity of the sunlight, as shown in Figures 5.9 and 5.10. An estimate of the uncertainty resulting from neglecting these sources is, however, included in the error analysis.

The error analysis for the 12 - 28 km partial column amounts was carried out exactly as given in Section 5.2.5, though a smaller zenith angle of 0.1 has been used to reflect the shorter measurement time of the solar observations, and the solar, rather than lunar, temperature has been used for the emission correction factor calculations. The net uncertainty in the partial column amounts due to the various error sources is presented in Table 5.6. Additionally, the uncertainties due to forward model parameters are presented in Appendix A.2.

Measurement Period	Smoothing Error	Forward model Error	Measurement Error	Total Uncertainty
September - April	0.85%	15.49%	0.70%	15.53%

Table 5.6: Estimated uncertainties in the 12 - 28 km partial column amounts for solar HNO_3 measurements.

5.2.7 Partial columns over smaller height ranges

As shown in Figure 5.14, there is some profile information contained in the winter HNO_3 measurements. There is even more in the solar measurements, which are at a higher resolution than the lunar observations as well as having higher S/N. Because denitrification mechanisms remain one of the more poorly understood aspects of polar ozone depletion (*Eyring et al.*, 2004), it is of considerable interest to have height-resolved, ground-based HNO_3 measurements. As such, the nitric acid measurements made during 2003 have been broken down to the full extent of the information contained in the measurements, in order to look for evidence of denitrification, sedimentation and nitrification.

Which partial columns?

To look for evidence of denitrification and nitrification, narrow partial columns are needed in order to avoid smearing out any results caused by denitrification at one height and nitrification at another. High-resolution satellite, aircraft and balloon measurements of HNO_3 in the Arctic suggest that denitrification there occurs in a height range of only 2 - 3 km, with nitrification directly below (*Arnold et al.*, 1998; *Waibel et al.*, 1999; *Kondo et al.*,

2000; *Irie et al.*, 2001; *Popp et al.*, 2001). This range is sufficiently small, with conflicting processes happening so close together, that the MLS instrument, with a vertical resolution of $\sim$ 6 km, was unable to observe it (*Santee et al.*, 1999; *Tabazadeh et al.*, 2001), or, in the very cold winter of 2000, observed some 40% less denitrification than in-situ aircraft measurements (*Santee et al.*, 2000; *Popp et al.*, 2001; *WMO*, 2002). Denitrification in the Antarctic is known to be much more widely spread than in the Arctic (e.g., *Santee et al.*, 1999), but nevertheless the best results will come from the smallest resolvable altitude ranges. That said, it is also very important not to over-interpret the profiles obtained from the FTIR measurements.

With this in mind, the degrees of freedom of signal, d_s, for a range of partial columns between 10 and 30 km has been determined for several typical solar and lunar nitric acid measurements made in 2003, as outlined in Chapter 3. The smallest possible partial columns with d_s values greater than 0.7, showing more information to be coming from the signal than the noise, have been determined. The partial columns, with their average associated d_s values, are shown in Table 5.7. Smaller columns are possible for the solar measurements, as the higher resolution of the observations gives them better vertical resolution.

Source	Partial column	d_s
Moon	10 - 20 km	0.83
Moon	20 - 28 km	0.78
Sun	10 - 16 km	0.86
Sun	16 - 20 km	0.72
Sun	20 - 24 km	0.82
Sun	24 - 28 km	0.77
Sun	10 - 20 km	1.54
Sun	20 - 28 km	1.54

Table 5.7: Smallest resolvable partial columns from lunar and solar HNO_3 observations, as determined from the degrees of freedom of signal, d_s. 10 - 20 km and 20 - 28 km solar partial columns are shown for comparison.

While the partial columns resolvable from the lunar measurements are large compared to the partial columns resolvable from the solar measurements, it is hoped that the lunar altitude ranges will provide some information about where denoxification processes are occurring early in the winter (permanent loss of nitrogen, denitrification, cannot be identified purely from gas phase measurements at this time of year). The much better resolution of the solar measurements, with the correspondingly smaller partial columns, should provide additional information on denitrification and nitrification occurring in the spring.

Sensitivity of the retrievals

Partial column averaging kernels for each of the partial columns listed in Table 5.7 are presented in Figure 5.16 for typical lunar and solar HNO_3 measurements.

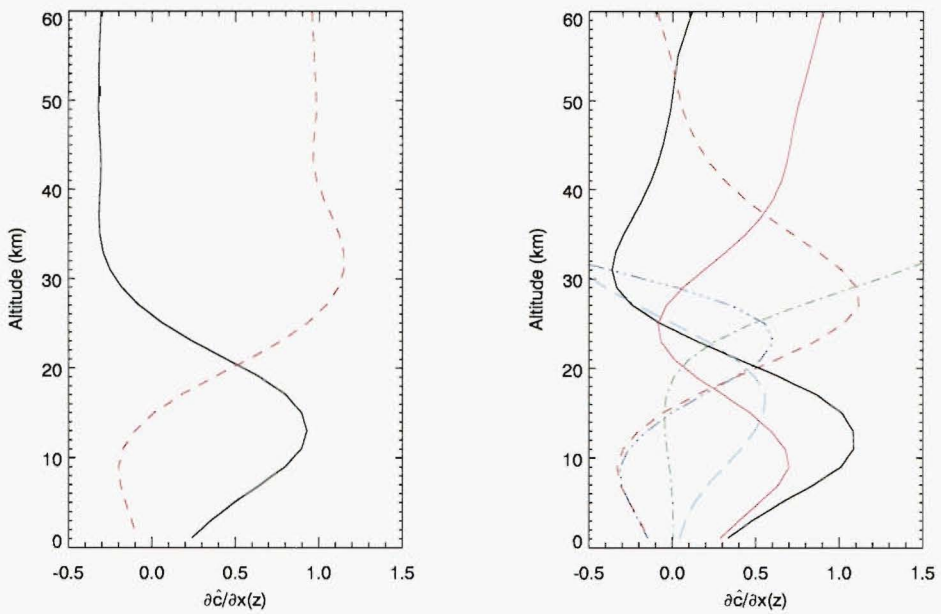

Figure 5.16: Partial column averaging kernels corresponding to the June 14th lunar (left) and January 12th solar (right) measurements. Columns are as follows: 10 - 20 km, black; 20 - 28 km, red; 10 - 16 km, pink; 16 - 20 km, cyan; 20 - 24 km, blue; 24 - 28 km, green.

It can be seen that these partial columns are not completely individually resolved and that the retrieval has difficulty in the distribution of the changes, especially between the 20 - 24 and 24 - 28 km solar partial columns. It should be remembered that the interpretation of the partial column averaging kernels is the effect of a change at that height on the retrieved column amount. As such, a negative averaging kernel makes physical sense – an increase in the gas profile at this altitude will be interpreted as a decrease in the retrieved column amount. This means that increases above 30 km will be interpreted as an increase in the 24 - 28 km partial column amount and a decrease in the 20 - 24 km partial column amount. A look back at the HNO_3 profile (Figure 5.12), however, shows that above 30 km there is very little HNO_3 in the atmosphere, and as this is above the altitude range of PSCs, changes to the gas in this region are likely to be negligible. Regardless, care should be taken in the interpretation of the partial column amounts, and an accurate estimate of the smoothing error, which accounts for the smoothing of the profile as well as the contribution to the retrieved column amount of changes in other regions, is essential.

Error analysis

The error analysis for each of the partial column amounts has been carried out as presented in Section 5.2.5. Results are summarized in Table 5.8, with the errors associated with individual forward model parameters given in Appendix A.3.

Partial Column	Smoothing Error	Forward model Error	Measurement Error	Total Uncertainty
10 - 20 km (l)	10.4%	13.2%	8.4%	18.8%
20 - 28 km (l)	14.0%	22.3%	8.2%	27.6%
10 - 20 km (s)	10.1%	12.9%	6.2%	17.5%
20 - 28 km (s)	12.0%	23.9%	5.8%	27.4%
10 - 16 km (s)	25.0%	47.6%	12.7%	55.3%
16 - 20 km (s)	26.7%	35.3%	6.8%	44.8%
20 - 24 km (s)	24.7%	27.7%	10.0%	38.5%
24 - 28 km (s)	25.6%	67.7%	9.9%	73.0%

Table 5.8: Estimated uncertainties in the narrow partial column amounts of HNO_3, for lunar (l) and solar (s) measurements.

While the total uncertainties are large, especially for the 4 km partial column layers, the uncertainties are again dominated by the systematic uncertainties in the line parameters. Excluding the uncertainties associated with the line parameters, the total uncertainty is less than 30% for the smallest partial columns and less than 20% for the slightly larger columns.

Chapter 6

Results and Discussion

As outlined in Chapters 4 and 5, measurements of the stratospheric trace gases HCl and HNO_3 have been made from Arrival Heights throughout the 2003 year. In this chapter, these results will be presented in conjunction with the meteorological analyses and potential vorticity information introduced in Chapter 4, allowing a complete picture of the evolution of the trace gases through 2003 to be developed.

The chapter has been divided into two sections. The first section presents the 12 - 28 km partial column measurements of both HCl and HNO_3. It has been structured temporally, with measurements presented for each of the pre-winter, early winter, late winter, and spring periods. The second section focuses specifically on the HNO_3 measurements, with partial columns broken down into narrower altitude regions in order to investigate the processes of denoxification, denitrification and nitrification.

6.1 The 2003 Antarctic winter

Figure 6.1 shows the 12 - 28 km HCl and HNO_3 partial column measurements made in 2003. In order to better quantify the conditions resulting in the observed trends, these have been shown with Ertel's potential vorticity on the 450 K potential temperature surface and the temperature at 50 hPa. Both of these measurements correspond to an altitude of approximately 19 km (i.e., in the centre of the partial column being observed) and have been determined for the Arrival Heights site as introduced in Sections 4.2.1 and 4.2.2. The potential vorticity identified as the vortex edge using the Nash PV criteria (*Nash et al.*, 1996) has also been shown.

Indications of the threshold temperatures at which polar stratospheric clouds are likely to exist have been shown in Figure 6.1d. This information is important for the interpretation of reductions in the gas phase HNO_3 and the corresponding destruction of HCl, which is known to occur on the surface of nitric acid-containing PSCs (e.g., *Solomon et al.*, 1986; *Solomon*, 1999; *WMO*, 1994, 1998). Typical early winter conditions of 9 ppb of nitric acid, as determined from the May HNO_3 profile retrievals, and 4 ppm of water vapour, as given in the ILAS water vapour climatology for 72°S in May (*SPARC*, 2000) have been used for determining these threshold temperatures. T_{NAT} and T_{ice} have been calculated on the 50 hPa surface using the Hanson and Mauersberger relation (*Hanson*

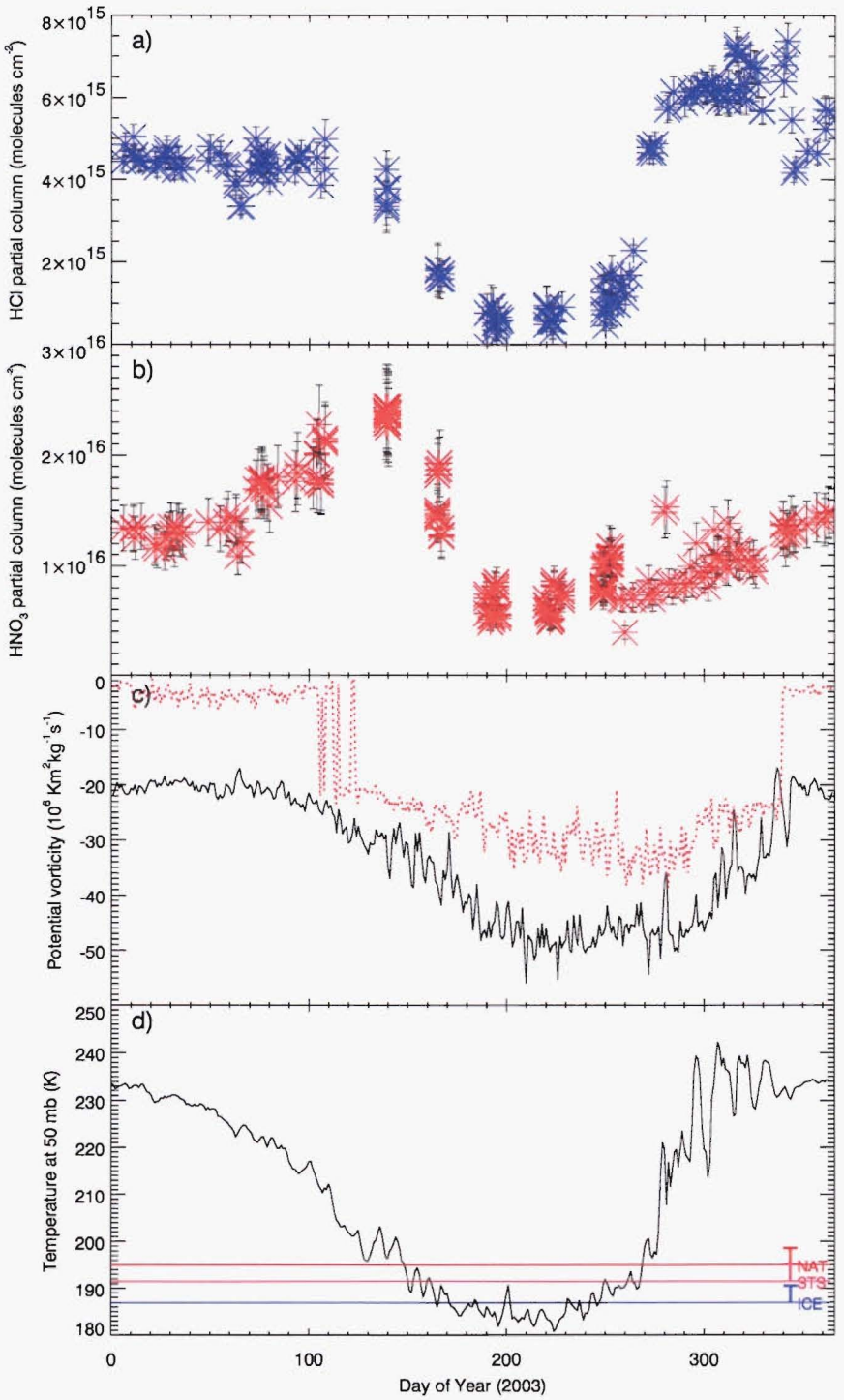

Figure 6.1: a) and b) HCl and HNO_3 12 - 28 km partial column amounts, incorporating both solar and lunar observations. Error bars are as discussed in Sections 5.1.5 and 5.2.5. c) Potential vorticity on the 450 K potential temperature surface above Arrival Heights (solid black line) and the potential vorticity corresponding to the vortex edge (dotted red line). d) Temperature on the 50 mb pressure surface. Approximate condensation temperatures for NAT (T_{NAT}), STS (T_{STS}) and ice (T_{ice}) PSC particles are also shown, as calculated for typical early-winter conditions.

and Mauersberger, 1988) and the Marti and Mauserberger relation (*Marti and Mauersberger*, 1993) respectively. T_{STS} has been assumed to be 3.5 K below T_{NAT}, consistent within the range of results obtained from models (e.g., *Tabazadeh et al.*, 1994a; *Luo et al.*, 1995; *Carslaw et al.*, 1995) and measurements (e.g., *Rosen et al.*, 1997; *Beyerle et al.*, 1997; *WMO*, 1998).

Figure 6.1 shows the general trend to be of stable conditions through the summer followed by a rapid loss of HCl and HNO_3 when temperatures drop below PSC existence thresholds. Loss of gas phase HCl and HNO_3 is nearly total through the winter months. Spring is characterized by a rapid increase in the HCl partial column amount as chlorine is deactivated, accompanied by a slow increase in the HNO_3 partial column amount as the nitric acid recovers from the extensive denitrification that has occurred during the winter. The sections that follow will look at each phase of the 2003 year in more detail.

6.1.1 Pre-winter (days 1 - 120)

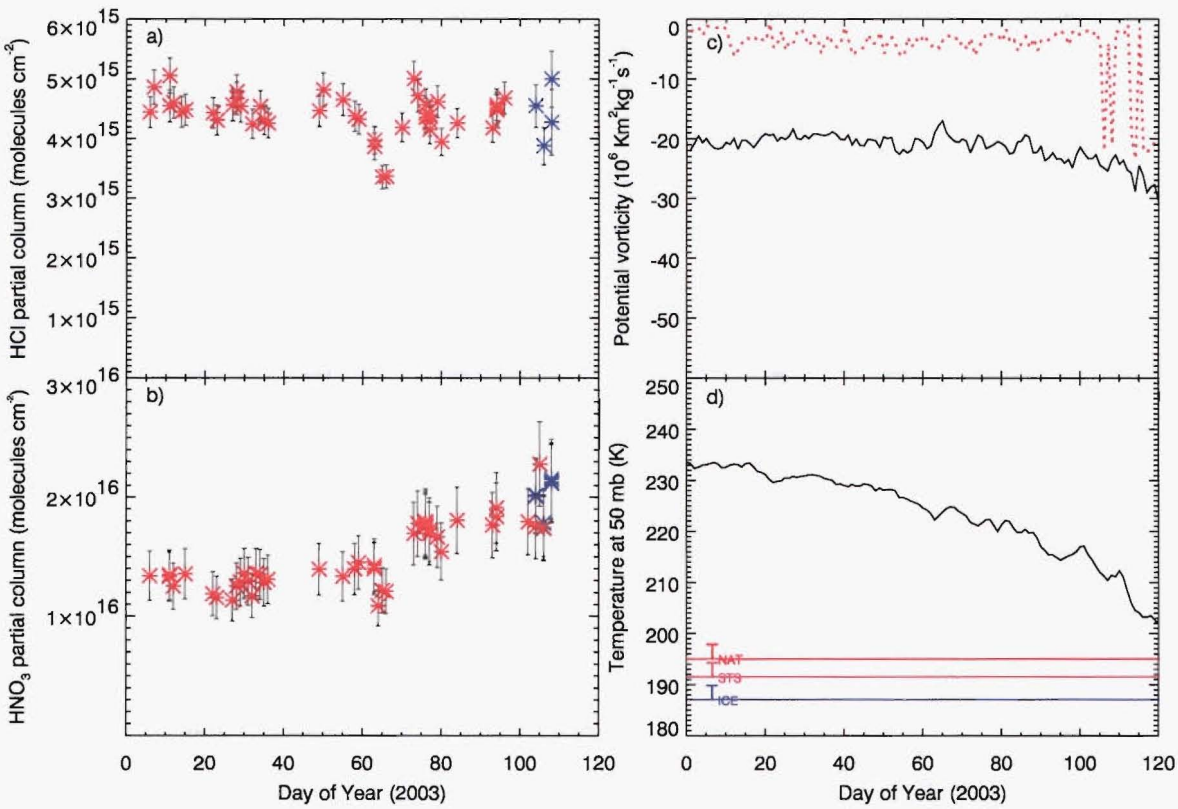

Figure 6.2: As for Figure 6.1, except over only days 1 - 120. HCl and HNO_3 plots show measurements obtained using the sun (red) and moon (blue) as a light source.

Prior to the onset of the polar night, the HCl and HNO_3 measurements are representative of stable, well-mixed conditions in the stratosphere. Figure 6.2 shows the data

presented in Figure 6.1, focusing on the start of the year until the end of April. During this time the potential vorticity values corresponding to the vortex edge remain near zero (Figure 6.2c), indicating that the polar vortex has not yet developed, and mixing of air between the polar and mid-latitudes is unrestricted. Continuous sunlight in the polar atmosphere means that temperatures are well above PSC existence thresholds (Figure 6.2d), and dynamics and photochemical processes drive the observed HCl and HNO_3 trends.

The HCl partial column amount observed over Arrival Heights remains fairly stable through this time (Figure 6.2a), with values of $\sim 4.4 \times 10^{15}$ molecules cm^{-2}. HCl is a very stable gas in the stratosphere (*Wayne*, 2000), with its long lifetime resulting in a latitudinal gradient driven by global dynamics, as indicated in Chapter 2. Small variations in the observed HCl column amounts can be attributed to this latitudinal gradient as a result of movement of the air prior to its observation. HCl concentrations in the partial column increase towards the poles (*Russell et al.*, 1996; *Beaver and Russell*, 1998), so air coming from low latitudes will contain less HCl than air coming from higher ones. The dip in the HCl partial column amounts on days 64 - 66 (March 4th - 6th) is a good example of this effect. The trajectory of air parcels measured over Arrival Heights has been shown for the five days prior to these observations in Figure 6.3. These trajectories have been calculated for air parcels arriving on the 450 K potential temperature surface using the Goddard Auto-mailer back-trajectory model (*Schoeberl and Sparling*, 1994; *Lait et al.*, 2004). The trajectory of air parcels on the days on either side of the dip, which are more typical of the trajectories of air parcels usually observed at the site, are also shown.

Nitric acid partial column amounts (Figure 6.2b) also show small fluctuations due to the source region of the air parcel being observed. While not as dramatic as the dip shown in the HCl measurements, the HNO_3 measurements also capture the movement of air from lower latitude regions on days 64 - 66. In addition to the small-scale dynamically driven variations, however, the overall trend observed in the HNO_3 partial column amount is driven by photolytic processes. The first sunset observed at Arrival Heights in 2003 occurred on February 20th (day 51), with a rapid transition to 24-hour darkness from April 24th (day 114). Prior to the first sunset, the HNO_3 partial column amount remains fairly constant at $\sim 1.3 \times 10^{16}$ molecules cm^{-2}. As the day length shortens, however, photolysis of HNO_3 to NO_x decreases. Additionally, NO_x is efficiently converted to N_2O_5 and then to HNO_3 during the night (e.g., *Findlayson-Pitts and Pitts*, 1986; *Weisenstein et al.*, 1991; *Wayne*, 2000). This results in the gradual increase observed from day 60 to day 120 in Figure 6.2b and the continued increase in the nitric acid partial column amount into the winter (Figure 6.1b). As the days get shorter, temperatures also begin to decrease (Figure 6.2d) and the polar vortex begins to develop.

In addition to the trends outlined above, Figures 6.2a and 6.2b show a short period of overlap between solar and lunar observations. These are in excellent agreement, even

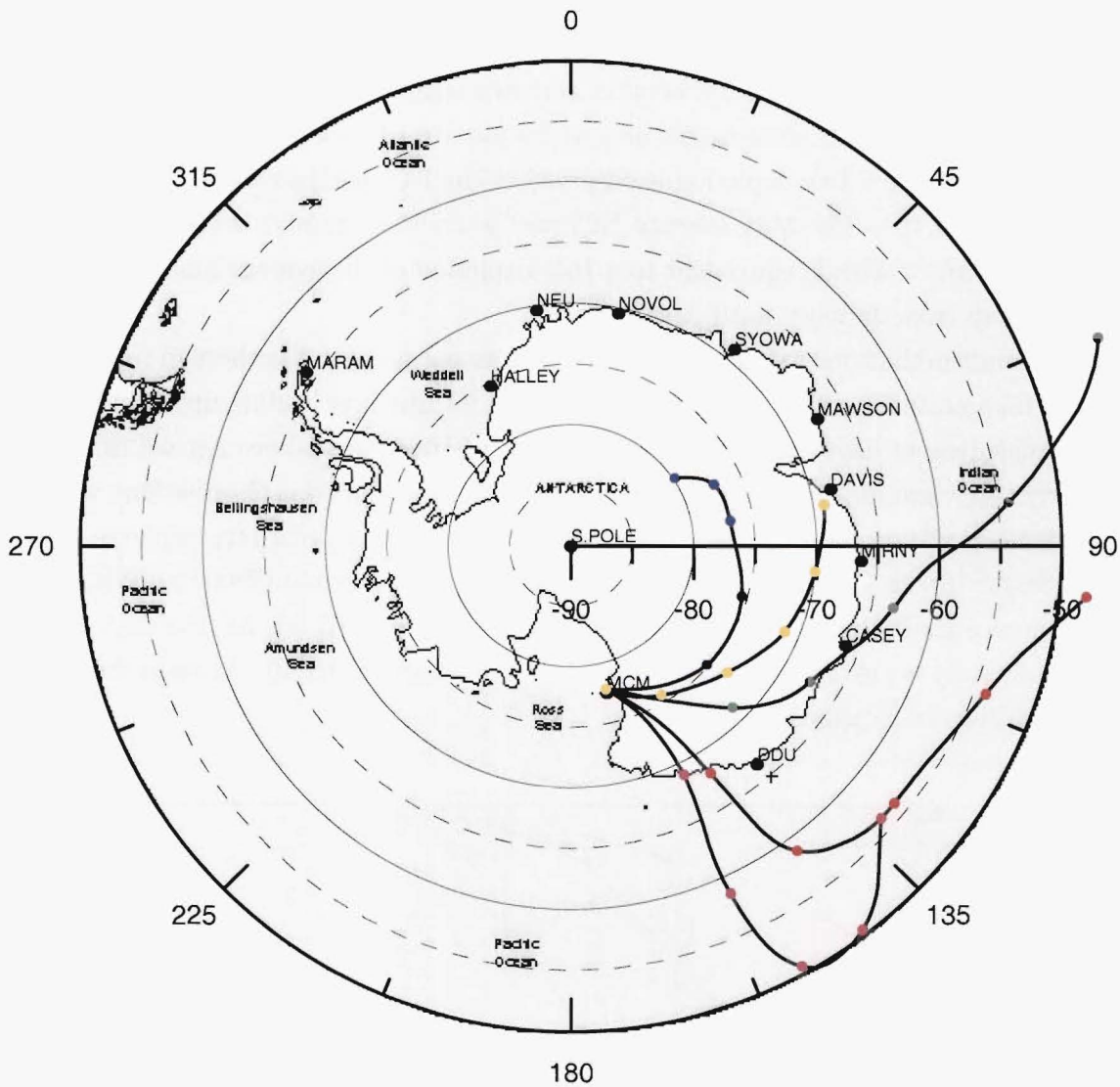

Figure 6.3: Five-day back-trajectories of air-parcels reaching Arrival Heights in March. Days 64, 65 and 66 (green, red and pink respectively) correspond to days where reduced amounts of HCl were observed in the partial column. Days 63 (blue) and 70 (yellow) correspond to 'normal' partial column amounts observed on either side. Trajectories have been calculated using the Goddard Auto-mailer system (*Schoeberl and Sparling*, 1994; *Lait et al.*, 2004) on the 450 K potential temperature surface, at 00:00 UT.

capturing the fluctuation observed in the nitric acid partial column amounts between days 100 and 110 as the vortex forms (Figure 6.2c).

6.1.2 Early winter (days 120 - 145)

With the establishment of the polar vortex ($\sim$ day 125, Figure 6.1c), mixing of air from the polar regions with warmer mid-latitude air is no longer possible and the temperature of the air decreases further due to radiative cooling (Figure 6.1d). The 24-hour darkness

means the amount of HNO_3 continues to increase, with partial column values reaching a winter maximum of 2.5×10^{16} molecules cm^{-2} in May (days 139 and 140).

While high nitric acid partial column amounts suggest that polar stratospheric clouds have not yet formed, and temperatures at 50 mb are not yet low enough for NAT condensation (Figure 6.1d), depletion is observed in the HCl partial column on days 139 and 140 (Figure 6.1b). The May average HCl partial column amount is equal to 3.7×10^{15} molecules cm^{-2}. This is equivalent to a 16% depletion of the average amount recorded in the column from January until April.

To confirm that polar stratospheric clouds were not present elsewhere in the partial column, temperature profiles above Arrival Heights for the days leading up to and including the measurement days are shown in Figure 6.4. Temperatures above Arrival Heights were clearly too warm for nitric acid condensation. Additionally, lidar observations were made at McMurdo Station on day 139 and showed no evidence of polar stratospheric clouds at any height [Paola Massoli, Institute for Atmospheric Science and Climate, CNR, personal communication]. Preliminary backtrajectory analyses carried out for the days preceding the observations also suggest that processing on polar stratospheric clouds in the air parcel prior to the observations was unlikely.

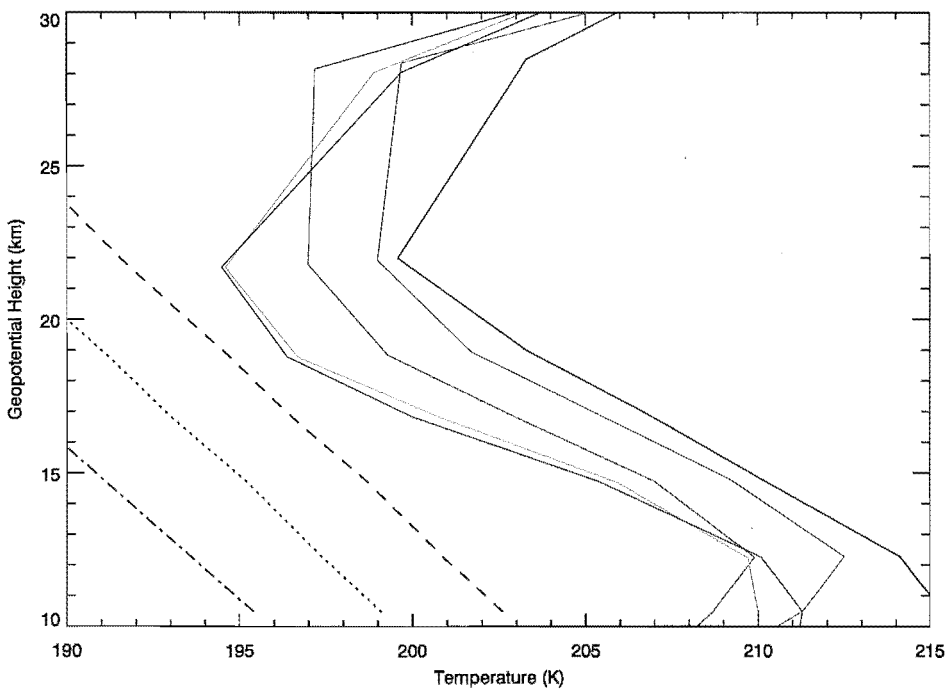

Figure 6.4: Temperature profiles above Arrival Heights on day 136 - 140, from the NCEP temperature data (Section 4.2.1). Day 136, red; day 137, green; day 138, blue; day 139, cyan; day 140, pink. Dashed, dotted and dash-dotted lines show T_{NAT}, T_{STS} and T_{ice} respectively.

Without polar stratospheric clouds present to provide a surface for heterogeneous

chemistry, an alternative explanation for the observed chlorine activation is necessary. *Hanson et al.* (1994) used a simple model to show that the reactions of $ClONO_2$ and HOCl with HCl at temperatures below about 200 K could cause some chlorine activation on background sulfate aerosols, prior to the onset of PSCs. In agreement with this, temperatures below 200 K were observed over a substantial portion of the partial column for several days prior to the May measurements (Figure 6.4). As such, it seems likely that reactions occurring on background sulfate aerosols were responsible for the observed decrease in the HCl partial column.

6.1.3 PSC onset (days 145 - 170)

By the time FTIR measurements could be made in June, temperatures over Arrival Heights were sufficiently low that polar stratospheric clouds were almost certainly present over a large portion of the partial column. At 50 mb, the temperature was first observed to fall below T_{NAT} on day 148 and below T_{STS} on day 150 (Figure 6.1d). The first PSC was recorded by lidar measurements on day 153 and was a liquid cloud between 19 and 20 km ($\sim$ 50 mb) [Paola Massoli, Institute for Atmospheric Science and Climate, CNR, personal communication].

If we had had nitric acid measurements during that time, we would have expected to see a rapid depletion of the gas phase nitric acid as PSC particles were formed, followed by fluctuations as temperatures decreased and increased about T_{STS}, allowing liquid particles to form and re-evaporate. Temperatures during this time have been highlighted in Figure 6.5 and are seen to settle to values consistently below T_{STS} (and T_{NAT}) on day 162. Lidar observations during this period also showed clouds to be forming and disappearing, before becoming a permanent feature of the stratosphere from day 162 [Paola Massoli, Institute for Atmospheric Science and Climate, CNR, personal communication].

Whenever PSCs were present, we would also expect to see depletion in the HCl partial column as chlorine was activated. The dominant chlorine activation reactions

$$ClONO_2 + HCl \longrightarrow Cl_2 + HNO_3 \tag{6.1}$$

and

$$HOCl + HCl \longrightarrow Cl_2 + H_2O \tag{6.2}$$

have been shown to occur rapidly on both solid and liquid PSCs (*Molina et al.*, 1993; *Hanson and Ravishankara*, 1994; *Ravishankara and Hanson*, 1996; *WMO*, 1994, and references therein). While the exact reaction rates for these and other contributing reactions are still uncertain, especially on solid surfaces (*WMO*, 1998, 2002), the reactions are rapid and the full chlorine activation of an air parcel is expected to occur within a day (*Moore*

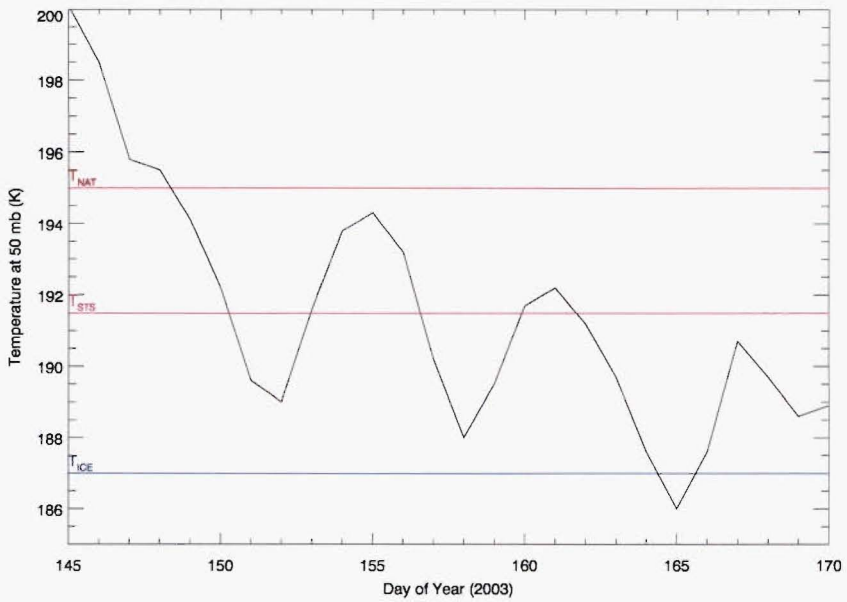

Figure 6.5: Temperature over Arrival Heights on days 145 - 170 (late May to mid June) at 50 mb, from NCEP temperature data. T_{NAT}, T_{STS} and T_{ice} condensation temperatures are shown, as outlined for Figure 6.1d.

et al., 1990; *Newman et al.*, 1993).

Unfortunately no measurements were possible around the PSC onset period, and by day 165, when the moon was sufficiently full for the first FTIR measurements to be made, significant depletion had occurred in both the gas phase HNO_3 and HCl partial columns (Figures 6.1a and 6.1b).

The nitric acid partial column amounts recorded in June are very scattered, with values as high as 2.0×10^{16} molecules cm^{-2} and as low as 1.2×10^{16} molecules cm^{-2} occurring during the three-day period (Figure 6.1b). In contrast, the HCl partial column amounts show very little scatter (Figure 6.1a), recording a constant value of $\sim 1.7 \times 10^{15}$ molecules cm^{-2}. This inconsistency can be explained by the PSC type. While the gas phase nitric acid uptake varies depending on the phase of the PSC particle, the chlorine activation reactions which destroy HCl have been shown to occur rapidly on all PSC types, as outlined above. The link between the HNO_3 column amount and the PSC type, as well as the rate of depletion observed in the HNO_3 measurements during the PSC onset time, will be further investigated in Chapter 8.

In order to account for the depletion observed in the HCl partial column, calculations have been made based on the HALOE summertime profile. These calculations suggest that complete conversion of HCl to active species must have occurred in the 16 - 24 km region where temperatures were sufficiently low for PSCs to form. While the limitation of this calculation should be noted, as it has been based on an average, unsubsided profile,

the result is in agreement with the complete activation predicted by *Newman et al.* (1993). A more detailed quantification of the extent of activation in the region requires a chemical transport model with PSC formation and heterogeneous chemistry rates. A comparison of the data with output from the chemical transport model SLIMCAT will be presented in Chapter 7.

6.1.4 Late winter (days 190 - 250)

By the July full moon (days 190 - 196), polar stratospheric clouds had been present throughout the partial column region for some time, and nearly all the chlorine has been activated by HCl-destroying reactions on their surfaces. HCl partial column amounts are essentially zero (Figure 6.1a). Likewise, HNO_3 partial column amounts are at very low levels (Figure 6.1b), indicating almost complete conversion of the HNO_3 to non-gas phases. While denitrification due to the sedimentation of HNO_3-containing particles may well have occurred by this time, temperatures are still sufficiently low that the particles cannot evaporate back to the gas phase (Figure 6.1d). As such, denitrification cannot be observed by these measurements. Similar conclusions can be drawn for the August full moon measurements (days 220 - 228).

The September full moon measurements (days 249 - 253) are a little unusual, in that while values are still considerably lower than pre-vortex values, a spike is seen in the HNO_3 measurements (Figure 6.1b). Potential vorticity data (Figure 6.1c) shows Arrival Heights to still be well within the vortex, and the temperature plot in Figure 6.1d suggests that it is still too cold for the clouds to be evaporating. By this time of year, however, the Antarctic atmosphere is typically dehydrated (e.g., *Kelly et al.*, 1989; *Morrey and Harwood*, 1998; *Randel et al.*, 1998; *Nedoluha et al.*, 2000; *SPARC*, 2000), and the combination of less water vapour and less gas phase HNO_3 combine to reduce the NAT and ice condensation temperatures. Figure 6.6 shows an enlarged plot of the data, with PSC formation temperatures more typical of spring conditions indicated in Figure 6.6d. T_{NAT}, T_{ice} and T_{STS} have been determined as outlined at the start of the chapter but use values of 3.4 ppb of HNO_3 and 2 ppm of water. The HNO_3 amount has been determined from the September lunar and solar retrievals, and the water is as given by POAM (*SPARC*, 2000) and by balloon measurements (*Rosen et al.*, 1988b).

Evaporation of PSC particles does not happen instantaneously, but depends on the particle composition, size, surface area and temperature (*Wofsy et al.*, 1990; *Tolbert and Middlebrook*, 1990; *Middlebrook et al.*, 1996). As we have little knowledge of any of these parameters, the formation temperatures should only be used as an indication of evaporation temperatures. There is, however, a fairly good correlation between the spike seen in the temperature around day 250 and the spike observed in the HNO_3 partial

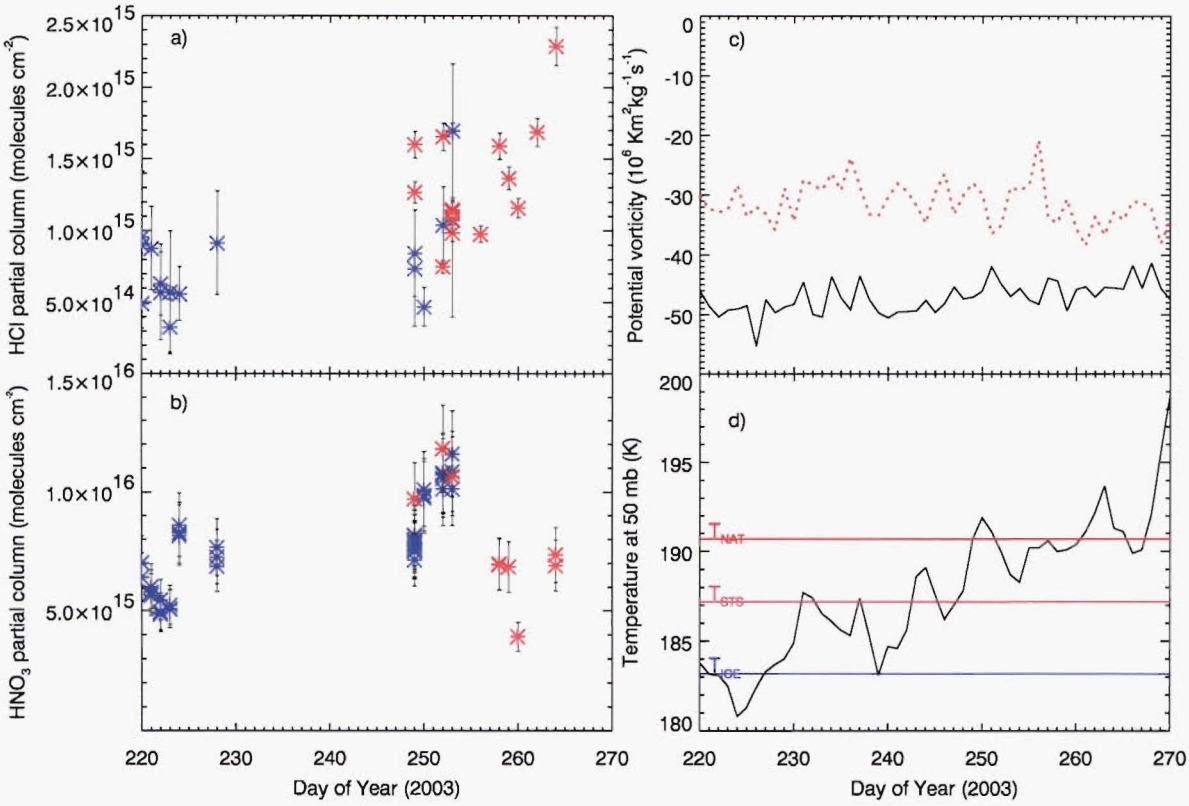

Figure 6.6: As for Figure 6.1, over only days 220 - 270 and with T_{NAT}, T_{STS}, and T_{NAT} calculated for more typical spring conditions of 2 ppm water vapour and 3.4 ppb nitric acid. HCl and HNO_3 plots show measurements obtained using the sun (red) and moon (blue) as a light source.

column amounts on days 252 and 253, indicating that gas phase nitric acid has been released by evaporation of PSCs. The return to low HNO_3 partial column amounts in the following days additionally corresponds to the temperature decreasing back below T_{NAT}.

The spike presents an interesting case study for the location of the nitric acid remaining in the column in the spring, which will be looked at in more detail in Section 6.2, and the relationship between gas phase nitric acid measurements and PSCs, which will be investigated in Chapter 8.

Lunar and solar measurements made on the same days during this time again show good agreement, particularly for the HNO_3 partial column amounts. The differences between the solar and lunar HCl measurements are more significant, but they are unsurprising if rapid chlorine activation is occurring, as the solar and lunar measurements have been made at different times of the day and through different airmasses.

6.1.5 Spring (day 250 onwards)

From September onwards, the sun is once again visible from Arrival Heights, and measurements are made daily using direct sunlight. The return of the sun drives many of the

springtime processes, not only through the increase in temperature, but also through its ability to photolyse compounds that have built up during the winter. While the processes directly involved in ozone depletion in the spring are outside the realm of this project (and well understood, see e.g., *Solomon*, 1988, 1900, 1999), the deactivation of chlorine and the subsequent partitioning of the chlorine reservoir species remain an interesting subject that can be well addressed by these observations. This section will look specifically at the HCl and HNO_3 measurements made at Arrival Heights during 2003, but will also introduce O_3 and $ClONO_2$ data made from the site in order to compare and contrast the observed results with southern and northern hemisphere studies in the literature.

Chlorine deactivation is driven predominantly by two reactions:

$$ClO + NO_2 + M \rightarrow ClONO_2 + M \tag{6.3}$$

and

$$Cl + CH_4 \rightarrow HCl + CH_3 \tag{6.4}$$

While these two processes are able to occur early in spring, the subsequent re-activation of the reservoir species on PSCs masks any recovery associated with the processes until the clouds are no longer present. With the increase of temperatures above the PSC threshold, however, the active chlorine is rapidly converted back to its inactive reservoir forms.

In the absence of denitrification, Reaction 6.3 is a much faster reaction than Reaction 6.4 (*Wayne*, 2000). This leads to the active chlorine being partitioned more quickly into $ClONO_2$ than into HCl, with chlorine nitrate amounts tending to 'overshoot' their pre-winter amounts, reaching a more typical balance with HCl later in the season (*Roche et al.*, 1994; *Santee et al.*, 1996; *Blumenstock et al.*, 1997). This is shown in Figure 6.7, taken from *WMO* (1994).

While Figure 6.7 is in good agreement with observations made in the Arctic (e.g., *Webster et al.*, 1993b; *Santee et al.*, 1996; *Notholt et al.*, 1997b), conditions in the Antarctic spring are quite different. Figure 6.8 presents springtime measurements of HNO_3 (Figure 6.8a), HCl (Figure 6.8b), $ClONO_2$ (Figure 6.8c), O_3 (Figure 6.8e), potential vorticity (Figure 6.8f) and temperature (Figure 6.8g) over Arrival Heights.

Additionally, the ratio of $ClONO_2$ to HCl has been shown (Figure 6.8d). $ClONO_2$ measurements have been made using the same instrument and at the same time as the HNO_3 and HCl measurements, and are thus completely comparable. The data is available from the NDSC database (http://www.ndsc.ncep.noaa.gov) and has been processed using SFIT2. The large error bars are due to the difficulty of retrieving $ClONO_2$ column amounts from the spectra. Ozone measurements have been made using the Dobson spectrophotometer at Arrival Heights and, unlike the FTIR observations, are total column measurements. These have been provided by Silvia Nichol [National Institute of

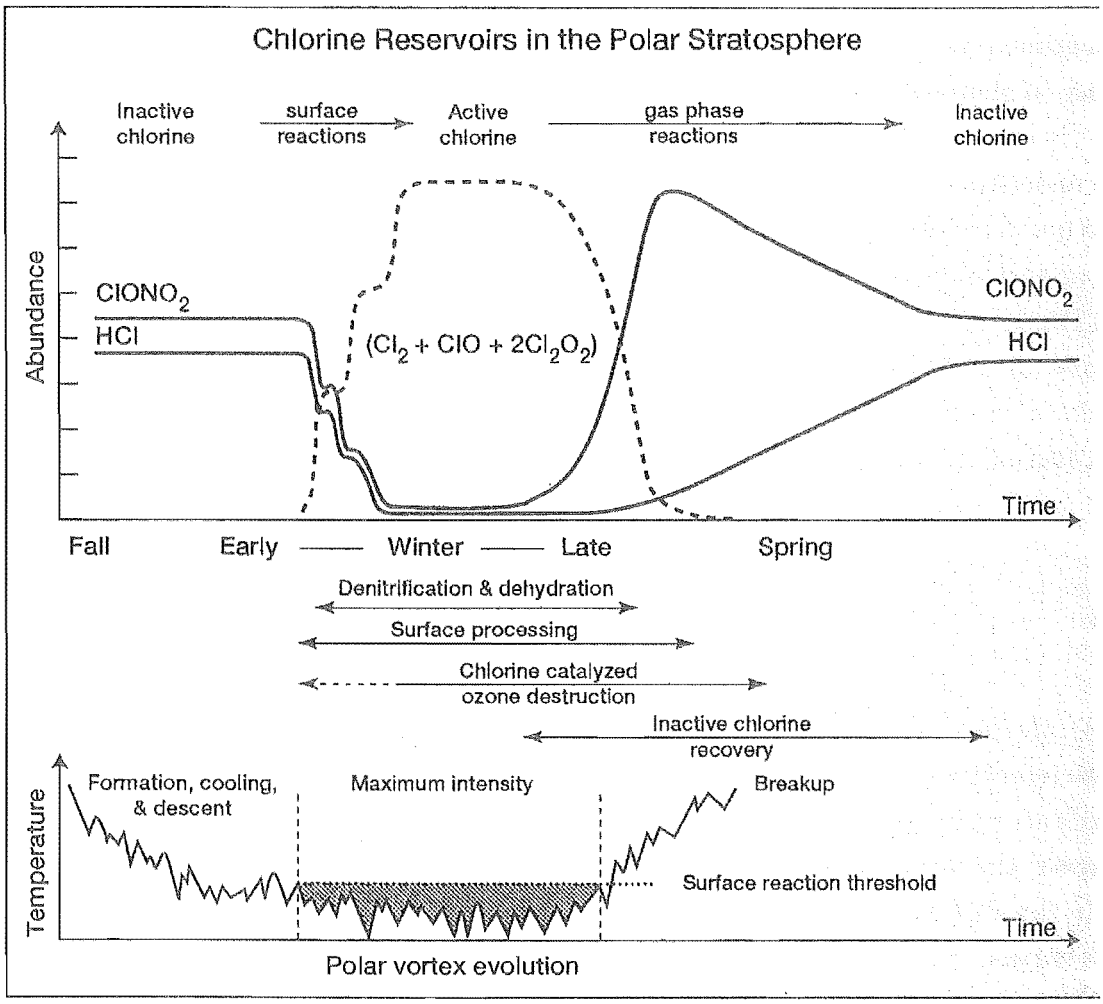

Figure 6.7: Schematic of the chlorine activation and deactivation occurring as a result of chemical and dynamical processes occurring in the polar stratosphere. Figure reproduced from *WMO* (1994), page 3.4, originally adapted from *Webster et al.* (1993b). It should be noted that while this is typical for Arctic conditions, conditions in the Antarctic lead to very different partitioning in the spring, as described in the text.

Water and Atmospheric Research, personal communication], but are also available from the NDSC database.

Looking first at the time when temperatures are still cold enough that PSCs may exist (i.e., up to day 270), the most obvious feature is the spike in the trace gases on days 252 and 253. While this has already been discussed in Section 6.1.4, it is especially interesting to see the spike in the $ClONO_2$ measurements (Figure 6.8c). This is likely to be a response to photolysis of the evaporated HNO_3, which provides NO_2 for Reaction 6.3. The subsequent drop in temperatures following the spike (Figure 6.8g), coupled with a decrease in HNO_3 (Figure 6.8a), is consistent with PSCs reforming. While the HCl partial column amounts at this time are too variable to be definitive, the $ClONO_2$ column amounts drop again at this time (Figure 6.8c), suggestive of continuing chlorine

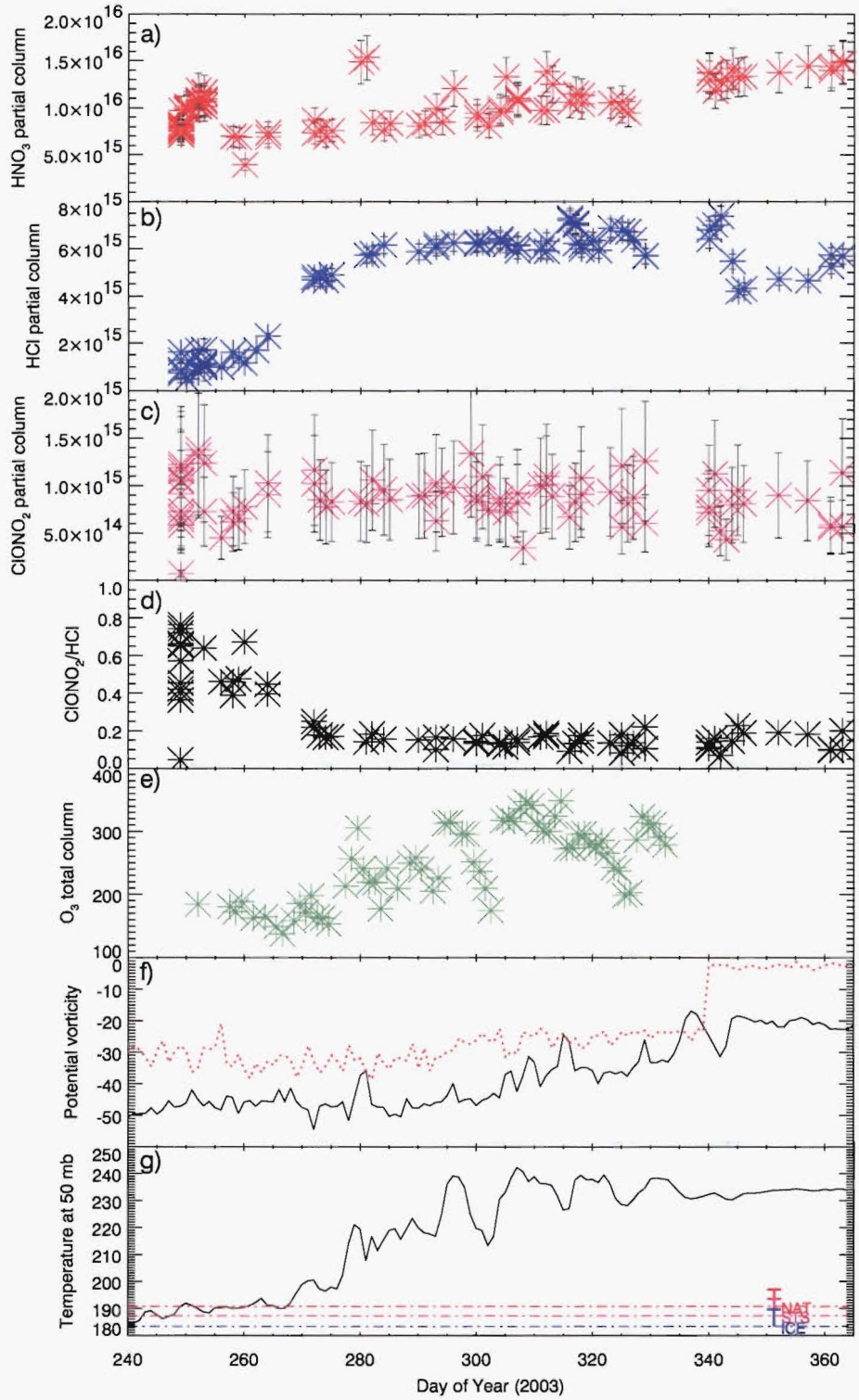

Figure 6.8: (From top to bottom) HNO_3, HCl and $ClONO_2$ 12 - 28 km partial column amounts (molecules cm^{-2}), as determined by FTIR observations; $ClONO_2$/HCl ratio; O_3 total column amounts (DU), as determined from the Dobson spectrophotometer; potential vorticity (10^6 $Km^2kg^{-1}s^{-1}$) on the 450 K potential temperature (solid black line) and the potential vorticity corresponding to the vortex edge (dotted red line); temperature (K) on the 50 mb pressure surface with approximate formation temperatures for NAT, STS, and ice PSCs, as calculated for spring conditions (see Section 6.1.4). All measurements for the Arrival Heights site, Antarctica.

activation.

Ozone measurements during this period (Figure 6.8e) show ozone hole values of less than 220 Dobson units[1], consistent with almost complete ozone loss in the 12 - 25 km region of the partial column (e.g., *Hofmann*, 1988; *Gardiner*, 1988; *McCormick and Larsen*, 1988). This is in agreement with Antarctic-wide observations showing the ozone hole to be at its peak size of approximately 34 million square kilometres (*WMO*, 2003a), the largest on record (*WMO*, 2003b).

As temperatures rise above the PSC formation threshold, the scene is set for chlorine deactivation. $ClONO_2$ leads the reservoir species' recovery, as evident in both the $ClONO_2$ and the $ClONO_2$/HCl ratio plots (Figures 6.8c and 6.8d), but this is quickly overtaken by a very rapid rise in the HCl partial column amount (Figure 6.8b). A small decrease in the $ClONO_2$ with the HCl rise is also observed. *Douglass et al.* (1995) used a box model to study the chemical changes occurring during this period and compared the results with HALOE observations. While their model predicted an increase in the $ClONO_2$ in late August and September, prior to the rapid HCl recovery, they commented that this calculated increase was not observed in the data (*Douglass et al.*, 1995). While the error bars are large on our $ClONO_2$ observations, we believe that this increase has been captured by our data, supporting the trend observed in their model results.

What is *not* observed is a rapid increase in the HNO_3 partial column amount, which would be expected if polar stratospheric clouds were simply evaporating. Rather, the partial column values stay very low, consistent with those observed throughout the winter (Figure 6.8a). This is evidence of substantial denitrification having occurred in the column. While this will be further investigated in Section 6.2, it is important for the understanding of how the chlorine reservoirs are re-partitioned.

Model simulations of vortex air transported to warmer mid-latitudes by *Prather and Jaffe* (1990) show that after warming, ClO decays and $ClONO_2$ increases, consistent with the picture painted in Figure 6.7. In the case of denitrified air with ozone depletion, however, NO_x levels reach a critical threshold after the first few days, and the Cl-ClO-$ClONO_2$ partitioning shifts in favour of Cl, leading to a rapid increase in HCl formation.

To translate these results to the Arrival Heights atmosphere observed in Figure 6.8, we look first at the production of chlorine nitrate. By Reaction 6.3 we see that $ClONO_2$ forms when ClO and NO_2 are present. ClO is a dominant chlorine species at this time of year (*Santee et al.*, 1996), but the NO_2 concentration is driven by the photolysis of HNO_3. As evident in Figure 6.8a, there is a lack of HNO_3 for photolysis, and as such, the NO_x threshold suggested by *Prather and Jaffe* (1990) will be quickly reached and

[1]The Dobson unit (DU) is the traditional measurement unit of the total column ozone amount, with 1 DU equal to 2.69×10^{16} molecules cm^{-2}. The 'ozone hole' is defined as the region where the total column amount of ozone is less than 220 DU, as compared to the pre-ozone hole springtime value of $\sim$ 300 DU (*Wayne*, 2000).

$ClONO_2$ production limited. This is observed in Figure 6.8c, with $ClONO_2$ reaching its maximum amount around day 265 (Figure 6.8c).

At this time, HCl is seen to rapidly increase (Figure 6.8b). In order to understand this increase, we look at the rate of HCl formation, which is given by

$$\frac{d[HCl]}{dt} = k_1.[CH_4].[Cl] \tag{6.5}$$

where k_1 is the rate of Reaction 6.4 (*Grooss et al.*, 1997).

Because the concentration of CH_4 remains fairly constant, Equation 6.5 shows the rate determining factor to be the concentration of Cl. In a denitrified atmosphere with ozone loss, Cl creation is dominated by the photolysis of ClO and its dimer, Cl_2O_2 (*Prather and Jaffe*, 1990; *Douglass et al.*, 1995). Additionally, the destruction of Cl through the reaction $Cl + O_3 \rightarrow ClO + O_2$ is limited. As such, the Cl + ClO partitioning will be shifted towards Cl, as predicted by *Prather and Jaffe* (1990), and the HCl formation will be rapid. Additionally, a lack of ozone will shift the partitioning of any NO_x towards NO, as photolysis drives the production of NO from NO_2, but reaction with ozone drives NO_2 production from NO (*Grooss et al.*, 1997). This serves to further reduce the production of $ClONO_2$, favouring the formation of HCl. Model analyses show the Cl/ClO ratio to be up to 30 times higher in the southern hemisphere than in the northern hemisphere, and NO/NO_x is lower in the north, even for similar concentrations of HNO_3 (*Douglass et al.*, 1995).

From these calculations and predictions, we can see that the partitioning of the chlorine reservoir species observed in Figure 6.8 is being driven by two processes: denitrification resulting from the sedimentation of PSC particles slowing the recovery to chlorine nitrate; and ozone loss speeding the recovery of HCl. The observed pattern is in reasonably good agreement with Antarctic observations made from the UARS instruments (*Douglass et al.*, 1995; *Santee et al.*, 1996), but is in stark contrast to Arctic observations, as shown in Figure 6.7.

Once the chlorine has all returned to its reservoir species but before the vortex breaks down (i.e., from day 280 to 340, Figure 6.8), the two chlorine reservoir gases are seen to be in a fairly stable equilibrium, in contrast to the repartitioning shown during this period in Figure 6.7. While Figure 6.8b clearly shows the HCl partial column amount to be greater than pre-vortex values, this can be attributed largely to the subsidence of air within the vortex, and the ratio of $ClONO_2$ to HCl shown in Figure 6.8d remains fairly constant throughout the period. It does, however, show the partitioning of the chlorine species to be slightly more in favour of HCl during this time than in the non-perturbed air seen when the vortex has broken down (Figure 6.8d). This may be purely dynamical, as the vertical profile of HCl has more gas at higher altitudes than the $ClONO_2$ profile, but without a

detailed transport model or comparable tracer observations, this can only be speculation. Regardless, the extent of the partitioning towards HCl is not large enough to support model predictions and observations that show complete conversion of Cl_y to HCl in a denitrified spring (*Grooss et al.*, 1997). The $ClONO_2$ partial column amounts during this time are definitely not negligible and are, in fact, comparable to the observed extra-vortex values. While large uncertainties in the $ClONO_2$ measurements limit the conclusiveness of these observations, it appears that the gases have reached a stable partitioning within the partial column without over-forming HCl, eliminating the need for re-partitioning later.

Also during this time, wave driving causes the polar vortex to become less circular and less stable (*Waugh and Randel*, 1999; *Waugh et al.*, 1999). The edge of the vortex occasionally moves so that Arrival Heights is no longer within it. When this happens, the air being sampled is no longer vortex air but is representative of the air around the outside edge of the vortex. An example of this is the spike observed in the nitric acid amount on day 280 (Figure 6.8a), corresponding to the potential vorticity over Arrival Heights moving outside the vortex edge (Figure 6.8f). The large jump in the amount of nitric acid can be associated with the collar region – a dynamically driven band of air containing very high values of HNO_3 immediately outside the polar vortex (*Roche et al.*, 1993b, 1994). Later in the year these excursions become more frequent, and similar spikes are observed in the nitric acid partial column amounts on several days before the vortex breaks up completely around day 340 (December 6th).

With the breakup of the vortex, mixing of mid-latitude air causes the amount of HCl in the partial column to rapidly return to typical summer equilibrium values (Figure 6.8b). The HNO_3 partial column amount has been gradually increasing throughout the period, but with the vortex breakup, mixing with extra-vortex air causes the amount to rapidly increase to values consistent with those observed at the start of the year (Figure 6.1b). By the end of the year, both HCl and HNO_3 partial column amounts are completely comparable with those observed before the vortex formed (Section 6.1.1).

6.2 A closer look: Evidence of HNO_3 redistribution?

Denitrification has been observed in the Antarctic spring stratosphere since the first ozone-loss campaigns occurred in Antarctica in the 1980s (*Keys and Johnston*, 1986; *Wahner et al.*, 1989a; *Fahey et al.*, 1989b). By preventing the return of active chlorine to the $ClONO_2$ reservoir, as outlined in Section 6.1.5, complete denitrification occurring in Antarctica has been estimated to account for a 10% increase in the observed ozone loss (*Portmann et al.*, 1996; *Brasseur et al.*, 1997). The mechanisms for denitrification, however, are still not well understood (*Eyring et al.*, 2004). While denitrification is clearly observable in the 12 - 28 km partial column amounts presented in Figure 6.1, by dividing

the columns up further, additional information on the redistribution of nitric acid within the stratosphere can be gained.

FTIR measurements provide an advantage over satellite observations in that they are very localized measurements and are thus less likely to average over the vortex and vortex-edge regions. While the partial column measurements are not as well resolved as in-situ measurements, the ease of making FTIR observations means that there is much more information available from which to draw conclusions. This section will look at two different sets of partial columns: slightly larger columns including lunar observations which will provide information on the location of early denoxification; and smaller solar-only partial columns which will be used to look at the redistribution of nitric acid within the stratosphere.

6.2.1 10-20 km and 20-28 km solar and lunar partial columns

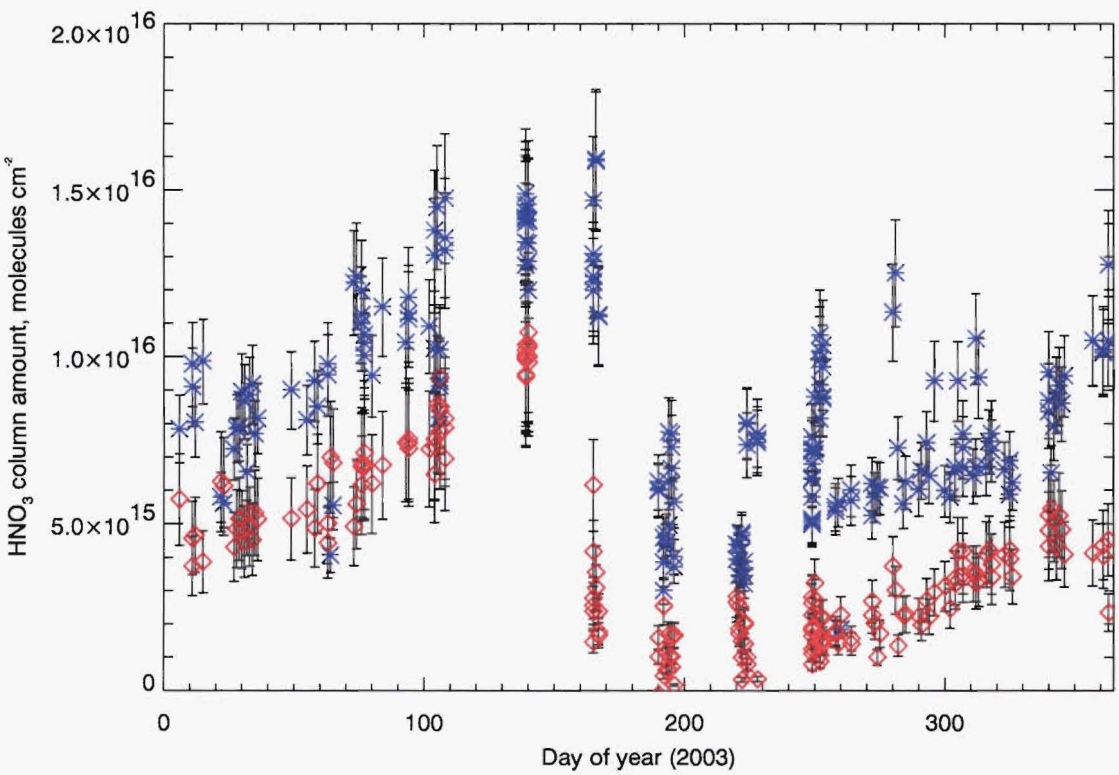

Figure 6.9: 10 - 20 km (blue) and 20 - 28 km (red) partial column measurements from solar and lunar HNO_3 observations.

Figure 6.9 shows 10 - 20 and 20 - 28 km HNO_3 partial column amounts, as described in Section 5.2.7. The choice of these partial columns is such that useful information can be derived from the lunar measurements as well as from the higher-resolution solar ones.

From the beginning of the year until the onset of polar stratospheric clouds, the nitric acid amount follows the trends outlined in Section 6.1.1 in both height ranges, showing that the nitrogen partitioning processes that lead to a winter HNO_3 maximum are occurring throughout the stratosphere. The lower 10 - 20 km partial column amounts show more variability than the 20 - 28 km column amounts. This can be explained by dynamical variation in this region due to the mixing of air from the troposphere. During the summer the tropopause is very close to the bottom boundary of the partial column, and as shown by the averaging kernels (Figure 5.16), there is not a clear distinction made between changes in the nitric acid at 10 km or changes slightly lower down.

The amount of HNO_3 in both partial columns is seen to reach its peak in May (days 139 and 140), consistent with the trend seen in the larger partial column (Figure 6.1b), but June measurements (days 165 - 167) show a significant difference between the higher and lower height ranges. Depletion of the gas phase partial column amount (denoxification) in the 20 - 28 km range is nearly total, while depletion in the 10 - 20 km range is significantly less.

The reason for this is two-fold. First, the density-weighted summertime nitric acid profile is sharply peaked at about 20 km. With the formation of the polar vortex, diabatic descent within the vortex causes this profile to subside, moving the peak into the lower partial column. Diabatic descent in the Antarctic stratosphere has been estimated at 0.4 - 0.9 km per month, with a subsidence within the upper partial column of approximately 3 km by June (*Rosenfield et al.*, 1994). Second, temperatures during this time fall below the PSC existence thresholds, as indicated in Figure 6.10.

As a result of subsidence, nearly all of the nitric acid in the 20 - 28 km partial column is in the region below 25 km, where temperatures are sufficiently low for the nitric acid to have condensed into solid NAT, liquid STS or even ice clouds. This explains the nearly complete loss of gas phase nitric acid in this partial column. In the 10 - 20 km partial column, temperatures are sufficiently low for PSC formation over the upper half of the region, in agreement with lidar observations showing PSCs to typically be located between 15 and 28 km during June (*Adriani et al.*, 2004). The lower half of the partial column, however, is still too warm for PSC formation. Combined with an increase in the nitric acid in this region due to subsidence, this warmer region of the column can still be expected to contain significant amounts of uncondensed gas, contributing to the nitric acid observed in the 10 - 20 km partial column.

The HNO_3 partial column amounts through the rest of winter paint a similar picture. In the higher 20 - 28 km altitude range, removal of the gas phase nitric acid is nearly complete, with little variation observed in the column. Lower down, the 10 - 20 km partial column amounts remain higher and show more variation than in the upper region.

As outlined above, much of the observed difference between the 10 - 20 and 20 - 28

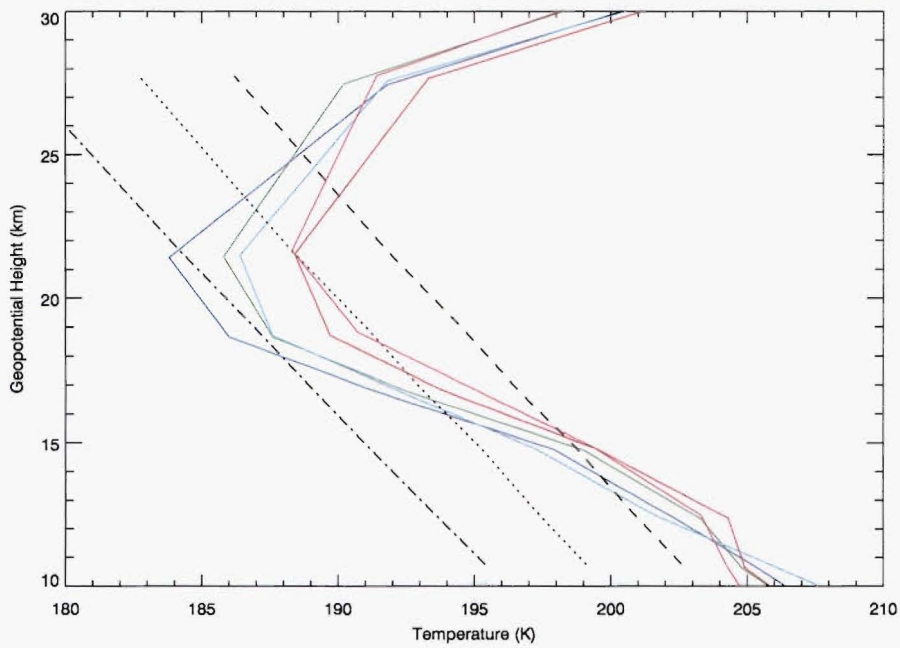

Figure 6.10: Temperature profiles for days 163 (red), 164 (green), 165 (blue), 166 (cyan) and 167 (pink), from the NCEP meteorological analyses (Section 4.2.1). FTIR measurements were made on days 165 - 167. NAT (dashed), STS (dotted) and ice (dash-dotted) condensation temperatures for early winter conditions, as outlined at the start of the chapter, are also shown.

km partial column amounts can be attributed to subsidence and the temperature in the region. Simple calculations, however, suggest that some of the partial column amounts observed in the 10 - 20 km region during July and August are higher than expected, even if assuming a subsided, denitrified and dehydrated atmosphere. While this is by no means conclusive, it seems likely that polar stratospheric cloud particles that have formed higher up have subsequently sedimented into the 10 - 20 km region, where the warmer temperatures have caused them to evaporate, contributing to the observed partial column amounts. Sedimentation rates of approximately 2 km day^{-1} for 10 μm ice or large NAT particles, or 0.05 km day^{-1} for typical 0.5 μm solid NAT particles (*Larsen*, 2000), indicate that this a reasonable assumption.

The September spike, on days 250 - 254, is again an interesting case study. Figure 6.9 clearly shows the spike to be occurring in the lower partial column, with the observed 10 - 20 km gas phase nitric acid amounts rising dramatically to values more consistent with those observed in March. Temperature profiles for the days around the spike are given in Figure 6.11.

The increase in temperatures above T_{NAT} on these days corresponds nicely to the spike, and at first glance it would seem that what is being observed is the evaporation of a large number of PSC particles in the partial column. Where this fails, however, is in

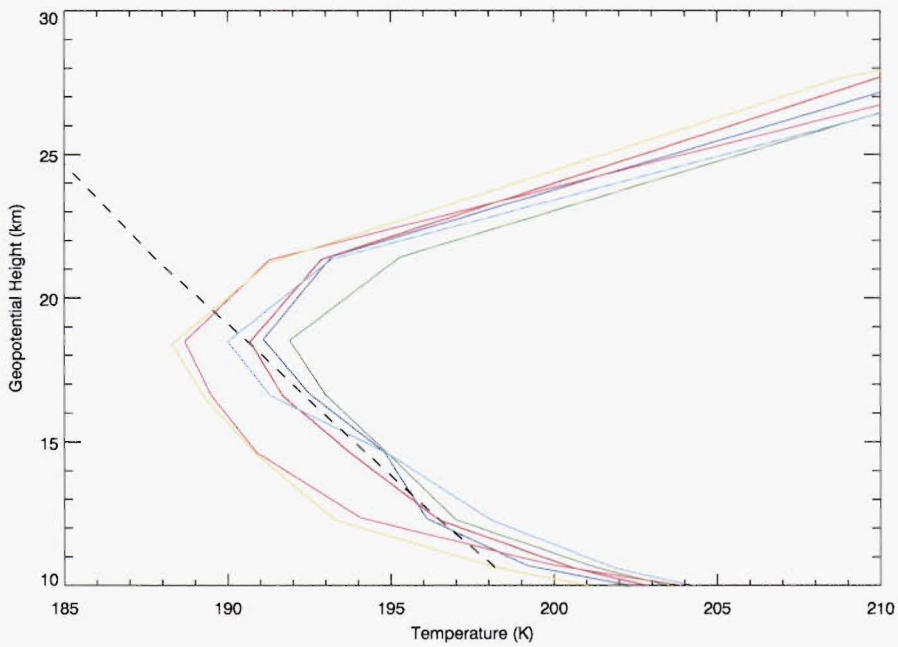

Figure 6.11: Temperature profiles for days 249 (red), 250 (green), 251 (blue), 252 (cyan) 253 (pink) and 254 (yellow), from the NCEP meteorological analyses (Section 4.2.1). The spike was observed on days 250 - 254. T_{NAT} (dashed line), as determined for denitrified, dehydrated spring conditions, is shown as an indication of likely PSC evaporation conditions.

the subsequent days, as nitric acid amounts in this partial column drop significantly and remain at low levels (Figure 6.9). Figure 6.11 clearly shows the coldest temperatures to be occurring around 19 km, or 50 mb, but Figure 6.8g showed temperatures at 50 mb to increase above T_{NAT}, and remain above T_{NAT}, from day 270. No corresponding increase in the 10 - 20 km partial column amount in Figure 6.9 is observed. Instead values remain low, even though temperatures are warm enough for PSC evaporation. This is clear evidence of denitrification in the partial column and can be attributed to the permanent loss of nitric acid due to sedimentation of PSC particles. The upper partial column amount likewise shows no clear jump when the temperature increases, showing it too is denitrified. Just days previously, however, there was enough nitric acid in the column to create a spike of gas phase nitric acid comparable to the pre-PSC partial column amount, and the question remains as to what is responsible for it. While the following section will again identify the spike, further investigation will be postponed until Chapter 8.

In addition to providing information about the location and extent of winter denoxification and springtime denitrification, Figure 6.9 also provides some information about the recovery of the nitric acid. Both the 10 - 20 and 20 - 28 km partial column amounts show a gradual increase in the spring due to photolytic processes, with the processes being much more pronounced higher up. Brief excursions outside the vortex show up clearly, as

already described in Section 6.1.5. The vortex breakup on day 340 is evident in both partial columns, with rapid increases in the observed nitric acid amounts due to the mixing of nitric acid-containing extra-vortex air.

6.2.2 10-16 km, 16-20 km, 20-24 km, and 24-28 km solar partial columns

Figure 6.12 shows the amount of HNO_3 in the more finely divided partial columns obtainable from higher resolution solar measurements. Early in the year, the amount of nitric acid in each of the lower three columns is comparable, though as a result of the close proximity to the tropopause, the lowest partial column amounts again shows considerable variability during this time. The 24 - 28 km partial column contains much less nitric acid than the lower columns, consistent with the atmospheric profile shown in 5.12. Of most interest in this plot are the springtime measurements. Figures 6.1 and 6.9 have already shown the greater partial column to be seriously denitrified, but Figure 6.12 allows the distribution of the denitrification and any nitrification to be observed.

The 24 - 28 km partial column shows the most obvious denitrification. The gas phase nitric acid has been nearly completely removed during the winter, and recovery is very gradual, with no clear signature of PSC evaporation causing a subsequent increase in the partial column amount at any point.

Slightly lower, the 20 - 24 km gas phase nitric acid has also been completely removed during the winter. Again, no clear increase due to the evaporation of PSCs is observed, showing the loss of nitric acid in this partial column to be permanent.

The 16 - 20 km partial column shows the first evidence of some nitric acid remaining in the column. While the first observations of the spring show very low values, consistent with nitric acid being completely removed from the gas phase, a rapid increase in nitric acid in the partial column is observed around day 270. This is consistent with the timing of PSC evaporation predicted by the 50 mb temperature plot (Figure 6.8g). The partial column amount continues to grow following this increase, when nitrogen partitioning and photolytic processes at this time of year would normally suggest HNO_3 destruction rather than creation. As such, it can be assumed that not all of the nitric acid that was in the partial column prior to PSC formation has been released back to the gas phase and that some has been permanently lost. Nonetheless, this is the first altitude range where any sign of springtime denoxification, rather than denitrification, has been seen.

The 10 - 16 km partial column does not show any signs of denitrification or denoxification at all. The first measurements clearly show the September spike to be occurring in this region, consistent with the theory suggesting evaporation as its main cause. Subsequent measurements are again lower than the spike, showing it to be an unusual event rather than a permanent process. The general trend in the partial column amount fol-

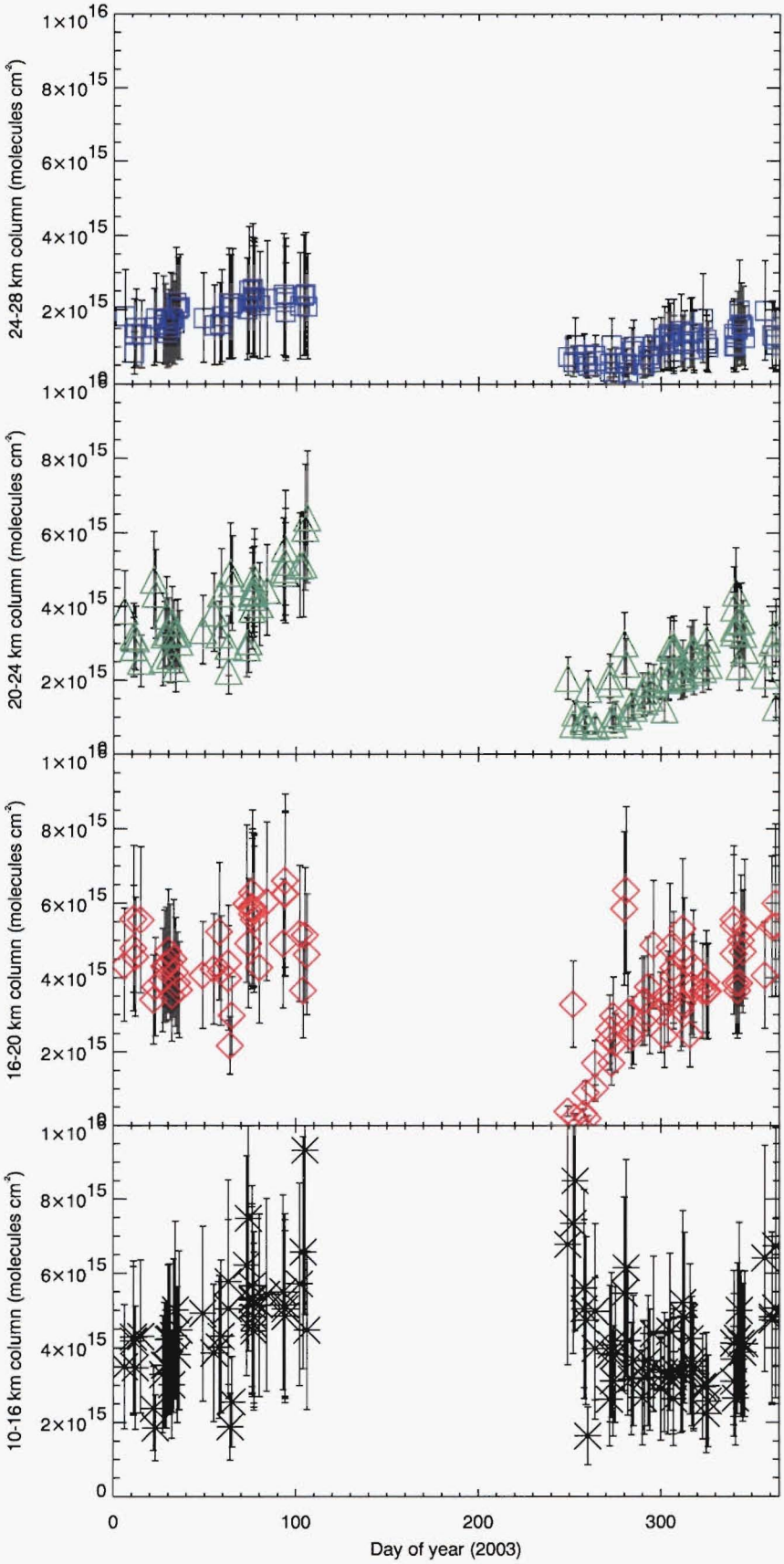

Figure 6.12: (From top to bottom) 24 - 28 km (blue), 20 - 24 km (green), 16 - 20 km (red), and 10 - 16 km (black) partial column measurements from solar HNO_3 observations.

lowing the spike is a decrease, consistent with expectations that HNO_3 will be photolysed as the day length increases. With the exception of the September spike, which is a clear example of nitrification in the partial column, there is no large increase in the partial column amounts compared to pre-winter amounts. This provides evidence that the nitric acid in the 10 - 28 km region has not just all settled to the lowest regions of the column but has mostly been removed from the stratosphere.

Frequent spikes are observed in the 10 - 16 km column, corresponding to the sampling of extra-vortex air as indicated in Section 6.1.5. Corresponding coincident spikes are also observed in the 16 - 20 km column and, to a lesser extent, in the 20 - 24 km column.

What does this tell us? The theory proposed for polar stratospheric denitrification is the sedimentation of nitric acid-containing PSC particles (*WMO*, 1994, 1998). This requires particles to grow sufficiently large that they are able to sediment into lower regions of the column, or out of it altogether. This process is still not well understood, and models still struggle to capture the observed denitrification (*Eyring et al.*, 2004). Recent observations in the Arctic of large NAT-containing particles, coined 'NAT rocks' (*Fahey et al.*, 2001), have provided an additional insight into these processes and are currently being incorporated into models [Martyn Chipperfield, University of Leeds, private communication]. While the FTIR measurements presented in Figure 6.12 are not able to provide direct evidence of any of these processes, they do clearly show denitrification to have occurred high in the column, in the 20 to 28 km range. They also show some nitric acid to remain in the 16 - 20 km region and show values even higher than expected in the 10 - 16 km column, especially in the September spike. They provide good evidence of sedimentation of nitric acid in the column and are suggestive of nitrification occurring in the lowermost regions as nitric acid-containing particles encounter warmer temperatures and evaporate.

6.2.3 Applications

While these FTIR measurements do not in themselves provide information that is new or unexpected, their biggest advantage is in the additional information they present to the modelling community. Observations provide important verification that the dynamical and chemical processes are being modelled sufficiently well to capture the true state of the atmosphere. By breaking the single partial column into multiple partial columns, better constraints on the location and extent of denoxification, sedimentation and the subsequent denitrification occurring within the region during the winter and spring periods have been provided.

High resolution solar FTIR measurements have been made at Arrival Heights, and at many other sites around the world, for some years. The range of trace species that

can be measured from these observations makes them an incredibly useful data source. While total or large partial column measurements provide good indications of the trends observed in the stratosphere or troposphere, the ability to retrieve the amount of gas in smaller partial columns, as shown here, provides additional information that can usefully be incorporated into our understanding and modelling of the processes that drive our atmosphere.

6.3 Conclusions

Partial column measurements of stratospheric reservoir species HCl and HNO_3 made using a Fourier transform infrared spectrometer from Arrival Heights, Antarctica, have been presented in this chapter. The inclusion of wintertime spectroscopic measurements of HCl, made using the moon as a light source, is a first for the Antarctic region. The partial column amounts of the two gases have been presented in conjunction with meteorological data, allowing the processes driving their formation and destruction to be investigated and a complete picture of their evolution through the year to be developed.

Section 6.1 presented 12 - 28 km partial column measurements of the trace gases and looked in detail at the trends observed in the gases during each phase of the year.

Prior to the formation of the polar vortex, January - April measurements showed conditions that were predominantly stable, with the main trends in the HCl and HNO_3 partial column amounts driven by dynamics and the change from 24-hour daylight in the Antarctic summer to 24-hour darkness in the Antarctic winter. With the formation of the polar vortex and the subsequent cooling of the stratosphere, processes unique to the polar regions began to dominate. Prior to the formation of polar stratospheric clouds over Arrival Heights, a small reduction in the HCl measurements was observed during the May full moon measurements. This was attributed to chlorine activation occurring on background sulfate aerosols at temperatures below 200 K.

The formation of PSCs over the region between the May and June full moon periods was the dominant process observed in the 2003 year. The HNO_3 gas phase partial column amount was rapidly reduced as nitric acid was incorporated into PSC particles. HCl amounts also showed a rapid reduction, consistent with the complete conversion of HCl to active chlorine species in the region where temperatures were below T_{NAT}. The June measurements were unusual in the scatter observed in the HNO_3 column amounts. This was attributed to the phase of the PSCs, which is to be further investigated in Chapter 8. HCl measurements showed no such scatter, consistent with chlorine activation reactions occurring rapidly on both solid and liquid clouds.

The rest of the polar winter was characterized by extremely low amounts of both HCl and HNO_3 observed in the partial column. This was consistent with expectations that

chlorine would be entirely activated in the region and that gas phase HNO_3 would be incorporated into aerosol particles. While denitrification may well have been occurring during this time, it wasn't until the temperatures increased above the NAT existence temperatures in September that this was able to be confirmed by these measurements. Nonetheless, extreme denitrification was observed in the column.

The spring period was looked at in some length in Section 6.1.5. Measurements of ozone and chlorine nitrate made from the same site provided additional information for the processes resulting in chlorine deactivation. Measurements clearly showed the deactivation to be dominated by conversion of active chlorine to HCl, in contrast to Arctic observations showing chlorine recovery to be first to $ClONO_2$. They did, however, show a small increase in the $ClONO_2$ to be occurring prior to the period of rapid HCl creation, as predicted by several models but not observed in previous measurements. Additionally, while the deactivation was predominantly to HCl, the partial column amounts of $ClONO_2$ were not negligible, and an equilibrium between the two gases was established from the outset.

With the breakdown of the polar vortex late in the year and the subsequent mixing of air from mid-latitudes, both HCl and HNO_3 partial column amounts were shown to return to levels consistent with the beginning of the year.

Section 6.2 went a step further and looked at nitric acid to the full extent of the height resolution contained in the FTIR measurements. This clearly showed denoxification to be occurring first at high altitudes in the stratosphere, consistent with subsidence, temperature and PSC observations made in the region. Additionally, these measurements were able to show extensive denitrification to be occurring above 20 km. Some, but not all, of the HNO_3 in the 16 - 20 km region was depleted during the winter, with the amount of HNO_3 in this partial column showing a rapid increase above PSC evaporation temperatures. The 10 - 16 km region showed evidence of nitrification, as expected by the sedimentation of particles in the region. While these observations were not new or unexpected, the use of FTIR measurements to look at small height ranges has generally been unexplored. The potential application of these, and other measurements made by FTIR instruments, to model verification are seen as an important addition to our understanding of ozone loss and climate change processes.

In conclusion, measurements of the stratospheric trace gases HCl and HNO_3 from Arrival Heights through the 2003 year have provided observational evidence of a wide range of processes occurring during the polar night. This is important verification of our current understanding of the processes which ultimately result in springtime ozone loss.

THE LIBRARY
UNIVERSITY OF CANTERBURY
CHRISTCHURCH, N.Z.

Chapter 7

Comparison with the SLIMCAT Off-line Chemical Transport Model

Because there have been so few trace gas measurements made during the Antarctic winter, much of our current understanding of the processes occurring during this time has come from models. In this chapter the HCl and HNO_3 measurements presented in Chapter 6 will be compared to model output from a recent run of the three-dimensional chemical transport model, SLIMCAT.

The chapter will begin by introducing the SLIMCAT model, specifically focusing on the model parameterizations that are important for characterizing polar ozone depletion. This will be followed by a description of the techniques used to make the SLIMCAT model output comparable to the measured partial column amounts, following the work of *Connor et al.* (1994, 1995); *Rodgers and Connor* (2003). Finally a direct comparison of the modelled and measured 12 - 28 km HCl and HNO_3 partial column amounts will be presented.

7.1 SLIMCAT

SLIMCAT is an off-line three-dimensional chemical transport model. This is different from a so-called general circulation model in that the chemistry component is not integrated into the dynamical model, but is performed separately for each dynamical time-step ('off-line'). The model was written by Martyn Chipperfield from the University of Leeds, UK. It is described in depth in *Chipperfield* (1999), *Chipperfield* (1996b) and *Chipperfield* (1996c), with the latest updates described in *Chipperfield* (2005). SLIMCAT is well known in the atmospheric modelling community and has been used for many studies of ozone and ozone-related gases in both the polar and lower latitude regions (e.g., *Chipperfield and Jones*, 1999; *Solomon et al.*, 2002; *Stowasser et al.*, 2002; *Chipperfield*, 2003).

While the model output used for this comparison has been provided directly by Martyn Chipperfield, a brief overview of the dynamical and chemistry schemes employed by the model will be given for completeness. Special attention has been paid to the heterogeneous chemistry scheme used to account for chemical processing on polar stratospheric clouds.

7.1.1 Dynamics and radiation

Transport in SLIMCAT is determined using real wind and temperature data from meteorological analyses. Horizontal transport is determined directly from these analyses, with values interpolated linearly in potential temperature to match the SLIMCAT grid. SLIMCAT has recently been converted to allow model layers to extend to the surface (*Feng et al.*, 2004; *Chipperfield*, 2005). As such, a hybrid vertical co-ordinate scheme has been used, with isentropic levels used in the stratosphere and terrain-following sigma co-ordinates allowing the model to extend through the troposphere to the ground. With the extension of the model to the ground, the vertical transport scheme has also been modified from the original radiation scheme of Shine (*Shine*, 1987) to a Delta-Eddington approximation based radiation scheme (*Joseph et al.*, 1976; *Briegleb*, 1992). This radiation scheme accurately computes the absorbed solar radiation and calculates fluxes at the layer interfaces in both the upward and downward directions (*Briegleb*, 1992).

There are several tracer advection schemes incorporated in SLIMCAT (*Chipperfield*, 1996a; *Chipperfield and Nikiforakis*, 1997). The standard scheme, and one used here, is the second-order moments scheme of *Prather* (1986), based on the exchange of mass between boxes. The mass in each layer is determined from the isentropic density using the full three-dimensional analyses, and both the tracer mass and the total mass are advected. Because the scheme does not constrain horizontal and vertical motions, the isentropic density is used to reinitialize the mass of the box on each time-step to ensure that the net transport in or out of the box matches the expected mass. Tracers within are scaled to conserve volume mixing ratios (*Chipperfield*, 1996a).

7.1.2 Stratospheric chemistry

For each dynamical time-step, the chemical scheme may be called several times. Details of the chemistry are given in *Chipperfield* (1996c) and *Chipperfield* (1999). The model uses a limited number of chemical families containing species which are in rapid photochemical equilibrium, in order to reduce the number of gases that must be advected. The partitioning of individual species within the family is given in *Chipperfield* (1999, 1996c). Species showing a strong diurnal variation, as well as other short-lived species, are integrated separately. Long-lived and source gases are integrated according to continuity equations, and the concentrations of several gases, including oxygen, nitrogen, and hydrogen, are treated as fixed. Reactions are generally computed using the photochemical data of *Sander et al.* (2003), with photolysis rates calculated using a scheme based on *Lary and Pyle* (1991). A four-dimensional lookup table is used to interpolate photolysis rates to a particular time and location in the atmosphere.

Heterogeneous chemistry

Reactions occurring on the surface of NAT, liquid STS, and ice PSC particles are included in the SLIMCAT model. PSC formation is based on the assumption that particles are in equilibrium rather than on a full microphysical scheme.

Solid NAT cloud formation is based on the equilibrium equation of *Hanson and Mauersberger* (1988). Model mixing ratios of H_2O and HNO_3, as well as temperature fields, are used to determine whether clouds and the subsequent heterogeneous reactions are thermodynamically possible. The available surface area for heterogeneous reactions on solid clouds is calculated from the amount of HNO_3 condensed. Gas diffusion limitation is also included to account for the potentially large size of NAT PSC particles. Of particular importance to this research is the reaction rate on solid clouds of Reaction 6.1, between the chlorine reservoir species HCl and $ClONO_2$, which has been determined from *Hanson and Ravishankara* (1994).

In this version of the model run, a bimodal distribution of the NAT particles has been assumed, as detailed in *Davies et al.* (2003). This is to include the effect of large nitric acid containing particles (NAT rocks) observed in the Arctic atmosphere (*Fahey et al.*, 2001). In this scheme, HNO_3 is first condensed into small NAT particles with a radius of 0.5 μm, to a maximum number density of 1 particle cm^{-3}. Any condensed HNO_3 above this limit is condensed into the large mode particles, which have an assumed radius of 10 μm [Martyn Chipperfield, University of Leeds, UK, personal communication].

The composition of liquid PSC aerosols has been determined from the analytical scheme of *Carslaw et al.* (1995) using the model temperature and H_2SO_4 fields. Earlier versions of SLIMCAT had no heterogeneous reactions occurring on supercooled liquid aerosols below the NAT condensation point. The model has recently been extended to include these reactions at all appropriate temperatures, resulting in more realistic chlorine activation in the Arctic [Martyn Chipperfield, University of Leeds, UK, personal communication]. Reactions of HCl and $ClONO_2$ on the liquid clouds again come from the parameterizations of *Hanson and Ravishankara* (1994), using the HCl solubility of *Luo et al.* (1995).

The existence of ice particles is tested using the saturation pressure of H_2O over ice, with particles assumed to form whenever thermodynamically possible (*Chipperfield*, 1996c). HNO_3 is removed from the gas phase in the the presence of ice particles by assuming a coating of NAT and using the NAT equilibrium expression of *Hanson and Mauersberger* (1988). The available surface area for heterogeneous reactions occurring on the ice crystals is determined from the amount of H_2O that is condensed, with the assumption that ice particles have a radius of 10 μm.

Denitrification and dehydration are treated using a simple sedimentation scheme. In

this model run, the larger mode NAT and ice particles are sedimented from the model layers using fall velocities appropriate for particles of radius 10 μm. In the layer below, the sedimented particles may evaporate, be involved in further heterogeneous reactions or continue to sediment, depending on ambient conditions (*Chipperfield*, 1999). The small mode NAT and liquid aerosol particles are assumed to not sediment [Martyn Chipperfield, University of Leeds, UK, personal communication].

7.1.3 Model initialization

The SLIMCAT model run used for this comparison has been determined at a horizontal resolution of 7.5° latitude by 7.5° longitude, with 24 levels included from $\sim$ 60 km to the surface. The model was initialized on January 1st, 1977, and has been forced using 6-hourly European Centre for Medium-range Weather Forecasts (ECMWF) analyses. ERA-40 reanalyses (*ECMWF*, 2002) were used until December 31st, 1999, and operational analyses were used from January 1st, 2000, onwards. A chemical time-step of 20 minutes was used, with a 30 minute dynamical time-step. The initial chlorine loading was taken from the *WMO* (2002) halocarbon scenarios, with an additional 100 pptv assumed to come from short-lived species applied as a boundary condition at the surface. The model transport and chemistry determine the distribution of the species [Martyn Chipperfield, University of Leeds, UK, personal communication].

Model data has been saved at 0 UT every 2 days and linearly interpolated to the Arrival Heights site from the four nearest model grid-points at each output time.

7.2 Preparing SLIMCAT output for comparison with FTIR measurements

SLIMCAT output contains high resolution vertical profile information on a 24-layer hybrid vertical co-ordinate grid. To make it comparable with the FTIR partial column measurements, the model data must be converted to altitude-dependent partial column amounts and smoothed to match the lower resolution of the FTIR measurements.

7.2.1 Determining partial column amounts

Partial column amounts in the 12 - 28 km region have been determined from the SLIMCAT model profiles for both HCl and HNO_3. These calculations have been made using the hydrostatic equation, the ideal gas law, and an assumption that the gas mixing ratios are constant within each layer. Pressure and geopotential height information included in the SLIMCAT output has been interpolated to the SFIT2 standard vertical profile, with 2 km spacing throughout the stratosphere, for use in the calculations. Partial column amounts

for the days not included in the saved SLIMCAT output have been calculated from linear interpolation of the model profiles from the days on either side.

SLIMCAT model data for HCl and HNO_3 over the 12 - 28 km altitude range are shown in Figure 7.1.

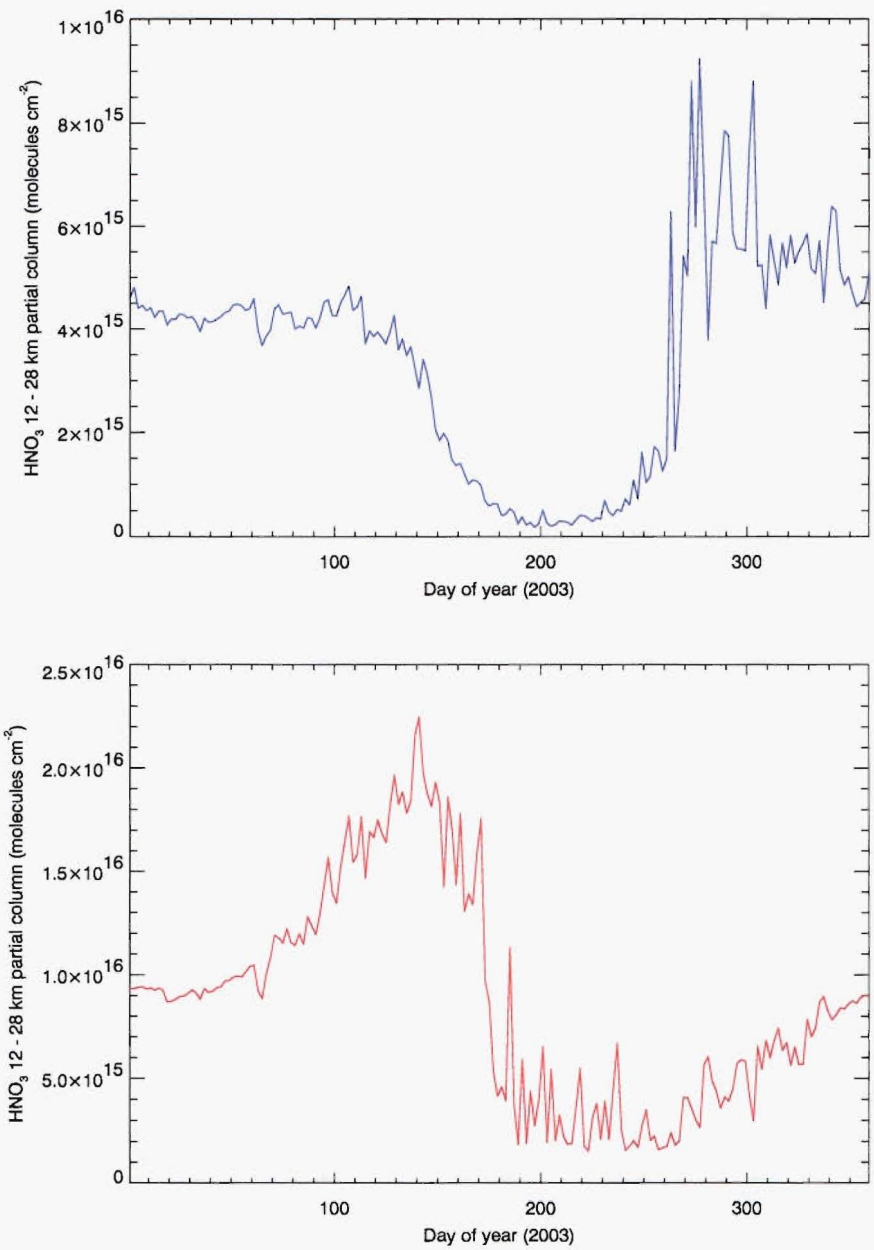

Figure 7.1: 12 - 28 km HCl (top) and HNO_3 (bottom) partial column amounts from SLIMCAT model output for 2003.

While the trends in the model output appear to be consistent with the observations presented in Figure 6.1, the model output in this form is not directly comparable with

the FTIR data due to the higher resolution of the model and the effect of smoothing and *a priori* on the measurements.

7.2.2 Convolving the model

As discussed in Section 3.2.1, the atmospheric profile retrieved from the FTIR measurements is a smoothed version of the true profile, with the smoothing explicitly defined by the averaging kernel and the *a priori* profile. The error introduced as a result of this smoothing must be considered when making comparisons between measurements from different instruments or between instruments and models. In the case of a high resolution measurement or model being compared with a low resolution measurement, the smoothing error can be mostly eliminated by using the *a priori* profile and averaging kernels to compute the profile which would be retrieved by the lower resolution measurement if the high resolution profile were the true atmospheric profile (*Connor et al.*, 1994, 1995; *Rodgers and Connor*, 2003). Using the definition of the retrieved profile given in Equation 3.9, excluding the error terms, the smoothed version, x_s, of the high resolution or model profile, x_h, is given by

$$x_s = x_a + A(x_h - x_a) \tag{7.1}$$

where x_a and A are the *a priori* profile and averaging kernel respectively (as defined in Section 3.2.1). By comparing the retrieved FTIR profile with x_s rather than directly with x_h, the effect of the smoothing error on the low resolution measurement has been removed, and the two quantities are completely comparable (*Rodgers and Connor*, 2003).

For comparison with the measured HCl and HNO_3 partial column amounts, a smoothed SLIMCAT model profile has been calculated to compare to each FTIR measurement, using Equation 7.1 and the averaging kernel and *a priori* profile relevant to that measurement. The averaging kernels used for this process are individual layer averaging kernels, as demonstrated in Figures 5.6 and 5.14. For the alternate days when SLIMCAT data was not saved, an un-smoothed SLIMCAT profile has been derived from linear interpolation of the previous and subsequent day's profiles, which has then been smoothed.

Following the smoothing of the model profiles, calculation of the 12 - 28 km partial column amounts has been performed from the profiles as explained in Section 7.2.1.

7.3 Winter 2003 - SLIMCAT and FTIR comparisons

7.3.1 Hydrogen chloride

The HCl FTIR partial column measurements are shown in Figure 7.2 with the processed SLIMCAT model results. Error bars shown are as calculated in Chapter 5, but exclude the

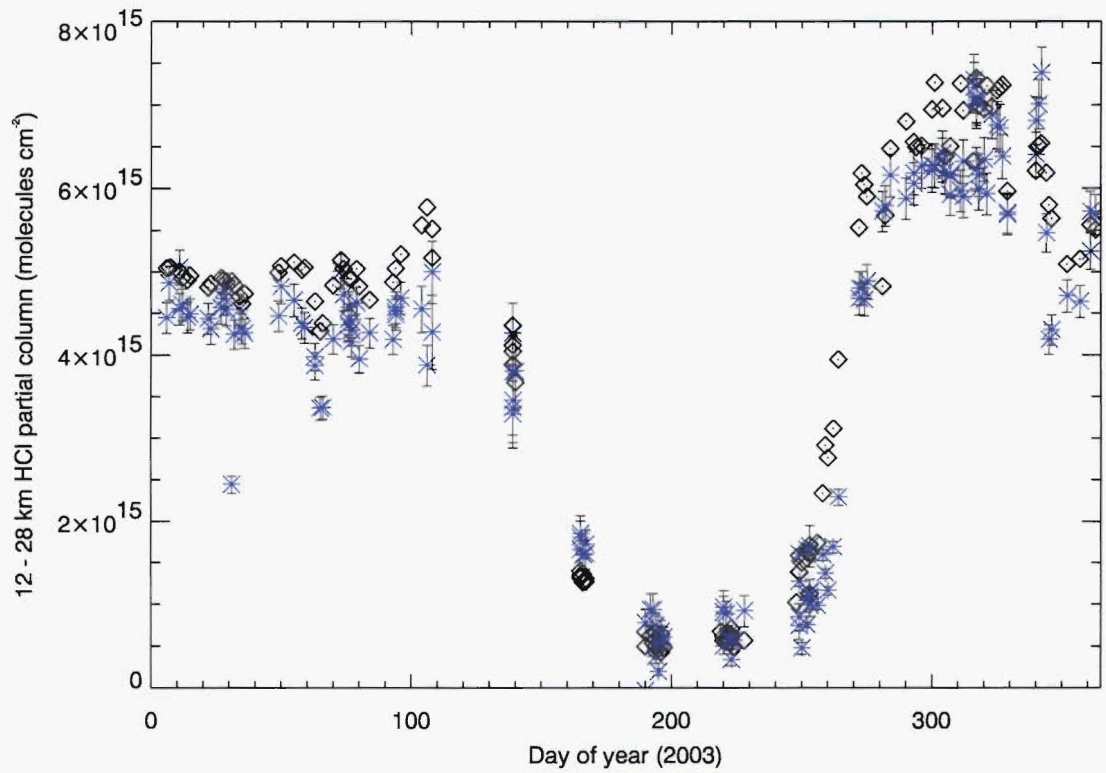

Figure 7.2: 12 - 28 km HCl partial column amounts from FTIR measurements and SLIMCAT model output. FTIR measurements are shown as blue crosses. Error bars are as determined in Section 5.1.5, excluding smoothing error as described in the text. SLIMCAT model output are shown as black diamonds and have been convolved with the averaging kernels to correspond to each FTIR measurement, as described in Section 7.2.2.

smoothing error contribution, which has been essentially eliminated by this comparison method.

Looking first at the pre-winter period, we see that while Figure 7.2 shows a generally good agreement between the measurements and the model, the total amount of HCl is slightly higher in the model than observed, with modelled partial column amounts just above the upper limit of the measurement error bars. This overestimate may be a result of an initial chlorine loading that was slightly higher than present in the atmosphere, or an incorrect partitioning of chlorine into its reservoir species during the summer months. The general trends in the HCl are, however, well captured by the model and the daily fluctuations caused by the movement of air from other regions, as detailed in Chapter 6.1.1, are in good agreement with the measurements.

The May modelled partial column amounts (days 139 and 140) show excellent agreement with the observations. The slight depletion of HCl during this month's FTIR observations has been discussed in Section 6.1.2, with heterogeneous reactions on background aerosols at temperatures below 200 K proposed as the explanation for the observed de-

pletion. This has obviously been well addressed by the meteorological analyses and heterogeneous chemistry incorporated in the model.

The June model output (days 165 - 167), show values that are slightly lower than the observations suggest. This is likely to be a result of the equilibrium treatment of PSCs in the model. Measurements of PSCs in the Antarctic show that the first clouds are typically liquid clouds (*Adriani et al.*, 2004; *Santee et al.*, 1998) which form at temperatures several degrees lower than the NAT equilibrium temperature (*Carslaw et al.*, 1994; *Tabazadeh et al.*, 1994a). Because the PSC formation in SLIMCAT is based on equilibrium conditions, PSCs are formed as soon as temperatures get below the NAT existence temperature (*Hanson and Mauersberger*, 1988), and thus PSC onset in the model is likely to occur sooner than in the atmosphere. As such, more HCl depletion can be expected in the model output than would be expected in the FTIR observations, as evident in Figure 7.2. Unfortunately, due to the timing of the full moon, the 2003 PSC formation has not been captured by the FTIR measurements and thus this hypothesis cannot be fully confirmed by the observations.

The July and August lunar measurements (days 190 - 196 and 220 - 228) show excellent agreement with the model output, with almost complete depletion of the HCl observed within the partial column. As demonstrated by *Ravishankara and Hanson* (1996), the HCl-depleting heterogeneous reactions occur rapidly on both solid and liquid clouds, so the equilibrium treatment of PSCs is sufficient to explain the widespread destruction of HCl during this part of the year.

Modelled and measured HCl partial column amounts during spring, however, do not show such good agreement. In the model data the HCl increases several days prior to what is observed. There are many factors that could influence the modelled recovery rate. As shown in Section 6.1.5, the extent of denitrification and ozone depletion both affect the partitioning between HCl and $ClONO_2$ and the recovery back into the reservoir species. As such, if the model fails to accurately predict the ozone loss or the denitrification then the HCl recovery will be affected. While this data provides no way of testing the extent of ozone depletion in the model, Section 7.3.2 addresses modelled HNO_3 and shows SLIMCAT to be overestimating the extent of denitrification. Hence it can be expected that the small change of active chlorine into $ClONO_2$ which was observed in the FTIR data prior to the HCl recovery (Figure 6.8) would not be observed in the model output, and all chlorine recovery would go immediately to HCl. This would result in HCl recovering more quickly in the model than in the atmosphere, in agreement with the trend shown in Figure 7.2.

Following the chlorine deactivation, HCl is again higher in the model than observed, consistent with model results prior to the HCl depletion. Fluctuations have typically been captured well, though on occasion spikes seen in the measurements as a result of sampling

air from outside the vortex are not captured in the model output. This is expected, since the movement of the vortex edge around the Arrival Heights site late in the spring is rapid, and the model output is at a coarse resolution both spatially and temporally.

7.3.2 Nitric acid

Figure 7.3 shows the FTIR 12 - 28 km HNO_3 partial column amounts with the SLIMCAT modelled partial column amounts. Saved SLIMCAT data is total (gas phase + condensed phase) nitric acid, and as such, in order to make comparisons during the winter when PSCs are present, the gas phase has been separated from the solid phase. In this comparison, this separation has been made using the NAT equilibrium condition and hence assumes that all nitric acid beyond saturation will condense into NAT (*Hanson and Mauersberger*, 1988). While this is a simplistic representation, it should approximately represent the modelled gas phase HNO_3. Total HNO_3 values have also been shown for comparison.

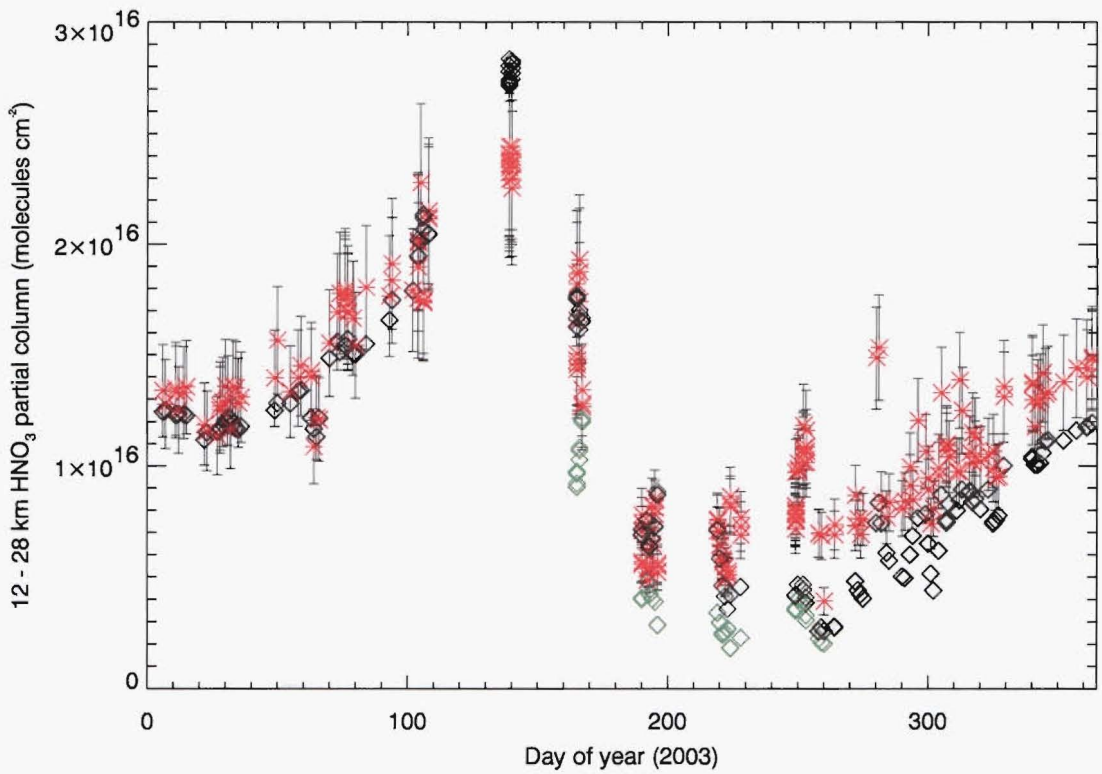

Figure 7.3: 12 - 28 km HNO_3 partial column amounts from FTIR measurements and SLIMCAT model output. FTIR measurements are shown as red crosses. Error bars are as determined in Section 5.2.5, excluding smoothing error as described in the text. SLIMCAT HNO_3 data are total (gas + condensed) amounts, shown as black diamonds. Gas only amounts, determined from the total amounts using the simple equilibrium equation of *Hanson and Mauersberger* (1988), are shown as green diamonds. The SLIMCAT profiles have been convolved with the averaging kernels to correspond to each FTIR measurement, as described in Section 7.2.2.

Again beginning with the pre-winter period, the modelled HNO_3 shows excellent agreement with the measurements. The modelled partial column amounts are consistently within the measurement error bars and track variations due to the motion of the airmass well. This suggests that the long-term transport and HNO_3 profiles have been accurately represented within the model.

Interestingly, the May modelled partial column amounts (days 139 and 140) are much higher than those observed by the FTIR. As the model HNO_3 is all in the gas phase, this cannot be explained by early formation of PSC particles, but must be attributable to either dynamical or photochemical processes. As the dynamical processes have been well captured in the summer and early autumn, it seems likely that the conversion of nitrogen trace gases (NO_y) to HNO_3 during 24-hour darkness has been overestimated. Comparisons of SLIMCAT model data to NO_y measurements made using the balloon-borne Michelson Interferometer for Passive Atmospheric Sounding (MIPAS) instrument during a warm Arctic winter showed SLIMCAT to underestimate N_2O_5, resulting in an overestimation of HNO_3 below 18 km (*Stowasser et al.*, 2002). This was attributed to an overestimation of the aerosol loading and subsequent overestimation of the reaction $N_2O_5 + H_2O \rightarrow 2\ HNO_3$. While there is nothing to confirm that this observation also applies to the current model comparison, it seems likely that the NO_y partitioning early in the winter has not yet been adequately characterized.

In June (days 165 - 167), PSC formation means that the nitric acid must be split into gas and condensed phases. It should be noted that lidar observations leading up to and including the June HNO_3 measurements showed the PSCs to mainly contain Type Ib (liquid) particles [Paola Massoli, Institute for Atmospheric Science and Climate, CNR, personal communication]. As such, the NAT equilibrium characterization that has been used to separate gas and condensed phases is not expected to give realistic gas phase results for this period, consistent with what is seen in Figure 7.3. The total HNO_3 from the model is, however, also much lower than would be expected from the observations. Again this discrepancy can be attributed to the equilibrium treatment of PSC formation. As described in Section 7.3.1, this treatment would tend to form NAT clouds as soon as temperatures dropped below the NAT existence threshold, rather than forming liquid clouds first, as is actually observed. The drop in the total HNO_3 since the May observations shows that significant sedimentation has occurred in the model, though in reality, denitrification is highly unlikely because the clouds are mostly liquid. The addition of large NAT particles in this model run is likely to have further contributed to the denitrification, as the larger particle size allows sedimentation of NAT particles to occur.

The July - September modelled partial column amounts also show too little nitric acid compared with the FTIR observations, which is unsurprising if the early winter denitrification has been overestimated. While the equilibrium treatment of PSCs is unlikely to

be particularly important at this time in the year, permanent loss of nitric acid by sedimentation is irreversible. While NAT rocks have been shown to occur in the Antarctic (*Adriani et al.*, 2004), the formation mechanism and the number density of these particles is not well known. As such, it is hardly surprising that their inclusion in a simple way has resulted in an overestimation of the denitrification in the region. The effect of NAT rocks on the amount of HNO_3 in the partial column will be further investigated in Chapter 8.

The overestimation of denitrification occurring in the partial column continues to affect the HNO_3 measurement and model comparison in the spring. While denitrification has clearly occurred in the atmosphere, as shown by the FTIR measurements in Section 6.1.5, the extent is less than that predicted by SLIMCAT. As such, the modelled amount of HNO_3 in the partial column remains too low. The modelled HNO_3 does, however, reach the bottom limit of the FTIR error bars by the year's end. Overestimation of denitrification has important ramifications for the deactivation of chlorine and hence the recovery of the ozone hole. As outlined in Sections 6.1.5 and 7.3.1, the extent of denitrification determines the partitioning between the HCl and $ClONO_2$ reservoirs. Conversion of active chlorine to $ClONO_2$ is much faster than conversion to HCl, influencing the length of time that ozone depletion is able to occur. Because there is still significant denitrification in the Antarctic atmosphere, however, this effect is likely to be much smaller than it would be for the warmer and more variable Arctic atmosphere.

Excursions outside the vortex are poorly captured by the model, as noted in Section 7.3.1. This effect is more pronounced in the HNO_3 partial column amounts than in the HCl partial column amounts, as a result of the large amount of nitric acid present in the collar region (*Roche et al.*, 1993b, 1994). The spike observed in the FTIR results in September, and investigated in Chapter 6, does not appear in the SLIMCAT output. While it is possible that this is a result of the extreme denitrification in the model, it is also plausible that the spike has been caused by a process not included or accurately quantified in the SLIMCAT model. This will be further investigated in Chapter 8.

7.4 Conclusions

In this chapter, 12 - 28 km partial column measurements of HCl and HNO_3 made from Arrival Heights have been compared with output from the SLIMCAT three-dimensional chemical transport model.

The model has been shown to capture the general trend in both gases well, including the variations due to air movement. This suggests that the long-range transport and profiles used for the SLIMCAT model are very good, though the amount of HCl in the partial column has been slightly overestimated. The modelled and measured HNO_3 partial column amounts in particular show excellent agreement during the summer and autumn.

For an accurate representation of winter and spring processes, however, the model is limited by its equilibrium treatment of polar stratospheric cloud formation. By assuming cloud formation at NAT equilibrium temperatures, PSCs are formed earlier than lidar and satellite observations suggest. This results in a slight overestimate of the HCl activation around the PSC onset time and denitrification occurring too early. This is further compounded by the inclusion of an additional large NAT rock particle size, which sediments rapidly from the stratosphere.

While the equilibrium PSC treatment does not affect the HCl through most of the winter, and measured and modelled results show good agreement during this time, an accurate representation of all the processes occurring during the winter period is vital. Denitrification in the model is overestimated throughout the winter, resulting in too little HNO_3 in the spring. This not only has potentially important consequences for the extent of ozone depletion, but is the likely cause of SLIMCAT failing to correctly capture the conversion of active chlorine into HCl at this time. Discussions with Martyn Chipperfield, however, suggest that a complete microphysical PSC treatment scheme for SLIMCAT is in development. This should result in better agreement between the modelled and measured partial column amounts of HCl and HNO_3 in the future.

A final comment should be made on the inclusion of large-sized NAT particles. While NAT rocks no doubt contribute significantly to the denitrification of the polar stratosphere, their treatment in the parameterization of atmospheric models requires care. As shown by this model run, denitrification resulting from rapid sedimentation of large NAT particles early in the winter can result in significant overestimation of denitrification later in the season. As an accurate representation of the extent of denitrification is necessary to correctly model springtime ozone depletion and chlorine partitioning, a more thorough understanding of these particles in the Antarctic stratosphere is clearly needed.

Chapter 8

Nitric Acid and Polar Stratospheric Cloud Coupling

Observations of gas phase nitric acid presented in Chapter 6 clearly showed the link between PSC formation and nitric acid removal. In this chapter, we go a step further and make a first ever coupling between ground-based lidar observations of PSCs, measured from McMurdo Station, and the FTIR measurements of nitric acid made from Arrival Heights during the polar winter. This work was a collaborative project with Paola Massoli, Institute for Atmospheric Science and Climate (ISAC), CNR, Rome.

The chapter will begin with a brief introduction to the lidar and the data sets used in the comparison, before addressing the links between nitric acid and PSC processes. Specifically, an empirical estimation of the rate of nitric acid uptake following PSC onset will be made, followed by an investigation of HNO_3 fluctuations in relation to PSC type. Finally a link between nitric acid spikes and large nitric acid-containing particles will be proposed.

8.1 Instrumentation

Concurrent measurements of HNO_3 and PSCs from ground-based instruments allow us to look at the processes that are occurring in a specific region, to a precision much greater than that possible using satellite images. This section provides an overview of the aerosol lidar which operates from McMurdo Station, located just 4 km from the FTIR instrument at Arrival Heights. A brief introduction to the HNO_3 and ancillary data sets used for this study, as well as a description of the spatial and temporal compatibility of the data sets, will also be presented.

8.1.1 The lidar

Light detection and ranging (lidar) systems are valuable tools in the study of the atmosphere and have been used in many forms for a number of years, both from the ground and from airborne platforms (e.g., *Browell et al.*, 1990; *Gobbi et al.*, 1991; *Adriani et al.*, 1992; *David et al.*, 1997). While there are a range of different types of lidar used to study aerosols, atmospheric composition, winds, and temperature, all lidars are similar in that a pulsed beam of light from a laser is emitted into the atmosphere and the signal returned

due to the scattering of the beam as it passes through the atmosphere is captured by a telescope and analysed.

The lidar used for this coupling is a ground-based aerosol lidar system owned by the Institute for Atmospheric Science and Climate (ISAC), CNR, Italy, and operated from McMurdo Station (Figure 8.1). The system uses an Nd:YAG laser with frequency doubling, which emits pulses of linearly polarized light at 532 nm. Each laser pulse is typically 9 ns in duration, repeated at a 10 Hz frequency, with an output energy of approximately 140 mJ/pulse. The returned signal is captured by a 41 cm Newtonian telescope with a 0.6 mrad field of view. The lidar has two channels which measure the returned signal, at polarizations either parallel or crossed with respect to the laser signal (*Gobbi et al.*, 1991; *Adriani et al.*, 1992, 2004).

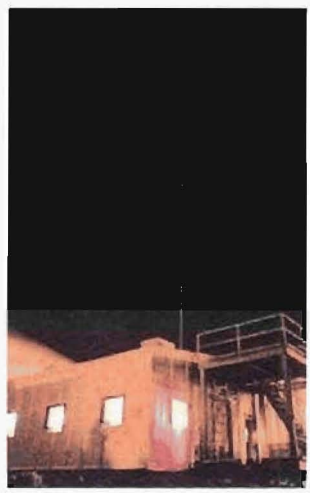

Figure 8.1: Aerosol lidar operating out of the Crary Laboratory, McMurdo Station.

The McMurdo lidar was installed in the spring of 1990 and has been run on clear weather days through the polar winter since 1993 (*Gobbi et al.*, 1991; *Adriani et al.*, 1992, 1995, 2004).

Lidar Output

There are two pieces of information determined from the returned signal which are used for the identification of PSCs. Both are determined as a function of altitude. The first is the particle backscattering ratio, BR, where

$$BR = \frac{\beta_p}{\beta_m} = R_T - 1 \tag{8.1}$$

β_p and β_m are the particle and molecular backscattering coefficients, and R_T is the total backscattering ratio of the atmosphere (*Adriani et al.*, 2004). Molecules in the atmosphere

scatter the light beam by Rayleigh scattering in a well defined way. Particles also scatter the light beam, hence changes in the backscattering ratio provide direct information on the vertical structure and optical density of the particle (cloud) layer.

The second important piece of information is the volume depolarization ratio, D_P, which in this study has been defined as

$$D_P = \frac{\beta_p^{\perp}}{\beta_p^{\parallel}} \tag{8.2}$$

where $\beta_p^{\perp}$ and $\beta_p^{\parallel}$ are the crossed and parallel polarization volume particle backscattering coefficients relative to the polarization of the light, as determined from the crossed and parallel polarization channels (*Adriani et al.*, 2004). Because spherical (liquid) particles are symmetric in shape, they do not change the polarization plane of the incident polar light. In contrast, aspherical (solid) particles do change the polarization, resulting in a scattered beam that is depolarized with respect to the incident one. As such, the depolarization ratio serves as a means of identifying the PSC type (*Browell et al.*, 1990; *Toon et al.*, 1990b).

Examples of the plots used for PSC identification, showing backscattering ratio and depolarization ratio as a function of altitude, are given for a solid (Type Ia) and a liquid (Type Ib) cloud in Figure 8.2.

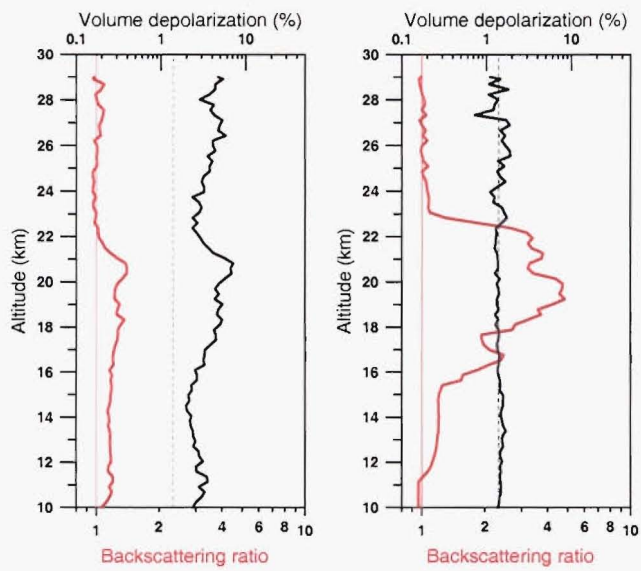

Figure 8.2: Typical solid (Type Ia, left) and liquid (Type Ib, right) PSCs. Solid clouds show an increase in depolarization (black) simultaneous to an increase in backscattering ratio (red), while liquid clouds show a large backscatter ratio but no change in the depolarization. Dotted lines indicate the background depolarization which would be seen in the absence of clouds. Observations were made on August 22nd (solid) and June 15th (liquid), 2003.

8.1.2 The nitric acid measurements

Lunar 12 - 28 km HNO_3 partial column measurements, as presented in Chapters 4 - 6, have been used for this study. Measurements from the 1998 - 2002 Antarctic winters have also been included in order to increase the number of coincidences between lidar and FTIR observations. These FTIR observations were presented in *Wood et al.* (2004). Total column measurements, as presented in *Wood et al.* (2004), are comparable to the partial column measurements by adding approximately 9×10^{14} molecules cm^{-2} to the partial column amount, as shown by the total versus partial column plot in Figure 8.3. This simple conversion is a result of the HNO_3 stratospheric distribution being nearly entirely within the 12 - 28 km partial column, as shown in Figure 5.12, combined with the lack of sensitivity of the retrieval to regions outside this altitude range, as shown by the averaging kernels in Figure 5.14. The correction factor is composed nearly entirely of the HNO_3 molecules below 12 km and above 28 km, as determined from the *a priori* profile.

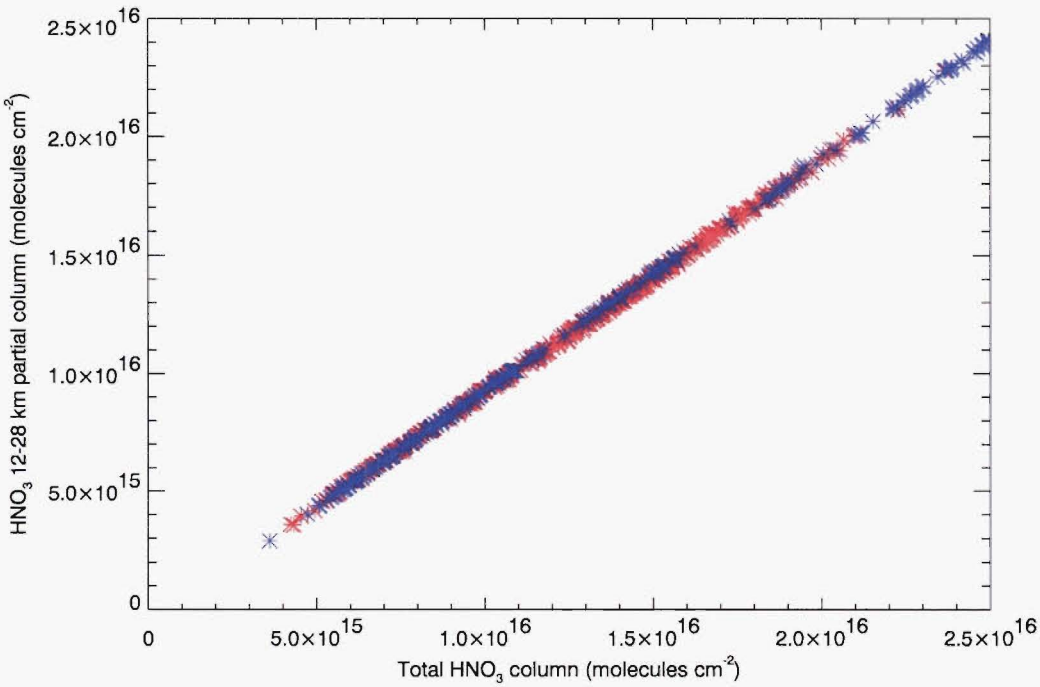

Figure 8.3: Total versus 12 - 28 km partial column HNO_3 measurements. Solar measurements are shown in red and lunar in blue. The correlation coefficient between the total and partial column amounts is 0.9996.

HNO_3 measurements are largely missing from 2000 due to instrumental problems. Solar observations, as described in Chapters 4 - 6 and in *Wood et al.* (2004), have also been used in some end-of-season case studies.

8.1.3 Spatial and temporal compatibility

While the lidar at McMurdo Station and the FTIR at Arrival Heights are physically located only 4 km apart (Figure 3.6), there are some limitations on the spatial and temporal coincidence of the data sets. As outlined in Chapter 4, nitric acid measurements were made for approximately one week around the full moon along a slanted optical path in the direction of the moon. While the lidar observations also required clear weather, they could be carried out at any time of the day or month and would always sample the airmass directly overhead. In the stratospheric altitude range of interest, the horizontal separation between these airmasses ranges from approximately 10 to 25 km, depending on the altitude and the observational angle. The temporal difference may also increase this separation by an amount dependant on the stratospheric weather conditions at the time. Satellite observations of PSCs in the Antarctic show polar stratospheric clouds to be spread over large areas of the continent (*McCormick et al.*, 1989; *Poole and Pitts*, 1994) and to be mostly caused by long periods of sustained cold conditions (*Tabazadeh and Toon*, 1996; *Tabazadeh et al.*, 2000). Likewise, lidar observations show trends in the PSC type and location to typically vary slowly, over a period of days [Paola Massoli, Institute for Atmospheric Science and Climate, CNR, personal communication]. *Santee et al.* (1998) use the Microwave Limb Sounder data to study PSCs, using a range of sources to show that the horizontal extent of PSCs in the Antarctic is sufficiently large that the assumption of constant PSCs throughout the MLS field of view ($\sim$ 400×100×5 km) is justified. As such, the comparatively small spatial differences between the airmasses sampled by the lidar and the FTIR are unlikely to significantly affect our conclusions.

8.1.4 Ancillary data

In addition to the lidar and FTIR measurements, the temperature and potential vorticity data sets introduced in Chapter 4 have been used to relate the observations to processes occurring in the polar stratospheric winter. Additionally, back-trajectory temperature analyses have been used to fill some holes in the lidar data set. These are from the Goddard Auto-mailer system introduced in Chapter 6 (*Schoeberl and Sparling*, 1994; *Lait et al.*, 2004) and have generally been calculated over six days on the 465 K ($\sim$ 20 km) potential temperature surface, as determined in *Adriani et al.* (2004). Radio soundings made daily from McMurdo Station have also been used for some T_{NAT} calculations [Paola Massoli, Institute for Atmospheric Science and Climate, CNR, personal communication].

8.2 Methodology

This work has been carried out by directly comparing periods between 1998 and 2003 when both nitric acid and PSC observations were made. Thus the work is, to some extent, a series of case studies which are used to address several aspects of the winter polar processes. Each aspect is addressed individually in the sections to follow, complete with several case studies supporting the conclusions that have been reached. A final summary of all of these results is presented in Section 8.4.

8.3 Results and discussion

8.3.1 PSC onset

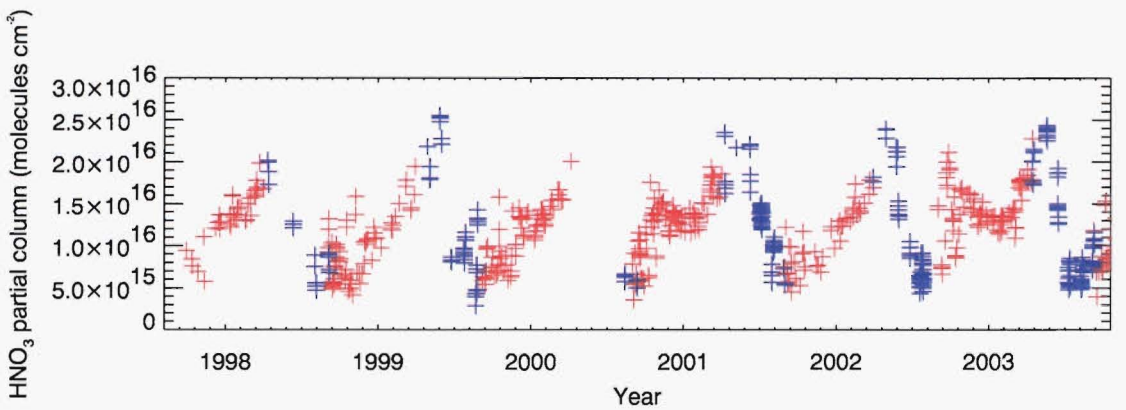

Figure 8.4: 12-28 km partial column measurements of nitric acid. Lunar measurements are shown in blue and solar in red, for ease of comparison. Error bars have been omitted for clarity, but are ~15.5%, as indicated in Section 5.2.5.

Figure 8.4 shows a time series of HNO_3 12 - 28 km partial column amounts from 1998 to 2003. A rapid depletion is seen in the time series half way through each year, corresponding to the time when gas phase nitric acid is condensed or absorbed into polar stratospheric cloud particles. While the exact day of the onset varies from year to year, this pattern is remarkably consistent. This suggests that a semi-empirical determination of the speed of nitric acid uptake relative to the date of PSC onset can be made.

Determining the date of PSC onset

The date of PSC onset over McMurdo Station and Arrival Heights for each year has been determined using lidar measurements. In 1998, 1999, and 2001, unfavourable weather meant that lidar observations were not available on the days preceding the first observed cloud. As such, thermal histories of the airmasses over McMurdo were determined on these

days using the Goddard Auto-mailer. If the thermal history corresponded to conditions when PSCs could be expected, then the date of PSC onset was shifted back accordingly. PSCs have been considered likely when the synoptic back-trajectory temperatures dropped below T_{STS} and remained below T_{NAT} for three to four days (*Tabazadeh et al.*, 1994b; *Larsen et al.*, 1997; *Tabazadeh et al.*, 2000; *Adriani et al.*, 2004). Back-trajectory analyses performed for days when lidar measurements were available showed this interpretation to be consistent with the observations. The thermal histories were consistent with the formation of liquid clouds, showing smoothly decreasing temperatures to below T_{STS} (*Larsen et al.*, 1997). This is in agreement with lidar and satellite measurements showing the first cloud to typically be liquid (*Santee et al.*, 1998; *Tabazadeh et al.*, 2000; *Adriani et al.*, 2004). The PSC onset dates determined for each year are shown in Table 8.1.

Year	Onset Date	Day Number
1998	6th of June	157
1999	3rd of June	154
2001	10th of June	161
2002	29th of May	149
2003	2nd of June	153

Table 8.1: PSC onset dates, as determined from lidar observations and back-trajectory analyses. 2000 has been excluded due to the lack of HNO_3 measurements in that year.

Quantifying the speed of nitric acid uptake

Figure 8.5 shows the partial column nitric acid amounts, relative to the PSC onset date. There are several observations that can be made from this figure.

First, there is a small reduction in the gas phase HNO_3 partial column amount prior to the determined PSC onset date. This is shown clearly in both the 1999 and the 2002 measurements. While this may be a result of a bias in the deduction of the PSC onset date, measurements in the Arctic winter have also observed fluctuations in the amount of nitric acid when lidar observations do not show PSC formation (*Notholt et al.*, 1997b), and the cause of these fluctuations remains uncertain. Possibilities include: PSCs that were present in the region but not in the lidar beam; PSCs of sufficiently small surface area that they were not observed by the lidar [Paola Massoli, Institute for Atmospheric Science and Climate, CNR, personal communication]; mesoscale temperature fluctuations as a result of lee-waves off the Trans-Antarctic mountains, which would not be observed in the synoptic scale back-trajectories but may have resulted in PSC formation (*Meilinger et al.*, 1995; *Murphy and Gary*, 1995; *Adriani et al.*, 2004); or perhaps advection of air

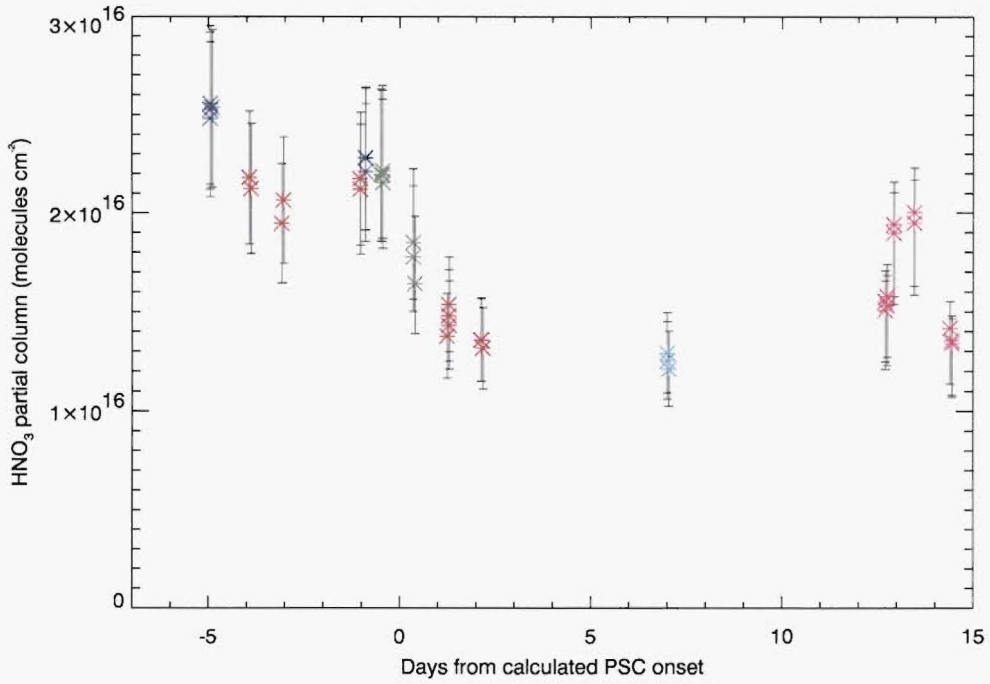

Figure 8.5: Gas phase HNO_3 relative to the date of PSC onset. Colours indicate measurements made in 1998 (cyan), 1999 (blue), 2001 (green), 2002 (red) and 2003 (pink). 2003 measurements are outliers as a result of temperatures returning above PSC formation temperatures after the initial onset, as detailed in Section 6.1.3.

from colder regions, where some PSC formation and sedimentation events had already occurred (*Toon et al.*, 1992).

Second, the amount of nitric acid drops very quickly with PSC onset. Regardless of the depletion occurring before the onset, measurements one day prior to the determined onset show a remarkably consistent HNO_3 partial column amount of $\sim 2.2 \times 10^{16}$ molecules cm^{-2} (1999, 2001 and 2002). This amount was used as an initial value for the estimation of the rate of depletion. Measurements from 2001 made on the day of onset show an average value of $\sim 1.7 \times 10^{16}$ molecules cm^{-2}, which is equivalent to a depletion in the gas phase nitric acid column of 23%. A day later, measurements from 2002 show a column value of $\sim 1.4 \times 10^{16}$ molecules cm^{-2}, corresponding to a further depletion of 14% of the pre-PSC column amount. A day after that, a column value of $\sim 1.3 \times 10^{16}$ molecules cm^{-2}, or a further 4% depletion, is observed. In total, over three days 41% of the 12 - 28 km partial column gas phase nitric acid has been converted into polar stratospheric clouds. An alternative calculation, based on a pre-PSC onset column amount of $\sim 2.5 \times 10^{16}$ molecules cm^{-2} five days prior to PSC onset, has 45% depletion of the total column amount occurring in a week.

We can understand the effect this is having on the atmosphere by looking at the

typical stratospheric distribution of HNO_3 (Figure 5.12). The first clouds observed by the lidar in any year are typically liquid clouds between 15 and 24 km in height (*Adriani et al.*, 2004), consistent with observations from MLS (*Santee et al.*, 1998; *Tabazadeh et al.*, 2000). Assuming that all of the gas phase nitric acid depletion is occurring within this region, approximately half of the 15 - 24 km nitric acid must be condensed or absorbed into clouds over the three day period in order to explain the magnitude of the depletion. The data sequence suggests that the first day of PSC formation has the most dramatic effect on the gas phase HNO_3, with subsequent days having less impact on HNO_3 removal. This is in agreement with the microphysics of liquid clouds, which form rapidly by the absorption of gas phase HNO_3 and H_2O onto aqueous H_2SO_4 aerosols (*Tabazadeh et al.*, 1994a; *Carslaw et al.*, 1995; *Luo et al.*, 1995) but reach a maximum size of around 0.5 μm (*Tabazadeh et al.*, 1994b), limiting the amount of HNO_3 that will be absorbed. This is observed in Figure 8.5 as a slowing down and levelling out of the partial column amount at around 1.2×10^{16} molecules cm^{-2}. Solid clouds are not limited in the size they can reach or the amount of HNO_3 they can absorb (though this is limited by the available HNO_3 and H_2O). They do, however, grow more slowly and require longer periods of time at cold temperatures in order to form (*Larsen et al.*, 1997; *Tabazadeh et al.*, 2000). As such, the effect of solid cloud formation is not observed in the days immediately following PSC onset, but contributes to the further decrease in the partial column amount later in the season.

A final observation that can be made from Figure 8.5 relates to the 2003 HNO_3 measurements. As shown in Chapter 6, the temperature following the initial PSC onset in 2003 fluctuated around PSC formation temperatures (Figure 6.5). This resulted in the formation and evaporation of liquid PSCs several times during this period, with clouds observed on days 153 and 162 and no clouds on days 155 and 156. Temperatures were not stable enough to meet the PSC lifetime conditions for solid Type Ia NAT cloud formation (*Tabazadeh et al.*, 2000), and hence while denoxification might be observed, no particle sedimentation or denitrification was likely to occur. As such, all nitric acid was returned to the gas phase when the temperatures warmed. This essentially resulted in PSC onset being repeated several times. The column amounts observed 13 days following the quoted PSC onset, as shown in Figure 8.5, are more comparable with those which would be expected 3 days from the original onset, consistent with the most recent re-onset on day 162.

The 2003 nitric acid observations in Figure 8.5 are also seen to fluctuate considerably, as introduced in Chapter 6. This will be addressed in the next section.

8.3.2 PSC type and fluctuations in the gas phase nitric acid

For similar atmospheric conditions, models have shown NAT (solid) particles to be more efficient at depleting gas phase nitric acid than STS (liquid) droplets (*Tabazadeh et al.*, 1994b; *Santee et al.*, 1998). As such, the detection of solid clouds should be accompanied by lower levels of gas phase nitric acid than would be seen with the detection of liquid clouds. Additionally, heterogeneous reactions occurring on STS particles result in the formation of HNO_3, which further increases the observed nitric acid when the particles evaporate (*Riviere et al.*, 2003).

In this section, measurements made during the June 2003 full moon are used as a case study to look for observational evidence of these processes. Measurements were made with both the FTIR and lidar several times through the course of three days, June 14th to 16th, providing a data set which was temporally and atmospherically comparable and which captured several changes in the polar stratospheric cloud distribution and type. Additionally, measurements made in August 1999 are presented, outlining the effect of temperature changes low in the partial column region as well as providing evidence for the effect of PSC type on the gas phase nitric acid amount.

June 2003

Figure 8.6 shows the June 2003 nitric acid partial column amounts as given in Figure 6.1. Superimposed on this plot are the lidar observations made during the same period. These identify the type and location of the clouds above McMurdo Station. While the plots are small, the general trend through the time period is observable, and solid and liquid clouds have been labelled for clarity.

From Figure 8.6 we see that prior to the first FTIR observation on day 165 (June 14th) there were PSCs already present. These were observed by the lidar around 10 am and were shown to be in layers of solid clouds (13 - 16 km, 19 - 21 km and 23 - 24 km) and liquid clouds (16 - 19 km and 21 - 23 km). The first gas phase nitric acid measurements, made several hours after the lidar observations, show the partial column to have experienced considerable nitric acid depletion from the pre-PSC values evident in Figures 6.1 and 8.5, with partial column amounts of $\sim 1.4 \times 10^{16}$ molecules cm^{-2}.

Three hours after the first FTIR observations, lidar observations were made again. These showed the solid clouds to be nearly completely gone, with two liquid clouds dominating the region from 15 to 24 km. The subsequent FTIR observations, made at $\sim$ 8 pm, show a correspondingly large increase in the nitric acid partial column amount, with values increasing nearly 30% and reaching $\sim 1.8 \times 10^{16}$ molecules cm^{-2}. While the error bars on the graph suggest that these values are within the uncertainty of the previous measurements, it should be remembered that most of the uncertainty in the HNO_3 partial

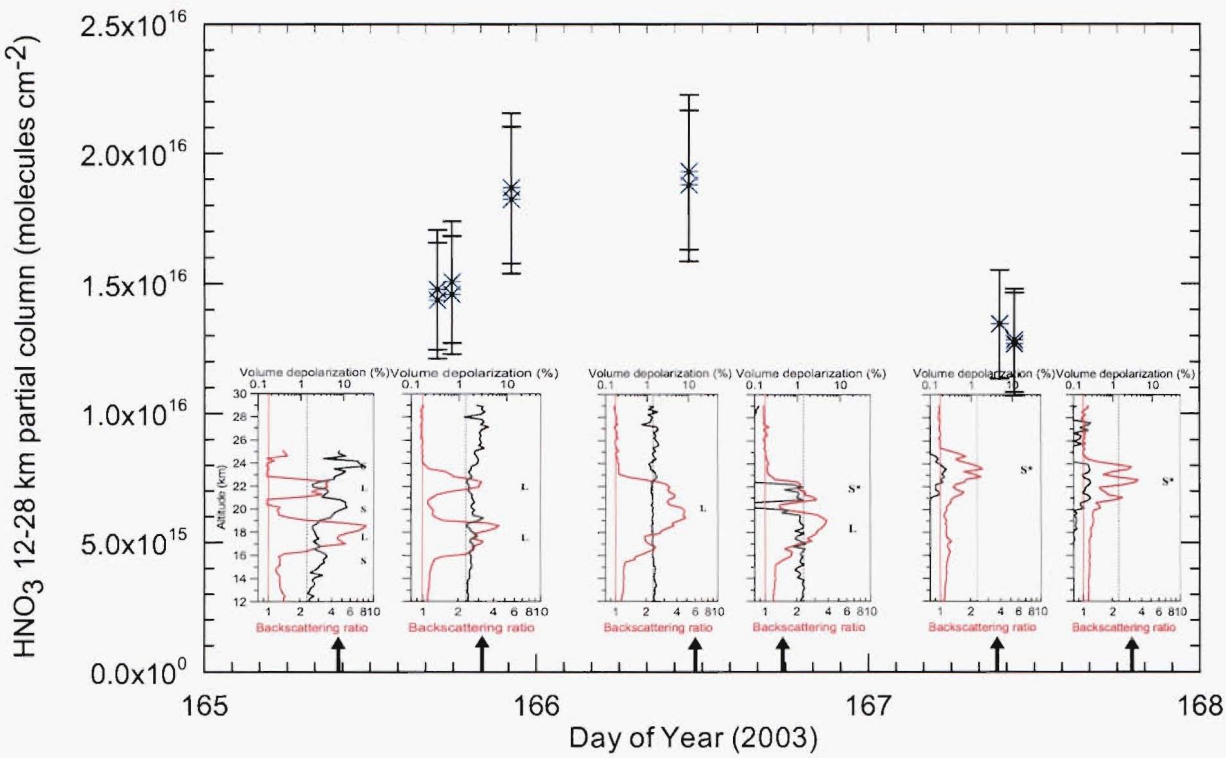

Figure 8.6: 12-28 km partial column measurements of nitric acid made in June, shown with PSC observations made during the same period. Arrows indicate the approximate time of the lidar observations. Liquid and solid clouds have been identified with an L or an S. S* indicates identification based on measurements with abnormal depolarization ratios, caused by an instrument problem.

column amount was a result of the line parameters, which provide a systematic bias (Section 5.2.5). For the purpose of trend analysis, as presented in this case, the uncertainties can be more rightly thought of as 6%, or approximately 0.1×10^{16} molecules cm^{-2}.

Lidar observations were also made the following morning (day 166) and showed that the two layered liquid cloud had evolved into a single large cloud extending from 15 to 25 km. The constant depolarization ratio clearly shows that there were no solid clouds in the region. Nitric acid measurements made at this time continue to support predictions of higher column amounts in the presence of liquid clouds than solid ones, with values marginally higher than those recorded the previous day.

Later on day 166, and during the morning of day 167, lidar observations showed the liquid cloud to be evolving first into a layered solid and liquid cloud, then into a large, purely solid cloud between 20 and 25 km. FTIR measurements made on the morning of day 167 were almost simultaneous with the lidar observations and show a 27% decrease in the nitric acid partial column amount to $\sim 1.3 \times 10^{16}$ molecules cm^{-2}. Unfortunately no further FTIR observations were made, so the investigation could not be continued. Nonetheless, the decrease in the nitric acid observed in the morning can be clearly attributed to the large solid cloud, which remained over the station throughout the day and

was observed by subsequent lidar measurements.

These observations have been made over a very short time period, where the temporal coincidence between FTIR and lidar observations is good, the temperature profiles remain fairly constant, and the airmasses being sampled by the two instruments are likely to be highly correlated. The measured fluctuations in the nitric acid partial column amounts show good agreement with the trends observed in the polar stratospheric clouds, matching predictions of more gas phase nitric acid in the presence of liquid clouds than in the presence of solid ones.

August 1999

Lidar and FTIR measurements were made during the August full moon period in 1999, between days 234 and 240 (August 22nd - 28th). These results are presented in Figure 8.7. Because this period is longer than the June case study presented above, atmospheric conditions do not remain stable for the period and temperature variations become important. *Santee et al.* (1999) attribute the fluctuations in the HNO_3 observed in MLS data late in the winter to small changes in the temperature. As such, the temperatures relative to T_{NAT} for each altitude have been determined daily using HNO_3 values consistent with the FTIR measurements, POAM III water vapour data, and pressure and temperature data from daily radio-soundings made from McMurdo station [Paola Massoli, Institute for Atmospheric Science and Climate, CNR, personal communication]. Regions warmer than the NAT existence temperature have been highlighted as shaded regions in the PSC plots. By August, PSCs are present at altitudes comparable with the bottom of the partial column, and subsidence means that temperature changes low in the partial column can be more significant than earlier in the season.

From Figure 8.7, we see that for the first days of the period, on days 234, 236 and 237 (August 22nd, 24th and 25th), polar stratospheric clouds were present from the bottom of the partial column to approximately 24 km. Solid clouds were present over most of this region, with a small liquid cloud also visible between 17 and 18 km on day 234. By this time of the year, polar stratospheric clouds had been present for some time and it is highly likely that some denitrification within the partial column had occurred. While denitrification itself cannot be observed in these measurements, the nitric acid plot in Figure 8.7 shows the region to contain very little gas phase HNO_3, with values of $\sim 5 \times 10^{15}$ molecules cm^{-2} observed in the partial column on days 235 and 237. This is consistent with expectations, as the temperature throughout this period was sufficiently cold that the entire partial column was below T_{NAT}, and as such, almost all nitric acid was likely to be in a condensed form.

On day 238, the temperature increased markedly, and all regions of the partial column

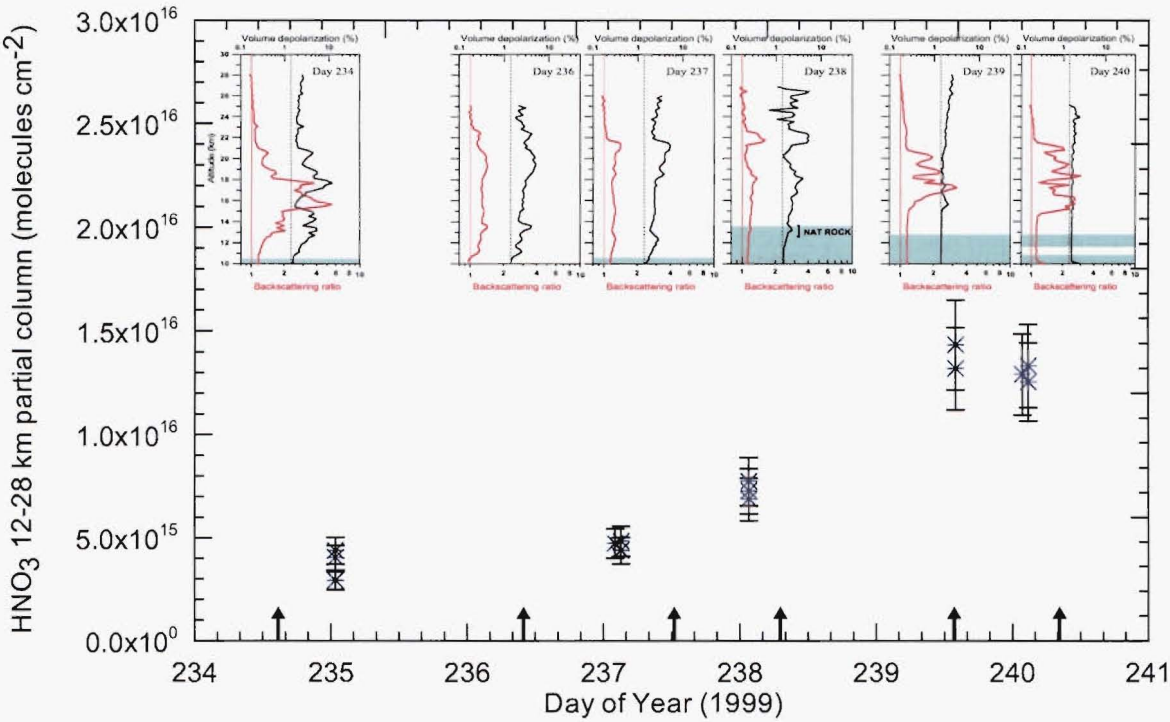

Figure 8.7: 12-28 km partial column measurements of nitric acid made in August, shown with PSC observations made during the same period. Blue shaded regions in the PSC plots indicate where temperatures are above the NAT existence temperature.

below 13.6 km were at temperatures above T_{NAT}. While the evaporation of the PSC particles is complex and depends on the particle size, the HNO_3/H_2O ratio or thickness of the NAT coating, and the vapour pressure of the air immediately above the particles, as well as on the temperature (*Tolbert and Middlebrook*, 1990; *Peter et al.*, 1994), the smallest particles are expected to evaporate rapidly above T_{NAT} (*Larsen*, 2000). Correspondingly, polar stratospheric clouds in the lidar signal disappeared below 13 km. Additionally, NAT rocks, which have a smaller number density but much bigger radius than typical NAT clouds (*Fahey et al.*, 2001), were observed in the lidar signal. This indicates that the smaller particles, which typically mask NAT rock signals due to their larger number density, had evaporated, exposing the NAT rocks. Correspondingly, the nitric acid partial column amount is seen to increase by around 30%, reaching values of $\sim 7 \times 10^{15}$ molecules cm^{-2}. Polar stratospheric clouds remained in the partial column where temperatures were below T_{NAT} and remained consistent in form and type with those observed prior to the temperature increase. As such, the increase in the nitric acid partial column amount can be firmly attributed to the temperature fluctuation, in agreement with the suggested explanation of *Santee et al.* (1999).

On days 239 and 240, however, nitric acid partial column amounts are seen to increase even more significantly, with the gas phase amount doubling to reach values of $\sim 1.4 \times$

10^{16} molecules cm^{-2}. This cannot be sufficiently explained by temperature fluctuations, as the region above T_{NAT} is no larger than on the previous day. Instead we propose that the increase may be caused by a change in the type of PSC in the airmass. As observed in June 2003, a change from solid to liquid type clouds can result in significant differences in the nitric acid column amount. Lidar observations on day 239 show the solid PSCs observed over the previous days to have been replaced by a single large liquid cloud stretching from 16 - 21 km. The almost flat depolarization ratio shows there to be very little solid cloud in the region. Lidar observations on day 340 likewise show liquid clouds from 14 - 22 km, with no solid cloud present, in agreement with this theory.

While a detailed microphysical model incorporating the formation and evaporation processes for solid and liquid PSCs would be required to completely characterize these results, the observational evidence suggests that while some fluctuations in the HNO_3 amounts can be attributed to temperature, as suggested by *Santee et al.* (1999), fluctuations in the gas phase nitric acid may also be attributable to the PSC type.

8.3.3 Spring spikes - a link with NAT rocks?

As introduced in Chapter 6, the nitric acid measurements made in September 2003 showed an unusual spike occurring on days 250 - 253, in the 10 - 16 km altitude range (Section 6.2.2). Looking at the spring period in other years, spikes were also found in August 1999 (as detailed above) and in September 1998. In all three cases these spikes were followed by days of significantly lower nitric acid amounts. Measurements made from day 230 until day 265 are shown for these three years in Figure 8.8.

There are several factors that could contribute to the observed spikes. Temperature increases low in the partial column have already been linked with the 2003 spike (Section 6.2.1) and with the 1999 spike (Section 8.3.2). Additionally, the phase of the clouds observed in the partial column has been shown to contribute to changes in the observed nitric acid. These observations do not, however, explain where the nitric acid came from. In order for such large spikes to appear, polar stratospheric clouds need to evaporate low in the column, yet both the FTIR measurements and the lidar data suggest extensive denitrification was present. While some PSCs were observed in the lidar measurements on days prior to the spikes, these were small, and there were days when PSCs were not observed, even though conditions were suitable for their existence. The SLIMCAT modelled HNO_3, as given in Chapter 7, also suggested significant denitrification in the spring partial column amounts. In addition, the model output failed to capture the 2003 spike, even though temperature fields and both solid and liquid clouds were included in the model.

As such, the question should be asked – what is responsible for providing the nitric

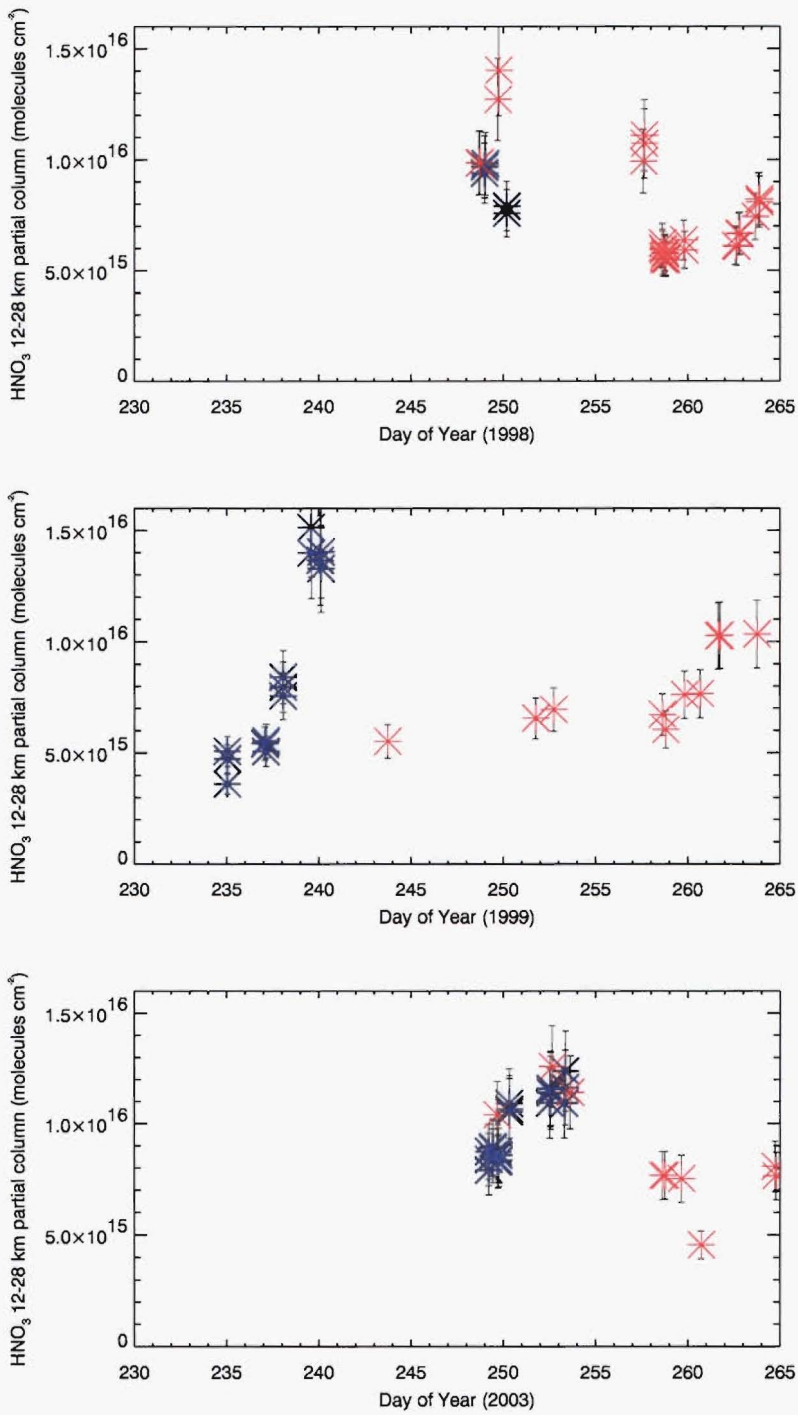

Figure 8.8: 12-28 km partial column measurements of nitric acid made in the spring of 1998, 1999 and 2003, showing spikes.

acid observed in the spring spikes? While a detailed microphysical model incorporating transport, PSC formation, evaporation, and phase would be needed to conclusively investigate this question, we suggest that the spikes observed in the nitric acid partial column amounts may be a result of the evaporation of NAT rocks.

In situ observations during the 1999/2000 Arctic winter showed a small number density of large (10 - 20 μm) nitric acid containing particles to exist in the winter stratosphere (*Fahey et al.*, 2001). These large particles have the potential to transport significant amounts of nitric acid out of the stratosphere, with estimates of a flux of 5×10^9 molecules cm^{-3} km day^{-1} made at 16 km (*Fahey et al.*, 2001). Lidar observations in the Antarctic have since shown NAT rocks to also be occurring in the southern winter (*Adriani et al.*, 2004). While the formation mechanism for NAT rocks is still not well known, a mechanism known as the 'mother cloud' theory has been proposed by *Fueglistaler et al.* (2002). In this theory, NAT rocks are formed within solid NAT clouds, with their growth and sedimentation governed by a region of HNO_3 supersaturation beneath the cloud. The number density of the NAT rocks is a result of rapid acceleration during growth and is also limited by the HNO_3 depletion of growing rocks beneath the cloud (*Fueglistaler et al.*, 2002). Because the particles are large and must form at high altitudes in order to reach the observed sizes (*Fahey et al.*, 2001), gravitational sedimentation, long-range transport and wind shear result in the rocks being transported away from the mother cloud. As such, NAT rocks may be responsible for denitrification observed far from their origin. While the larger size of the particles slows their evaporation relative to smaller particles, NAT rocks can be expected to begin evaporation at temperatures above T_{NAT}, resulting in regions of nitrification (*Fahey et al.*, 2001).

Lidar measurements made in the days preceding the observed spring spikes were shown to contain signatures consistent with NAT rocks. These have been identified as regions with a high depolarization ratio (aerosol depolarization ratio > 30%, corresponding to a volume depolarization ratio (D_p) $\approx$ 3 - 5%) and a very low backscattering ratio (BR = 0.25) (*Adriani et al.*, 2004). Each of the spikes and the accompanying lidar measurements will be investigated in the sections that follow.

September 2003

As mentioned in Chapter 6, the 2003 winter was particularly cold, and solid clouds were observed throughout the partial column almost constantly from June until August. The first NAT rock signatures were detected in solid NAT clouds at a height of around 20 km on days 221, 227, 230 and 233, consistent with the mother cloud theory of formation of NAT rocks within solid clouds (*Adriani et al.*, 2004). From day 237, the altitude region containing PSCs began to shrink, and on several occasions leading up to the full moon

measurements the lidar observations showed no PSCs at all, even though temperatures remained below T_{NAT}. This suggests that significant denitrification had occurred in the region. Without large number density solid clouds to mask them, NAT rocks were observed nearly every day. Measurements showed them to be moving from altitudes of approximately 22 km on day 236 to just 13 km on days 244 and 245, consistent with expectations of rapid sedimentation of the NAT rock particles.

Unfortunately, due to instrument problems, no lidar observations were made on days 246 - 251. FTIR observations on day 249 showed low values of nitric acid, consistent with either denitrification or the remaining nitric acid in the column being in a non-gas phase. Measurements on days 250, 252 and 253, however, showed much higher values (Figure 8.8). As shown in Chapter 6, temperatures at this time increased above the NAT condensation threshold low in the partial column region, and as such, any PSCs at this altitude would be expected to evaporate. While lidar data is absent from the onset of these measurements, the previous days' observations suggested that the region had been mostly denitrified, resulting in few clouds being present to evaporate. As such, it seems likely that the NAT rocks observed in the lidar data were responsible for transporting nitric acid from other regions into the partial column, where their evaporation resulted in the observed spike in the gas phase HNO_3. Lidar measurements made on day 252 showed a small liquid cloud to be forming at 14 - 15 km, with a similarly small solid cloud observed even lower the following day. This suggests that the released HNO_3 is quickly converted to PSCs when temperatures are cold enough, and as such, may be responsible for prolonging the activation of chlorine. Subsequent low values observed in the nitric acid partial column amounts indicate that NAT rock induced nitrification is a localized effect, with the expected denitrification prevailing in most of the sampled airmasses.

September 1998

Figure 8.9 shows lidar observations made on days 248 - 250 in 1998. The NAT rock signatures are particularly clear in these examples.

As in 2003, 1998 was a cold year, and few PSCs had been observed in the partial column for some days prior to these observations, consistent with significant denitrification having occurred. The FTIR sun and moon measurements on day 248, however, showed HNO_3 partial column amounts of $\sim 9.4 \times 10^{15}$ molecules cm^{-2} (Figure 8.8), significantly higher than those observed in the earlier winter observations. NAT rocks on this day were observed in the partial column between 12 and 13 km. At this altitude, temperatures were close to T_{NAT}, as shown in Figure 8.9, thus it seems likely that this increase can be attributed to the evaporation of the rocks. The following day, temperatures low in the partial column increased significantly, and a corresponding jump in the nitric acid was

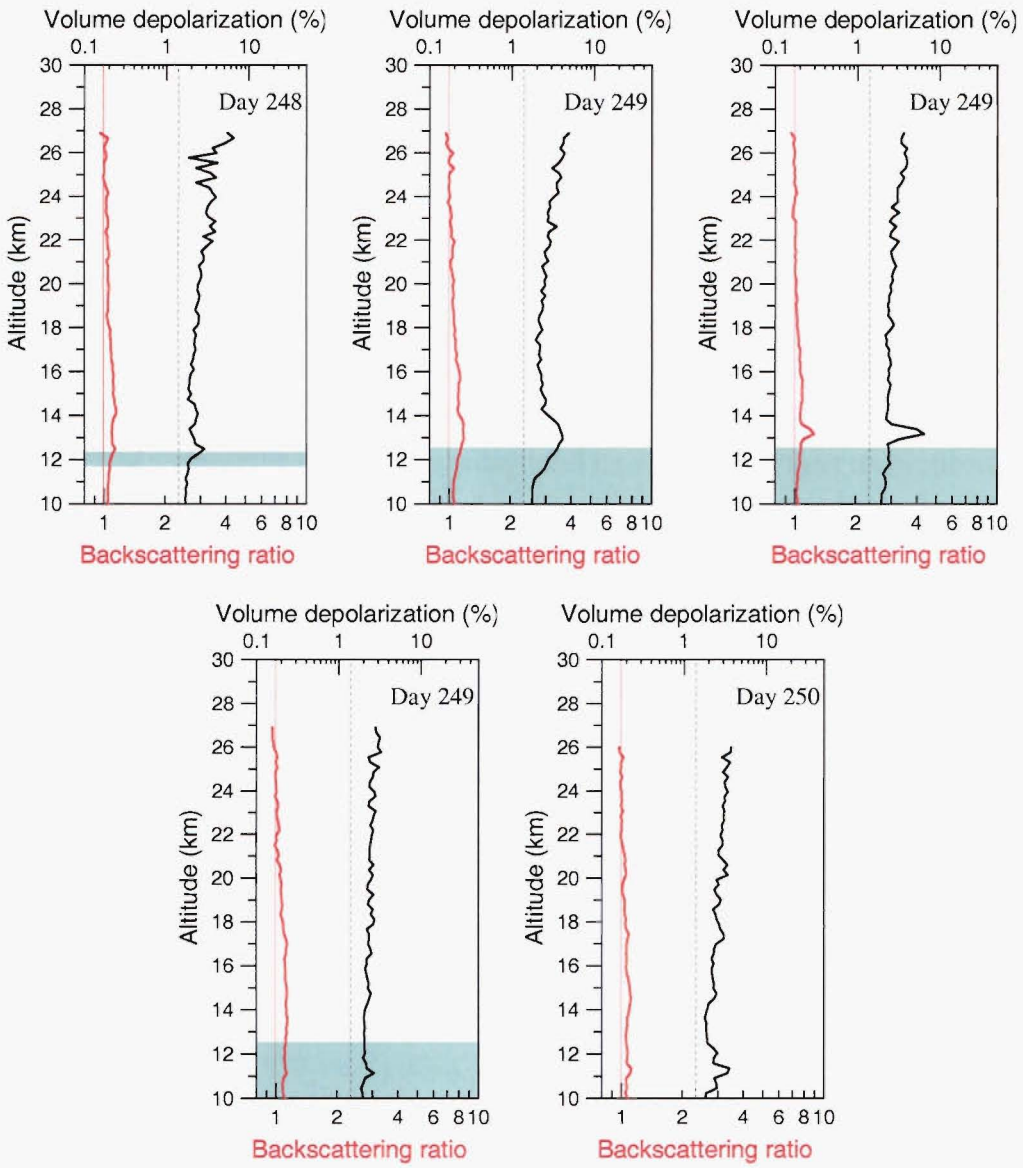

Figure 8.9: Lidar observations made on days 248 - 250 (September 5th - 7th) 1998. NAT rocks have been identified on days 248 and 250 and in the first and third observations of day 249. The middle observation shows a small solid cloud just above the region of PSC evaporation. Blue shaded regions in the PSC plots indicate where temperatures are above the NAT existence temperature.

observed, with solar HNO_3 measurements reaching values of $\sim 1.3 \times 10^{16}$ molecules cm^{-2} near midday (Figure 8.8). Lidar observations were made in the morning (first plot) and the early and late evening (second and third plots) on day 249. NAT rocks were observed early in the morning, but by early evening these had disappeared, with just a small solid cloud observed between 13 and 14 km. The nitric acid spike can be attributed to the gas released by the evaporating NAT rocks. By late evening, the solid cloud was gone and NAT rocks were again observed. Temperatures on day 250 fell below T_{NAT} over the entire partial column, and this was accompanied by a corresponding drop in the gas phase nitric acid to $\sim 7.4 \times 10^{15}$ molecules cm^{-2}.

The second spike in the 1998 data, on day 257 (Figure 8.8), occurred on a day when no PSCs were observed in the lidar data, but a NAT rock was observed the previous day. Temperatures were sufficiently warm to evaporate any PSCs in the region. Again, it seems likely that the spike can be attributed to NAT rock evaporation low in the partial column. The significantly lower nitric acid amounts recorded on the following days suggest that this spike was also caused by the localized evaporation of NAT rocks sedimenting from elsewhere in the vortex.

August 1999

The 1999 spike has been detailed in Section 8.3.2, with the increase in the nitric acid attributed to the change in phase from solid to liquid clouds observed in the column. In addition to this, however, it should be noted that NAT rocks were observed on the day preceding the spike, at altitudes consistent with temperatures around T_{NAT}, as highlighted in Figure 8.7. As such, it is highly likely that the observed increase in the nitric acid partial column amount on days 239 and 240 has been supplemented by evaporation of NAT rocks low in the partial column.

While these scenarios are somewhat speculative, it seems the identification of a spike in the nitric acid amounts during otherwise denitrified conditions may be an additional signature of NAT rocks in the Antarctic atmosphere. This is consistent with the prediction of nitrification in the regions where NAT rocks evaporate, as indicated by *Fahey et al.* (2001).

The observations support the theory of nitric acid being transported by NAT rocks from the region of formation into other regions, as detailed by *Fueglistaler et al.* (2002) and *Fahey et al.* (2001). This has important implications for denitrification and the subsequent increase in ozone loss, especially in the Arctic where a small reduction in temperature deep within the vortex could lead to the formation of more NAT rock particles and thus more widespread denitrification. A measurable increase in the HNO_3 column amount as a result of NAT rock transport and evaporation means that FTIR measurements in

polar regions could be used as a means of testing models that simulate the formation, sedimentation and transport of large nitric acid-containing particles.

8.4 Conclusions

In this chapter, ground-based FTIR observations of nitric acid have been coupled with measurements of polar stratospheric clouds made using a co-located ground-based aerosol lidar. To the best of our knowledge, this is the first ever such combination. Ground-based measurements have a much smaller footprint than satellite measurements, and as such, we were able to address questions related to the conditions directly observable over McMurdo Station.

The link between the rapid reduction of gas phase nitric acid and polar stratospheric cloud formation was conclusively demonstrated, with nitric acid measurements relative to the date of PSC onset giving a qualitative estimate of the speed of nitric acid depletion of 41% in 3 days. Depletion was observed to occur most rapidly on the first of these days, in agreement with the understood microphysics of liquid polar stratospheric cloud formation. A 'levelling off' of the nitric acid depletion after 3 to 5 days was believed to be caused by liquid PSC particles reaching their equilibrium sizes. Back-trajectory analyses of airmasses reaching the station around the time of onset were consistent with lidar observations showing that the clouds were in liquid form, supporting this conclusion.

Fluctuations in the observed nitric acid partial column amounts were shown to be linked not only with temperature, as suggested by *Santee et al.* (1999), but also with the phase of the clouds present over the station. The gas phase nitric acid was seen to increase during periods where liquid clouds were observed and decrease when solid clouds were present, in agreement with modelled microphysics showing solid clouds to be more efficient at removing gas phase HNO_3 than liquid clouds (*Tabazadeh et al.*, 1994b; *Santee et al.*, 1998).

Finally, a link between spikes in the HNO_3 column amount during otherwise denitrified conditions and observations of large nitric acid containing particles (NAT rocks) was postulated. These observations support theories of NAT rocks being formed at cold, high altitudes and then being transported away from their mother cloud into regions where denitrification may already exist. The evaporation of the NAT rocks at temperatures above T_{NAT} results in localized nitrification, causing a spike in the observed HNO_3 partial column amounts. Rapid formation of polar stratospheric clouds from the released nitric acid when temperatures cool may additionally contribute to continued chlorine activation and subsequent ozone loss late in the spring.

Ideally a complete microphysical model incorporating dynamics and PSC microphysics would be used to further enhance these observations and provide a more detailed study

of the conditions observed over the station during the case study periods. Nonetheless, these results show qualitative links between several processes occurring in the Antarctic stratosphere. In addition, the measurements provide observational evidence that can be used to better constrain models incorporating PSC processes and denitrification. This will ultimately result in a much better understanding of ozone loss and allow us to better quantify the impact of future climate change on the polar regions.

Chapter 9

Conclusions, Contributions, and Where To Next?

This chapter provides a brief overview of the work included in this thesis and how this contributes to our overall scientific knowledge. In addition, ideas for the possible extension of this work are proposed.

9.1 Research summary

The aim of this work was to further our knowledge of the processes occurring during the Antarctic winter, by extending Fourier transform spectroscopic measurements made from Arrival Heights into the polar night. This goal has been achieved by making measurements of two stratospheric trace gases, HCl and HNO_3, using the light of the full moon. The measurements have been presented with meteorological data in the context of the Antarctic year, allowing the observed seasonal behaviour to be compared and contrasted with studies in the literature. Additionally, the measurements have been compared with output from a well-known atmospheric chemical transport model, SLIMCAT. Taking the results a step further, measurements of nitric acid have been coupled with lidar observations of polar stratospheric clouds, providing empirical evidence for a range of wintertime processes.

While detailed conclusions have already been made at the end of each of Chapters 6, 7 and 8, a brief outline of the work presented in each chapter will be made here. The reader is encouraged to refer back to the appropriate chapter for further details.

A brief history of ozone-related trace gas research in the polar regions was presented in Chapter 1. The lack of a comprehensive set of winter measurements in Antarctica was demonstrated, providing context for the work detailed in the following chapters. This was followed in Chapter 2 with an introduction to the chemistry and physics necessary to explain polar ozone depletion.

Chapters 3, 4 and 5 showed the experimental details relevant to making the trace gas measurements. Chapter 3 introduced the tools used for the work, including both the FTIR instrument and the retrieval algorithms used. Chapter 4 showed the observational methods for making the measurements and Chapter 5 presented details of the analysis and error analysis carried out on both the HCl and HNO_3 data sets.

The partial column measurements of HCl and HNO_3 were presented in Chapter 6.

Solar and lunar measurements were shown for the entire 2003 year, in context with each other and with the meteorological conditions at the time. The measurements clearly showed dynamics to be driving non-perturbed conditions prior to the vortex formation, and the domination of polar stratospheric cloud formation and the heterogeneous chemistry occurring on the surface of these clouds during the winter months. Denitrification was shown to have occurred within the partial column and was identified as occurring predominantly in the 20 - 28 km altitude range. The rapid deactivation of chlorine to HCl in the spring was also clearly demonstrated, with measurements of $ClONO_2$ used to address the question of repartitioning between the chlorine reservoir species at this time.

Chapter 7 presented a comparison of the HCl and HNO_3 measurements with the three-dimensional chemical transport model SLIMCAT. This comparison showed that while SLIMCAT generally captured the summer and autumn trends in both gases well, the model was limited by the equilibrium treatment of PSCs early in the winter. While this had no significant effect on the modelled HCl later in the winter months, the resulting sedimentation of PSC particles meant that too much HNO_3 was depleted and the extent of denitrification was significantly overestimated. As such, the deactivation of chlorine was incorrectly captured in the spring and the recovery of HNO_3 was slower than observed.

The results of coupling ground-based measurements of HNO_3 with co-located measurements of polar stratospheric clouds from an aerosol lidar were given in Chapter 8. As well as confirming the link between HNO_3 and PSC formation, these measurements showed several interesting results. The speed of nitric acid uptake into polar stratospheric cloud particles was estimated at 41% of the partial column amount in three days and clearly showed the most dramatic uptake to be occurring on the first day. A link between fluctuations in the HNO_3 partial column amount and the phase of the aerosols was demonstrated, with a significant increase in the partial column amount observed in the presence of liquid clouds and a decrease in the presence of solid clouds. Temperature fluctuations low in the partial column were also shown to contribute to the observed fluctuations. Additionally, a link between the recently discovered large nitric acid-containing particles 'NAT rocks' and spikes occurring in the nitric acid partial column amount during the otherwise denitrified conditions of the spring stratosphere has been postulated.

In summary, the extension of measurements of just two trace gases into the Antarctic winter has provided a sufficiently large data set that investigation of a range of polar processes has been made possible. These measurements provide an important verification of our current understanding of the processes that result in springtime ozone loss and provide observational constraint for the models being used to predict the effect of human influence on ozone and climate processes in the future.

9.2 Contribution to knowledge

Measurements of stratospheric trace gases during the Antarctic winter have thus far been extremely limited, as a result of the lack of sunlight for spectroscopic measurements. This challenge has been overcome in this thesis by using the light of the full moon to extend measurements of HCl and HNO_3 into the polar night.

The HCl measurements presented here are, to the best of my knowledge, the first spectroscopic HCl measurements made throughout the Antarctic polar winter. As such, they are an important verification of the generally-accepted chemistry occurring during the months of darkness. The HCl partial column measurements have been presented with measurements made through the sunlit parts of the year, in context with the meteorological conditions and the processes occurring at every phase of the annual cycle.

The HNO_3 measurements presented in this thesis also present a substantial contribution to scientific knowledge. While measurements of HNO_3 have been made from satellites through the Antarctic winter (*Santee et al.*, 1996, 1998), ground-based FTIR measurements present a more detailed view of processes occurring on a local scale. Nitric acid measurements have been made using the moon as a light source since 1998, under the direction of my supervisor, Stephen Wood, but the analysis and interpretation of these measurements and the subsequent publication of these results in *Wood et al.* (2004) has been very much a part of this research. By putting these measurements in the context of the Antarctic winter with the measurements of HCl, the implications of the removal of gas phase HNO_3 as it is absorbed into PSCs and subsequently removed from the stratosphere become apparent, especially in relation to the effect this has on chlorine partitioning in the spring.

Because real observations in the Antarctic winter have been limited, both the HCl and HNO_3 measurements have been examined with reference to predictions and model output presented in the literature, showing generally good agreement with expectations. In addition, the measurements have been compared with output from the chemical transport model SLIMCAT. These have shown the limitations of the equilibrium treatment of PSCs in the model, especially in the early winter, and the subsequent over-prediction of denitrification.

Two other important additions to the knowledge have been made. The first is the breakdown of FTIR observations into the smallest partial columns possible within the limitations of their resolution. This demonstrates not only the denitrification, sedimentation and nitrification processes known to be occurring during the polar night, but also the ability of FTIR measurements to provide some height-resolved data. Because FTIR measurements have been made from a wide range of locations, this data source is potentially very important for the verification of atmospheric models.

The other important addition to the knowledge comes from the combination of ground-based FTIR observations of HNO_3 and lidar observations of PSCs. This was collaborative research with Paola Massoli, and is, to the best of our knowledge, the first such coupling. This research has established several interesting links between PSCs and the observed nitric acid trends, including a quantification of the speed of HNO_3 depletion, a link between the phase of the cloud and the observed nitric acid, and evidence for NAT rocks as shown by spikes occurring in the nitric acid partial column amounts during otherwise denitrified conditions.

While so far only the nitric acid measurements have been published, it is anticipated that three further papers will come out of this work in the near future. A paper based on the work included in Chapter 8, preliminarily entitled 'Nitric acid and polar stratospheric cloud coupling: denitrification processes and ozone-related chemistry in the lower stratosphere' is in preparation. Additionally, a paper publishing the new wintertime HCl measurements (Chapter 6) is expected. Finally, a paper incorporating the breakdown of the partial columns into smaller altitude regions as an extension of the information contained in ground-based FTIR observations (Section 6.2), has been proposed.

9.3 Future work

The beauty of scientific research is that every time a question is answered, five new ones come forward to take their place. This work naturally extends itself in many directions.

Spectroscopic measurements of a wide range of trace gases have traditionally been made using the sun as a light source, and an obvious extension of this work would be to extend many of those measurements into the polar night. Of particular interest would be to look at a tracer such as hydrogen fluoride (HF), which has a very similar profile to HCl but does not react heterogeneously and would thus allow the effects of dynamics and subsidence on the HCl partial column amounts to be better quantified. Measurements of $ClONO_2$ during the polar night would also be useful, though the weakness of the $ClONO_2$ absorption and the difficulty of the retrieval currently makes that very challenging. In addition, measurements of ClO would allow further quantification of the partitioning of chlorine from inactive to active forms during the winter and into the spring period. The retrieval of ClO from FTIR spectra is theoretically feasible and is something that might be worth investigating in the future. Springtime microwave measurements of ClO are, however, already being made from Scott Base, and I understand that these are likely to be extended into the winter in the near future [Brian Connor, NIWA Lauder, personal communication].

It would also be interesting to compare the winter observations made in the Antarctic directly with observations made in the Arctic. *Notholt et al.* (1993, 1997b) have

made many of these Arctic measurements from Ny Alesünd, Norway, and while a general comparison based on published literature has been presented in Chapter 6, a direct comparison of the two data sets would potentially be of value. Nitric acid measurements have also been made during the Arctic winter from Eureka, Canada, using a Bomen Fourier transform spectrometer [Richard Mittermeier, Meteorological Service of Canada, Ontario, personal communication]. In addition, the comparison of both these and the Antarctic measurements with model output from a model such as SLIMCAT has value. The SLIMCAT data used in Chapter 7 have been constrained based on Arctic observations, and as such, can be expected to show different results there to those observed in the Antarctic and presented in Chapter 7. By combining the observational data from both hemispheres to help constrain the model, a more accurate representation of the processes occurring in the polar regions may be possible.

In terms of the lidar and nitric acid coupling presented in Chapter 8, the introduction of a microphysical model for comparison and quantification of the observed effects would be of great interest. While observations suggest that NAT rocks are responsible for the spikes in the spring, having access to a model which was able to form, sediment and evaporate these particles would make the conclusions based on our observations much stronger. A microphysical model would also allow us to more firmly quantify the effect of temperature and phase on the nitric acid amounts that are observed.

Finally, I'd like to note that there are many of different measurements being made in the Antarctic at any one time. Even within the Arrival Heights laboratory, a whole suite of instruments is making measurements around the clock. The potential for new and interesting science by combining the results from these different instruments, as demonstrated by the HNO_3 and lidar coupling in Chapter 8, is huge. The most exciting research occurs through collaboration with other scientists, whether they are traditionally in the same field or not, and I anticipate that the future of scientific investigation in the Antarctic will be through the willingness of scientists to come together and share their observations of land, ice, ocean and atmosphere.

Appendix A

Measurement Uncertainties

A.1 Lunar measurement errors

Individual smoothing and measurement errors have been calculated for each lunar spectrum for both HCl and HNO_3 partial column measurements. These are listed below, with the forward model errors calculated for that period and an estimate of the total uncertainty in the quoted 12 - 28 km partial column amount.

A.1.1 HCl measurements

Filename	Date	S/N	S_M(%)	S_S (%)	S_F (%)	S_T (%)
D1040A29	14/04/2003	54.7	3.88	4.88	4.76	7.85
D1060A29	16/04/2003	71.5	4.17	5.14	4.76	8.15
D1080A29	18/04/2003	56.7	5.89	5.46	4.76	9.34
D1081A29	18/04/2003	37.3	9.37	7.46	4.76	12.89
D1390A29	19/05/2003	41.3	10.45	9.06	4.76	14.62
D1391A29	19/05/2003	23.7	11.27	12.24	4.76	17.31
D1392A29	19/05/2003	28	10.89	10.02	4.76	15.54
D1393A29	19/05/2003	63.6	7.22	6.15	4.76	10.62
D1394A29	19/05/2003	27.7	11.29	12.33	4.76	17.38
D1400A29	20/05/2003	22.4	11.25	14.20	4.76	18.73
D1650A29	14/06/2003	28.2	11.21	27.91	3.83	30.33
D1651A29	14/06/2003	21.6	10.43	34.70	3.83	36.44
D1652A29	14/06/2003	44.3	11.18	24.28	3.83	27.00
D1660A29	15/06/2003	31.7	11.27	27.85	3.83	30.29
D1661A29	15/06/2003	49.1	10.07	16.88	3.83	20.02
D1670A29	16/06/2003	58.2	10.41	18.05	3.83	21.19
D1671A29	16/06/2003	55.6	9.16	14.58	3.83	17.64
D1900A29	9/07/2003	43.6	15.54	24.83	3.62	29.52
D1901A29	9/07/2003	34.5	21.05	54.10	3.62	58.16
D1920A29	11/07/2003	30.6	20.97	52.12	3.62	56.29
D1930A29	12/07/2003	32.6	21.04	44.09	3.62	48.99
D1940A29	13/07/2003	34	20.21	60.70	3.62	64.08
D1941A29	13/07/2003	72.7	17.45	27.46	3.62	32.73
D1942A29	13/07/2003	43.4	20.09	35.76	3.62	41.18

Filename	Date	S/N	S_M(%)	S_S (%)	S_F (%)	S_T (%)
D1950A29	14/07/2003	45.8	20.72	41.04	3.62	46.12
D1951A29	14/07/2003	49	18.23	29.41	3.62	34.79
D1960A29	15/07/2003	30.2	19.98	61.74	3.62	64.99
D1961A29	15/07/2003	52.2	19.00	31.52	3.62	36.98
D1970A29	16/07/2003	36.7	21.17	44.38	3.62	49.30
D2190A29	7/08/2003	45.3	21.08	52.02	3.62	56.24
D2200A29	8/08/2003	49.3	20.93	42.99	3.62	47.95
D2201A29	8/08/2003	44	18.24	29.42	3.62	34.81
D2210A29	9/08/2003	70.8	17.65	27.68	3.62	33.02
D2220A29	10/08/2003	41.4	21.20	54.46	3.62	58.55
D2221A29	10/08/2003	51	18.51	29.51	3.62	35.02
D2230A29	11/08/2003	41.4	21.24	54.56	3.62	58.66
D2231A29	11/08/2003	29.2	18.12	71.58	3.62	73.93
D2240A29	12/08/2003	54	18.03	28.13	3.62	33.61
D2280A29	16/08/2003	37.1	19.74	34.02	3.62	39.50
D2480A29	5/09/2003	48.4	21.09	50.43	3.62	54.78
D2490A29	6/09/2003	52.6	18.63	30.20	3.62	35.67
D2500A29	7/09/2003	99	15.16	23.97	3.62	28.59
D2520A29	9/09/2003	42.5	12.66	21.83	3.62	25.49
D2530A29	10/09/2003	74.8	14.42	23.24	3.62	27.59
D2531A29	10/09/2003	20.9	20.36	59.48	3.62	62.97

Table A.1: Uncertainties for each averaged HCl lunar measurement. Details as described in Chapter 5, Section 5.1.5

A.1.2 HNO_3 measurements

Filename	Date	S/N	S_M(%)	S_S (%)	S_F (%)	S_T (%)
D1040808	14/04/2003	113.8	1.40	1.61	15.26	15.41
D1041808	14/04/2003	142.3	1.11	1.58	15.26	15.38
D1042808	14/04/2003	149.3	1.07	1.58	15.26	15.38
D1060808	16/04/2003	183.2	2.06	1.85	15.26	15.51
D1061808	16/04/2003	207.9	1.92	1.78	15.26	15.48
D1062808	16/04/2003	168.0	2.32	1.99	15.26	15.56
D1080808	18/04/2003	205.8	2.29	1.99	15.26	15.56
D1081808	18/04/2003	191.3	2.47	2.10	15.26	15.60
D1082808	18/04/2003	213.3	2.33	2.02	15.26	15.57
D1390808	19/05/2003	158.5	4.15	2.89	15.26	16.07
D1391808	19/05/2003	152.9	4.19	2.91	15.26	16.09
D1392808	19/05/2003	163.4	3.85	2.78	15.26	15.98

Filename	Date	S/N	$S_M(\%)$	S_S (%)	S_F (%)	S_T (%)
D1393808	19/05/2003	179.8	2.87	2.28	15.26	15.69
D1394808	19/05/2003	226.0	2.50	2.06	15.26	15.60
D1395808	19/05/2003	189.3	2.90	2.30	15.26	15.70
D1396808	19/05/2003	202.9	3.19	2.48	15.26	15.79
D1397808	19/05/2003	153.0	3.99	2.83	15.26	16.02
D1398808	19/05/2003	169.5	3.73	2.73	15.26	15.94
D1400808	20/05/2003	153.9	4.58	3.04	15.26	16.22
D1401808	20/05/2003	172.7	4.11	2.87	15.26	16.06
D1402808	20/05/2003	190.6	3.77	2.73	15.26	15.95
D1403808	20/05/2003	178.1	3.45	2.59	15.26	15.86
D1404808	20/05/2003	169.6	3.53	2.62	15.26	15.88
D1405808	20/05/2003	184.6	3.29	2.51	15.26	15.81
D1650808	14/06/2003	228.9	1.76	1.61	15.20	15.39
D1651808	14/06/2003	208.1	1.89	1.66	15.20	15.41
D1652808	14/06/2003	184.4	2.09	1.76	15.20	15.44
D1653808	14/06/2003	200.8	2.00	1.72	15.20	15.43
D1654808	14/06/2003	185.5	3.26	2.48	15.20	15.74
D1655808	14/06/2003	151.6	4.05	2.84	15.20	15.98
D1656808	14/06/2003	159.4	4.14	2.88	15.20	16.01
D1660808	15/06/2003	251.2	2.17	1.81	15.20	15.46
D1661808	15/06/2003	206.6	2.44	1.97	15.20	15.52
D1662808	15/06/2003	106.8	3.81	2.72	15.20	15.90
D1670808	16/06/2003	245.6	2.48	1.99	15.20	15.53
D1671808	16/06/2003	230.8	2.55	2.03	15.20	15.55
D1672808	16/06/2003	273.2	2.25	1.84	15.20	15.48
D1900808	9/07/2003	156.6	1.23	1.43	15.13	15.25
D1901808	9/07/2003	174.3	1.19	1.43	15.13	15.24
D1902808	9/07/2003	158.4	2.83	2.13	15.13	15.54
D1903808	9/07/2003	187.1	2.55	1.97	15.13	15.47
D1904808	9/07/2003	160.6	2.92	2.19	15.13	15.56
D1920808	11/07/2003	195.3	3.39	2.47	15.13	15.70
D1921808	11/07/2003	187.7	3.52	2.54	15.13	15.74
D1922808	11/07/2003	210.7	3.31	2.43	15.13	15.68
D1930808	12/07/2003	171.7	2.56	1.97	15.13	15.47
D1931808	12/07/2003	214.8	2.12	1.74	15.13	15.38
D1932808	12/07/2003	196.0	2.24	1.79	15.13	15.40
D1940808	13/07/2003	233.1	2.65	2.08	15.13	15.50
D1941808	13/07/2003	248.6	2.51	1.99	15.13	15.47
D1942808	13/07/2003	247.8	2.48	1.97	15.13	15.46
D1950808	14/07/2003	220.6	2.32	1.85	15.13	15.42
D1951808	14/07/2003	219.5	2.31	1.85	15.13	15.42
D1952808	14/07/2003	254.3	1.99	1.68	15.13	15.35
D1960808	15/07/2003	209.7	2.62	2.04	15.13	15.49
D1961808	15/07/2003	187.8	2.79	2.15	15.13	15.53
D1962808	15/07/2003	265.1	2.18	1.77	15.13	15.39

Filename	Date	S/N	S_M(%)	S_S (%)	S_F (%)	S_T (%)
D2190808	7/08/2003	132.5	2.67	1.98	15.13	15.49
D2191808	7/08/2003	137.9	2.63	1.96	15.13	15.48
D2192808	7/08/2003	123.4	2.94	2.10	15.13	15.56
D2200808	8/08/2003	179.6	3.53	2.47	15.13	15.73
D2201808	8/08/2003	194.9	3.26	2.35	15.13	15.65
D2202808	8/08/2003	176.0	3.46	2.44	15.13	15.71
D2210808	9/08/2003	147.0	3.65	2.47	15.13	15.76
D2211808	9/08/2003	165.3	3.38	2.36	15.13	15.68
D2212808	9/08/2003	203.8	2.96	2.18	15.13	15.57
D2220808	10/08/2003	222.8	2.26	1.80	15.13	15.40
D2221808	10/08/2003	210.2	2.32	1.83	15.13	15.52
D2222808	10/08/2003	234.5	2.11	1.73	15.13	15.37
D2230808	11/08/2003	255.1	2.36	1.87	15.13	15.43
D2231808	11/08/2003	225.0	2.68	2.04	15.13	15.50
D2232808	11/08/2003	276.0	2.35	1.87	15.13	15.43
D2240808	12/08/2003	228.0	2.56	1.97	15.13	15.47
D2241808	12/08/2003	220.4	2.54	1.95	15.13	15.47
D2242808	12/08/2003	281.0	2.10	1.73	15.13	15.37
D2280808	16/08/2003	204.9	1.88	1.62	15.13	15.33
D2281808	16/08/2003	191.8	1.96	1.65	15.13	15.35
D2282808	16/08/2003	246.7	1.60	1.52	15.13	15.29
D2490808	6/09/2003	221.4	3.07	2.21	15.13	15.60
D2491808	6/09/2003	176.3	3.61	2.44	15.13	15.74
D2492808	6/09/2003	214.9	3.06	2.21	15.13	15.59
D2495808	6/09/2003	267.8	1.78	1.62	15.13	15.32
D2496808	6/09/2003	214.5	2.07	1.73	15.13	15.37
D2497808	6/09/2003	178.5	2.35	1.84	15.13	15.42
D249A808	6/09/2003	211.5	2.35	1.85	15.13	15.42
D249D808	6/09/2003	186.5	2.96	2.14	15.13	15.56
D249E808	6/09/2003	184.2	2.98	2.16	15.13	15.57
D249F808	6/09/2003	214.3	2.71	2.03	15.13	15.50
D2500808	7/09/2003	251.4	2.32	1.84	15.13	15.42
D2501808	7/09/2003	234.3	2.42	1.88	15.13	15.44
D2502808	7/09/2003	185.4	2.81	2.06	15.13	15.53
D2520808	9/09/2003	230.7	1.19	1.49	15.13	15.25
D2521808	9/09/2003	203.6	1.26	1.50	15.13	15.26
D2522808	9/09/2003	233.3	1.09	1.48	15.13	15.30
D2523808	9/09/2003	219.8	1.11	1.48	15.13	15.24
D2530808	10/09/2003	298.0	1.82	1.66	15.13	15.33
D2531808	10/09/2003	230.9	2.17	1.79	15.13	15.39
D2532808	10/09/2003	306.0	1.72	1.63	15.13	15.31

Table A.2: Uncertainties for each lunar HNO_3 measurement. Details as described in Chapter 5, Section 5.2.5

A.2 Solar model parameter errors

A detailed error analysis was conducted for the 12 - 28 km partial column amounts for both HCl and HNO_3 solar measurements made in 2003. A typical spectrum in January was chosen for both of these analyses. The tables below present the uncertainties due to individual forward model parameters.

A.2.1 HCl measurements

Uncertainty Source	% uncertainty in partial column amount
Temperature profile	2.90%
CH_4 profile scale factor	1.14%
NO_2 profile scale factor	0.02%
Zenith angle	0.30%
Instrument line shape	0.29%
HCl line intensity	2.11%
HCl air-broadened half width	0.35%
CH_4 line intensity	0.02%
CH_4 air-broadened half width	0.02%
Total forward model uncertainty	**3.80%**

Table A.3: Forward model parameter errors for solar HCl measurements.

A.2.2 HNO_3 measurements

Uncertainty Source	% uncertainty in partial column amount
Temperature profile	4.50%
H_2O profile scale factor	0.04%
OCS profile scale factor	0.06%
NH_3 profile scale factor	0.01%
Zenith angle	0.30%
Instrument line shape	0.15%
HNO_3 line intensity	14.43%
HNO_3 air-broadened half width	3.20%
Zero-level	1.04%
Total forward model uncertainty	**15.49%**

Table A.4: Forward model parameter errors for solar HNO_3 measurements. Note the effect due to uncertainty in the temperature profile includes an emission correction factor, though this contributes less than 0.005% to the uncertainty.

A.3 Smaller partial column model parameter errors

A detailed error analysis has also been carried out for the HNO_3 amounts in each of the narrow altitude range partial columns. A typical spectrum in January has been used for the solar analyses, and a typical spectrum from June has been used for the lunar ones.

Uncertainty Source	10-20 km (lunar)	20-28 km (lunar)	10-20 km (solar)	20-28 km (solar)
Temperature profile	6.54%	3.05%	7.00%	2.86%
H_2O profile scale factor	0.03%	0.19%	0.04%	0.03%
OCS profile scale factor	0.03%	0.19%	0.00%	0.02%
NH_3 profile scale factor	0.00%	0.21%	0.03%	0.02%
Zenith angle	1.22%	1.31%	0.26%	0.33%
Instrument line shape	5.82%	7.85%	1.23%	1.07%
HNO_3 line intensity	11.59%	16.31%	9.46%	19.91%
HNO_3 air-broadened half width	2.01%	12.63%	5.00%	12.80%
Zero-level	0.84%	0.98%	0.95%	1.11%
Total forward model uncertainty	**13.20%**	**22.34%**	**12.88%**	**23.90%**

Uncertainty Source	10-16 km (solar)	16-20 km (solar)	20-24 km (solar)	24-28 km (solar)
Temperature profile	7.42%	6.93%	3.79%	1.86%
H_2O profile scale factor	0.10%	0.00%	0.05%	0.00%
OCS profile scale factor	0.01%	0.00%	0.02%	0.01%
NH_3 profile scale factor	0.05%	0.02%	0.03%	0.01%
Zenith angle	0.24%	0.27%	0.30%	0.39%
Instrument line shape	0.25%	1.87%	1.14%	5.09%
HNO_3 line intensity	24.52%	0.41%	22.11%	15.92%
HNO_3 air-broadened half width	40.13%	34.52%	16.20%	65.51%
Zero-level	0.83%	1.03%	1.00%	1.31%
Total forward model uncertainty	**47.62%**	**35.28%**	**27.72%**	**67.65%**

Table A.5: Forward model parameter errors for small HNO_3 partial column measurements. Temperature estimate includes the effect of emission, as detailed in Section 5.2.5.

References

Adriani, A., T. Deshler, G. P. Gobbi, B. J. Johnson, and G. Di Donfrancesco, Polar stratospheric clouds over McMurdo Station, Antarctica, during the 1991 spring: lidar and particle counter measurements, *Geophys. Res. Lett.*, *17*, 1755–1758, 1992.

Adriani, A., T. Deshler, G. Di Donfrancesco, and G. Gobbi, Polar stratospheric clouds and volcanic aerosol during spring 1992 over McMurdo Station, Antarctica: lidar and particle counter comparisons, *J. Geophys. Res.*, *100*, 25877–25897, 1995.

Adriani, A., P. Massoli, G. Di Donfrancesco, F. Cairo, M. L. Moriconi, and M. Snels, Climatology of polar stratospheric clouds based on lidar observations from 1993 to 2001 over McMurdo Station, Antarctica, *J. Geophys. Res.*, *109*(D24), doi: 10.1029/2004JD004800, 2004.

Ajtic, J., B. J. Connor, C. E. Randall, B. N. Lawrence, G. E. Bodeker, J. E. Rosenfield, and D. N. Heuff, Antarctic air over New Zealand following vortex breakdown in 1998, *Ann. Geophys.*, *21*, 2175–2183, 2003.

Ajtic, J., B. J. Connor, B. N. Lawrence, G. E. Bodeker, K. W. Hoppel, J. E. Rosenfield, and D. N. Heuff, Dilution of the Antarctic ozone hole into southern midlatitudes, 1998-2000, *J. Geophys. Res.*, *109*(D17107), doi: 10.1029/2003JD004500, 2004.

Alpert, N. L., W. E. Keiser, and H. A. Szymanski, *IR Theory and Practice of Infrared Spectroscopy.* Plenum Press, New York, 1 edn., 1970.

Anderson, J., and O. Toon, Airborne Arctic Stratospheric Expedition II: An overview, *Geophys. Res. Lett.*, *20*(22), 2499–2502, 1993.

Antarctic Treaty Secretariat, Final report of the twenty-seventh Antarctic Treaty consultative meeting, Tech. rep., Antarctic Treaty XVII consultative meeting, Cape Town, 2004, Available from http://www.ats.org.ar, 2004.

Arnold, F., and S. Spreng, Balloon-borne mass spectrometer measurements of HCl and HF in the winter Arctic stratosphere, *Geophys. Res. Lett.*, *21*(13), 1255–1258, 1994.

Arnold, F., V. Burger, K. Gollinger, M. Roncossek, J. Schneider, and S. Spreng, Observations of nitric acid perturbations in the winter Arctic stratosphere: Evidence for PSC-sedimentation, *J. Atmos. Chem*, *30*, 49–59, 1998.

Atkinson, R. J., and R. A. Plumb, Three-dimensional ozone hole transport during the ozone hole breakup in December 1987, *J. Geophys. Res.*, *102*(D1), 1451–1466, 1997.

Barath, F., et al., The Upper Atmosphere Research Satellite Microwave Limb Sounder Experiment, *J. Geophys. Res.*, *98*, 10751–10762, 1993.

Bates, D., and M. Nicolet, The photochemistry of atmospheric water vapour, *J. Geophys. Res.*, *55*, 301, 1950.

Beaver, G. M., and J. M. Russell, The climatology of stratospheric HCl and HF observed by HALOE, *Adv. Space. Res.*, *21*(10), 1373–1382, 1998.

Bell, R., *Introductory Fourier transform spectroscopy.* Academic Press, 1972.

Beyerle, G., and R. Neuber, The stratospheric aerosol count above Spitsbergen during winter 1991/92, *Geophys. Res. Lett.*, *21*(13), 1291–1294, 1994.

Beyerle, G., R. Neuber, O. Schrems, F. Wittrock, and B. Knudsen, Multiwavelength lidar measurements of stratospheric aerosols above Spitsbergen during winter 1992/93, *Geophys. Res. Lett.*, *21*, 57–60, 1994.

Beyerle, G., B. Luo, R. Neuber, T. Peter, and I. S. McDermid, Temperature dependence of ternary solution particle volumes as observed by lidar in the Arctic stratosphere during winter 1992/1993, *J. Geophys. Res.*, *102*(D3), 3603–3609, 1997.

Blom, C., H. Fischer, N. Glatthor, T. Gulde, and M. Hopfner, Airborne measurements during the European Arctic Stratospheric Ozone Experiment: column amounts of HNO_3 and O_3 derived from FTIR emission sounding, *Geophys. Res. Lett.*, *21*(13), 1351–1354, 1994.

Blumenstock, T., H. Fischer, A. Friedle, F. Hase, and P. Thomas, Column amounts of $ClONO_2$, HCl, HNO_3 and HF from ground-based FTIR measurements made near Kiruna, Sweden, in late winter 1994, *J. Atmos. Chem*, *26*, 311–321, 1997.

Bowman, K. P., Large-scale isentropic mixing properties of the Antarctic polar vortex from analyzed winds, *J. Geophys. Res.*, *98*(D12), 23013–23027, 1993.

Braathen, G., Executive summary of QUOBI, from the QUOBI website http://www.nilu.no/quobi, visited 1/05, last updated 1/02, 2002.

Brandtjen, R., T. Klupfel, D. Perner, and B. Knudsen, Airborne measurements during the European Arctic Stratospheric Ozone Experiment: Observations of OClO, *Geophys. Res. Lett.*, *21*(13), 1363–1366, 1994.

Brasseur, G., X. Tie, P. Rasch, and F. Lefevre, A three-dimensional simulation of the Antarctic ozone hole: impact of anthropogenic chlorine on the lower stratosphere and upper troposphere, *J. Geophys. Res.*, *102*, 8909–8930, 1997.

Brewer, A., and J. Milford, The Oxford-Kew Ozonesonde, *Proc. Roy. Soc. London, A256*, 470–495, 1960.

Brewer, A. W., Evidence for a world circulation provided by the measurements of helium and water vapour distribution in the stratosphere, *Quart. J. Roy. Meteor. Soc*, *75*, 351–363, 1949.

Briegleb, B. P., Delta-Eddington approximation for solar radiation in the NCAR Community Climate Model, *J. Geophys. Res.*, *97*(D7), 7603–7612, 1992.

Browell, E. V., C. F. Butler, S. Ismail, P. A. Robinette, A. F. Carter, N. S. Higdon, O. B. Toon, M. R. Schoeberl, and A. F. Tuck, Airborne lidar observations in the wintertime Arctic stratosphere: Polar Stratospheric Clouds, *Geophys. Res. Lett.*, *17*(4), 385–388, 1990.

Brune, W., J. Anderson, and K. Chan, In situ observations of ClO in the Antarctic: ER-2 aircraft results from 54°S to 72°S latitude, *J. Geophys. Res.*, *94*(D14), 16649–16663, 1989.

Brune, W., D. Toohey, J. Anderson, and K. Chan, In situ observations of ClO in the Arctic stratosphere: ER-2 aircraft results from 59°N to 80°N latitude, *Geophys. Res. Lett.*, *17*(4), 505–508, 1990.

Carroll, M., R. Sanders, S. Solomon, and A. Schmeltekopf, Visible and near-ultraviolet spectroscopy at McMurdo Station, Antarctica 6. Observations of BrO, *J. Geophys. Res.*, *94*(D14), 16633–16638, 1989.

Carroll, M., D. Montzka, G. Hubler, and K. Kelly, In situ measurements of NO_x in the Airborne Arctic Stratospheric expedition, *Geophys. Res. Lett.*, *17*(4), 493–496, 1990.

Carslaw, K., B. Luo, S. Clegg, T. Peter, P. Brimblecombe, and P. Crutzen, Stratospheric aerosol growth and HNO_3 gas phase depletion from coupled HNO_3 and water uptake by liquid particles, *Geophys. Res. Lett.*, *21*, 2479–2482, 1994.

Carslaw, K. S., B. Luo, and T. Peter, An analytic expression for the composition of aqueous HNO_3-H_2SO_4 stratospheric aerosols including gas phase removal of HNO_3, *Geophys. Res. Lett.*, *22*(14), 1877–1880, 1995.

Chapman, S., A theory of upper atmospheric ozone, *Mem. Roy. Meteorol. Soc*, *3*, 103–125, 1930.

Chipperfield, M., Implementation of a semi-Lagrangian advection scheme in SLIMCAT, Internal Report 40, UK Universities Global Atmospheric Modelling Programme (UGAMP), Available from http://www.env.leeds.ac.uk/~Martyn/slimcat.html, 1996a.

Chipperfield, M., The SLIMCAT offline transport model, Internal Report 39, UK Universities Global Atmospheric Modelling Programme (UGAMP), Available from http://www.env.leeds.ac.uk/~Martyn/slimcat.html, 1996b.

Chipperfield, M., The TOMCAT offline transport model, Part 1. Stratospheric chemistry code, Internal Report 44a, UK Universities Global Atmospheric Modelling Programme (UGAMP), Available from http://www.env.leeds.ac.uk/~Martyn/slimcat.html, 1996c.

Chipperfield, M., Multiannual simulations with a three-dimensional chemical transport model, *J. Geophys. Res.*, *104*, 1781–1805, 1999.

Chipperfield, M., A three-dimensional model study of long-term mid-high latitude lower stratosphere ozone changes, *Atmos. Chem. Phys*, *3*, 1253 –1265, 2003.

Chipperfield, M., and N. Nikiforakis, Implementation of a weighted average flux advection scheme in SLIMCAT, Internal Report 46, UK Universities Global Atmospheric Modelling Programme (UGAMP), Available from http://www.env.leeds.ac.uk/~Martyn/slimcat.html, 1997.

Chipperfield, M. P., New version of the TOMCAT/SLIMCAT off-line chemical transport model, *Q. J. Roy. Met. Soc*, in preparation, 2005.

Chipperfield, M. P., and R. L. Jones, Relative influences of atmospheric chemistry and transport on Arctic ozone trends, *Nature*, *400*, 551–554, 1999.

Cicerone, R., S. Walters, and S. Liu, Nonlinear response of stratospheric ozone column to chlorine injection, *J. Geophys. Res.*, *88*, 3647–3661, 1983.

Coffey, M., A. Mankin, and A. Goldman, Airborne measurements of stratospheric constituents over Antarctica in the austral spring, 1987 2. Halogen and nitrogen trace gases, *J. Geophys. Res.*, *94*(D14), 16597–16613, 1989.

Connor, B. J., D. E. Siskind, J.-J. Tsou, A. Parrish, and E. E. Remsberg, Ground-based microwave observations of ozone in the upper stratosphere and mesosphere, *J. Geophys. Res.*, *99*, 16757–16770, 1994.

Connor, B. J., A. Parrish, J.-J. Tsou, and M. P. McCormick, Error analysis for the ground-based microwave ozone measurements during STOIC, *J. Geophys. Res.*, *100*, 9283–9291, 1995.

Connor, B. J., A. Parrish, J.-J. Tsou, and M. P. McCormick, Retrieval of HCl and HNO_3 profiles from ground-based FTIR data using SFIT2, in *Proceedings of the XVIII Quadrennial Ozone Symposium*, edited by R. D. Bojkov, and G. Visconti, vol. 2 of *Atmospheric Ozone*, pp. 485–488, L'Aquila, Italy. Parco Scientifico e Technologico d'Abruzzio, 1998.

Crewell, S., K. Kunzi, H. Nett, and T. Wehr, Aircraft measurements of ClO and HCl during EASOE, *Geophys. Res. Lett.*, *21*(13), 1267–1270, 1994.

Cronn, D. R., W. L. Bamesberger, F. A. Menzia, S. F. Waylett, A. S. Waylett, T. W. Ferrara, H. M. Howard, and E. Robinson, Atmospheric trace gas trends at Palmer Station, Antarctica: 1982-1985, *Geophys. Res. Lett.*, *13*(12), 1272–1275, 1986.

Crützen, P., The influence of nitrogen oxides on the atmospheric ozone content, *Q. J. R. Meteorol. Soc*, *96*, 320–325, 1970.

Crützen, P. J., and F. Arnold, Nitric acid cloud formation in the cold Antarctic stratosphere: A major cause for the springtime 'ozone hole', *Science*, *324*, 651–655, 1986.

David, C., S. Godin, G. Megie, Y. Emery, and C. Flesia, Physical state and composition of polar stratospheric clouds inferred from airborne lidar measurements during SESAME, *J. Atmos. Chem*, *27*(1), 1–16, 1997.

David, C., S. Bekki, S. Godin, G. Megie, and M. Chipperfield, Polar stratospheric cloud climatology over Dumont d'Urville between 1989 and 1993 and the influence of volcanic aerosols on their formation, *J. Geophys. Res.*, *103*(D17), 22163–22180, 1998.

Davies, S., et al., Modeling the effect of denitrification on Arctic ozone depletion during winter 1999/2000, *J. Geophys. Res.*, *108*(D5), doi: 10.1029/2001JD000445, 2003.

Davis, S. P., M. C. Abrams, and J. W. Brault, *Fourier Transform Spectroscopy*. Academic Press, San Diego, San Francisco, New York, Boston, London, Sydney, Tokyo, 2001.

Derber, J., D. Parrish, and S. Lord, The new global operational analysis system at the National Meteorological Center, *Weather and Forecasting*, *6*, 538–548, 1991.

Deshler, T., A. Adriani, D. Hofmann, and G. Gobbi, Evidence for denitrification in the 1990 Antarctic spring stratosphere: II Lidar and aerosol measurements, *Geophys. Res. Lett.*, *18*, 1999–2002, 1991.

Dessler, A., B. M.D., J. U. Grooss, J. R. Holton, J. L. Lean, S. Massie, M. Schoeberl, A. R. Douglass, and C. H. Jackman, Selected science highlights from the first 5 years of the Upper Atmosphere Research Satellite (UARS) program, *Rev. Geophys.*, *36*(2), 183–210, 1998.

deZafra, R., M. Jaramillo, A. Parrish, P. Solomon, B. Connor, J. Barrett, and L. Emmons, High concentrations of chlorine monoxide at low altitudes in the Antarctic spring stratosphere: Diurnal variation, *Nature*, *328*(6129), 408–411, 1987.

deZafra, R., M. Jaramillo, J. Barrett, L. Emmons, P. Solomon, and A. Parrish, New observations of a large concentration of ClO in the springtime lower stratosphere over Antarctica and its implications for ozone-depleting chemistry, *J. Geophys. Res.*, *94*(D9), 11429–11436, 1989.

deZafra, R., L. Emmons, J. Reeves, and D. Shindell, An overview of millimetre-wave spectroscopic measurements of chlorine monoxide at Thule, Greenland, February-March 1992: Vertical profiles, diurnal variation and longer-term trends, *Geophys. Res. Lett.*, *21*(13), 1271–1274, 1994.

Dobson, G., Forty years' research on atmospheric ozone at Oxford: a history, *Applied Optics*, *17*(3), 387–405, 1968.

Dobson, G., and D. Harrison, Measurements of the amount of ozone in the Earth's atmosphere and its relation to other geophysical conditions, *Proc. Roy. Soc. London*, *A110*, 660–693, 1926.

Dobson, G., D. Harrison, and J. Lawrence, Measurements of the amount of ozone in the Earth's atmosphere and its relation to other geophysical conditions - Part II, *Proc. Roy. Soc. London*, *A114*, 521–541, 1927.

Dobson, G., H. Kimball, and E. Kidson, Observations of the amount of ozone in the Earth's atmosphere and its relation to other geophysical conditions Part IV, *Proc. Roy. Soc. London*, *A129*, 411–433, 1930.

Douglass, A. R., M. R. Schoeberl, R. S. Stolarski, J. W. Waters, J. M. Russell III, A. E. Roche, and S. T. Massie, Interhemispheric differences in springtime production of HCl and $ClONO_2$ in the polar vortices, *J. Geophys. Res.*, *100*(D7), 13967–13978, 1995.

ECMWF, The ERA-40 project plan, Tech. rep., European Centre for Medium-Range Weather Forecasts, Available from www.ecmwf.int/research/era/Project/Plan, 2002.

Emmons, L., J. Reeves, D. Shindell, and R. deZafra, N_2O as an indicator of Arctic vortex dynamics: Correlations with O_3 over Thule, Greenland in February and March, 1992, *Geophys. Res. Lett.*, *21*(13), 1275–1278, 1994.

Eyring, V., et al., Comprehensive summary on the workshop on 'Process-orientated validation of Coupled Chemistry-climate Models', *SPARC Newsletter*, *23*, 2004.

Fabian, P., R. Borchers, and K. Kourtidis, Bromine-containing source gases during EASOE, *Geophys. Res. Lett.*, *21*(13), 1219–1222, 1994.

Fabry, C., and H. Buisson, L'absorption de l'ultraviolet par l'ozone et la limite du spectre solaire, *J. Phys.*, *3*, 196–206, 1913.

Fahey, D., K. Kelly, G. Ferry, L. Poole, J. Wilson, D. Murphy, M. Loewenstein, and K. Chan, In situ measurements of total reactive nitrogen, total water and aerosol in a polar stratospheric cloud in the Antarctic, *J. Geophys. Res.*, *94*(D9), 11299–11315, 1989a.

Fahey, D., D. Murphy, K. Kelly, M. Ko, M. Proffitt, C. Eubank, G. Ferry, M. Loewenstein, and K. Chan, Measurements of nitric oxide and total reactive nitrogen in the Antarctic stratosphere: observations and chemical implications, *J. Geophys. Res.*, *94*(D14), 16665–16681, 1989b.

Fahey, D., S. Kawa, and K. Chan, Nitric oxide measurements in the Arctic winter stratosphere, *Geophys. Res. Lett.*, *17*(4), 489–492, 1990.

Fahey, D., et al., The detection of large HNO_3 containing particles in the winter Arctic stratosphere, *Science*, *291*, 1026–1031, 2001.

Farman, J., B. Gardiner, and J. Shanklin, Large losses of total ozone in Antarctica reveal seasonal ClO_x/NO_x interaction, *Nature*, *315*, 207–210, 1985.

Farmer, C., O. Toon, P. Schaper, J.-F. Blavier, and L. Lowes, Stratospheric trace gases in the spring 1986 Antarctic atmosphere, *Nature*, *329*, 126–130, 1987.

Feng, W., et al., Three-dimensional model study of the Arctic ozone loss in 2002/2003 and comparison with 1999/2000 and 2003/2004, *Atmos. Chem. Phys. Discuss*, *4*, 5045–5074, Submitted to Atmos. Chem. Phys., 2004.

Findlayson-Pitts, B. J., and J. N. Pitts, *Atmospheric Chemistry: Fundamentals and Experimental Techniques*. Wiley-Interscience, 1986.

Fish, D., R. Jones, R. Freshwater, H. Roscoe, D. Oldham, and J. Harries, Total ozone measured during EASOE by a UV-visible spectrometer which observes stars, *Geophys. Res. Lett.*, *21*(13), 1387–1390, 1994.

Fueglistaler, S., B. P. Luo, C. Voigt, K. S. Carslaw, and T. Peter, NAT-rock formation by mother clouds: a microphysical model study, *Atmos. Chem. Phys.*, *2*, 93–98, 2002.

Gandrud, B., J. Dye, D. Baumgardner, G. Ferry, M. Loewenstein, K. Chan, L. Sanford, B. Gary, and K. Kelly, The January 30, 1989 Arctic polar stratospheric clouds (PSC) event: evidence for a mechanism of dehydration, *Geophys. Res. Lett.*, *17*(4), 457–460, 1990.

Gardiner, B., Comparative morphology of the vertical ozone profile in the Antarctic spring, *Geophys. Res. Lett.*, *15*(8), 901–904, 1988.

Gelman, M. E., A. J. Miller, K. W. Johnson, and R. M. Nagatani, Detection of long-term trends in global stratospheric temperature from NMC analyses derived from NOAA satellite data, *Adv. Space. Res*, *6*, 17–26, 1986.

Gobbi, G. P., T. Deshler, A. Adriani, and D. J. Hofmann, Evidence for denitrification in the 1990 Antarctic spring stratosphere: I. Lidar and temperature measurements, *Geophys. Res. Lett.*, *18*(11), 1995–1998, 1991.

Goldman, A., C. Paton-Walsh, W. Bell, G. C. Toon, J. F. Blavier, B. Sen, M. T. Coffey, J. W. Hannigan, and W. G. Mankin, Network for the Detection of Stratospheric Change Fourier transform infrared intercomparison at Table Mountain Facility, November 1996, *J. Geophys. Res.*, *104*, 30481–30503, 1999.

Götz, F., A. Meetham, and G. Dobson, The vertical distribution of ozone in the atmosphere, *Proc. Roy. Soc. London*, *A145*, 416–446, 1934.

Goutail, F., J. Pommereau, A. Sarkissian, E. Kyro, and V. Dorokhov, Total nitrogen dioxide at the Arctic polar circle since 1990, *Geophys. Res. Lett.*, *21*(13), 1371–1374, 1994.

Grooss, J. U., R. B. Pierce, P. J. Crutzen, W. L. Grose, and J. M. Russell III, Re-formation of chlorine reservoirs in southern hemisphere polar spring, *J. Geophys. Res.*, *102*(D11), 13141–13152, 1997.

Gunson, M., et al., The Atmospheric Trace Molecule Spectroscopy (ATMOS) experiment: Deployment on the ATLAS space shuttle missions, *Geophys. Res. Lett.*, *23*(17), 2333–2336, 1996.

Hamill, P., O. Toon, and R. Turco, Characteristics of polar stratospheric clouds during the formation of the Antarctic ozone hole, *Geophys. Res. Lett.*, *13*(12), 1288–1291, 1986.

Hampson, J., Photochemical behaviour of the ozone layer, *Tech. Note, Can. Armament Res. and Dev. Estab, TN 1627/64*, 1964.

Hanson, D., and K. Mauersberger, Laboratory studies of the nitric acid trihydrate: implications for the south polar stratosphere, *Geophys. Res. Lett.*, *15*(8), 855–858, 1988.

Hanson, D., and A. Ravishankara, The reaction $ClONO_2$ + HCl on NAT, NAD and frozen sulfuric acid and the hydrolysis of N_2O_5 and $ClONO_2$ on frozen sulfuric acid, *J. Geophys. Res.*, *98*, 22931–22936, 1994.

Hanson, D. R., A. R. Ravishankara, and S. Solomon, Heterogeneous reactions in sulfuric acid aerosols: A framework for model calculations, *J. Geophys. Res.*, *99*(D2), 3615–3629, 1994.

Hase, F., T. Blumenstock, and C. Paton-Walsh, Analysis of the instrumental line shape of high-resolution Fourier transform IR spectrometers with gas cell measurements and new retrieval software, *App. Optics*, *38*, 3417–3422, 1999.

Hase, F., J. Hannigan, M. T. Coffey, A. Goldman, M. Höpfner, N. Jones, C. Rinsland, and S. Wood, Intercomparison of retrieval codes used for the analysis of high-resolution, ground-based FTIR measurements, *J. Quant. Spectrosc. Radiat. Transfer*, *87*, 25–52, 2004.

Hofmann, D., Balloon-borne measurements of middle atmosphere aerosols and trace gases in Antarctica, *Reviews of Geophysics*, *26*, 113–130, 1988.

Hofmann, D., Stratospheric cloud microlayers and small-scale temperature variations in the Arctic in 1989, *Geophys. Res. Lett.*, *17*(4), 369–372, 1990.

Hofmann, D., J. Rosen, and J. Harder, Aerosol measurements in the winter/spring Antarctic stratosphere 1. Correlative measurements with ozone, *J. Geophys. Res.*, *93*(D1), 665–676, 1988.

Hofmann, D., J. Harder, J. Rosen, J. Hereford, and J. Carpenter, Ozone profile measurements at McMurdo Station, Antarctica, during the spring of 1987, *J. Geophys. Res.*, *94*(D14), 16527–16536, 1989a.

Hofmann, D., T. Deshler, P. Aimedieu, W. A. Matthews, P. Johnston, Y. Kondo, W. Sheldon, G. Byrne, and J. Benbrook, Stratospheric clouds and ozone depletion in the Arctic during January 1989, *Nature*, *340*, 117–121, 1989b.

Hofmann, D., S. Ottmans, J. Harris, B. Johnson, and J. Lathrop, Ten years of ozonesonde measurements at the South Pole: Implications for the recovery of springtime Antarctic ozone, *J. Geophys. Res.*, *102*, 8931–8943, 1997.

Hubler, G., et al., Redistribution of reactive odd nitrogen in the lower Arctic stratosphere, *Geophys. Res. Lett.*, *17*(4), 453–456, 1990.

Irie, H., M. Koike, K. Kondo, G. E. Bodeker, M. Y. Danilin, and Y. Sasano, Redistribution of nitric acid in the Arctic lower stratosphere during the winter of 1996-1997, *J. Geophys. Res.*, *106*(D19), 23139–23150, 2001.

ISO, *Guide to the Expression of Uncertainty in Measurement.* International Organisation for Standardization, Switzerland, 1 edn., 1993.

Jaegle, L., et al., Evolution and stoichiometry of heterogeneous processing in the Antarctic stratosphere, *J. Geophys. Res.*, *102*, 13235–13253, 1997.

Jaramillo, M., R. deZafra, J. Barrett, L. Emmons, P. Solomon, and A. Parrish, Measurements of hydrogen cyanide at McMurdo station Antarctica: Further evidence of winter stratospheric subsidence, *J. Geophys. Res.*, *94*(D14), 16773–16777, 1989.

Johnston, H., Reduction of stratospheric ozone by nitrogen dioxide catalysts from supersonic transport exhaust, *Science*, *173*, 517, 1971.

Jones, A. E., R. Weller, A. Minikin, E. W. Wolff, W. T. Sturges, H. P. McIntyre, S. R. Leonard, O. Schrems, and S. Bauguitte, Oxidised nitrogen chemistry and speciation in the Antarctic troposphere, *J. Geophys. Res.*, *104*(D17), 21355–21366, 1999.

Joseph, J. K., W. J. Wiscombe, and J. A. Weinman, The Delta-Eddington approximation for radiative flux transfer, *J. Atmos. Sci.*, *33*, 2452–2459, 1976.

Judson-Technologie, Judson Technologie online documentation, from http://www.polytec-pi.fr/Judson, Visited 01/05, 2005.

Kanamitsu, M., Description of the NMC global data assimilation and forecast system, *Weather and Forecasting*, *4*, 335–342, 1989.

Kawa, S., et al., Activation of chlorine in sulfate aerosol as inferred from aircraft observations, *J. Geophys. Res.*, *102*, 3921–3933, 1997.

Kelly, K., A. Tuck, L. Heidt, M. Loewenstein, J. Podolske, S. Strahan, and J. Vedder, A comparison of ER-2 measurements of stratospheric water vapour between the 1987 Antarctic and 1989 Arctic missions, *Geophys. Res. Lett.*, *17*(4), 465–468, 1990.

Kelly, K. K., et al., Dehydration in the lower Antarctic stratosphere during late winter and early spring 1987, *J. Geophys. Res.*, *94*(D9), 11317–11357, 1989.

Kempler, S. J., NMC gridded data for UARS Project - Data Set Document, Available from http://eosdata.gsfc.nasa.gov/ guides/GSFC/guide/uars _nmc_gridded_dataset.gd.html, 2002.

Keys, J., and P. Johnston, Stratospheric NO_2 and O_3 in Antarctica: Dynamic and chemically controlled variations, *Geophys. Res. Lett.*, *13*(12), 1260–1263, 1986.

Keys, J., P. Johnston, R. Blatherwick, and F. Murcray, Evidence for heterogeneous reactions in the Antarctic autumn stratosphere, *Nature*, *361*, 49–51, 1993.

Keys, J. G., S. W. Wood, N. B. Jones, and F. J. Murcray, Spectral measurements of HCl in the plume of the Antarctic volcano Mount Erebus, *Geophys. Res. Lett.*, *25*(13), 2421–2424, 1998.

Kinne, S., O. Toon, G. Toon, C. Farmer, E. Browell, and M. McCormick, Measurements of size and composition of particles in polar stratospheric clouds from infrared solar absorption spectra, *J. Geophys. Res.*, *94*(D14), 16481–16491, 1989.

Kondo, Y., et al., Balloon-borne measurements of total reactive nitrogen, nitric acid and aerosol in the cold Arctic stratosphere, *Geophys. Res. Lett.*, *17*(4), 437–440, 1990.

Kondo, Y., W. A. Matthews, S. Solomon, M. Koike, M. Hayashi, K. Yamazaki, H. Nakajima, and K. Tsukui, Ground based measurements of column amounts of NO_2 over Syowa Station, Antarctica, *J. Geophys. Res.*, *99*(D7), 14535–14548, 1994a.

Kondo, Y., U. Schmidt, T. Sugita, P. Aimedieu, M. Koike, H. Ziereis, and Y. Iwasaka, Total reactive nitrogen, N_2O, and ozone in the winter Arctic stratosphere, *Geophys. Res. Lett.*, *21*(13), 1247–1250, 1994b.

Kondo, Y., H. Irie, M. Koike, and G. E. Bodeker, Denitrification and nitrification in the Arctic stratosphere during the winter of 1996-1997, *Geophys. Res. Lett.*, *27*, 337–340, 2000.

Kreher, K., J. G. Keys, P. V. Johnston, U. Platt, and X. Liu, Ground-based measurements of OClO and HCl in austral spring 1993 at Arrival Heights, Antarctica., *Geophys. Res. Lett.*, *23*(12), 1545–1548, 1996.

Kreher, K., P. Johnston, S. Wood, B. Nardi, and U. Platt, Ground-based measurements of tropospheric and stratospheric BrO at Arrival Heights, Antarctica, *Geophys. Res. Lett.*, *24*(23), 3021–3024, 1997.

Kruger, B., Observations of polar stratospheric clouds in the Arctic winter 1989 at 79°N, *Geophys. Res. Lett.*, *17*(4), 365–268, 1990.

Kuester, S., P. Franchois, and M. Fanning, Total ozone, ozone vertical distributions and stratospheric temperatures at South Pole, Antarctica in 1986 and 1987, *J. Geophys. Res.*, *94*(D9), 11429–11436, 1989.

Lait, L. R., P. A. Newman, and M. R. Schoeberl, *Using the Goddard Automailer*, Goddard Space Flight Center, Available from http://code916.gsfc.nasa.gov/Data_services/Automailer/index.html, 2004.

Larsen, N., Polar Stratospheric Clouds: Microphysical and optical models, Scientific Report 00-06, Danish Meteorological Institute, 2000.

Larsen, N., B. M. Knudsen, J. M. Rosen, N. Kjome, and E. Kyro, Balloon-borne backscatter observations of type I PSC formation: Inference about physical state from trajectory analysis, *Geophys. Res. Lett.*, *23*, 1091–1094, 1996.

Larsen, N., B. M. Knudsen, J. M. Rosen, N. T. Kjome, R. Neuber, and E. Kyro, Temperature histories in liquid and solid polar stratospheric cloud formation, *J. Geophys. Res.*, *102*(D19), 23505–23517, 1997.

Lary, D. J., and J. A. Pyle, Diffuse radiation, twilight and photochemistry, *J. Atmos. Chem*, *13*, 373–392, 1991.

Luo, B., K. Carslaw, T. Peter, and S. Clegg, Vapour pressures of $H_2SO_4/HNO_3/HCl/HBr/H_2O$ solutions to low stratospheric temperatures, *Geophys. Res. Lett.*, *22*, 247–250, 1995.

Mankin, W., M. Coffey, A. Goldman, M. Schoeberl, L. Lait, and P. Newman, Airborne measurements of stratospheric constituents over the Arctic in the winter of 1989, *Geophys. Res. Lett.*, *17*(4), 473–476, 1990.

Manney, G. L., R. W. Zurek, O. A., and R. Swinbank, On the motion of air through the stratospheric polar vortex, *J. Atmos. Sci.*, *51*(20), 2973–2994, 1994.

Marti, J., and K. Mauersberger, A survey and new measurements of ice vapor pressure at temperatures between 170 and 250K, *Geophys. Res. Lett.*, *20*, 363–366, 1993.

Massoli, P., Study of polar stratospheric clouds in Antarctica through LIDAR measurements, Ph.D. thesis, University of Siena, c/o Institute for Atmospheric Sciences and Climate, ISAC-CNR, Rome, 2005.

McCormick, M., and J. Larsen, Antarctic measurements of ozone by SAGE II in the spring of 1985, 1986 and 1987, *Geophys. Res. Lett.*, *15*(8), 907–910, 1988.

McCormick, M., and C. Trepte, SAM II measurements of Antarctic PSCs and aerosols, *Geophys. Res. Lett.*, *13*(12), 1284–1287, 1986.

McCormick, M., H. Steele, P. Hamill, W. Chu, and T. Swissler, Polar stratospheric cloud sightings by SAM II, *J. Atmos. Sci*, *39*, 1387–1397, 1982.

McCormick, M., C. Trepte, and M. Pitts, Persistence of polar stratospheric clouds in the southern polar region, *J. Geophys. Res.*, *94*(D9), 11241–11251, 1989.

McCormick, M., G. Kent, W. Hunt, M. Osborn, L. Poole, and M. Pitts, Arctic polar stratospheric cloud observations by airborne lidar, *Geophys. Res. Lett.*, *17*(4), 381–383, 1990.

McElroy, M., R. Salawitch, and S. Wofsy, Antarctic O_3: Chemical mechanisms for the spring decrease, *Geophys. Res. Lett.*, *13*(12), 1296–1299, 1986a.

McElroy, M., R. Salawitch, S. Wofsy, and J. Logan, Reductions of Antarctic ozone due to synergistic interactions of chlorine and bromine, *Nature*, *321*, 759–762, 1986b.

McPherson, R., B. K.H, R. Kistler, G. Rasch, and D. Gordon, The NMC operational global data assimilation system, *Mon. Weather Rev.*, *107*, 1445–1461, 1979.

Meier, A., *Determination of atmospheric trace gas amounts and corresponding natural isotopic ratios by means of ground-based FTIR spectroscopy in the high Arctic*, Reports on Polar Research. Alfred Wegener Institute for Polar and Marine Research, Bremerhaven, 1997.

Meier, A., A. Goldman, P. S. Manning, T. M. Stephen, C. P. Rinsland, N. B. Jones, and S. W. Wood, Improvements to air mass calculations from ground-based infrared measurements, *J. Quant. Spectrosc. Radiat. Transfer*, *83*, 109–113, 2004.

Meilinger, S., T. Koop, B. P. Luo, T. Huthwelker, K. S. Carslaw, U. Krieger, P. J. Crutzen, and T. Peter, Size-dependent stratospheric droplet composition in mesoscale temperature fluctuations and their potential role in PSC freezing, *Geophys. Res. Lett.*, *22*, 3031–3034, 1995.

Michelson, A. A., and E. W. Morley, On the relative motion of the Earth and the luminiferous aether, *Philos. Mag.*, *24*, 449–463, 1887.

Middlebrook, A., B. Koehler, L. McNeill, and M. Tolbert, Formation of model polar stratospheric cloud films, *Geophys. Res. Lett.*, *12*(24), 2417–2420, 1992.

Middlebrook, A. M., M. A. Tolbert, and K. Drdla, Evaporation studies of model polar stratospheric cloud films, *Geophys. Res. Lett.*, *23*(16), 2145–2148, 1996.

Miller, A. J., NDSC NMC data set description, Documentation provided with the NDSC NMC meteorological analyses, Available from http://badc.nerc.ac.uk/ cgi-bin/data_browser/badc/ndsc/doc/meta/ncep, 2004.

Molina, L. T., and M. J. Molina, Production of Cl_2O_2 through the self-reaction of the ClO radical, *J. Phys. Chem.*, *91*, 433–436, 1987.

Molina, M., and F. Rowland, Stratospheric sink for chlorofluoromethanes: chlorine atom-catalysed destruction of ozone, *Nature*, *249*, 810–812, 1974.

Molina, M., R. Zhang, P. Woodridge, J. McMahon, J. Kim, H. Chang, and K. Beyer, Physical chemistry of $H_2SO_4/HNO_3/H_2O$ system: Implications for polar stratospheric clouds, *Science*, *261*, 1418–1423, 1993.

Moore, S. B., L. Keyser, M.-T. Leu, R. Turco, and R. Smith, Heterogeneous reactions on nitric acid trihydrate, *Nature*, *345*, 333–335, 1990.

Morrey, M. W., and R. S. Harwood, Interhemispheric differences in stratospheric water vapour during late winter, in version 4 MLS measurements, *Geophys. Res. Lett.*, *25*(2), 147–150, 1998.

Mount, G., R. Sanders, A. Schmeltekopf, and S. Solomon, Visible spectroscopy at McMurdo Station, Antarctica 1. Overview and daily variations of NO_2 and O_3, austral spring 1986, *J. Geophys. Res.*, *92*(D7), 8320–8328, 1987.

Mount, G., S. Solomon, R. Jakoubek, and A. Schmeltekopf, Observations of stratospheric NO_2 and O_3 at Thule, Greenland, *Science*, *242*, 555–558, 1988.

Murcray, D., T. Kyle, F. Murcray, and W. Williams, Nitric acid and nitric oxide in the lower stratosphere, *Nature*, *218*, 78–79, 1968.

Murcray, F., A. Goldman, R. Blatherwick, W. Matthews, and N. Jones, HNO_3 and HCl amounts over McMurdo during the spring of 1987, *J. Geophys. Res.*, *94*, 16615–16618, 1989.

Murcray, F., J. Starkey, W. Williams, W. Matthews, U. Schmidt, P. Aimedieu, and C. Camy-Peyret, HNO_3 profiles obtained during the EASOE campaign, *Geophys. Res. Lett.*, *21*(13), 1223–1226, 1994.

Murphy, D. M., and B. L. Gary, Mesoscale temperature fluctuations and polar stratospheric clouds, *J. Atmos. Sci.*, *52*, 1753–1760, 1995.

Nakajima, H., X. Liu, I. Murata, Y. Kondo, F. J. Murcray, M. Koike, Y. Zhao, and H. Nakane, Retrieval of vertical profiles of ozone from high-resolution infrared solar spectra at Rikubetsu, Japan, *J. Geophys. Res.*, *102*(D5), 29981–29990, 1997.

Nash, E. R., P. A. Newman, J. E. Rosenfield, and M. R. Schoeberl, An objective determination of the polar vortex using Ertel's potential vorticity, *J. Geophys. Res.*, *101*(D5), 9471–9478, 1996.

Nedoluha, G. E., R. M. Bevilacqua, K. W. Hoppel, M. Dähler, E. P. Shettle, J. H. Hornstein, M. D. Fromm, J. D. Lumpe, and J. E. Rosenfield, POAM III measurements of dehydration in the Antarctic lower stratosphere, *Geophys. Res. Lett.*, *27*, 1683–1686, 2000.

Neuber, R., et al., Latitudinal distribution of stratospheric aerosols during the EASOE winter 1991/92, *Geophys. Res. Lett.*, *21*(13), 1283–1286, 1994.

Newman, P., et al., Stratospheric meteorological conditions in the Arctic polar vortex, 1991-1992, *Science*, *261*, 1143–1146, 1993.

Newman, P., et al., An overview of the SOLVE/THESEO2000 campaign, *J. Geophys. Res.*, *107*(D20), doi:10.1029/2001JD001303, 2002.

Newman, P. A., About the NCEP data, Available from http://code916.gsfc.nasa.gov/Data_services/met/about_nmc_data.html, 1996.

Nichol, S. E., and C. Valenti, Intercomparison of total ozone measured at low sun angles by the Brewer and Dobson spectrophotometers at Scott Base, Antarctica, *Geophys. Res. Lett.*, *20*(19), 2051–2054, 1993.

Nichol, S. E., J. G. Keys, S. W. Wood, P. V. Johnston, and G. E. Bodeker, Intercomparison of total ozone data from a Dobson spectrophotometer, TOMS, visible wavelength spectrometer, and ozonesondes, *Geophys. Res. Lett.*, *23*(10), 1087–1090, 1996.

Notholt, J., The moon as a light source for FTIR measurements of stratospheric trace gases during the polar night: Application for HNO_3 in the Arctic, *J. Geophys. Res.*, *99*, 3607–3614, 1994.

Notholt, J., and R. Lehmann, The moon as a light source for atmospheric trace gas observations: measurement technique and analysis method, *J. Quant. Spectrosc. Radiat. Transfer*, *76*, 435–445, 2003.

Notholt, J., and O. Schrems, Ground-based FTIR measurements of vertical column densities of several trace gases above Spitsbergen, *Geophys. Res. Lett.*, *21*(13), 1351–1354, 1994.

Notholt, J., and O. Schrems, Ground-based FTIR spectroscopic absorption measurements of stratospheric trace gases in the Arctic with the sun and the moon as light sources, *J. Mol. Struct.*, *347*, 407–416, 1995.

Notholt, J., R. Neuber, O. Schrems, and T. V. Clarmann, Stratospheric trace gas concentrations in the Arctic polar night as derived by FTIR-spectroscopy with the moon as IR light source, *Geophys. Res. Lett.*, *20*(19), 2059–2062, 1993.

Notholt, J., P. von der Gathen, and S. Peil, Heterogeneous conversion of HCl and $ClONO_2$ during the Arctic winter 1992/1993 initiating ozone depletion, *J. Geophys. Res.*, *100*, 11269–11274, 1995.

Notholt, J., G. Toon, R. Lehmann, B. Sen, and J.-F. Blavier, Comparison of Arctic and Antarctic trace gas column abundances from ground-based Fourier transform infrared spectrometry, *J. Geophys. Res.*, *102*, 12863–12869, 1997a.

Notholt, J., G. Toon, F. Stordal, S. Solberg, N. Schmidbauer, E. Becker, A. Meier, and B. Sen, Seasonal variations of atmospheric trace gases in the high Arctic at 79°N, *J. Geophys. Res.*, *102*, 12855–12861, 1997b.

Notholt, J., G. Toon, C. Rinsland, N. S. Pougatchev, N. B. Jones, B. J. Connor, R. Weller, M. Gautrois, and O. Schrems, Latitudinal variations of trace gas concentrations in the free troposphere measured by solar absorption spectroscopy during a ship cruise, *J. Geophys. Res.*, *105*(D1), 1337–1349, 2000.

Peter, T., R. Muller, P. J. Crutzen, and T. Deshler, The lifetime of leewave-induced ice particles in the Arctic stratosphere: II. Stabilization due to NAT-coating, *Geophys. Res. Lett.*, *21*(13), 1331–1334, 1994.

Pommereau, J., and J. Piquard, Observations of the vertical distributions of stratospheric OClO, *Geophys. Res. Lett.*, *21*(13), 1231–1234, 1994a.

Pommereau, J., and J. Piquard, Ozone and nitrogen dioxide vertical distributions by UV-visible solar occultation from balloons, *Geophys. Res. Lett.*, *21*(13), 1227–1230, 1994b.

Poole, L., and M. Pitts, Polar stratospheric cloud climatology based on Stratospheric Aerosol Measurement II observations from 1978 to 1989, *J. Geophys. Res.*, *99*, 13083–13089, 1994.

Popp, P., et al., Severe and extensive denitrification in the 1999-2000 Arctic winter stratosphere, *Geophys. Res. Lett.*, *28*(15), 2875–2878, 2001.

Portmann, R., S. Solomon, R. Garcia, L. Thomason, L. Poole, and M. McCormick, Role of aerosol variations in anthropogenic ozone depletion in polar regions, *J. Geophys. Res.*, *101*, 22991–23006, 1996.

Pougatchev, N. S., B. J. Connor, and C. P. Rinsland, Infrared measurements of the ozone vertical distribution above Kitt Peak, *J. Geophys. Res.*, *100*(D8), 16689–16697, 1995.

Pougatchev, N. S., B. J. Connor, N. B. Jones, and C. P. Rinsland, Ground-based infrared measurements of the ozone vertical distribution in the troposphere and lower stratosphere, in *Proceedings of the XVIII Quadrennial Ozone Symposium*, edited by R. D. Bojkov, and G. Visconti, vol. 1 of *Atmospheric Ozone*, pp. 167–170, L'Aquila, Italy. Parco Scientifico e Technologico d'Abruzzio, 1998.

Prather, M., and A. H. Jaffe, Global impact of the Antarctic ozone hole: Chemical propagation, *J. Geophys. Res.*, *95*(D4), 3473–3492, 1990.

Prather, M., M. McElroy, and S. Wofsy, Reductions in ozone at high concentrations of stratospheric halogens, *Nature*, *312*, 227–231, 1984.

Prather, M. J., Numerical advection by conservation of second-order moments, *J. Geophys. Res.*, *91*, 6674–6681, 1986.

Preiswerk, D., and R. G. Najjar, A global, open-ocean model of carbonyl sulfide and its air-sea flux, *Global Biogeochem. Cycles*, *14*(2), 585–598, 2000.

Pueschel, R., K. Snetsinger, P. Hamill, J. K. Goodman, and M. P. McCormick, Nitric acid in polar stratospheric clouds: similar temperature of nitric acid condensation and cloud formation, *Geophys. Res. Lett.*, *17*(4), 429–432, 1990.

Pyle, J., et al., An overview of the EASOE campaign, *Geophys. Res. Lett.*, *21*(13), 1191–1194, 1994.

Ramaswamy, V., Dehydration mechanism in the Antarctic stratosphere during winter, *Geophys. Res. Lett.*, *15*(8), 863–866, 1988.

Randel, W. J., R. Wu, J. M. Russell III, A. Roche, and J. W. Waters, Seasonal cycles and QBO variations in stratospheric CH_4 and H_2O observed in UARS HALOE data, *J. Atmos. Sci.*, *55*, 163–185, 1998.

Ravishankara, A., and D. Hanson, Differences in the reactivity of Type I polar stratospheric clouds depending on their phase, *J. Geophys. Res.*, *101*, 3885–3890, 1996.

Reber, C., C. Trevathan, R. McNeal, and M. Luther, The Upper Atmosphere Research Satellite (UARS) Mission, *J. Geophys. Res.*, *98*, 10643–10647, 1993.

Ricaud, P., et al., Stratosphere over Dumont d'Urville, Antarctica, in winter 1992, *J. Geophys. Res.*, *103*(D11), 13267–13284, 1998.

Rinsland, C., et al., Long-term trends of inorganic chlorine from ground-based infrared solar spectra: Past increases and evidence for stabilization, *J. Geophys. Res.*, *108*(D8), doi: 10.1029/2002JD003001, 2003.

Rinsland, C. P., J. S. Levine, A. Goldman, N. D. Sze, M. K. W. Ko, and D. W. Johnson, Infrared measurements of HCl and HF total column abundances above Kitt Peak, 1977-1990: Seasonal cycles, long-term increases, and comparisons with model calculations, *J. Geophys. Res.*, *96*, 15523–15540, 1991.

Riviere, E. D., Y. Terao, and H. Nakajima, A Lagrangian method to study stratospheric nitric acid variations in the polar regions as measured by the Improved Limb Atmospheric Spectrometer, *J. Geophys. Res.*, *108*(D23), doi: 10.1029/2003JD003718, 2003.

Roche, A., J. Kumer, J. Mergenthaler, G. Ely, W. Uplinger, J. Potter, T. James, and L. Sterritt, The Cryogenic Limb Array Etalon Spectrometer (CLAES) on UARS: Experiment description and performance, *J. Geophys. Res.*, *98*(D6), 10763–10775, 1993a.

Roche, A. E., J. B. Kumer, and J. L. Mergenthaler, CLAES observations of $ClONO_2$ and HNO_3 in the Antarctic stratosphere between June 15 and September 17, 1992, *Geophys. Res. Lett.*, *20*, 1223–1226, 1993b.

Roche, A. E., et al., Observations of lower-stratospheric $ClONO_2$, HNO_3, and aerosol by the UARS CLAES experiment between January 1992 and April 1993, *J. Atmos. Sci.*, *51*(20), 2877–2902, 1994.

Rodgers, C., *Inverse Methods for Atmospheric Sounding. Theory and Practice*, vol. 2 of *Series on Atmospheric, Oceanic and Planetary Physics*. World Scientific, Oxford, 1 edn., 2000.

Rodgers, C. D., Retrieval of atmospheric temperature and composition from remote measurements of thermal radiation, *Rev. Geophys. Space Phys.*, *14*(4), 609–625, 1976.

Rodgers, C. D., Characterization and error analysis of profiles retrieved from remote sounding measurements, *J. Geophys. Res.*, *95*, 5587–5595, 1990.

Rodgers, C. D., and B. J. Connor, Intercomparison of remote sounding instruments, *J. Geophys. Res.*, *108*, doi:10.1029/2002JD002299, 2003.

Rosen, J., D. Hofmann, and J. Harder, Aerosol measurements in the winter/spring Antarctic stratosphere 2. Impact on polar stratospheric cloud theories, *J. Geophys. Res.*, *93*(D1), 677–686, 1988a.

Rosen, J. M., D. J. Hofmann, J. R. Carpenter, and J. W. Harder, Balloon borne Antarctic frost point measurements, *Geophys. Res. Lett.*, *15*(8), 859–862, 1988b.

Rosen, J. M., N. T. Kjome, N. Larsen, B. M. Knudsen, E. Kyrō, R. Kivi, J. Karhu, R. Neuber, and I. Beninga, Polar stratospheric cloud threshold temperatures in the 1995-1996 Arctic vortex, *J. Geophys. Res.*, *102*(D23), 28195–28202, 1997.

Rosenfield, J. E., P. Newman, and M. Schoeberl, Computations of diabatic descent in the stratospheric polar vortex, *J. Geophys. Res.*, *99*(D8), 16677–16689, 1994.

Rothman, L. S., et al., The HITRAN molecular spectroscopic database edition of 2000 including updates through 2001, *J. Quant. Spectrosc. Radiat. Transfer*, *82*, 5–44, 2003.

Russell, J., et al., The Halogen Occultation Experiment, *J. Geophys. Res.*, *98*, 10777–10797, 1993.

Russell, J. M., et al., Validation of hydrogen chloride measurements made by the Halogen Occultation Experiment from the UARS platform, *J. Geophys. Res.*, *101*(D6), 10151–10162, 1996.

Salby, M. L., *Fundamentals of Atmospheric Physics*, vol. 61 of *International Geophysics Series*. Academic Press, 1996.

Sander, S. P., et al., Chemical kinetics and photochemical data for use in stratospheric modeling: Evaluation number 14, JPL Publication 02-25, JPL, NASA, 2003.

Sanders, R., S. Solomon, G. Mount, M. Bates, and A. Schmeltekopf, Visible spectroscopy at McMurdo Station, Antarctica 3. Observations of NO_3, *J. Geophys. Res.*, *93*(D7), 8339–8342, 1987.

Sanders, R., S. Solomon, M. Carroll, and A. Schmeltekopf, Visible and near-ultraviolet spectroscopy at McMurdo Station, Antarctica 4. Overview and daily measurements of NO_2, O_3 and OClO during 1987, *J. Geophys. Res.*, *94*(D9), 11381–11391, 1989.

Santee, M., G. Manney, N. Livesey, and J. Waters, UARS Microwave Limb Sounder observations of denitrification and ozone loss in the 2000 Arctic late winter, *Geophys. Res. Lett.*, *27*(19), 3213–3216, 2000.

Santee, M. L., W. G. Read, J. W. Waters, L. Froidevaux, G. L. Manney, D. A. Flower, R. F. Jarnot, R. S. Harwood, and G. E. Peckham, Interhemispheric differences in polar stratospheric HNO_3, H_2O, ClO and O_3, *Science*, *267*, 849–852, 1995.

Santee, M. L., et al., Chlorine deactivation in the lower stratospheric polar regions during late winter: Results from UARS, *J. Geophys. Res.*, *101*(D13), 18835–18859, 1996.

Santee, M. L., A. Tabazadeh, G. L. Manney, R. J. Salawitch, L. Froidevaux, W. G. Read, and J. W. Waters, UARS microwave limb sounder HNO_3 observations: Implications for Antarctic polar stratospheric clouds, *J. Geophys. Res.*, *103*(D11), 13285–13313, 1998.

Santee, M. L., G. L. Manney, L. Froidevaux, W. G. Read, and J. W. Waters, Six years of UARS Microwave Limb Sounder HNO_3 observations: seasonal, interhemispheric, and interannual variations in the lower stratosphere, *J. Geophys. Res.*, *104*(D7), 8225–8246, 1999.

Schiller, C., A. Wahner, U. Platt, H.-P. Dorn, J. Callies, and D. Ehhalt, Near UV atmospheric absorption measurements of column abundances during Airborne Arctic Stratospheric Expedition, January - February 1989: 2. OClO observations, *Geophys. Res. Lett.*, *17*(4), 501–504, 1990.

Schmidt, U., R. Bauer, A. Engel, R. Borchers, and J. Lee, The variation of available chlorine, Cl_y, in the Arctic polar vortex during EASOE, *Geophys. Res. Lett.*, *21*(13), 1215–1218, 1994.

Schoeberl, M., L. Lait, P. Newman, and J. Rosenfield, The structure of the polar vortex, *J. Geophys. Res.*, *97*(D8), 7859–7882, 1992.

Schoeberl, M., et al., The evolution of ClO and NO along airparcel trajectories, *Geophys. Res. Lett.*, *20*(22), 2511–2514, 1993.

Schoeberl, M. R., and L. C. Sparling, Trajectory modelling, in *Diagnostic Tools in Atmospheric Physics, Proc S.I.F Course CXVI*, edited by G. Fiocco, and G. Visconti, North Holland, Amsterdam. 1994.

Shine, K. P., The middle atmosphere in the absence of dynamical heat fluxes, *Q. J. R. Meteorol. Soc.*, *113*, 603–633, 1987.

Smith, B. C., *Fundamentals of Fourier transform infrared spectroscopy.* CRC Press, 1996.

Solomon, P., B. Connor, R. deZafra, A. Parrish, J. Barrett, and M. Jaramillo, High concentrations of chlorine monoxide at low altitudes in the Antarctic spring stratosphere: secular variation, *Nature*, *328*, 411–413, 1987a.

Solomon, P., J. Barrett, B. Connor, S. Zoonematkermani, A. Parrish, A. Lee, J. Pyle, and M. Chipperfield, Seasonal observations of chlorine monoxide in the stratosphere over Antarctica during the 1996-1998 ozone holes and comparison with the SLIMCAT 3D model, *J. Geophys. Res.*, *105*(D23), 28979–29001, 2000.

Solomon, P., B. Connor, J. Barrett, T. Mooney, A. Lee, and A. Parrish, Measurements of stratospheric ClO over Antarctica in 1996-2000 and implications for ClO dimer chemistry, *Geophys. Res. Lett.*, *29*(15), doi: 10.1029/2002GL015232, 2002.

Solomon, S., Progress towards a quantitative understanding of Antarctic ozone depletion, *Nature*, *347*, 347–354, 1900.

Solomon, S., The mystery of the Antarctic ozone 'hole', *Rev. Geophys.*, *26*(1), 131–148, 1988.

Solomon, S., Stratospheric ozone depletion: a review of concepts and history, *Rev. Geophys.*, *37*(3), 275–316, 1999.

Solomon, S., R. Garcia, F. Rowland, and D. Wuebbles, On the depletion of Antarctic ozone, *Nature*, *321*, 755–758, 1986.

Solomon, S., G. Mount, R. Sanders, and A. Schmeltekopf, Visible spectroscopy at McMurdo Station, Antarctica 2. Observations of OClO, *J. Geophys. Res.*, *92*(D7), 8329–8338, 1987b.

Solomon, S., R. Sanders, M. Carroll, and A. Schmeltekopf, Visible and near-ultraviolet spectroscopy at McMurdo station, Antarctica 5. Observations of the diurnal variations of BrO and OClO, *J. Geophys. Res.*, *94*(D9), 11393–11403, 1989.

SPARC, Sparc Assessment of Upper Tropospheric and Stratospheric Water Vapour, Tech. rep., WMO/ICSU/IOC, 2000.

Special Edition, AAOE Special Edition, *J. Geophys. Res.*, *94*(D9), 11179–11737, 1989a.

Special Edition, AAOE Special Edition 2, *J. Geophys. Res.*, *94*(D14), 16437–16857, 1989b.

Special Edition, AASE II Special Edition, *Geophys. Res. Lett.*, *20*(22), 2499–2578, 1993a.

Special Edition, AASE II Special Edition, *Science*, *261*, 1128–1158, 1993b.

Special Edition, UARS Special Edition, *Geophys. Res. Lett.*, *20*(12), 1215–1330, 1993c.

Special Edition, EASOE Special Edition, *Geophys. Res. Lett.*, *21*(13), 1189–1490, 1994.

Special Edition, ASHOE/MAESA Special Edition, *J. Geophys. Res.*, *102*(D3), 3899–3949, 1997a.

Special Edition, ASHOE/MAESA Special Edition, *J. Geophys. Res.*, *102*(D11), 13113–13299, 1997b.

Steele, H. M., P. Hamill, M. P. McCormick, and T. J. Swissler, The formation of polar stratospheric clouds, *J. Atmos. Sci.*, *40*, 2055–2067, 1983.

Stolarski, R., and R. Cicerone, Stratospheric chlorine: A possible sink for ozone, *Can. J. Chem*, *52*, 1610–1615, 1974.

Stowasser, M., et al., A characterization of the warm 1999 Arctic winter by observations and modelling: NO_y partitioning and dynamics, *J. Geophys. Res.*, *107*(D19), doi: 10.1029/2001JD001217, 2002.

Tabazadeh, A., and O. Toon, Observational constraints on the formation of Type 1a polar stratospheric clouds, *Geophys. Res. Lett.*, *23*, 2109–2112, 1996.

Tabazadeh, A., R. P. Turco, and M. Z. Jacobson, A model for studying the composition and chemical effects of stratospheric aerosols, *J. Geophys. Res.*, *99*(D6), 12897–12914, 1994a.

Tabazadeh, A., R. P. Turco, and M. Z. Jacobson, A study of Type I polar stratospheric cloud formation, *Geophys. Res. Lett.*, *21*(15), 1619–1622, 1994b.

Tabazadeh, A., M. L. Santee, M. Y. Danilin, H. C. Pumpfrey, P. A. Newman, P. J. Hamill, and J. L. Mergenthaler, Quantifying denitrification and its effect on ozone recovery, *Science*, *288*, 1407–1411, 2000.

Tabazadeh, A., E. J. Jensen, O. B. Toon, K. Drdla, and M. R. Schoeberl, Role of the stratospheric polar freezing belt in denitrification, *Science*, *291*, 2591–2594, 2001.

Taylor, F. W., et al., Remote sensing of atmospheric structure and composition by pressure modulator radiometry from space: The ISAMS experiment on UARS, *J. Geophys. Res.*, *98*(D6), 10799–10814, 1993.

Tolbert, M. A., and A. M. Middlebrook, Fourier transform infrared studies of model polar stratospheric cloud surfaces: growth and evaporation of ice and nitric acid/ice, *J. Geophys. Res.*, *95*(D13), 22423–22431, 1990.

Toohey, D., J. Anderson, W. Brune, and K. Chan, In situ measurements of BrO in the Arctic stratosphere, *Geophys. Res. Lett.*, *17*(4), 513–516, 1990.

Toohey, D., L. Avallone, L. Lait, P. Newman, M. Schoeberl, D. Fahey, E. Woodbridge, and J. Anderson, The seasonal evolution of reactive chlorine in the northern hemisphere stratosphere, *Science*, *261*, 1130–1134, 1993.

Toon, G., C. Farmer, L. Lowes, P. Schaper, J.-F. Blavier, and R. Norton, Infrared aircraft measurements of stratospheric composition over Antarctica during September 1987, *J. Geophys. Res.*, *94*(D14), 16571–16596, 1989.

Toon, G., C. B. Farmer, P. W. Schaper, L. L. Lowes, and R. H. Norton, Composition measurements of the 1989 Arctic winter stratosphere by airborne infrared solar absorption spectroscopy, *J. Geophys. Res.*, *97*, 7939–7961, 1992.

Toon, G., et al., Comparison of MkIV balloon and ER-2 aircraft measurements of atmospheric trace gases, *J. Geophys. Res.*, *104*, 26779–26790, 1999.

Toon, G. C., The JPL MkIV Interferometer, *Opt. Photonics News*, *2*, 19–21, 1991.

Toon, O., P. Hamill, R. Turco, and J. Pinto, Condensation of HNO_3 and HCl in the winter polar stratospheres, *Geophys. Res. Lett.*, *13*(12), 1284–1287, 1986.

Toon, O., R. Turco, and P. Hamill, Denitrification mechanisms in the polar stratospheres, *Geophys. Res. Lett.*, *17*(4), 445–448, 1990a.

Toon, O. B., E. V. Browell, S. Kinne, and J. Jordan, An analysis of lidar observations of polar stratospheric clouds, *Geophys. Res. Lett.*, *17*(4), 393–396, 1990b.

Toth, R. A., L. R. Brown, and E. A. Cohen, Linestrengths of nitric acid from 850 to 920 cm^{-1}, *J. Mol. Spectrosc.*, *218*, 151–168, 2003.

Trenberth, K., and J. G. Olson, Evaluation of NMC global analyses: 1979-1987, NCAR Technical Note NCAR/TN-299+STR, National Center for Atmospheric Research (NCAR), 1988.

Tuck, A., R. Watson, E. Condon, J. Margitan, and O. Toon, The planning and execution of ER-2 and DC-8 aircraft flights over Antarctica, August and September 1987, *J. Geophys. Res.*, *94*(D9), 11181–11222, 1989.

Tuck, A., W. Brune, and R. Hipskind, Airborne Southern Hemisphere Ozone Experiment/Measurements for Assessing the Effects of Stratospheric Aircraft (ASHOE/MAESA): A road map, *J. Geophys. Res.*, *102*, 3901–3904, 1997.

Turco, R., A. Plumb, and E. Condon, The Airborne Arctic Stratospheric Expedition: Prologue, *Geophys. Res. Lett.*, *17*(4), 313–316, 1990.

UNEP, Environmental effects of ozone depletion and its interactions with climate change: 1994 assessment, Tech. rep., United Nations Environment Programme (UNEP), 1994.

UNEP, Environmental effects of ozone depletion and its interactions with climate change: 1998 assessment, Tech. rep., United Nations Environment Programme (UNEP), 1998.

UNEP, Environmental effects of ozone depletion and its interactions with climate change: 2002 assessment, Tech. rep., United Nations Environment Programme (UNEP), 2002.

Voigt, C., et al., Nitric acid trihydrate (NAT) in polar stratospheric clouds, *Science*, *290*(5497), 1756–1758, 2000.

Wahner, A., R. Jakoubek, G. Mount, A. Ravishankara, and A. Schmeltekopf, Remote sensing observations of daytime column NO_2 during the Airborne Antarctic Ozone Experiment, August 22 to October 2 1987, *J. Geophys. Res.*, *94*(D14), 16619–16632, 1989a.

Wahner, A., R. Jakoubek, G. Mount, A. Ravishankara, and A. Schmeltekopf, Remote sensing observations of nighttime OClO column during the Airborne Antarctic Ozone Experiment, September 8, 1987, *J. Geophys. Res.*, *94*(D9), 11405–11411, 1989b.

Waibel, A., T. Peter, and H. Fischer, Arctic ozone loss due to denitrification, *Science*, *283*(5410), 2064, 1999.

Waterhouse, E. (ed.), *Ross Sea Region 2001: A state of the environment report for the Ross Sea region of Antarctica.* New Zealand Antarctic Institute, 2001.

Wauben, W. M. F., R. Bintanja, P. F. J. van Velthoven, and H. Kelder, On the magnitude of transport out of the Antarctic polar vortex, *J. Geophys. Res.*, *102*(D1), 1229–1238, 1997.

Waugh, D., and W. J. Randel, Climatology of Arctic and Antarctic polar vortices using elliptical diagnostics, *J. Atmos. Sci.*, *56*(11), 1594–1613, 1999.

Waugh, D., W. J. Randel, S. Pawson, P. A. Newman, and E. R. Nash, Persistence of the lower stratospheric polar vortices, *J. Geophys. Res.*, *104*(D22), 27191–27201, 1999.

Wayne, R. P., *Chemistry of Atmospheres.* Oxford University Press, 3 edn., 2000.

Webster, C., R. May, D. Toohey, L. Avallone, J. Anderson, and S. Solomon, In situ measurements of the ClO/HCl ratio: heterogeneous processing on sulfate aerosols and polar stratospheric clouds, *Geophys. Res. Lett.*, *20*(22), 2523–2526, 1993a.

Webster, C. R., et al., Chlorine chemistry on polar stratospheric cloud particles in the Arctic winter, *Science*, *261*, 1130–1133, 1993b.

Weisenstein, D. K., M. K. W. Ko, J. M. Rodriguez, and N. D. Sze, Impact of heterogeneous chemistry on model-calculated ozone change due to high speed civil transport aircraft, *Geophys. Res. Lett.*, *18*, 1991–1994, 1991.

WMO, Scientific assessment of ozone depletion, Tech. rep., World Meteorological Organization, 1994.

WMO, Scientific assessment of ozone depletion, Tech. rep., World Meteorological Organization, 1998.

WMO, Scientific assessment of ozone depletion, Tech. rep., World Meteorological Organization, 2002.

WMO, Antarctic Ozone Bulletin, #3/2003, Tech. Rep. 18 September 2003, World Meteorological Organization, 2003a.

WMO, Antarctic Ozone Bulletin, #6/2003, Tech. Rep. 30 October 2003, World Meteorological Organization, 2003b.

Wofsy, S., M. McElroy, and Y. Yung, The chemistry of atmospheric bromine, *Geophys. Res. Lett.*, *2*(6), 215–218, 1975.

Wofsy, S. C., R. J. Salawitch, J. H. Yatteau, M. B. McElroy, B. W. Gandrud, J. E. Dye, and D. Baumgardner, Condensation of HNO_3 on falling ice particles: Mechanism for denitrification of the polar stratosphere, *Geophys. Res. Lett.*, *17*, 449–452, 1990.

Wood, S., et al., Validation of version 5.20 ILAS HNO_3, CH_4, N_2O, O_3 and NO_2 using ground-based measurements at Arrival Heights and Kiruna, *J. Geophys. Res.*, *107*(D24), doi: 10.1029/2001JD000581, 2002.

Wood, S., R. L. Batchelor, A. Goldman, C. Rinsland, B. J. Connor, F. Murcray, T. M. Stephen, and D. N. Heuff, Ground-based nitric acid measurements at Arrival Heights, Antarctica, using solar and lunar Fourier transform infrared observations, *J. Geophys. Res.*, *109*(D18307), doi: 10.1029/2004JD004665, 2004.

Worsnop, D., L. Fox, M. Zahniser, and S. Wofsy, Vapour pressure of solid hydrates of nitric acid: implications for polar stratospheric clouds, *Science*, *259*, 71–74, 1993.

Wuebbles, D. J., Chlorocarbon emission scenarios: potential impact on stratospheric ozone, *J. Geophys. Res.*, *88*(C2), 1433–1443, 1983.

Yung, Y., J. Pinto, R. Watson, and S. Sander, Atmospheric bromine and ozone perturbations in the lower stratosphere, *J. Atmos. Sci*, *37*(2), 329, 1980.

Zeilik, M., S. A. Gregory, and E. v. P. Smith, *Introductory Astronomy and Astrophysics.* Saunders College Publishing, 3 edn., 1992.